Mark Wobrock

MICROPLASTICITY OF IDEALIZED SINGLE CRYSTALLINE AG CANTILEVERS CHARACTERIZED WITH METHODS OF HIGH RESOLUTION

SCHRIFTENREIHE DES INSTITUTS
FÜR ANGEWANDTE MATERIALIEN

BAND 68

KIT Scientific Publishing

Mark Wobrock

Microplasticity of idealized single crystalline Ag cantilevers characterized with methods of high resolution

Schriftenreihe
des Instituts für Angewandte Materialien
Band 68

Karlsruher Institut für Technologie (KIT)
Institut für Angewandte Materialien (IAM)

Eine Übersicht aller bisher in dieser Schriftenreihe erschienenen Bände finden Sie am Ende des Buches.

Microplasticity of idealized single crystalline Ag cantilevers characterized with methods of high resolution

by
Mark Wobrock

Scientific
Publishing

Dissertation, Karlsruher Institut für Technologie
KIT-Fakultät für Maschinenbau

Tag der mündlichen Prüfung: 04. Mai 2017
Gutachter: Prof. Dr. Oliver Kraft, Prof. Dr. Gerhard Dehm

Impressum

KIT Scientific
Publishing

Karlsruher Institut für Technologie (KIT)
KIT Scientific Publishing
Straße am Forum 2
D-76131 Karlsruhe

KIT Scientific Publishing is a registered trademark
of Karlsruhe Institute of Technology.
Reprint using the book cover is not allowed.

www.ksp.kit.edu

This document – excluding the cover, pictures and graphs – is licensed under a Creative Commons Attribution-Share Alike 4.0 International License (CC BY-SA 4.0): https://creativecommons.org/licenses/by-sa/4.0/deed.en

The cover page is licensed under a Creative Commons Attribution-No Derivatives 4.0 International License (CC BY-ND 4.0): https://creativecommons.org/licenses/by-nd/4.0/deed.en

Print on Demand 2017 – Gedruckt auf FSC-zertifiziertem Papier

ISSN 2192-9963
ISBN 978-3-7315-0682-9
DOI 10.5445/KSP/1000070130

Microplasticity of idealized single crystalline Ag cantilevers characterized with methods of high resolution

zur Erlangung des akademischen Grades eines

Doktors der Ingenieurwissenschaften

von der Fakultät für Maschinenbau
des Karlsruher Instituts für Technologie (KIT)

genehmigte

Dissertation

von

Mark Christian Wobrock

aus Saarbrücken

Tag der mündlichen Prüfung: 04.05.2017
Erster Gutachter: Prof. Dr. Oliver Kraft
Zweiter Gutachter: Prof. Dr. Gerhard Dehm

Das Wissen ist nicht der Zweck des Menschen auf Erden. Nur das Handeln gibt dem Manne ein würdiges Dasein; also entweder die praktische Anwendung des Gewussten oder die Vermehrung der Wissenschaft selbst muss sein Zweck sein. Denn auch das Letztere ist ein Handeln für den Fortschritt der Menschheit.

Hermann Ludwig Ferdinand von Helmholtz

Kurzfassung

Reduziert man die Größe eines Bauteils bis in den Mikro- und Submikrometerbereich, so verändert sich dessen Verhalten unter plastischer Verformung signifikant. Die physikalischen Mechanismen, die für dieses Phänomen verantwortlich sind, das für gewöhnlich als Größeneffekt bekannt ist, sind nicht vollständig verstanden und eine quantitative Vorhersage der Veränderungen der mechanischen Eigenschaften ist nicht möglich.

Ziel dieser Dissertation ist es durch Biegeexperimente an einseitig eingespannten Biegebalken aus Silber ein tiefgründiges Verständnis für Mikroplastizität zu entwickeln. Durch ihr Design können die Experimente als idealisiert angesehen werden: Die einseitig eingespannten Balken sind einkristallin, ihre Kristallorientierung rechtfertigt die Annahme eines ebenen Dehnungszustandes und schließlich weisen sie keine herstellungsbedingten Schädigungen oder Modifikationen auf. Der letztere Aspekt ist insbesondere deswegen relevant, da Forschungsgruppen im Gebiet der Mikroplastizität fast ausschließlich auf Focused Ion Beam (FIB) Geräte zur Probenherstellung zurück greifen, was einen Unsicherheitsfaktor hinsichtlich Verunreinigung durch Ga^+ Ionen schafft, dessen Einfluss auf die mechanischen Eigenschaften sich nicht quantifizieren lässt. Die Balken in dieser Arbeit wurden über eine auf Lithographie basierender Prozesskette hergestellt, bei dem diese prozessbedingten Schädigungen nicht auftreten. Darüber hinaus ist die FIB Prozedur sehr zeitaufwändig, wohingegen die neue Herstellungsroute mehrere 100 vergleichbare Teststrukturen gleichzeitig generiert. Das Design wurde so ausgelegt, dass auch Balken verschiedener Größe und Orientierung hergestellt werden konnten. Die fertigen Strukturen wurden dann mithilfe eines Nanoindentersystems belastet. Für die Gefügeanalyse wird die Methode der Transmission Kikuchi Diffraction (TKD) angewendet, welche eine laterale Auflösung von bis zu 10nm ermöglicht. Dies ermöglicht die gezielte Analyse von Versetzungsstrukturen nach der Verformung als Funktion der aufgebrachten Dehnung. Weiterhin wurde zur Datenauswertung ein auf dem Nye

Tensor basierendes Verfahren verwendet, welches tiefgründige Informationen hinsichtlich Burgersvektoren und Gleitebenen liefert.

Das Skalierungsgesetz für Balkendicken von 3 bis 1 µm, das in dieser Arbeit bestimmt wurde, weist einen Exponenten von 0,69 auf. Darüber hinaus konnte der Einfluss von Ga^+ Implantation infolge FIB für den gegebenen Fall quantifiziert werden, indem einige ausgewählte Teststrukturen bewusst bestrahlt wurden. Es wird beobachtet, dass eine Bestrahlung, welche vergleichbar zur Standard FIB Prozedur ausgelegt ist, die Fließspannung um etwa 20-30 % erhöht, den Exponenten des Skalierungsgesetzes um 0,12 wachsen lässt und das Verfestigungsverhalten verändert, sodass sich ein zunehmend kürzerer und abrupterer Übergang in ein elastisch-plastisches Lastplateau zeigt. Es wird festgestellt, dass die Veränderungen im Gefüge, die für dieses Verhalten verantwortlich sind, bereits während des Bildeinzugs mittels FIB, also noch vor dem eigentlichen Schneidprozess erzeugt werden.

Es wird gezeigt, dass plastische Deformation durch Gleiten entlang zweier effektiver Gleitsysteme erfolgt, welche auch im Einklang mit dem Schmid Gesetz sind. Für größere Balken wird zudem Zwillingsbildung beobachtet. Innerhalb eines Querschnittes durch den Balken ordnen sich die Versetzungen in Liniensegmenten an, deren Ausrichtung stets parallel zu den Burgersvektoren der effektiven Gleitsysteme läuft. Die mechanischen und mikrostrukturellen Beobachtungen können durch eine Kombination verschiedener Verformungsmechanismen gedeutet werden: Zum einen eine erhöhte Versetzungsdichte infolge des Dehnungsgradienten und zum anderen eine Versetzungsquellenlimitierung. Dies ist in Einklang mit bestehenden Theorien.

Abstract

When reducing the size of a given sample to the micro and sub-micrometer scale, its mechanical response to plastic deformation changes significantly. The underlying physical mechanisms of this phenomenon usually denoted as the size effect are not fully understood and a quantitative prediction of the changes is not possible.

The aim of this thesis is to gain deeper insights into microplasticity by carrying out bending experiments on silver cantilevers. By design, the experiments can be considered to be idealized: The cantilevers are single crystalline, their crystallographic orientation justifies a plane strain assumption and finally they show no fabrication-related damage or modifications. The latter is particularly important because research groups in the field of microplasticity rely almost exclusively on Focused Ion Beam (FIB) machining for sample preparation, creating an uncertainty due to contamination from Ga^+ ions, whose impact on mechanical properties cannot be quantified. The cantilevers tested in this work are made by a lithography-based process to avoid process-induced damage. Moreover, while FIB is a strongly time-consuming procedure, the new fabrication route generates several hundreds of equivalent testing structures at once. The layout is chosen to include cantilevers of different size and orientation. The cantilevers were deflected using a nanoindenter system. For microstructural analysis, the Transmission Kikuchi Diffraction (TKD) technique is used which offers a lateral resolution down to 10nm. After deformation, this allows analyzing dislocation structures with high precision as a function of imposed strain. Moreover to evaluate the data, a method based on Nye's tensor was used, providing profound information on Burgers vectors and glide planes.

The scaling law for the range of 3 to 1 µm of cantilever height found in this work has a scaling exponent of 0.69. Moreover, the impact of Ga^+ implantation during FIB was quantified for the given case by purposely contaminating selected testing structures. An irradiation comparable to the standard FIB milling procedure is found to increase the flow stress by about 20-30 %, to rise the scaling exponent of the size effect by 0.12 and to cause a change in hardening mechanisms which manifests in a shorter and more abrupt transition regime from the elastic part towards an elastic-plastic plateau. It is found that the microstructural alterations responsible for this behavior are induced during the FIB scanning of the cantilever when taking a micrograph, i.e. before executing the milling operation.

It is shown that plastic deformation is realized by two effective glide systems, which are expected from Schmid's law. For larger cantilevers, deformation by twinning is observed as well. Within a given cross section, dislocations are found to arrange on line segments that run parallel to either one of the Burgers vectors of the effective glide system. Due to the chosen crystal orientation which allows a plane strain approximation, any cross section scanned in 2D with TKD can justifiably be considered to be representative for the entire cantilever volume. The mechanical and microstructural observations could be interpreted by a combination of deformation mechanisms: These are an increased dislocation density due to the strain gradient and a limitation of available dislocation sources. This is in agreement with existing theories.

Danksagung

Die vorliegende Arbeit wurde im Zeitraum vom November 2011 bis zum Juli 2015 am Institut für angewandte Materialien (IAM) am Karlsruher Institut für Technologie (KIT) angefertigt.

Ich bedanke mich bei Herrn Prof. Dr. Oliver Kraft für die Annahme als Doktorand an seinem Institut, die wertvollen fachlichen Diskussionen und die Möglichkeit zur Teilnahme an verschiedenen internationalen und nationalen Konferenzen und Tagungen. Ferner möchte ich mich bei Herrn Dr. Stefan Sandfeld, für die Integration in die Forschungsgruppe FOR1650 bedanken. Der Deutschen Forschungsgemeinschaft DFG und der Karlsruhe Nano and Micro Facility (KNMF) danke ich für die Finanzierung des Projektes bzw. aller Reinraumprozesse.

Einen besonderes Dank möchte ich Herrn Dr. Patric Gruber aussprechen für die fachliche Betreuung der Arbeit. Ein hohes Maß an Freiheit bei der Gestaltung des Projektes verbunden mit ständiger Ansprechbarkeit und der Bereitschaft zu Diskussionen ermöglichten mir, meine Ideen zu verfolgen und die Arbeit in geordneten Bahnen durchzuführen.

Vor allem bedanke ich mich auch bei Herrn Moritz Wenk für die hilfreiche Unterstützung bei EBSD und TKD Experimenten und insbesondere für das von ihm entworfene MatLab Programm, mit dessen Hilfe die mikrostrukturellen Analysen möglich gemacht wurden. Sehr herzlich möchte ich bei Herrn Michael Ziemann bedanken für seine Unterstützung bei Datenauswertungen mittels Cross Court.

Bei den Mitarbeitern des Max-Planck Instituts für intelligente Systeme in Stuttgart, Herrn Dr. Gunther Richter und Frau Ilse Lakemeyer, möchte ich mich für die Herstellung der einkristallinen Ag Dünnschichten bedanken. Ferner danke ich Herrn Dr. Richter für die Bereitschaft zur Etablierung eines KNMF Projektes.

Ich bedanke mich bei den Mitarbeitern des Instituts für Mikrostrukturtechnik (IMT), insbesondere Herrn Dr. Alban Muslija, Herrn Andreas Bacher, Frau Birgit Hübner, Herrn Stefan Hengsbach, Herrn Peter-Jürgen Jakobs, Herrn Dr. Uwe Köhler und Frau Heike Fornasier für die Durchführung sämtlicher Reinraumprozesse und die kompetente Beratung bei der Entwicklung von geeigneten Strategien.

Ein weiteren Dank möchte ich Herrn Dr. Daniel Weygand und Herrn Markus Stricker aus der Forschungsgruppe FOR1650 ausrichten für die Durchführung der DDD Simulationen.

Bedanken möchte ich mich außerdem bei Herrn Dr. Holger Geßwein für die Ermöglichung von XRD Experimenten und die Beratung hierbei.

Bei Herrn Dr. Marc Legros bedanke ich mich für die Durchführung von TEM Analysen an den as-depsosited Ag Dünnschichten.

Sehr herzlich bedanke ich mich bei Frau Dr. Ruth Schwaiger für die Beratung bei Experimenten am Nanoindenter, sowie deren Auswertung. Dabei möchte ich insbesondere hervorheben, dass die Errechnung der Fließspannung auf einem von ihr erdachten Konzept beruht.

Für zahlreiche fachliche Gespräche, Denkanstöße und Diskussionen möchte ich mich in besonderer Weise bei Herrn Dr. Christian Brandl vom IAM, bei Frau Dr. Katrin Schulz aus der Forschungsgruppe FOR1650 und Herrn Christoph Pauli vom MECS (Uni Saarland) bedanken.

Schließlich bedanke ich mich bei allen Mitarbeitern vom IAM danken für ein überaus angenehmes Arbeitsklima, die zahlreichen freizeitlichen Aktivitäten, ihre Kollegialität und Unterstützung bei fachlichen Problemen.

Zuletzt möchte ich meinen Eltern herzlichst danken, die durch ihre Unterstützung und Motivation einen sehr entscheidenden Beitrag zum erfolgreichen Abschluss der Arbeit geliefert haben.

Contents

Kurzfassung i
Abstract iii
Danksagung v
List of symbols and abbreviations ix

1 Introduction and literature review 1
- 1.1 Principles of microplasticity 3
- 1.2 Strain gradient plasticity 8
- 1.3 Characteristics of cantilever bending 10
- 1.4 Fabrication of µm-sized cantilevers 16
- 1.5 Experimental investigation of dislocations 20
- 1.6 Summary of literature review and aims of this study 27

2 Sample preparation 31
- 2.1 Choice of cantilever orientation 31
- 2.2 Choice of cantilever layout 35
- 2.3 Epitaxial Ag thin film deposition by PVD 39
- 2.4 Electron beam lithography 47
- 2.5 Patterning with IBE 49
- 2.6 Isotropic wet-etching to remove redeposited Ag 55
- 2.7 Anisotropic Si etching 57

3 Characterization of the as-fabricated cantilevers 63
- 3.1 Characterization of initial shape 63
- 3.2 FIB treatment of the as-fabricated cantilevers 72

4 Mechanical Testing 77
- 4.1 Experimental setup 77
- 4.2 Calculation of flow stress 86
- 4.3 Normalized bending moment curves 89
- 4.4 Evaluation of the size effect 97
- 4.5 Effect of the flow stress criterion used 102
- 4.6 Influence of cantilever orientation 104

4.7 Characterization of hardening behavior 104
4.8 Influence of FIB contamination 110

5 Microstructural analysis 119
5.1 Experimental Setup 120
5.2 Estimating GND densities from misorientation data 125
5.3 Results 134
5.3.1 Slip systems 134
5.3.2 Glide steps 137
5.3.3 Dislocation arrangement and densities 137
5.3.4 Cross court 165

6 Summary and Discussion 169
6.1 Evaluation of specific dislocation types 169
6.2 Evolution of dislocation networks 175
6.3 Interpretation of the size effect 183
6.4 FIB contamination 186
6.5 Concluding remarks 192

Appendix 195
Framework for DDD simulations 195

List of figures 197
List of tables 205
References 207

List of symbols and abbreviations

CBED	Convergent electron beam diffraction
DDD	Discrete dislocation dynamics
DG	Dual glide
EBSD	Electron backscatter diffraction
ECCI	Electron channeling contrast imaging
ECP	Electron channeling pattern
EDM	Electronic discharge milling
EDP	Ethylene di-amine pyro-catechol
EDX	Energy dispersive X-ray spectroscopy
FIB	Focused ion beam
FWHM	Full width at half maximum
GND	Geometrically necessary dislocations
hcp	Hexagonal close packed
HS	High symmetry
HFW	Horizontal field width
ICCD-PDF	International centre of diffraction data - powder diffraction file
SF_6	Sulfur hexafluoride

TKD	Transmission Kikuchi diffraction
MEMS	Micro-electro-mechanical systems
KOH	Potassium hydroxide
SEM	Scanning electron microscopy
SACP	Selected area channeling pattern
SSD	Statistically stored dislocations
SRIM	Stopping and range of ions in matter
TMAH	Tetra-methyl ammonium hydroxide
TEM	Transmission electron microscopy
TKD	Kernel average misorientation
WDX	Wavelength dispersive X-ray spectroscopy
XRD	X-ray diffraction
XRR	X-ray reflectometry
σ_y	Yield strength
σ_0	Bulk strength
d	Characteristic length
τ	Resolved shear stress, flow stress for solid solution strengthening
G	Shear modulus
b	Burgers vector

ρ	Dislocation density
m	Schmid factor
E	Young's modulus
ν	Poisson ratio
S	Cantilever stiffness
I	Axial moment of inertia
l_0	Total cantilever length
l_{eff}	Effective cantilever length
h	Cantilever height
w	Cantilever width
l_u	Undercut length
l_i	Distance visual imprint to indentation site
u	Cantilever deflection
u_0	Cantilever pre-deflection
$\bar{u}$	Normalized cantilever deflection
h_u	Etch pit depth
l_v	Visible undercut
$l_{u,t}$	Total undercut length
Q	Electrical charge
I_{Ga+}	Gallium ion current

n_{Ga+}	Number of Ga ions
t	Time
e	Electron charge
A	Area
$\dot{h}$	Drift during indentation
$u_{i,corr}$	Drift corrected cantilever deflection
F	Force
φ	Ion fluence
M	Bending moment
$\overline{M}$	Normalized bending moment
σ	Stress
ε	Strain
R_{sat}	Saturation stress during hardening (Voce)
σ_f	Flow stress
l_c	Compliance length
$\boldsymbol{\overline{g}}$	Orientation matrix
$\mathbf{C_C}$	Crystal coordinate system
$\mathbf{C_S}$	Sample coordinate system
c	Concentration
$\mathbf{r}$	Misorientation axis

r	Atomic radius
θ, $\boldsymbol{\Delta\theta}$	Misorientation/Bragg angle, misorienation vector
u	Unit length
$\bar{\kappa}$	Curvature tensor
$\bar{\boldsymbol{\alpha}}$	Nye tensor
δ	Kronecker symbol, dielastic interaction
L	Minimization norm
w_L	Full width at half maximum (Lorentzian)
ξ	Correlation length
h_f	Critical thickness
κ	Strain gradient
α	Angle between Si{111} and Si{100} plane
φ	Ion fluence
η	Drag coefficient, parelastic interaction

1 Introduction and literature review

Scaling laws may be thought of as "ancient" knowledge: Galileo Galilei stated in his "Discourses and mathematical demonstrations relating to two new sciences" in 1632 that when comparing two machines of different size which are made of the same material and proportional in all of their parts "the bigger machine will always have the bigger weakness". He referred to the fact that the load a machine is able to support does not change linearly with its size, so a machine of twice the size cannot carry twice as much load. Instead, the smaller machine can carry more load with respect to its own weight. Nowadays the corresponding scaling laws for this case and many more (not only in the field of mechanics) are precisely known and are successfully applied to predict the behavior of machines and materials. The size reduction of machines and devices down to the µm scale is an ongoing trend which is rigorously pursued on an industrial basis, for example in the field of micro-electro-mechanical systems (MEMS) or semiconductor technology. Besides the benefit that using smaller parts for a such devices saves both design space and material cost, downscaling is further motivated by physical scaling laws which often predict considerable improvement of device performance when its respective parts are fabricated on a smaller scale.

However, when downscaling is pushed to the micro- and nanometer regime, a new trend is observed which can no longer be explained by these conventional scaling laws. At this scale, materials are generally found to have various extraordinary properties. Probably the most important manifestation of this "size effect" is the particularly high mechanical strength of small samples. Other properties such as ductility do not scale favorably with decreasing sample size. Nevertheless, the trend is usually denoted "smaller is stronger". The problem of being unable to predict and quantify mechanical behavior at this scale, however, is a crucial issue, especially for MEMS applications.

The size effect is not only triggered by reduction of the total sample size (external constraint). Instead, it is also observed, if a relevant microstructural feature such as grain size in polycrystals is reduced (internal constraint), which is reviewed in the work of Arzt (E. Arzt, 1998) or Zhu et al. (Zhu et al., 2008). A prominent example in the field of plasticity for such an internal constraint is the Hall-Petch relation (Hall, 1951; Petch, 1953) which can be used to calculate yield stress of a polycrystalline sample as a function of grain size. However, when entering the nanometer regime, this relation no longer holds true (Meyers et al., 2006; Carlton & Ferreira, 2007; Pande & Cooper, 2009). Numerous investigations of the deformation processes have been carried out, but there is still no overall agreement on various aspects, such as how different deformation mechanisms interact with each other, at which point or for which physical reason the dominance of a certain mechanism switches in favor of another one, etc. Due to this change in plastic deformation behavior and its complexity, it was stated that there is no universal scaling law like in the bulk regime (Kraft et al., 2010). At the same time, industry keeps pushing devices to ever smaller dimensions so the ability to predict the mechanical response of small samples under plastic deformation is indispensable. Therefore, the lack in fundamental understanding of plastic deformation mechanisms at small scale needs to be overcome first which will be an ongoing challenge.

Gaining fundamental knowledge about the size effect is best done by conducting idealized experiments. In this project, the samples are single crystalline which allows studying a certain aspect – in this case the behavior of dislocations – only as a function of the spatial confinement of the sample itself unimpaired from any internal constraints. Another vital aspect that needs to be met in order to gain information on deformation mechanisms is the ability to detect and analyze dislocations structures. Dislocations are the most important aspect in plasticity of crystalline samples and their experimental characterization is a challenging task that calls for methods of very high lateral resolution. Establishing a suitable idealized experimental setup, which allows studying the size effect in a meaningful way, is one of the aims of this work.

1.1 Principles of microplasticity

In the 1930s, the understanding of plasticity in crystalline materials has been revolutionized by the concept of dislocations as carriers of plastic deformation (Orowan, 1934; Polanyi, 1934; Taylor, 1934). The existence of dislocations allowed explaining phenomena such as the considerable difference between experimentally observed and theoretically predicted shear strength. The development that followed can be summarized briefly by saying that research in this field of "dislocation-based" plasticity continuously delivered more information about the physical laws that describes the behavior of dislocations. A dislocation distorts the crystal lattice not only in its immediate surroundings but also gives rise to long range strain fields. This strain field is key to a fundamental understanding of how dislocations move through the crystal (e.g. dislocation glide (Schmid & Boas, 1935)), how they are created (e.g. Frank-Read Sources), how they interact with other microstructural features or obstacles (e.g. grain boundaries, precipitations, inclusions), when they are annihilated, what happens when they are leaving the sample (e.g. glide steps) and more. The mentioned findings suffice to fundamentally describe the mechanisms taking place in bulk samples during plastic deformation. The most interesting and still not entirely understood part of plasticity, however, deals with the question how materials behave in the µm and sub-µm regime, where some transition from the conventional dislocation behavior has been reported, usually denoted as the size effect (Arzt, 1998; Zhu et al., 2008; Uchic et al., 2009; Kraft et al., 2010; Uchic, 2012). In general, upon downscaling, the material strength increases and the first empirical relationship that describes this increase was developed by Hall and Petch in the 1950s. They suggested that the yield strength σ_y scales with a characteristic length scale d in the following way:

$$\sigma_y = \sigma_0 + kd^n \tag{1.1}$$

where σ_0 is the bulk strength and k and n are constants. The characteristic length d describes the dimension that limits dislocation movement the most and in the case of the classical Hall-Petch relation it refers to the grain size of the sample material. The value of n was found to be on the order of $n = -0.5$.

The grain size is not always the most limiting dimension. Instead, the characteristic length d can be equal to a variety of dimensions, depending on the sample under investigation and the loading geometry. As mentioned previously, all possible dimensions can be classified into two categories: Either the limiting dimension is given by an intrinsic constraint which means by microstructural features, such as grain boundaries or precipitations, or by an extrinsic constraint, i.e. by the volume of the sample (E. Arzt, 1998; Zhu et al., 2008). A prominent example for the latter are single crystalline thin films, where the issue that needs to be addressed is whether a dislocation line "fits" within the confined space and how it can "channel" through it. Of course, there are cases, where it is hard to distinguish which constraint is the most limiting one, and/or how the two constraints influence each other (e.g. polycrystalline thin films). This is summarized in the work of Zhu et al. (Zhu et al., 2008). The authors distinguish the interaction between intrinsic and extrinsic constraints even further by the nature of the spatial confinement being either 1D, 2D or 3D. For example, a one dimensional constraint is given in thin films: From the works of Thompson (Thompson, 1993), the authors derive a yield stress σ_y by introducing a critical thickness value h_f in the form of

$$\sigma_y \propto \; C_1 {h_f}^{-1} + C_2 d^{-1} \tag{1.2}$$

where C_1 and C_2 are constants. This proportionality somewhat resembles critical thickness theory (Frank & van der Merwe, 1949; Matthews & Crawford, 1970). Using a different approach, Keller et al. (Keller et al., 1998) suggested a superposition of the critical thickness with the Hall-Petch effect described by equation (1.1) which leads to

$$\sigma_y \propto \; C_3 {h_f}^{-1} + C_4 d^{-0.5} \tag{1.3}$$

where C_3 and C_4 are constants. Both approaches (1.2) and (1.3) find agreement in literature. Therefore it can be seen, that the interactions between the two constraints are not fully understood and further work on existing models is desirable.

The reduction of d to the µm and sub-µm regime is accompanied by a change in deformation mechanisms which is responsible for the change in mechanical response of the samples. This is reviewed in the work of Kraft et al. (Kraft et al., 2010). The essential statement that can be made is that there is no universal scaling law that could describe the materials response to plastic deformation for any size along with the mechanisms involved. Instead plasticity has to be categorized into three individual sections, depending on the value of d. For characteristic lengths $d > 1\ \mu m$, plasticity is governed by the collective behavior of dislocations which are pre-existent in the sample. Furthermore, it can be assumed that potential dislocation sources are always at disposal and can be activated any time (mean-field assumption (Demir et al., 2010)). Within this bulk regime, stage I glide, as well as dislocation pile-ups at grain boundaries are among the dominant mechanisms determining the mechanical response of the samples. The corresponding increase in strength with decreasing size can be expressed by the classical Hall-Petch relation (Hall, 1951; Petch, 1953) expressed by equation (1.1).

If d drops to the sub-µm regime ($100\ nm < d < 1\ \mu m$) a transition is found as plastic deformation is determined by individual dislocations. The origin for the change in deformation mechanisms is that for a sample of typical dislocation density 10^{12} m^{-2} to 10^{13} m^{-2}, the spacing between dislocations is on the order of 1 µm and thereby higher than sample size itself. When the spatial confinement is pushed this far the availability and activation of dislocation sources becomes a limiting factor. For example due to the limited space, a dislocation generated by a Frank-Read source may already have reached the extremities of the sample volume and left the crystal, before the source can emit a new dislocation. Greer and Nix (Greer & Nix, 2006) suggested that if dislocations keep leaving the crystal, a dislocation starved state may be reached which results in a strong increase of material strength as high stresses are needed to generate new dislocations. In literature, the term exhaustion hardening is often used to describe the strengthening effect caused by a loss of dislocations due to shutdown of sources, mechanical annealing or dislocation starvation (Rao et al., 2008; Kiener & Minor, 2011). As elaborated dislocation networks are unable to form at this length scale, plasticity is carried by individual dislocations and the process becomes more stochastic in nature. This is for example seen by the appearance of strain bursts as a result of some dislocations that abruptly break free (Dimiduk et al., 2005; Ng & Ngan, 2008). Samples within this size regime tend to only reveal bulk-like behavior if they have been pre-deformed and in turn reveal a higher initial dislocation density. In that case, there are more dislocation structures and potential sources so the stochastic nature diminishes and source limitation is no longer the limiting factor.

An even more extreme case is represented by the nm regime, i.e. when $d < 100\ nm$. Here a strong discrepancy is found between the spatial and microstructural constraint, as samples such nanocrystalline thin films (internal constraint), reveal much lower strengths than whiskers which can be considered to be dislocation free (external constraint) even if their value of characteristic length d is comparable. The key factor that determines the strength of the sample is the initial defect density. The aforementioned behavior observed for thin films is met, if a sufficient amount of dislocation nucleation sites are available. The considerable mechanical strength of defect-free metallic whisker (above 1 µm size) which is close to the theoretical shear strength is demonstrated in the work of Brenner (Brenner, 1956).

The complex interaction of the all these mechanisms, their strong stochastic nature and dependence on microstructure and loading conditions manifests in a large variety of suggested scaling laws within the region $d < 1 \mu m$. Fig.1.1 displays a sketch of the material strength for the different regimes for various sample sets. For metallic whiskers, the measured strength values show a strong scatter and only a weak size effect is detected, which can be fitted mathematically by Weibull statistics, i.e. using a weakest-link argument. Moreover, Brenner (Brenner, 1956) found that whiskers can be deformed up to large plastic strains and that flow and yield strength of metallic whiskers differ significantly. This is indicated by the values entitled "whisker flow" in

Fig1.1, which represent flow stress values while "metallic whiskers" refers to yielding. While the size effect is weak for metallic whiskers, a higher scaling exponent of about $n = 0.8$ is found for microcrystals and thin films which is in agreement with a model based on dislocation source controlled plasticity. For more information, the reader is referred to Kraft et al. (Kraft et al., 2010).

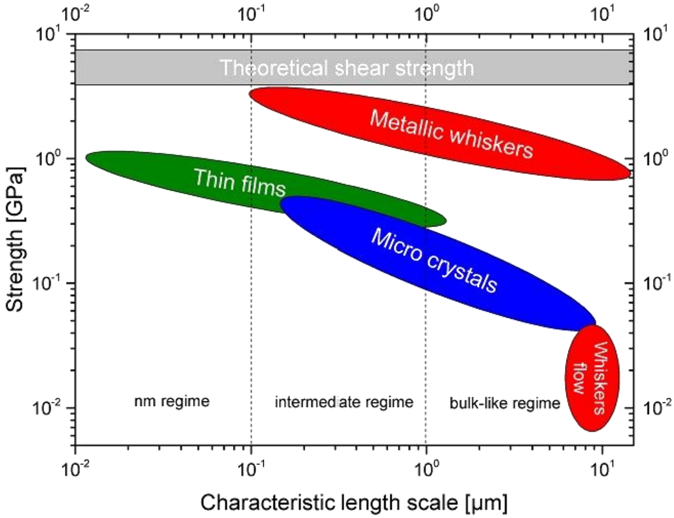

Figure 1.1: Some exemplary values of the measured material strength for a variety of small Cu samples tested by different research groups as a function of characteristic length *d.* The plot is based on Kraft et al. (Kraft et al., 2010). The theoretical shear strength for Cu is calculated along <110>.

In 2004 the influence of sample size on mechanical properties was impressively demonstrated by Uchic et al. (Uchic et al., 2004) who performed compression experiments on single crystalline pillar structures with different diameters. Even in the absence of a strain gradient, which plays an important role in the interpretation of the size effect (Evans & Stölken, 1998; Fleck & Hutchinson, 1997; Gao et al., 1999) as will be highlighted in the following section, a strong size effect was observed when the diameter of the pillars changed. With decreasing diameter, pillars are found to become higher in strength and the stress-strain curves more serrated, i.e. stochastic in nature. This corresponds essentially to the transition between size regimes mentioned earlier.

1.2 Strain gradient plasticity

An important aspect in the explanation of the unusually high mechanical strength upon downscaling is the loading geometry itself. This particularly refers to experiments where the load is applied such that a gradient is introduced as in torsion (Fleck et al., 1994) or in bending (Evans & Stölken, 1998). If the load is applied in the form of a gradient, dislocations will necessarily emerge in order to accommodate the change in shape and thus to uphold the continuity of the sample. The elevated dislocation density in turn affects mechanical properties of the sample. Fig.1.2 schematically illustrates how a set of edge dislocations is able to cause an overall curvature of the given sample. This particular kind of dislocations resulting from such strain gradients is therefore denoted geometrically necessary dislocations (GND). The existence of such dislocations to answer a geometrical necessity has been postulated by Nye (Nye, 1953) and furthered by Kröner (Kröner, 1958) and Ashby (Ashby, 1970). The counterparts of GND are dislocations which are caused by random trapping processes and do not invoke an overall curvature of the volume under consideration. These dislocations are denoted statistically stored dislocations (SSD).

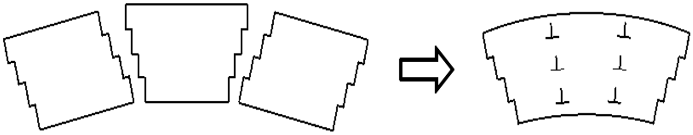

Figure 1.2: Schematic illustration how geometrically necessary edge dislocations accumulate within a sample to cause bending.

Plastic deformation arises from the combined behavior of both GND and SSD and the resolved shear stress τ of a material upon deformation can be related to their individual densities ρ_{GND} and ρ_{SSD} according to a modified Taylor relation

$$\tau = \alpha G b \sqrt{\rho_{GND} + \rho_{SSD}} \tag{1.2}$$

where G is the shear modulus, b is the Burgers vector and α is a numerical factor which is on the order of 0.1 to 0.4.

If a sample is exposed to a strain gradient and the size of the sample is reduced, the gradient required for the same amount of strain will be higher and in turn more GND are needed, resulting in a strengthening effect. The increase of dislocation density to satisfy a strain gradient is the basis of strain gradient theories (Fleck & Hutchinson, 1997; Huang et al., 2000; Hutchinson, 2000; Kubin & Mortensen, 2003). The dependence of GND density from the strain gradient applied is for example elaborated in the work of Fleck et al. (Fleck et al., 1994) who studied the torsion of µm-sized Cu wires. The strain gradient $\partial\gamma/\partial x_1$ along any given axis (radial axis in the case of torsion) is related to the dislocation density ρ_{GND} via the Burgers vector b according to:

$$\rho_{GND} = \frac{1}{b}\frac{\partial\gamma}{\partial x_1} \tag{1.3}$$

Further experiments and simulations dealing with strain gradients and their influence on plastic behavior of micro samples have been performed. These mostly include bending geometries (e.g. Weihs et al., 1988) or torsion (e.g. Ziemann et al., 2015). However, it is stated that apart from strain gradients, other factors such as texture or grain size (Chen et al., 2015; Bayerschen et al., 2016) affect the mechanical behavior as well and the size effect of micro samples cannot be fully explained solely by strain gradient plasticity.

1.3 Characteristics of cantilever bending

Cantilever bending is a particularly interesting loading condition in dislocation-based plasticity (Weihs et al., 1988; Evans & Stölken, 1998) as it naturally imposes a strain gradient. The geometry therefore allows studying both the influence of spatial confinement and the increase of the strain gradient on the size effect at the time. The geometry encountered in the aforementioned publications and many more (Motz et al., 2005; Matoy et al., 2009; Kiener et al., 2010; Sökmen et al., 2010; Tarleton et al., 2015) is usually that of a cantilever fixed at one side and loaded at the free end. This non-uniform bending setup results in a pronounced strengthening effect of the samples. The current understanding that allows explaining the increase in strength with decreasing cantilever size (limiting dimension is cantilever height) for the special case of bending assumes that two different mechanisms are active: (i) the aforementioned strain gradient and (ii) the limitation of available dislocation sources. They have been mentioned in the previous section, but in the following their effect for the particular case of cantilever bending is detailed.

The strain gradient aspect implies that the increase in flow stress with decreasing sample size can to some extent be attributed to a higher density of GND within the volume. As documented by Nye (Nye, 1953) and Ashby (Ashby, 1970), the strain gradient resulting from the cantilever geometry provokes GND to emerge in order to accommodate the strain. The plastic deformation is usually carried by glide of the dislocations on their respective slip planes. However, the total number of GND that can exist within one single slip plane is limited and because the sample size decreases, the slip plane spacing will also shorten as a consequence (Tarleton et al., 2015), if the same amount of curvature is imposed. As more GND are concentrated within a given volume element, the stress needed in order to cause plastic flow will increase according to equation (1.2). If SSD are neglected then the relation can be rewritten for the cantilever geometry (Motz et al., 2005) as

$$\tau = \alpha G b \sqrt{\frac{\omega}{x b}} \tag{1.4}$$

where ω and x describe the rotation angle and the size of the plastically deformed region respectively. ω/x can therefore be interpreted as the curvature or strain gradient of the cantilever. Motz et al. (Motz et al., 2005) showed for their single crystalline Cu cantilevers that the size of the region, where plastic deformation is localized, is on the order of the cantilever height h. Consequently, a scaling law for the flow stress σ_f could be established based on the concept of a strain gradient. If the dependence of the flow stress σ_f from h is expressed by a power law relationship of the form

$$\sigma_f = A \cdot h^{-n} \tag{1.5}$$

where A and n are constants, then the scaling exponent n should be equal to $n = 0.5$. However, they found a scaling law for the σ_f that considerably differs from this value. In fact, they found n to be about 0.75, if a function of the form shown in equation (1.5) is chosen. If a constant offset value σ_0 is added to the equation, an even higher exponent of $n = 1.14$ is obtained (Senger et al., 2011). That implies that strain gradient plasticity does not suffice to describe the deformation mechanisms in cantilever bending entirely. The explanation of the size-effect by a strain gradient imposes the assumption that there is always a sufficiently high number of dislocation sources available to accommodate plastic strain. The existence of these sources is crucial for plastic deformation, especially because by definition, GND are not mobile since they uphold the sample curvature. Dislocation sources such as Frank-Read sources are needed to provide new dislocations as the plastic strain increases. Following the concept of source limitation, Motz et al. (Motz et al., 2005) assumed that dislocation dipoles are being generated within the high stressed regions within the cantilever cross section and that these dipoles travel towards the free surface but also in the direction of the neutral fiber (Fig.1.3). Here they stop as the resolved shear stress approaches zero and in turn form dislocation pile-ups (more precisely soft pile-ups (Tarleton et al., 2015)). The back stress caused by the pile-ups will then in turn shield the dislocation sources nearby and therefore limit the availability of free dislocations. This pile-up arrangement has also been visualized by discrete dislocation dynamics (DDD) simulations (Senger et al., 2011). In their work, Motz et al. (Motz et al., 2005) also formulated a scaling law based on the back-stress of the pile-up limiting the availability of dislocation sources. They calculated an exponent of $n = 1$ for a power law of the form of equation (1.5). The authors stated that the combination of the source limitation and the dislocation pile-ups both contribute to the observed size effect, but the way in which they interact with each other is very complex.

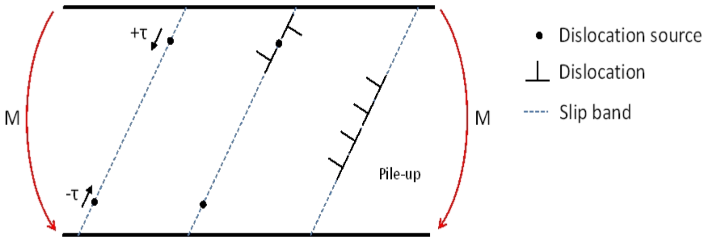

Figure 1.3: Schematic of the dislocation pile up near the neutral fiber upon bending as suggested by Motz et al. (Motz et al., 2005). Dislocation dipoles are emitted from the source at the outer fibers of the tensile (+τ) and compressive (-τ) half of the bending structure.

The pile-up assumption itself is supported by other experiments. In this regard especially the ones dealing with Bauschinger effect in cantilever structures are worth mentioning (Demir & Raabe, 2010; Kirchlechner et al., 2012). To study the effect, the authors loaded single crystalline Cu cantilevers up to a certain degree of plastic strain and then straightened them again by reversing the load direction. In single crystals the Bauschinger effect arises from cell wall structures which form through accumulation of dislocations during loading (Demir & Raabe, 2010). The authors observed a considerably lower flows stress and a smoother elastic-plastic transition during the reverse loading. Besides this "mechanical Bauschinger effect" they used electron backscatter diffraction (ESBD) on the deflected and straightened samples to map GND density. They visualized clear bands of GND that formed during bending and disappeared after straightening. Along with the mechanical one, this "microstructural Bauschinger effect" supports the pile up theory from Motz et al. (Motz et al., 2005): There is little interaction between the individual slip systems in the single crystal which leads to a very strong polarization of the dislocations and only weak entanglement. As soon as the external load is released, the backstress of the dislocation pile-up is no longer countered so the dislocations easily detangle and spread over the slip plane or leave the crystal. At the initial state of the straightening procedure there is therefore a large amount of free dislocations and potential sources which enables a continuous hardening behavior rather than an abrupt transition as the authors observed in forward loading.

Kirchlechner et al. (Kirchlechner et al., 2012) performed in-situ X-ray diffraction experiments for the bending of single crystalline Cu cantilevers. For the experiments, they used polychromatic X-rays (i.e. Laue diffraction) generated by a synchrotron source. Since the spot size can be reduced to a few µm in diameter, or even sub-µm, this method is often denoted as µLaue diffraction. The in-situ observation revealed that at the end of the unloading segment only 42 % of GND generated during loading are still stored within the sample. This is in agreement with the assumption of dislocations piling up and being pushed back as the load is released. Both Demir et al. (Demir & Raabe, 2010) and Kirchlechner et al. (Kirchlechner et al., 2012) further stated that while the density of GND increases upon loading and is released during reverse loading, the results imply that the amount of SSD is kept constant during the test, even if the absolute quantity of SSD is only partially accessible by EBSD or µLaue diffraction. Tarleton et al. (Tarleton et al., 2015) performed DDD simulations as well as experiments on single crystalline hcp Ti and Zr cantilevers. They also supported the size effect being influenced by geometrical necessity paired with dislocation pile-ups (and in turn source limitation). They further mentioned that the pile-up location is not necessarily concentrated at the neutral fiber because of the non-uniform nature of cantilever bending. Due to shear forces, only for pure bending conditions which are not met in the cantilever geometry the locus of the pile will coincide with the neutral fiber of the sample. Instead, for cantilever bending the pile-up location is dependent on the inclination of the activated slip system. In this geometry, the pile-up is only expected to coincide with the neutral fiber when the slip system inclination is 45°. For the scaling law attributed to the size effect they found the flow stress to scale with the cantilever height to the power of $n = 0.89$. It needs to be pointed out that they added a constant offset σ_0 to the fitting function, i.e. a size-independent flow stress value to equation (1.5) stating that the scaling exponent is strongly underestimated otherwise. This also matches the aforementioned observations from Motz et al. (Motz et al, 2008).

In summary, flow stress during bending of micro cantilevers is governed by both GND arising from the strain gradient and by forming soft pile-up structures resulting in a limitation of available dislocation sources. Both mechanisms affect each other and govern plasticity at different length scales. As mentioned, the first mechanism (strain gradient) is clearly dominant in micron sized samples and implies a scaling law of the flow stress according to (1.5) with an exponent $n = 0.5$ while source limitation is more important for very small volumes and might scale with $n = 1$. Upon downscaling, the question arises at which exact point and under which conditions the dominance switches over to the source limitation and how that transition happens. The work of Demir et al. (Demir et al., 2010) deals with this theory of mean-field breakdown. As a simplification it might be said that the mean-field assumption basically implies that dislocation sources are never limited and new dislocations can always be activated without any need for higher external stresses. The authors performed bending experiments on single crystalline Cu cantilevers and applied different criteria to evaluate flow stress. The authors assumed like Motz et al. (Motz et al., 2005) that the stress distribution within the cantilever cross section is constant at the yield point. In order to pinpoint the strain at which the yield is supposed to be reached, a criterion needs to be chosen which was varied in their work: A remarkable difference in the exponent of the scaling law is found when the criterion for yield is set to a strain of 0.02, 0.06 or 0.1. The exponent n of the scaling law (1.5) is only close to 0.5 if a high strain criterion is chosen (yield happens at a strain of

0.06 or 0.1). In this regime, the sample structures experienced a considerable amount of pre-straining so their deformation behavior should be governed by dislocation-dislocation interactions. The 0.02 criterion on the other hand leads to an exponent of only 0.12, implying that this kind of interaction is no longer dominating the deformation. That means that the mean-field theory is breaking down and source limitation gradually becomes the relevant factor. Such a large variation caused by a change in criterion can be related to a size dependence in strain hardening. To pinpoint the transition of the breakdown Demir et al. (Demir al., 2010) suggested a correlation length (or bow out length) ξ to characterize the point where the dominance of the mechanisms is switched. The minimal bow-out of the dislocations is given by their Burgers vector while the maximum corresponds to half the sample size (i.e. half of the height). Between theses extremes a statistical maximum can be found for the most occurring bow-out segment length with corresponds to the correlation length ξ. The authors derived an estimate for ξ to characterize the breakdown of the mean-field theory which is between 0.26 µm and 0.35 µm for their experiments.

A different approach to explain the origin of the dislocation networks upon bending was given by Motz and Dunstan (Motz & Dunstan, 2012). They found an analogy between bending of a thin film sample and the critical thickness theory established by Frank and Van-der-Merwe in 1949 (Frank & van der Merwe, 1949). The theory describes how a thin film growing epitaxially onto a substrate of different lattice parameter can accommodate strains that even exceed its own intrinsic strength. During growth the film is strained in order to adapt to the lattice misfit and the strain increases from the interface to the free surface. At some point, denoted as the critical thickness, the straining will be too severe and mismatch dislocations will form at the interface. There are various different theories to find the exact values for critical thickness but the one that is considered to be the correct one was established by Matthews and Crawford (Matthews & Crawford, 1970). When the critical thickness is reached or exceeded, two regions can be found within the layer: A plastically relaxed one filled with misfit dislocations and an elastically strained one with zero dislocation density. The critical thickness theory found application for problems dealing with spatial confinement

(Dunstan, 2012) and the analogy Motz and Dunstan (Motz & Dunstan, 2012) utilized is the following: In bending, the neutral fiber mimics the interface during the growth of a graded layer, as dislocations will pile-up here. The difference to the original critical thickness theory is that during layer growth the strain gradient is constant and the film thickness increases, while upon bending the film thickness is fixed and the strain gradient rises as a consequence of ongoing curvature. Nevertheless, the critical thickness theory is applicable and using DDD simulation the authors indeed detected that with increasing strain, dislocations are generated and pushed towards the neutral fiber of the sample leaving a dislocation-free layer at the surfaces. Therefore, the dislocation arrangement and its strong accumulation at the center of the cantilever may as well be interpreted in the framework of critical thickness theory.

1.4 Fabrication of µm-sized cantilevers

The work of Weihs et al. (Weihs et al., 1988) was one of the earliest projects dealing with the deflection of cantilevers at the µm scale. The cantilevers consisted of a bilayer thin film of Au-Ni and SiO_2 deposited onto a Si wafer substrate. Testing structures where fabricated using a lithography-based procedure. Another example for such a fabrication route to study cantilevers of Si oxides or nitrides is given in Matoy et al. (Matoy et al., 2009). In both cases the essential step in this process chain is the anisotropic wet etching of Si. Alternative fabrication routes rely for example on sacrificial layers (Oh et al., 2013) but benefiting from the anisotropy of Si is the most common way for cantilever fabrication with lithography-based processes. As will be shown in chapter 2, the cantilever geometry can easily be realized if the Si wafer substrate has {100} orientation and the cantilever axis is chosen parallel to the wafer flat. Such a fabrication route produces a large amount of samples but is only applicable to certain materials. The thin film out of which the cantilevers are shaped needs to be compatible with all processing steps. This includes the deposition of the film onto Si{100}, the ability of patterning the film by wet or dry etching and an immunity of the film material to the anisotropic Si etchant and the solvents used.

A remarkable change which enabled numerous cantilever experiments on the micron scale for a variety of different materials occurred when Focused Ion Beam (FIB) milling was established as a fabrication technique. FIB generates a beam of focused Ga^+ ions and if coupled with a Scanning Electron Microscope (SEM), the beam can be used as a precision tool to tailor almost any kind of shape out of the sample material. For a thorough review on FIB the reader is referred to Giannuzzi and Stevie (Giannuzzi & Stevie, 2005). While the time to fabricate one single structure this way is comparatively high, the simplicity of the method and the ease of accessibility pushed FIB micro machining to become by far the dominant fabrication procedure for µm and sub-µm sized testing structures for research purposes. For industrial applications, however, the method is far too time-consuming. The only conditions that a sample must meet in order to be suited for this processing is, that it must be electrically conductive (even isolating materials can be handled up to a certain degree) and that it is not covalently bound like Si, Ge, GaAs, and diamond C (Giannuzzi & Stevie, 2005) as these materials tend to amorphize under the influence of Ga^+ ions. FIB milling was also used in the pioneering work of Uchic et al. (Uchic et al., 2004) for the fabrication of the aforementioned single crystalline Au pillars. Pillars are by far the most frequent shape fabricated by FIB for µm and sub-µm scale testing (Uchic et al., 2004; R. Maaß et al., 2009; Kirchlechner et al., 2011), but cutting cantilever structures established quickly as well (Motz et al., 2005; Demir et al., 2010; Armstrong et al., 2011; Kupka et al., 2014).

One way to obtain cantilever structures with FIB for example is taking a bulk material und cutting the desired structures at the very edge of the sample. This way, the resulting cantilever can be of rectangular cross section and can for example be analyzed with EBSD. This procedure was demonstrated for single crystalline Cu (Motz et al., 2005; Demir et al., 2010; Kiener et al., 2010; Kirchlechner et al., 2012). Placing the cantilever at the very edge of the sample was further exploited in the work of Demir et al. (Demir & Raabe, 2010) to realize a back and forth bending by turning the sample upside down which allowed studying Bauschinger effect.

Another FIB-based procedure which is frequently used is the cutting of cantilevers of triangular cross section. This method used by various groups (Gong & Wilkinson, 2009; Armstrong et al., 2011), simplifies the fabrication procedure and it allows choosing the position of the cantilever freely at any location on the sample surface and not only at the edges. This becomes particularly useful when for example grain boundaries or other interesting features are to be studied in terms of mechanical behavior or if the volume under consideration is to be reduced to a single crystalline segment with a precisely known orientation. Some slightly more complex shapes tailored for special experiments are feasible as well: Kirchlechner et al (Kirchlechner et al., 2012) used a synchrotron-based Laue diffraction technique to study plasticity in cantilevers. The cantilevers in this work have a slightly larger cross section at the loaded end and they are shaped at the edge of the bulk sample in a way to assure the transmission of the X-rays through center part of the sample. In comparison to FIB processing, other fabrication routes are only scarcely used in microplasticity. Such alternative methods include beside the already mentioned lithography-based procedure for example electro discharge machining at micrometer scale, denoted μEDM (Jahan et al., 2011) or laser cutting (Pecholt & Molian, 2011).

While all these advantages grant FIB milling a dominant position for micro sample fabrication, there is an essential drawback to it: The sample is inevitably contaminated with a certain amount of Ga^+ ions. It is impossible to prevent the implantation of Ga^+ as a foreign species into the crystal matrix. Various research groups have taken efforts to evaluate the impact of this kind of contamination (Bei et al., 2007; Kiener et al., 2007). As mentioned in the case of covalently bound materials like semiconductors, an amorphization of the crystal structure is observed which is probably the most severe change that the FIB can induce. In metallic samples, the interaction of the Ga^+ ions with the material causes an implantation of ions into the matrix and a variety of defects have been reported including vacancies, interstitials, stacking faults, dislocation loops and precipitations (Bei et al., 2007; Kiener et al., 2007). In the work of Kiener et al. (Kiener et al., 2007) the severity of the implantation was quantified for perpendicular incidence of 30 kV Ga^+ ions. An altered boundary layer containing 20 at% Ga^+ with a depth of up to 50 nm is found. For a thorough review about possible interactions between Ga^+ and various samples inside FIB, the reader is referred to Giannuzzi and Stevie (Giannuzzi & Stevie, 2005). These lattice defects may affect the mechanical properties: For example FIB irradiation was found to cause local lattice rotations such as reported by Kheradmand (Kheradmand, 2012), who observed orientation gradients at the surface of micro pillars after FIB polishing. The penetration depth may be reduced by lowering acceleration voltage, ion current and angle of incidence but there are a lot more relevant factors that have to be taken into account that determine the actual impact, such as exposure time, type of material and lateral size of the irradiated area. Bei et al. (Bei et al., 2007) stated that the nature of the alterations, including the multiplicity of defects and their gradients is extremely complex and still lacks of a profound understanding. Besides the documentations of the microstructural changes upon FIB milling, the effect on mechanical properties is an important issue as well. It has been shown that the process-induced damage can have a tremendous influence on mechanical properties. Bei et al. (Bei et al., 2007) compared the mechanical response of directionally solidified Mo pillars with a purposely FIB treated counterpart, and furthermore the indentation behavior of a MoNb single crystal, if its surface is electro polished or FIB milled. For the pillar structures they found a tremendous difference in yield and flow behavior. While the grown pillars yielded at 9.2 GPa (i.e. close to the theoretical shear strength) and collapsed abruptly upon loading so that no plastic flow was observed, FIB milled pillars yielded at 0.85 GPa and showed strain hardening. This example where an "ideal" sample with strength close to the theoretical limit is being contaminated may be considered to represent the worst case scenario. They further stated that the FIB milled structures behaved somewhat like the non-contaminated ones after a prestraining of 8 %. Their indentation experiments on the other hand revealed that after the FIB treatment of the surface, no pop-in behavior was observed anymore and the hardness of the sample increased by about 28 %. From these experiments, they concluded that Ga^+ either induces dislocations or other defects which reduce the stress needed for dislocation nucleation.

Even though this negative side effect of FIB is known, it is still widely neglected in research due to all the advantages mentioned previously. Often it is argued that the implantation of Ga^+ should at least be minimal when the ion current used during the final cut is reduced. Large currents of several nA are used for the rough shaping but the final cut is executed at low currents like 20-200 pA (Iqbal et al., 2012), 100 pA (Kiener et al., 2010) or in some cases where the total size is too big, somewhat higher currents are used such as 500 pA (Demir & Raabe, 2010). Motz et al. (Motz et al., 2005) excluded any kind of FIB influence during their cantilever experiments with the additional argument that the penetration depth of Ga ions is below 100 nm which is negligible against the cantilevers being several µm in size. What is usually disregarded in literature is the influence of the snapshot(s) that is(are) taken before any kind of FIB patterning is executed. This matter will be detailed further throughout the project.

1.5 Experimental investigation of dislocations

Crystal defects such as dislocations are difficult to be visualized or quantified. The main approach to detect dislocations is by means of diffraction, since dislocations have a long range strain field causing distortions within the crystal lattice and consequently broaden/blur the diffraction pattern. The wavelength used for diffraction needs to be on the order of the lattice parameter to be sensitive to this kind of disturbance. Therefore promising results stem from X-rays which have a few 100 pm in wavelength or from electron diffraction which can even reach lower values in the pm regime depending on the parameters used for excitation.

Conventional X-ray diffraction (XRD) is only suited for global measurements on bulk samples since the probed volume is large. However, with the advent of new X-ray optics there are nowadays several synchrotron sources which allow the generation of high brilliance X-ray beams having spot sizes down to a few µm or even sub-µm in diameter. With such a powerful tool a strongly confined spot can be scanned over the sample within reasonable time intervals. Retrieving information on dislocations with such methods can be difficult because the broadening and asymmetry of the diffracted peaks are affected by a variety of aspects apart from dislocations. Those include other crystallographic defects, but also grain size or residual microstress is known to affect the shape of a diffraction peak. This is why care has to be taken when analyzing these experiments. Synchrotron-based methods have been used to gain deeper understanding on microstructural mechanisms taking place in the deformation of nanocrystalline samples (Lohmiller et al., 2013), bamboo structured torsion wires (Ziemann et al., 2015), single crystalline pillars (Maaß et al., 2009; Kirchlechner et al., 2011) or cantilevers (Kirchlechner et al., 2012) to name only a few. The greatest difference of X-ray diffraction methods with respect to the methods mentioned later in this section is the high penetration depth of the incident beam which is several µm. The most striking disadvantage of the method is its lateral resolution. If the spot is scanned with a step size of about 1 µm over the sample, up to this date, only large dislocation agglomerations and striking features can be detected, but there is an ongoing development towards even higher resolutions.

Electron diffraction can be carried out either in an SEM or a transmission electron microscope (TEM). Especially the TEM is a very powerful tool which allows actual visualization of dislocation networks. TEM experiments were the first methods which unambiguously proved the existence of dislocations experimentally. While for the aforementioned X-ray methods, the effect of dislocation structures can only be visualized in reciprocal space, in TEM, dislocations can even be seen directly in a real space image. Examples are for instance found the work of Phillips and Dash (Phillips & Dash, 1962). There are various TEM techniques like dark field images, convergent electron beam diffraction (CBED) or weak beam diffraction. For more information on the individual techniques the reader is referred to Williams and Carter (Williams & Carter, 1996). Apart from its ability to visualize dislocations, the TEM stands out with its particularly high lateral resolution which can go down to 2-3 nm for the aforementioned techniques. Some very advanced machines are even able to retrieve information from below this point. As an example illustrating the resolution of TEM, Kisielowski et al. (Kisielowski et al., 2015) reported that by using an aberration corrected TEM with a monochromated high brightness source, information transfer in the sub-Å regime is possible. The sample scanned with TEM is a small lamella which is cut out of the actual sample body. The lamella thinning process itself is often executed by FIB which may also induce some unwanted artifacts depending on chosen parameters and sample material (Giannuzzi & Stevie, 2005). Several research groups dedicated their work to in-situ TEM experiments. A thorough review is given in Yu et al. (Yu et al., 2015). Such in-situ setups can be quite complex and the results are difficult to evaluate but given the high lateral resolution and visualization capacities, they yield very profound information.

Electron diffraction inside an SEM only reaches lateral resolutions down to 50 nm but has been established as a standard method with a significantly reduced amount of preparations needed in contrast to TEM. Here the diffraction methods comprise Electron Channeling Pattern (ECP), Selected Area Channeling Pattern (SACP), Electron Channeling Contrast Imaging (ECCI) and Electron Backscatter Diffraction (EBSD). Apart from EBSD, the named methods use the channeling contrast of primary electrons and give only qualitative results on striking dislocation features (e.g. persistent slip bands) and are usually applied to single crystalline samples or subregions only. In contrast, EBSD uses primary electrons that are backscattered from the crystal lattice of the sample and relies on an additional detector able to capture the diffraction pattern of the backscattered electrons (Kikuchi diffraction). Because the EBSD technique is a very important part of the work at hand, it is detailed in the following.

The generation of an EBSD pattern is usually described to work in two consecutive steps (Zaefferer, 2011). First, the primary electrons striking the sample surface are scattered incoherently about large angles. This quasi-elastic scattering process can be imagined like an electron source within the sample sending out electrons in all possible directions. The second step is now a coherent scattering of these electrons at the crystallographic planes of the sample. In contrast to most XRD methods, each crystal plane satisfies the Bragg condition for diffraction, since step 1 causes the emission of electrons in all possible directions. From a geometrical point of view, the electrons are backscattered about a very small angle from the planes. The spatial arrangement of this backscattering process can be described geometrically as the shell of a cone (Kossel cone) with a very steep opening angle of about 1°. As mentioned, in order to experimentally record a diffraction pattern from this process, an additional detector is needed, capable of capturing the electrons along their paths. Typically a phosphor screen detector is used for that purpose which will show fluorescence when electrons impinge on its surface. Due to the steep opening angle of the Kossel cones, their intersection with the detector resembles straight lines. These lines, which occur as a pair of two for each reflection, are known as Kikuchi bands. From the pattern of Kikuchi bands captured on the screen the full orientation matrix $\overline{\boldsymbol{g}}$ of the scanned area can be retrieved. For more detailed information, the reader is referred to Schwartz et al. (Schwartz et al., 2011). To capture Kikuchi bands geometrically, the sample needs to be tilted by 70° with respect to the electron beam maximizing the amount of backscattered electrons that are able to reach the detector (Fig.1.4). The information depth, i.e. the depth from which backscattered electrons are obtained, is typically only about 10-20 nm (Zaefferer, 2011). So EBSD is highly surface sensitive and for producing good Kikuchi patterns the sample surface must be very carefully polished. EBSD can reach a lateral resolution down to 50 nm and an angular resolution of about 0.5°-1° (Zaefferer, 2011). Even if EBSD cannot directly visualize dislocations, it can be used to detect lattice misorientations which may be related to dislocation networks, because the full orientation matrix is known at each measurement point.

A new way to analyze EBSD patterns was developed by Wilkinson (Wilkinson, 2001) and relies on digital image correlation rather than Hough transformation. Observing the pattern shift with digital image correlation significantly increases the angular resolution. In their work on low-angle boundaries Bate et al. (Bate et al., 2005) found the mean orientation noise to be 0.3° with a maximum of 0.7° if the Hough transformation method is used while they stated mean values of 0.009° with a maximum of 0.02° when pattern shift is used for data evaluation. The method requires a very high Kikuchi pattern quality, i.e. a rigorously prepared, smooth sample surface and preferably high crystalline perfection.

The project at hand also uses transmission Kikuchi diffraction (TKD) for the study of dislocations which is a comparatively new technique. Keller et al. (Keller & Geiss, 2012) suggested this scanning method as a modification of standard EBSD. The modification consists in changing the diffraction geometry from backscattering to transmission and therefore they first named the technique transmission EBSD or in short t-EBSD. The term TKD was established later because it describes better the physical nature of the diffraction, as the combination of transmission and backscattering in one expression might be misleading. To allow a transmission geometry in SEM the sample has to be reduced to lamella size (thickness about 100-150 nm) just like for TEM investigations and the sample tilt has to be about 20° into the opposite tilt direction with respect to conventional EBSD so the diffraction pattern can be recorded on the phosphor screen (Fig.1.4). The restrictions considering the lamella thickness can even be regarded as less severe than in TEM, as samples slightly thicker than 100 nm may still provide evaluable diffraction patterns in TKD. The diffraction and thus the generation of Kikuchi bands follows the same physical principles. The reader will notice that this kind of electron diffraction can also be used in TEM for the visualization of Kikuchi Bands.

The great advantage of the geometrical change from backscattering to forward scattering becomes obvious when looking at the interaction volume of an incident electron beam with the sample (Fig 1.5). If under SEM conditions an electron beam strikes an electrically conductive material it will excite the following reactions: Emission of Auger and secondary electrons (used in conventional SEM imaging and Auger spectroscopy) at the very surface of the sample, emission of backscattered electrons (for orientation measurements) until depths of several 100 nm and generation of characteristic X-rays (for spectroscopy EDX, WDX) up to depth of a few µm. The shape and width of the volume in which such interactions take place is known mostly from Monte-Carlo simulations (Shimizu & Ze-Jun, 1999) and describes the shape of a pear (Fig.1.5). Its size is mainly dependant on the material and the electron beam voltage used. For EBSD and TKD, the lateral resolution can be determined when the width of this pear is known. The width reaches its maximum at values of about one to a few µm depending on sample material

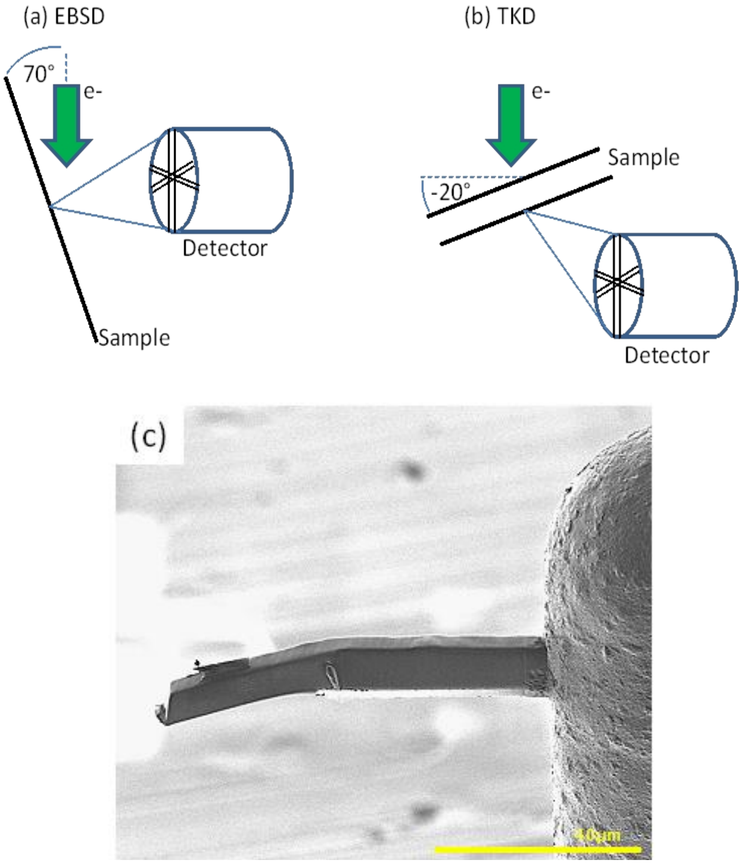

Figure 1.4: Illustration of the setups used for (a) EBSD and (b) TKD. (c) Cantilever transferred to a TEM grid (before thinning) as an example of a potential TKD sample.

and beam voltage. When the sample thickness is reduced to lamella size, it can now be seen that the lateral resolution of backscattered electrons will greatly improve, because the interaction volume is being reduced (Fig.1.5c). Keller and Geiss (Keller & Geiss, 2012) demonstrated that TKD considerably improves the lateral resolution with respect to standard EBSD, much like

TEM-based diffraction techniques do. While EBSD has a lateral resolution down to about 50 nm, which may already be considered optimistic under standard conditions, TKD can distinguish measurement points which are only about 10 nm distanced from each other. The authors further found using Monte-Carlo simulations that the diffractions patterns originate from the bottom surface of the lamella.

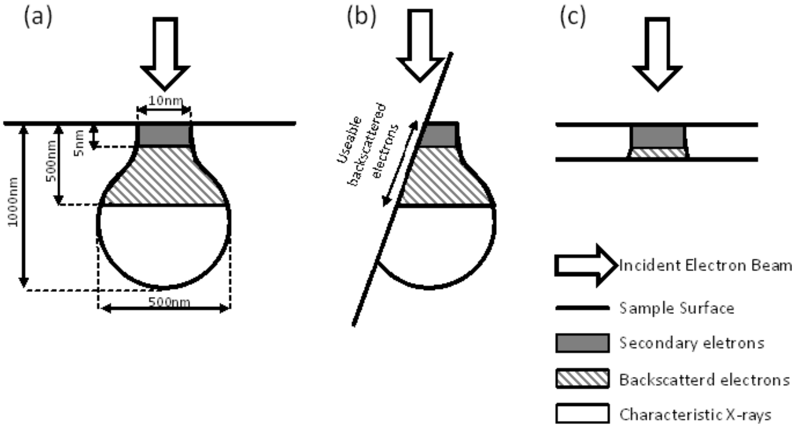
(a)
(b)
(c)
10nm
5nm
500nm
1000nm
500nm
Useable backscattered electrons
Incident Electron Beam
Sample Surface
Secondary eletrons
Backscatterd electrons
Characteristic X-rays

Figure 1.5: Illustration of the interaction volume of electrons in SEM with a conductive sample to illustrate lateral resolution. (a) General shape and some exemplary values, (b) situation for EBSD with increase of useable backscattered electron by 70° sample tilt and (c) situation for TKD with lamella of about 100 nm thickness.

Fig.1.4d shows an image of the experimental setup for TKD used in this work. With respect to standard EBSD, the pattern center on the phosphor screen is misplaced but this can be corrected inside the EBSD software. The different measurement parameters such as optimum tilt angle and sample thickness and how they influence the pattern quality are reported for example in the work of Suzuki (Suzuki, 2013).

Apart from its high lateral resolution, TKD furthermore benefits from using the software applied for standard EBSD, which can be automated and is fast, robust and has high angular resolution. It is definitely a technique complementary to TEM analysis. TEM-based methods may have superior lateral resolution and even if there are automated methods capable of recording and evaluating Kikuchi patterns inside TEM, the fact that TKD can be executed directly inside SEM is a considerable advantage. Due to its easier application and accessibility it is becoming a very useful tool for mapping crystallographic orientations with very high resolution, which has been used for various applications (Trimby, 2012; Brodusch et al., 2013; Sun et al., 2013).

In the work presented here the data gathered by TKD will be further evaluated with a particular method: In 2008, Pantleon (Pantleon, 2008) suggested a promising approach to evaluate orientation data (as contained in the orientation matrix based on Nye's tensor which yields very profound information on dislocation densities and even on the exact indices of the Burgers vectors and crystallographic planes. This approach was followed by some research groups like Kysar et al. (Kysar et al., 2010) on EBSD data sets. Due to the lateral resolution of EBSD being around 50 nm and its angular resolution of 0.5° only larger features, such as pronounced dislocation segments of high dislocation density can be detected. It can be expected that with the superior lateral resolution of TKD even more information can be gained.

1.6 Summary of literature review and aims of this study

Bending of µm-sized cantilevers reveals a strongly pronounced size effect due to the imposed strain gradient. According to the state of the art, the two principal models describing plastic behavior that may explain the effect are a dislocation source limitation caused by the backstress of a soft pile-up near the neutral fiber and on the other hand dislocation interactions arising from an elevated GND density caused by the strain gradient. The latter is dominant for bulk samples while the point at which the source limitation becomes more relevant is on the sub-µm scale, however, exact values for transition interval can only be estimated and the interaction of the two processes is complex.

Gaining deeper insights into the fundamental mechanisms taking place in microplasticity may be obtained by conducting idealized experiments. Here the term idealization means that dislocations are to be studied unimpaired from any other microstructural features such as grain boundaries, inclusions etc. Almost all experiments carried out so far which aim at obtaining a fundamental understanding rely on FIB milling for sample preparation. Especially for bending this might have a significant effect as the top surface of the cantilever, which corresponds to the zone where the resulting stresses will be highest, is inevitably irradiated during the process. Ga^+ implantation is known to alter both mechanical response and microstructure of the specimen and is therefore particularly impactful for such a geometry. Therefore the results obtained by experiments both concerning the mechanical response as well as the microstructural mechanisms taking place will always have an uncertainty which is hard to quantify.

The work presented here connects to many other works in the field of microplasticity. And like them all, it attempts to provide additional data both on the quantification of the mechanical size effect along with the scaling laws, and to gain further information on the dislocation activity within the microscale deformation. The uniqueness of this project relates to the following aspects:

- A new sample fabrication technique is introduced which avoids the conventional problem of process-induced damage (FIB) and thus allows more idealized testing conditions.

- It provides the possibility to purposely contaminate sample structures while having an ideal non-contaminated reference, allowing to also quantify the effect of FIB induced damage.

- For microstructural analysis the comparatively new technique TKD is utilized which allows capturing lattice orientations across the cantilever cross section with a lateral resolution down to 10 nm while profiting from the computational advantages of basic EBSD, allowing to generate detailed maps of misorientations, which allow a visualization and quantification of dislocations.

- The data gathered with TKD is combined with a promising data evaluation method developed by Pantleon for standard EBSD. Combining this approach with a five times higher lateral resolution shall grant deeper insights into dislocation networks even distinguishing their respective Burgers and line vectors.

- The lithography-based processing grants a large sample set, from which about 500 cantilevers were tested. This is a significant statistical advantage. Moreover, cantilevers of two different orientations, different thickness and aspect ratios are fabricated and investigated.

The project is organized in the following way: Chapter 2 deals with the sample preparation with focus on the new cantilever fabrication route that has been developed. In chapter 3, the as-fabricated sample structures are analyzed. This is relevant in order to assure that the several 100 cantilevers tested are in fact comparable to each other in terms of size and microstructure. The experimental setup used to realize bending is presented in chapter 4 and the results are highlighted, while chapter 5 focuses on microstructural investigations of the deformed cantilevers. The findings are discussed in the last chapter and also compared to discrete dislocation dynamics (DDD) simulations carried out by the research group FOR1650. Details on the parameters for the simulation itself are listed in the appendix.

2 Sample preparation

The sample structures used in this work are single crystalline Ag cantilevers supported on one side and deflected by a wedge type indenter tip at their free end. In this chapter, the experimental setup is introduced and the choice of orientation and sample size are detailed. The main focus of the chapter, however, is the development of a suitable fabrication route for the large scale production of single crystalline µm-sized Ag cantilevers. A particularly important aspect during fabrication is to keep the structures free from any kind of process-induced damage, such as implantation of another material into the single crystalline matrix. This statement refers to the conventionally used FIB-based fabrication route which is by far the dominant procedure to shape cantilevers at the µm scale for research purposes. The cantilevers used in the work at hand are fabricated by consecutive steps which have been specifically developed in this project.

2.1 Choice of cantilever orientation

The choice of crystal orientation is crucial, because TKD and EBSD are the main tools used for microstructural characterization. The apparent drawback of both of these methods is that they are highly surface sensitive. Even if they provide access to the full orientation matrix at each measurement point, it needs to be mentioned that the scan is only executed on a cross section of the cantilever volume ($\boldsymbol{x_1}$-$\boldsymbol{x_2}$-plane in Fig.2.1). Note that the indexing of the coordinate system as it is done in Fig.2.1 will be used throughout the project. Because the scanning procedure is 2D, its results are a priori not representative for the entire volume of the deflected samples. As mentioned in chapter 1, even within the slice that is actually scanned, the information depth is only a few 10-20 nm for both EBSD (Zaefferer, 2011) and TKD (Keller & Geiss, 2012) under given scanning conditions. Therefore the question arises, whether the dislocation arrangement revealed by a 2D scan can be considered to be representative for the cantilever or if instead a tomography technique would be necessary to obtain the whole picture. For the given case of cantilever bending, the assumption of the cross section being representative for the entire volume can be justified if the loading results in a state of plane strain deformation where the rotation axis of the bending process is perpendicular to the chosen cross section (i.e. rotation about x_3). If the crystallographic orientation of the sample is chosen to meet these conditions then each cross section taken in the x_1-x_2-plane should reveal essentially the same characteristics (dislocation arrangements) regardless at which point along x_3 it is taken. From the two orientations presented in the following, one matches this condition exactly (high symmetry) and one is close to satisfying it (dual glide).

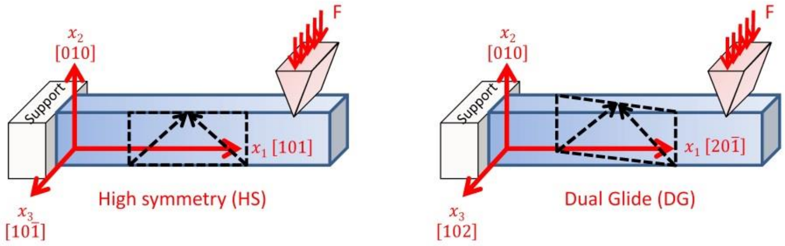

Figure 2.1: Schematic of the sample orientations HS and DG. The effective Burgers vectors are sketched in black.

Due to the single crystalline nature of the specimen the slip systems activated under bending can be predicted using Schmid's law (Schmid & Boas, 1935). Before applying the law, however, it has to be assumed that the load causes pure bending without any shear forces and that the tip geometry is sufficiently flat so it does not provoke any forms of inclined bending. Shear forces can be neglected if the aspect ratio is chosen adequately (see chapter 2.2) and the wedge type indenter tip should guarantee plane bending. The latter has also been verified experimentally using optical profilometry. With this setting, two orientations are chosen in this project: They are named High Symmetry (HS) and Dual Glide (DG) throughout the project and are illustrated in

Fig.2.1. In both cases the cantilever normal $\boldsymbol{x_2}$ corresponds to the crystallographic direction [010]. The cantilever width is described by the axis $\boldsymbol{x_3}$ and coincides with $[10\bar{1}]$ for HS and [102] for DG. Accordingly, the axis along the cantilever length $\boldsymbol{x_1}$ is [101] and $[20\bar{1}]$ for HS and DG, respectively. Under the mentioned assumption of negligible shear forces, the external load F causes the resulting normal stress within the cantilever to be directed solely along $\boldsymbol{x_1}$ and thus the Schmid parameters m are easily calculated. The results are shown in Tab.2.1. Throughout the project, Schmid-Boas notation will be used to index slip systems. As can be seen in Tab.2.1 the notation consists of a letter from A to D for the four individual {111} planes and a number from 1 to 6 for the six potential Burgers vectors <110>.

In HS orientation, there are four slip systems with a non-zero Schmid factor m and moreover they are identical in their value of m, which means they have the same probability of being activated. In Schmid-Boas notation their names are B2, B5, D1 and D6. Two sets of these four slip systems act on the same crystallographic plane (B and D). Therefore, the systems work cooperatively and the coplanar vectors can be added mathematically. In turn, the HS geometry results in two effective slip systems with two effective Burgers vectors only which are sketched by the black arrows in Fig.2.1. The strain imposed onto the crystal is therefore plane, coinciding perfectly with the $\boldsymbol{x_1}$-$\boldsymbol{x_2}$-plane, if all systems are activated to equal amounts. The name high symmetry (HS) is chosen because any other slip system should not be activated according to Schmid's law.

In DG geometry all twelve slip systems have a non-zero Schmid factor m, but only two of them, namely A6 and C5, stand out as their value of m reaches almost the maximum value possible of 0.5 (Tab.2.1). When comparing all of the calculated values, it is seen that this orientation should result in dual glide on these systems with only minor contributions of other systems. The two Burgers vectors determining the glide process span a plane that has a 18.4° inclination with respect to the cantilever axis $\boldsymbol{x_1}$. Therefore the microstructure seen in an $\boldsymbol{x_1}$-$\boldsymbol{x_2}$ cross section becomes a function of the position $\boldsymbol{x_3}$ where the image is taken. Nevertheless, due to the plane strain condition, images taken at different positions should reveal essentially the same dislocation structures only with a small in-plane translation due to the tilt. The amount of translation should not be significant since the angle of inclination is rather small.

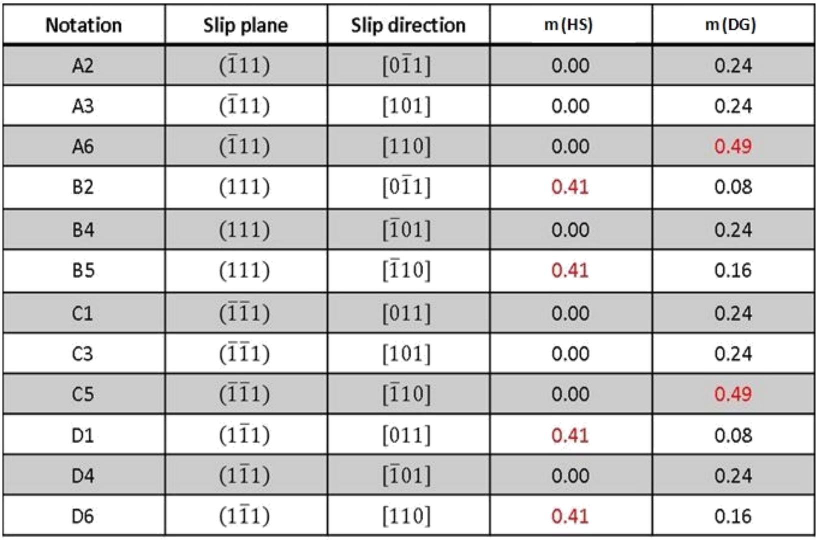

Notation	Slip plane	Slip direction	m (HS)	m (DG)
A2	$(\bar{1}11)$	$[0\bar{1}1]$	0.00	0.24
A3	$(\bar{1}11)$	$[101]$	0.00	0.24
A6	$(\bar{1}11)$	$[110]$	0.00	0.49
B2	(111)	$[0\bar{1}1]$	0.41	0.08
B4	(111)	$[\bar{1}01]$	0.00	0.24
B5	(111)	$[\bar{1}10]$	0.41	0.16
C1	$(\bar{1}\bar{1}1)$	$[011]$	0.00	0.24
C3	$(\bar{1}\bar{1}1)$	$[101]$	0.00	0.24
C5	$(\bar{1}\bar{1}1)$	$[\bar{1}10]$	0.00	0.49
D1	$(1\bar{1}1)$	$[011]$	0.41	0.08
D4	$(1\bar{1}1)$	$[\bar{1}01]$	0.00	0.24
D6	$(1\bar{1}1)$	$[110]$	0.41	0.16

Table 2.1: Schmid's factors *m* for the given orientations HS and DG following the Schmid-Boas notation.

To sum up, both HS and DG lead to a constellation where the glide situation can be approximated adequately by two effective Burgers vectors only, acting on two different planes. Therefore, the state of strain can be assumed to be plane, at least during the early stages of deformation. That means that the dislocation pattern seen in a 2D EBSD or TKD scan should not - or at least not significantly - be dependent on the width position x_3 at which a cross section is taken. Kysar et al. (Kysar et al., 2010) who used the HS orientation on single crystalline Cu samples as well but under different loading geometry (wedge indentation instead of bending), used basically the same argumentation to exclude any kind of lattice rotation or lattice curvature along the x_3 direction. The plane strain assumption thus saves the trouble of having to perform an EBSD tomography to represent the cantilever volume completely and justifies statements on the dislocation state of the entire cantilever out of a single 2D scan.

To determine mechanical strength of the two orientations, the Young's Modulus for HS and DG is calculated using values of the compliance tensor for single crystalline Ag from literature (Kittel, 2010). The Young's moduli along $\boldsymbol{x_1}$ found are 84.1 GPa and 63.5 GPa for HS and DG orientation, respectively.

2.2 Choice of cantilever layout

In order to study the mechanical size effect in a meaningful way, the tested cantilevers need to keep a constant aspect ratio while the total volume is continuously scaled down. More than that, the choice of aspect ratios and total size of the cantilevers must meet some additional criteria, which are detailed below.

The first criterion is the expected cantilever stiffness S. The structures need to be detectable by the indenter system used, which is only the case if they impose enough resistance to the tip as it is pushed downwards. At the same time the cantilevers should be fabricated as small as possible to retrieve as much valuable information as possible on the size effect. For the given resolution of the Agilent G200 nanoindenter system used in this project, the stiffness S should always be at least 25 Nm^{-1}. When designing the structures, the formula for the stiffness, derived from simple beam theory of a cantilever supported at one end can be used to give an approximate value of the expected stiffness S (e.g. Kraft & Volkert, 2001)

$$S = \frac{3EI}{(1 - v^2){l_{eff}}^3} \tag{2.1}$$

where E is Young's modulus, I is the axial moment of inertia, v is the Poisson ratio which is assumed to be 0.38 for the Ag cantilevers and l_{eff} is the effective cantilever length, i.e. the distance between the exact loading point and the support. Inevitably, the effective cantilever length l_{eff} will be slightly shorter than the total cantilever length l_0 since the free end of the structures cannot be pinpointed perfectly by the indenter tip.

The cantilever height h is preset to be 1 µm, 2 µm and 3 µm by the epitaxial thin film deposition step detailed in chapter 2.3. When designing sample dimensions, the values for width w and total length l_0 were chosen in a way that assures the aspect ratios l_0/w and l_0/h to be constant for each thickness. The given cantilever geometry causes non-uniform bending per definition but more importantly induces shear forces upon bending. In the idealized experiments, it is desirable to reduce the complexity of the mechanical problem as far as possible. Therefore, the shear forces have to be reduced so a pure bending assumption can be justified. Bernoulli's hypothesis suggests that shear forces can be neglected, if cross sections within the cantilever which were plane and perpendicular to the neutral fiber before the deformation remain plane and perpendicular to the neutral fiber throughout the deformation process (i.e. cross sections do not warp). It can be shown that this hypothesis holds true as long as the aspect ratio l_0/h is sufficiently high. In literature, different suggestions are made at which ratio the shear stresses are sufficiently small to be considered negligible. Gross et al. (Gross et al., 2009) derived that for a cantilever, the deflection resulting from shear forces is about 3 % of the total deflection if $l_0/h = 5$ and therefore suggests the influence of shear force to be negligible if the ratio is chosen bigger than 5. Other sources suggest different values, like Diebels (Diebels, 2005) who proposes an aspect ratio l_0/h of at least 10. In this project, the ratio was chosen to be of the order of ten or bigger.

In literature, only a few precise recommendations are found concerning the l_0/w ratio. The common statement is that the width should be "reasonably smaller" (Gross et al., 2009) than the length to assure plane bending. Armstrong et al. (Armstrong et al., 2011) performed bending experiments on cantilevers fabricated by FIB of triangular cross section and recorded the deviation of measured compliance from the expected one according to simple beam theory. They found that the differences are a function of the cantilever length and in turn of the aspect ratio l_0/w. Good agreement between simple beam theory and experiment is found for l_0/w values of at least 6. In the project at hand, however, the options are limited by the fact, that l_0/w ratios above 5 show an increase in redeposited Ag on the cantilever edges, as will be shown in chapter 2.6, which might have an effect on the bending behavior. Therefore, the ratios used throughout this project were chosen to be 5, 4 and 3 denoted as A, B and C in the sample identification, respectively (Tab.2.2). For one final sample set, denoted D, the lateral dimensions length and width are constant and only the height is varied. As a result, the aspect ratios are not constant for different heights and the increase in cantilever volume with increasing height is very small compared to the other sample sets. In contrast, the increase in stiffness is significant. This set of sizes was chosen to purposely fabricate some structures which are both very close to the mentioned recommendations as soon as the height equals 3 µm, so this effect on the mechanical behavior can be studied as well.

Name	Height h	Width w	Length l_0	l_0/h	l_0/w
A	1	2.5	12.5	12.5	5
B	1	3.5	14	14	4
C	1	5	15	15	3
D	1	6	18	18	3
A	2	5	25	12.5	5
B	2	7	28	14	4
C	2	10	30	15	3
D	2	6	18	9	3
A	3	7.5	37.5	12.5	5
B	3	10.5	42	14	4
C	3	15	45	15	3
D	3	6	18	6	3

Table 2.2: Cantilever dimensions in [µm] of the structures effectively used in this project. Note that these values are the ones used during lithography (i.e. from the layout), and not perfectly equal to the dimensions of the as-fabricated testing structures.

To sum up, all cantilevers sets at hand can be distinguished by three factors in total: The cantilever thickness which is 1 µm, 2 µm or 3 µm, the orientation being HS or DG and the aspect ratio being A, B, C or D. Each of these 24 categories (with some slight deviations) is represented by about 15-30 individual cantilevers. In one part of the project an additional category arises, as some selected samples with aspect ratio B and DG orientation are FIB contaminated, which will be explained chapter 3. The total number of cantilevers tested throughout the project is about 500.

The consecutive fabrication steps from layer deposition to anisotropic etching which lead to the final cantilever structures are illustrated in Fig.2.2. After deposition of an epitaxial Ag thin film by physical vapor deposition (PVD), the films are patterned using electron beam lithography (EBL) and ion beam etching (IBE). As a side effect of the purely physical IBE, redeposited Ag is found at the edges of the cantilevers and is attempted to be removed by wet-etching in a diluted NH_3:H_2O_2 solution with the PMMA resist still on top of the structures. This step is followed by stripping of the resist in acetone using ultrasound. To make the cantilevers free-standing, the final step consists in anisotropic Si etching using KOH.

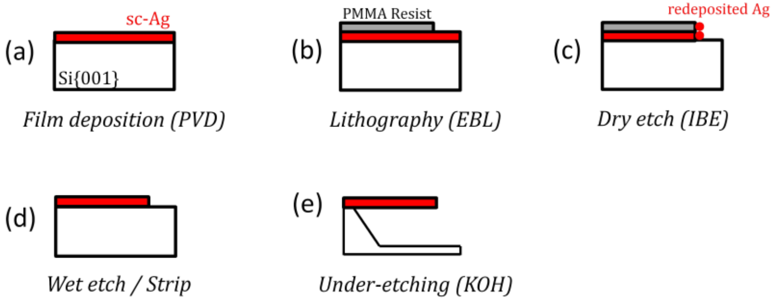

Figure 2.2: Cantilever fabrication procedure in five consecutive steps. (a) epitaxial thin film deposition, (b) lithography, (c) pattering by dry-etching, (d) redeposition removal by wet-etching and stripping of the resist, (e) under-etching of the structures using KOH.

2.3 Epitaxial Ag thin film deposition by PVD

The starting point of the fabrication procedure is the deposition of epitaxial Ag thin films onto 2" {100} Si wafer substrates. This step is done by PVD at the Thin Film Laboratory of the Max-Planck-Institute for Intelligent Systems in Stuttgart. There are several requirements which must be met in order to assure epitaxial film growth. Some of the key aspects are a suitable combination of film and substrate material assuring that lattice misfit can be handled and no unwanted reactions take place. This includes diffusion processes between film and substrate or for some combinations of film and substrate material even melting due to eutectics located at temperatures which might be reached during PVD (e.g. Au-Si eutectic at 643 K). Moreover, the cleanliness of the substrate plays an important role, as well as ultra-high vacuum conditions and sufficient adatom mobility. The term adatom refers to a sputtered atom in PVD which is about to be absorbed onto the growing film, but has some degree of freedom left to move. A high adatom mobility is crucial for epitaxy and its value depends on a variety of factors. The most common way to manipulate it, is by heating the substrate during deposition.

The lattice parameters for Ag and Si are 0.409 nm and 0.543 nm, respectively (Yang et al., 1997; Hur et al., 2007). The difference in parameters is quite large corresponding to a lattice misfit of about 24.7 %. The orientation relationship between the fcc lattice of the Ag film epitaxially grown onto the diamond cubic Si substrate is cube-on-cube, so the index notation of the interface writes Ag(001)[110]||Si(001)[110]. A 4x4 mesh of Ag unit cells fits almost perfectly onto a 3x3 mesh of Si unit cells, with a misfit of only 0.4 % (Yang et al., 1997; Hur et al., 2007) granting very good condition for epitaxial growth. This is schematically illustrated in Fig.2.3. It can also be seen that misfit dislocations are needed to merge the two unit cells correctly at the interface and that their spacing at the interface has to be 1 dislocation per 4 Ag unit cells, i.e. the misfit dislocation spacing becomes 1.636 nm. The growth is assumed to proceed in Stranski-Krastanov mode (Yang et al., 1997), where at first some monolayers of Ag form (and possibly some isolated islands at impurities on the substrate) and then the growth is continued in the form of islands only.

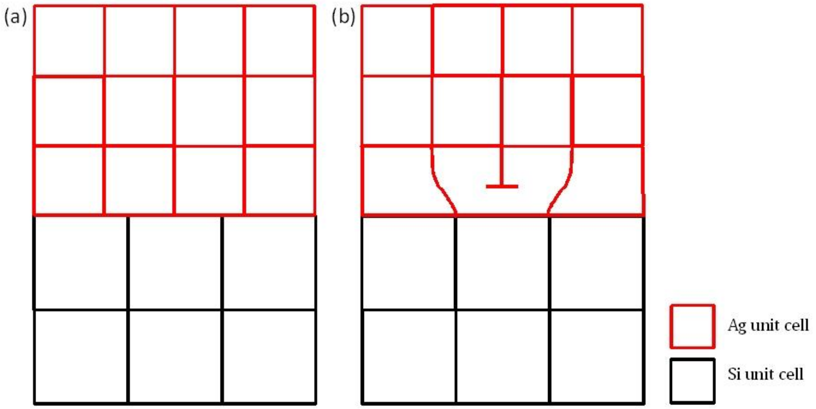

Figure 2.3: Illustration of a misfit dislocation arising from cube-on-cube growth of a 4x4 unit cell mesh (Ag) onto a 3x3 unit cell mesh (Si) (view in cross section). The stacking of unit cells (a) without and (b) with misfit dislocation is displayed.

To assure cleanliness, the 2” {100} Si wafer substrates are first pre-sputtered with Ar^+ ions to remove native oxides. For that purpose, a Kaufmann ion source is used at an acceleration voltage of 200 V (i.e. 200 eV ion energy) for 5 min. The pressure of the processing Ar gas is about $4 \cdot 10^{-4}$ mbar. Before deposition of the Ag layer, the pre-sputtered substrates are thermally annealed at 1273 K for 1 h under ultra-high vacuum conditions. It should be mentioned, that according to the work of Hur et al. (Hur et al., 2007) this excessive cleaning step might be left out. They found that during Ag deposition onto {100} Si wafers by PVD using a magnetron source the native oxides desorb when the substrate is heated to 473 K. If the temperature is raised up to 823 K, perfect epitaxial growth is seen even without the cleaning step. Nevertheless, in the project at hand the cleaning step is rigorously executed. After cleaning and annealing, the deposition of the Ag layer is performed by magnetron sputtering. The base pressure of the evacuated chamber is on the order of $5 \cdot 10^{-10}$ mbar and the pressure of the processing gas is about $2.8 \cdot 10^{-3}$ mbar. The power of the electrical discharge at the magnetron source is 100 W. The substrate-to-target distance measures 120 mm and, during deposition, the substrate holder is rotated continuously to assure homogeneity. The substrate is heated to 573 K. The deposition rate under these conditions is 100 nm in 131 s. The thickness of the single crystalline Ag layer is chosen to be 1 µm, 2 µm and 3 µm which will later correspond to the cantilever height.

Since the exact choice of substrate temperature is the most crucial factor which significantly affects crystal quality, several temperatures have been tested and the perfection of the grown single crystal was evaluated using XRD. For this purpose 100 nm thick Ag layers have been deposited following the PVD process described above onto {100} Si wafer pieces having an area of a few cm^2 at different substrate temperatures ranging from 423 K up to 673 K. While intuitively a higher deposition temperature increases the adatom mobility and should therefore be beneficial for the as-deposited layer, care has to be taken, as an increase in substrate temperature might also result in unwanted intermixing between growing film and substrate.

XRD is carried out in standard Bragg-Brentano geometry which is an easy way to rapidly check for single crystallinity (Fig.2.4). Due to this particular setup, only peaks belonging to {100} families, i.e. parallel to the surface normal direction contribute to the diffraction pattern, if the growth is indeed epitaxial. Indexing the respective reflections is done based on the powder diffraction file of the International Centre for Diffraction (ICDD) with the number 04-0783 and 27-1402 for Ag and Si, respectively. For all substrate temperatures chosen, no peaks from planes other than {100} could be detected. Some Ag films with thicknesses up to 3 µm have been tested as well, and they still show no unwanted peaks in the diffraction pattern. The intensity of the diffraction signal is so high, that for Ag{200}, even K_β peaks are seen and the absorption edge of the Ni filter used. When looking at the exact peak positions, a significant difference to the values from the powder diffraction files is found. It needs to be mentioned that the diffractometer used for scanning (Bruker D8 Advance) is conventionally used for powder samples only, i.e. the sample stage is unable to move up and down (only rotating and tilting is possible). The fact that the height of the sample holder cannot be manipulated implies that an error in sample alignment and thus in the absolute value of the measured 2θ positions is inevitable which becomes more significant for peak positions at low 2θ values.

After determining the peak center position of Ag{200} a rocking curve measurement is executed for this particular peak. To mimic the sample tilt needed for this kind of measurement, the X-ray source and detector are moved anti-symmetrical to one another on the goniometer circle. The width of a peak scanned with this method gives detailed information on various parameters, such as grain size and defect density. In the sample used here, where no grains exist, the width is only affected by the defect density and also reveals the amount of misorientation of the film's surface normal. For peak fitting a Lorentzian function is used which is of the form

$$f(x) = y_0 + \frac{2A}{\pi}\frac{w_L}{4(x - x_c)^2 + w_L{}^2} \tag{2.2}$$

The parameters are y_0, A, x_c and w_L. In the following, the width of a diffraction peak will be characterized by the width parameter w_L which is equal to the full width at half maximum (FWHM).

In Fig2.5 can be seen, that the FWHM decreases with increasing substrate temperature which means that the quality of the single crystal becomes better. This decrease in FWHM finds a saturation at about 623 K. However, the thin films deposited above this point show a change in optical properties: They lose their metallic shine for a rather whitish appearance. Still, even for those samples, no unwanted peaks or different phases could be found in the XRD scans. It seems possible, that the surface roughness of the Ag films increased but no further investigations are taken concerning this aspect. Instead, it was decided to fix the deposition temperature for all samples at 573 K as a compromise between keeping the expected silver color of the film while having the highest crystalline perfection possible. Under these conditions the mean misorientation angle of the film's surface from its ideal position is about ± 0.5° (FWHM/2) as can also be seen on the blue curve in Fig.2.5a.

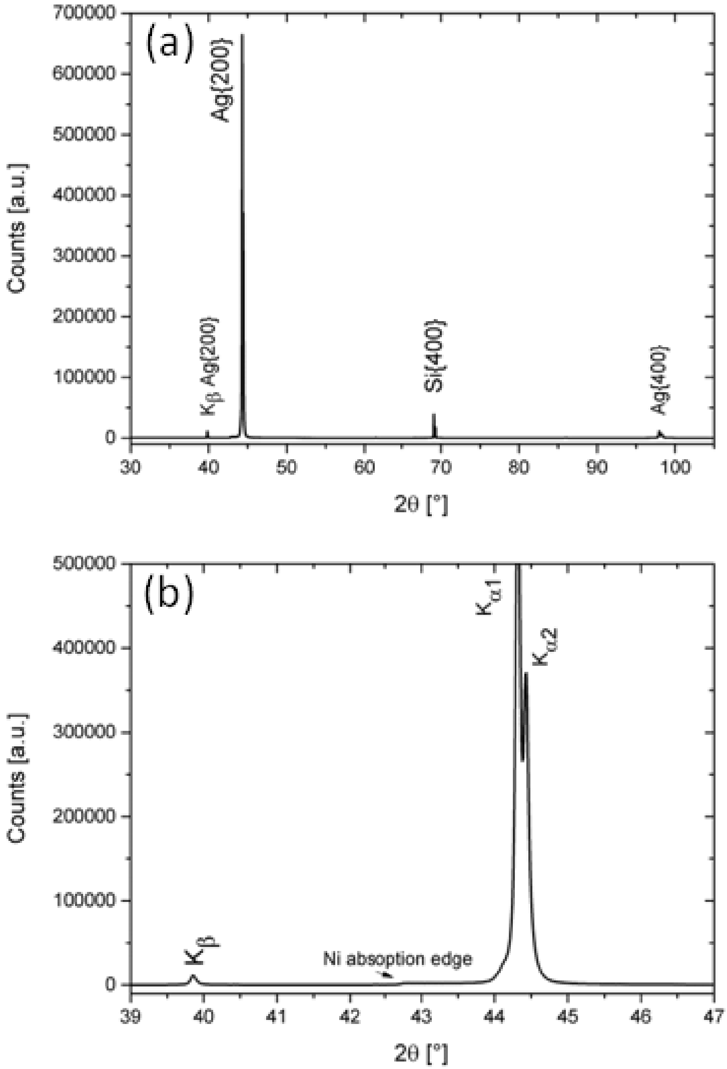

Figure 2.4: (a) Bragg-Brentano Scan of a 1 µm thick Ag thin film. (a) The entire phase diagram, (b) Zoom onto the Ag{200} peak.

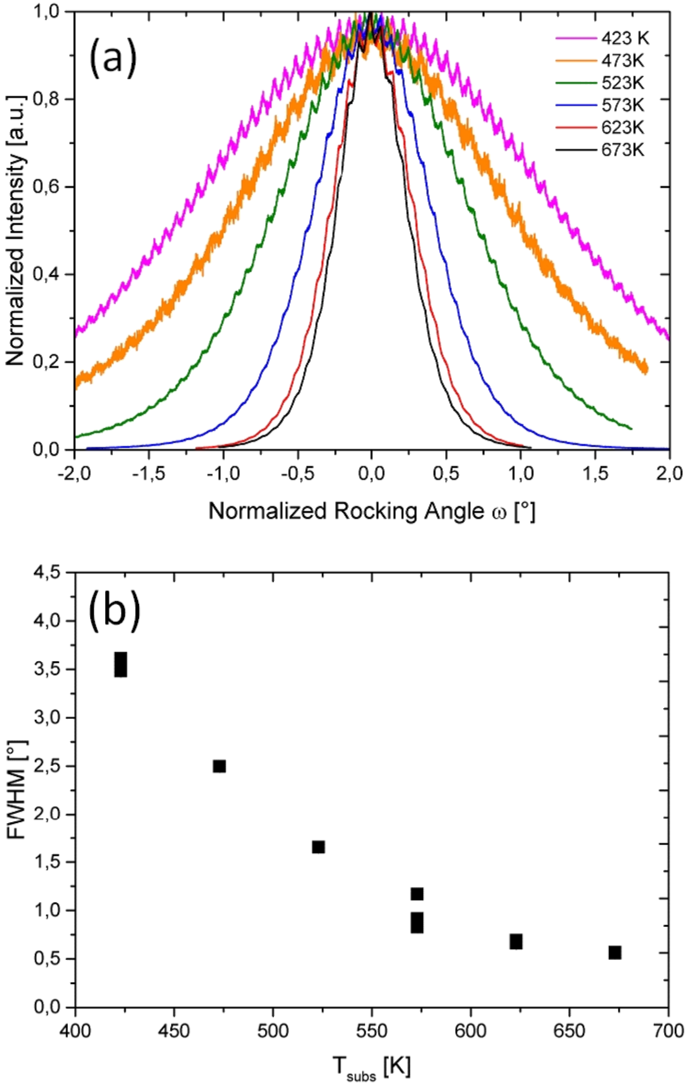

Figure 2.5: (a) Rocking Curves for 100 nm thick Ag films deposited at different temperatures. The intensity and the peak centers have been normalized for comparison. (b) FWHM for the rocking curves as a function of substrate temperature.

Residual stresses within the film are an important aspect that is likely to be influenced by substrate temperature during deposition. While the absolute amount of stress is inaccessible from a single Bragg-Brentano scan only, the relative change in residual stress from sample to sample can easily be estimated by the shift of a certain peak. To get an absolute value of the stress a more profound method such as $\sin^2(\Psi)$ would be required which has not been applied in this project because of the single crystalline nature of the specimen. The diffraction peaks can only be seen under very precise angular positions and vanish rapidly as the sample is tilted. The resulting limited amount of data points considerably increases the uncertainty when applying such a method. The Bragg-Brentano method is executed by measuring the peak centers and in turn the crystal plane spacing. The changes in spacing between two samples is transformed into a change in strain along the surface normal. Using the Young's Modulus for <110> direction, the residual stress value along <110> is obtained. Estimating the relative change in stresses via Bragg-Brentano scans is, however, difficult because the height position of the sample stage is fixed so no alignment can be performed. The thickness of the Ag layer is supposed to be very accurate while the thickness Si wafer substrates is indicated as 275 µm by the supplier (CrysTec GmbH) with an uncertainty of ± 25 µm. Since the height of the sample cannot be adjusted adequately, this uncertainty might lead to a change in 2θ position. Therefore, even such an estimation needs to be handled with care. For increasing substrate temperature, the peaks are shifting to lower 2θ positions which implies that the stress changes are of compressive nature. The amount of shift is significant and it is found that rising the substrate temperature by about 100 K leads to a change in stress of about 150 MPa.

Another interesting side effect during the Rocking Curve measurement is the appearance of periodical oscillations within the peak under consideration (Fig.2.5a). This is only detected in Ag thin films of thickness 100 nm or smaller, while samples of µm thickness reveal no such shape. The phenomenon is known as Kiessig-Oscillations and commonly occurs in X-Ray reflectometry (XRR) on thin films with thick nesses of 100 nm or below (Nayak et al., 2006). The physical reason behind this effect is the interference of the X-ray waves diffracted from the top surface of the thin film and the ones diffracted at the interface between substrate and thin film. The interference pattern is a sinusoidal function which is superimposed to the regular diffraction pattern. Besides the low thickness, additional criteria have to be met in order for Kiessig-Oscillations to become visible: The first criterion to be fulfilled is the use of parallel X-ray beams, which is given by the optics chosen for the rocking curve measurement (Göbel mirror). Additionally, since the signal of the oscillations is significantly low, the intensity of the diffraction pattern recorded must be very high. This factor is immediately given in XRR as the 2θ values are very low. In XRR, the oscillations usually already vanish for 2θ values bigger than 4°. The fact that the rocking curves shown above reveal Kiessig-Oscillations therefore stems from the fact that the intensity of the Ag{200} is significantly high which in turn can be interpreted as further proof of the very high crystalline perfection. In XRR the distances between the maxima of Kiessig-Oscillations can also be used for determination of the thickness of the analyzed layer. Because the oscillations vanish for the 1-3 µm thicknesses effectively used for cantilever fabrication, a thickness determination using XRD was not considered in this work.

As mentioned, the rocking curves' FWHM yields information on defect density within the samples. An important point is therefore to compare the rocking curves taken for samples of different thickness under the same deposition conditions. The results are shown in Fig.2.6. A decrease is seen once the Ag layer thickness is increased, implying that the defect density is dropping. This general trend can be seen but from this kind of measurement but no quantitative estimation on dislocation densities can be made.

A final, solely qualitative, characterization of the as-deposited thin film is done by TEM on a cross section of the thin film. Selected area diffraction patterns again confirm single crystallinity. Moreover, dislocations at the film-substrate interface can be detected (Fig.2.7) as expected from the lattice misfit argumentation. The samples are prepared by mechanical thinning and etching; the method is for example described in Arzt et. al. (Arzt et al., 2003).

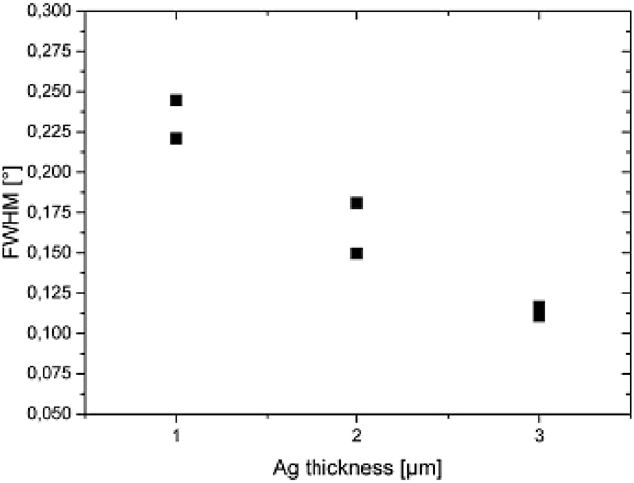

Figure 2.6: Change in rocking curve FWHM of the Lorentzian fit versus the Ag layer thickness. The peak used is Ag{200}.

2.4 Electron beam lithography

The following sections of this chapter detail the processing steps (section 2.4-2.7) for the as-deposited thin films. All the steps are carried out at the Institute for Microstructural Techniques (IMT) at KIT and are supported by Karlsruhe Nano and Micro Facility (KNMF).

The cantilevers are to be shaped out of the epitaxial Ag thin films. Therefore the next step is to use lithographic methods in order to pattern a polymeric resist on top of the layer. In this project Electron Beam Lithography (EBL) is used for that purpose. A PMMA 950k resist is deposited onto the film’s surface using spin coating. The dose of the electron beam exposure during EBL is 650 $\mu C \cdot cm^{-2}$ for all thicknesses. Afterwards, the patterning is done by ion beam etching (IBE). The term IBE is used instead of the more conventional reactive ion beam etching (RIBE) to emphasize that solely Ar is used as processing gas, so dry-etching is purely physical. Because this kind of sputtering is non-selective, the thickness of the resist is chosen according to the Ag layer thickness in a way that it exceeds it by several 100 nm: 1.5 µm resist for 1 µm film, 2.5 µm resist for 2 µm film and 3.2 µm resist for 3 µm film. The fact that 3.2 µm is the highest thickness up to which PMMA resist can be spin-coated homogeneously, also sets the maximum cantilever height that is feasible with this fabrication route to 3 µm.

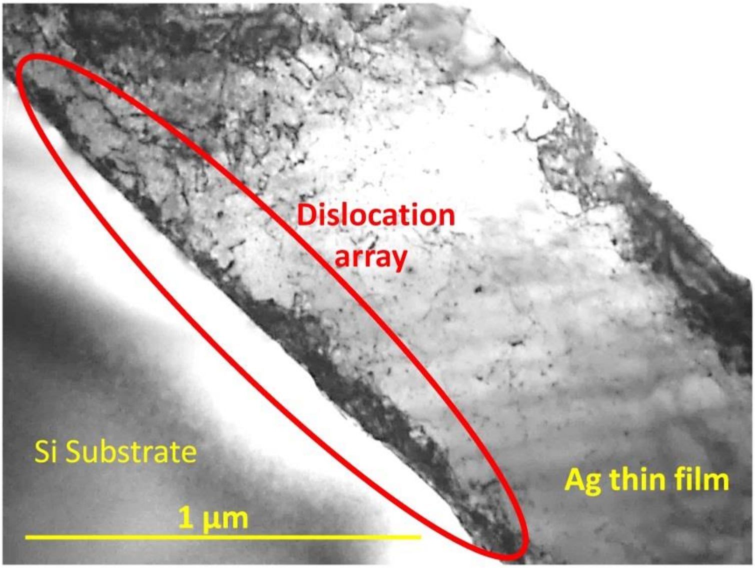

Figure 2.7: TEM bright field image of a cross section of an as-deposited Ag thin revealing misfit dislocations located at the film-substrate interface.

The lithographic mask itself is designed in a way that cantilevers with the two different orientations (HS, DG) and various combinations of aspect ratios (A, B, C, D) are obtained. While for the different sizes and aspect ratios it is sufficient to adjust the sizes of the rectangular patterns, an in-plane rotation is needed to realize HS and DG orientation. For HS the cantilever axis is simply parallel to the flat, while for DG, the cantilever axis is tilted by 18.4° away from the flat that cantilever axis x_1 coincides with a crystallographic direction $[20\bar{1}]$. For HS, all cantilevers of one particular aspect ratio, are lying on the same etch pit (red in Fig.2.8b), while in DG, the etch pit is divided into smaller elements (Fig.2.8c). Here a single pit contains only two cantilevers. The reasoning behind this design becomes obvious when the undercut is detailed (section 2.7 of this chapter). Three individual masks are needed – one for each Ag film thickness (1 µm, 2 µm, 3 µm) – but the layout has essentially the same design. Four identical arrays containing all aspect ratios for HS are found on the upper half of the wafer and four arrays of the same aspect ratios but with the 18.4° tilt are on the lower half (Fig.2.8a). The layout of the mask for EBL is chosen such that the entire wafer can be broken down into four individual chips of about 20 mm x 20 mm in size, each containing two full arrays of one orientation. The size of the chips fits perfectly for the sample holders used in SEM and in the nanoindenter system and assures that a micro manipulator inside the SEM, which is used to handle the lamellas cut with FIB, can reach each individual cantilever if needed. Since the feature size of the cantilevers are always bigger than 1 µm, direct laser writing might have been a suitable choice for lithography, as well. However, EBL has the advantage of offering more versatility in a way that the feature size could be reduced to the nm scale if desired. If the film thickness is reduced accordingly, much smaller single crystalline cantilever structures could be produced. Attempts to produce such nm-sized cantilevers were not pursued, but seem to be feasible based on the current process development.

2.5 Patterning with IBE

The main drawback that results from the choice of Ag as film material is that the possibility of patterning the as-deposited film by etching methods is very limited. In fact, for most MEMS applications, Ag is usually either entirely removed or grown only in selected areas (for example as mirror elements) using sputter masks or electro-deposition. The problem is that Ag resists most wet etchants, even aqua regia which is frequently chosen to remove noble metals such as Au or Pt. A typical wet-etchant for Ag is a diluted solution of

NH_4OH and H_2O_2. The solution has several critical issues when used for patterning: First of all the reaction is very fast and even if the solution is strongly diluted, it is still hard to guarantee sufficient control. Dissolving the Ag film this way is furthermore accompanied by a strong bubble formation due to the nature of H_2O_2 that is used as a reduction agent. This causes the

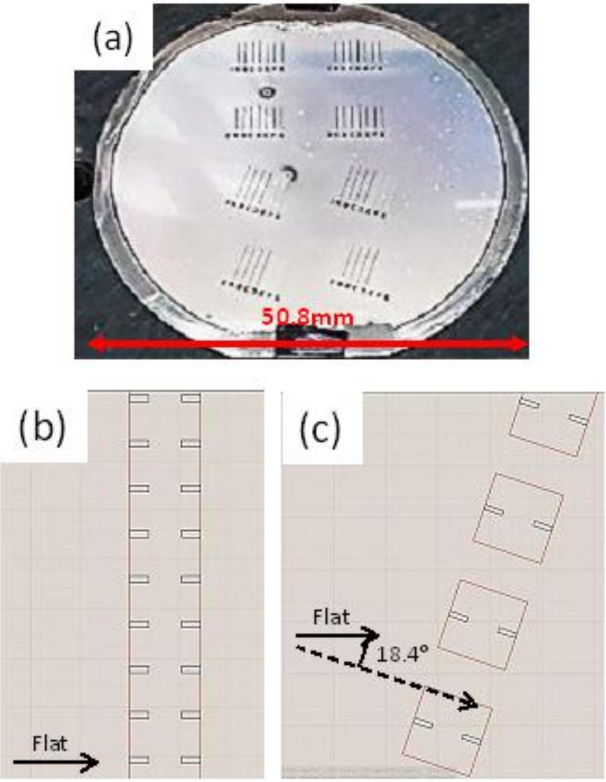

Figure 2.8: EBL mask design. (a) Shows the entire 2” wafer after fabrication with 4 HS arrays on the upper and 4 DG arrays on the lower half. (b) highlights the design for HS and (c) for DG. In (b) and (c) the black layer corresponds to the cantilevers, while the red one represents the etch pits. The logical subtraction operation of these both layers gives the area that is exposed to the electron beam in EBL.

process to become inhomogeneous which can only partially be corrected by etching in short time intervals with several breaks where the sample is neutralized in water. To reduce bubble size, the chemicals are usually diluted in CH_3OH instead of H_2O. However, this is not compatible with conventional photoresists because CH_3OH is capable of dissolving most of them. Another issue is that H_2O_2 is rapidly depleted, so the etchant needs to be renewed all over again after 1-2 min, if the etch rate is to be kept constant. The last problem is that generally processes based on wet-etchants tend to be isotropic in nature. In this case the edges of the cantilevers would be rounded after patterning as in (Matoy et al., 2009). In the early stages of this project, such a wet-etch approach was followed (Fig.2.9a) with the wet-etchant mentioned above in a concentration of $NH_4OH:H_2O_2:H_2O = 1:1:16$, but was not pursued any further when dry-etching was found to work significantly better (Fig.2.9b).

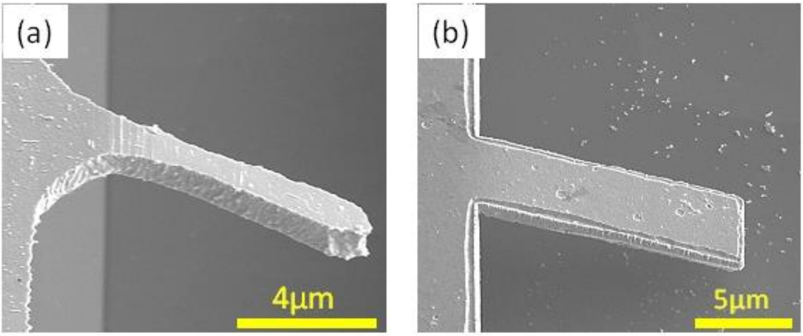

Figure 2.9: SEM images of single crystalline cantilevers. The patterning has been done by wet-etching (a) and dry-etching (b), respectively.

Dry-etch approaches, such as IBE usually have a noticeable advantage over wet-etching in terms of shape accuracy and feasible aspect ratios. Unfortunately, to the state of the art, there are no gases which form volatile components when reacting with Ag. That means that the IBE process is reduced to a purely physical, non-selective sputtering and the only element shielding the layer is the lithographically patterned mask itself. The machine used for IBE in this project is an Oxford Ionfab300Plus. The RF power used to create the Ar plasma is 300 W and the Ar flow is 13 sccm. The beam current is chosen to be 2 mA and the main operating voltage is 200 V with an additional 400 V applied to the accelerator. The substrate holder is rotated to assure homogeneity and cooled down to 293 K during the entire process. In contrast to most metals, the sputtering rate for Ag under Ar^+ ions is particularly high. Under these conditions a sputtering rate of 50 $nm \cdot min^{-1}$ has been found which means that even 3 µm thick Ag layers can be structured within a reasonable amount of time. The time of exposure is therefore 20 min, 40 min and 60 min of 1 µm, 2 µm and 3 µm thick Ag films, respectively. Si has a very low sputtering rate for Ar^+ ions and can thus be considered as a dry-etch stop.

During IBE, the PMMA resist is not immune to the sputtering either and is gradually thinned under the Ar^+ ion bombardment. Apart from the thinning, another remarkable aspect can be observed upon pattering: The formerly insulating PMMA resist changes its color and becomes electrically conductive during the IBE process. The color change is found to be dependent on the PMMA thickness and can be visualized by optical inspection (Fig.2.10). The change in conductivity can be visualized by SEM observations (Fig.2.11), where no charging of the resist is observed anymore. Furthermore, the modified resist does not dissolve in acetone anymore, as needed for stripping. These phenomena have already been reported in literature (Koval et al., 2003; Koval, 2004; Wolff et al., 2010) and the explanation is that under Ar^+ bombardment an outgasing of the PMMA takes places causing bubbles within the resist and changing its chemical structure into carbon or some polymeric compound (Borzenko at al., 1994). The crater-like surface observed in SEM (Fig.2.11c) of the remaining resist might be understood from this bubble formation. To strip the PMMA layer, a short treatment with ultrasound is found to work. The removal is thus purely mechanical and is believed to be possible mostly due to the crater-like surface after IBE.

Another important problem encountered during IBE is shown in Fig.2.12: After IBE, the resist not only changes its surface to a crater-like appearance, but it also changes its lateral shape. All contours which where straight and sharp after EBL are now rounded with an arbitrary shape (Fig.2.12). The cause of this problem was a malfunction of the chiller, i.e. the machine's cooling element. As a result of the ion bombardment, the sample which is supposed to be kept at 293 K, slightly heats up. The heat generated does not suffice to liquefy the resist but it does soften it causing a slight spread over the thin film's surface. This unwanted modification of the resist's shape causes in turn the cantilevers to take the unwanted form shown in Fig.2.12. The problem was fixed at the very end of the project and Fig.2.12 also demonstrates that the fabrication route developed here is indeed capable of producing large arrays of single crystalline cantilevers with accurate shapes.

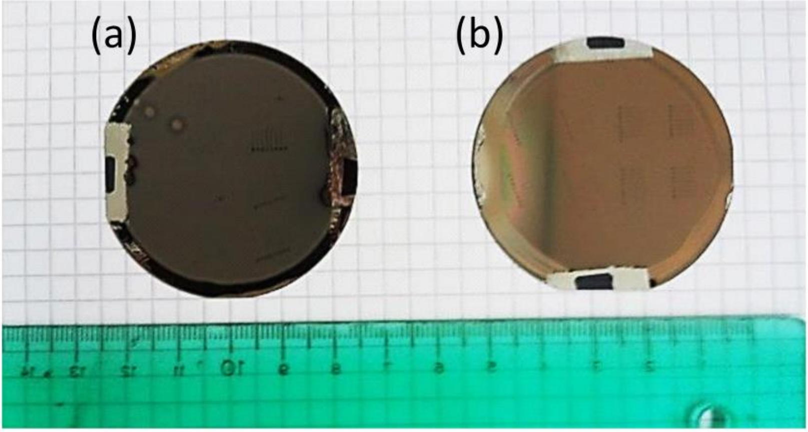

Figure 2.10: Wafers after IBE displaying the color change of the resist. Initial PMMA thickness: (a) 3.2µm, (b) 1.5µm. The remaining PMMA on (b) is supposed to be very thin which explains the high reflectivity of the wafer.

In the introduction of this chapter, it was mentioned that the conventional fabrication route which relies on the use of FIB ion milling has the potential of altering the mechanical properties of the as-fabricated structures. Therefore the question needs to be discussed whether the Ar^+ ions used in IBE can have a similar effect as the Ga^+ ions in FIB. The implantation of Ga^+ during FIB is inevitable and occurs already at the start of the fabrication procedure when a simple snapshot with the ions is taken in order to position the pattern that is to be cut. Such a direct implantation can mostly be excluded during IBE, as the thin films surface is protected by PMMA. In fact, the implantation of ions during IBE can probably only occur in two possible ways, which both seem unlikely: The ions might either be impinging under a certain angle into the unprotected flanks or penetrate the weak spots in the crater-like surface of the PMMA. It seems more than justified to assume the amount of ion implantation during IBE to be negligible.

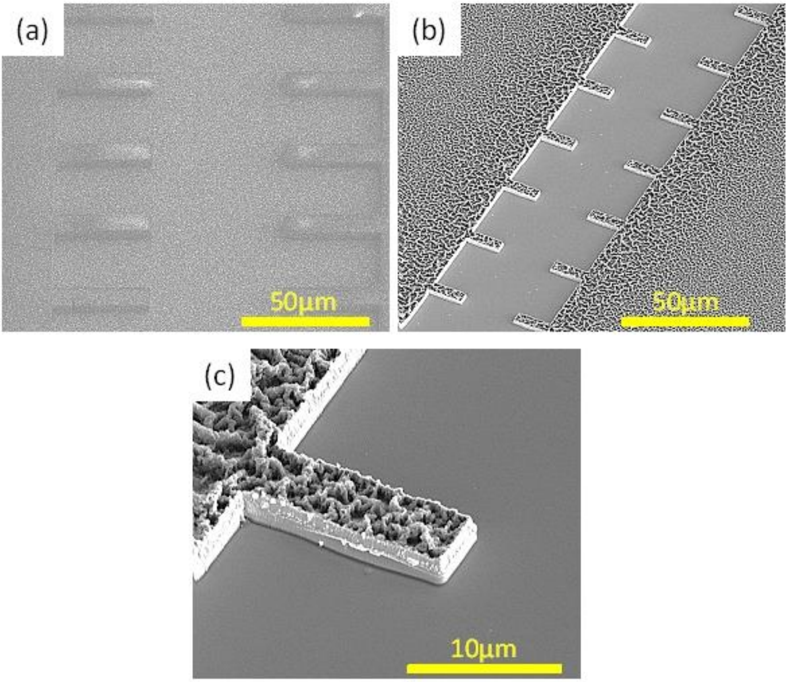

Figure 2.11: SEM images to visualize change in electrical conductivity of PMMA resist after IBE. (a) Sample after EBL, i.e. before dry-etching. Here the PMMA resist is insulating and the resist charges strongly causing bad image quality. (b) and (c) show the sample after IBE. The Si on the bottom of the etch pit appears to be unaffected.

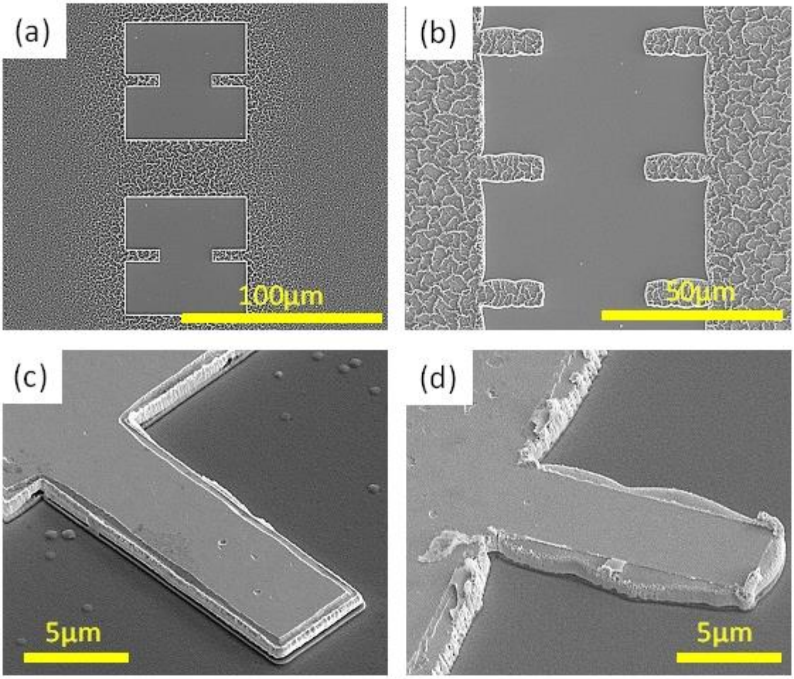

Figure 2.12: SEM images of cantilever structures after IBE (a, b) before and (c, d) after stripping. The process conditions as they are supposed to be result in sharp edges (a, c), while the images (b) and (d) display the state encountered in this work due to insufficient cooling during IBE.

2.6 Isotropic wet-etching to remove redeposited Ag

The downside of the purely physical IBE step is the redeposition of sputtered Ag atoms at the walls of the fabricated structures. Since reactive sputtering is impossible, there is no way to avoid redeposition. The effect is also found to be more significant, for thicker the Ag layer. When inspecting the cantilevers by SEM, another interesting phenomenon is seen: For the given layout, the height of redeposited Ag seems to be dependent of the aspect ratios of the structures (Fig.2.13).

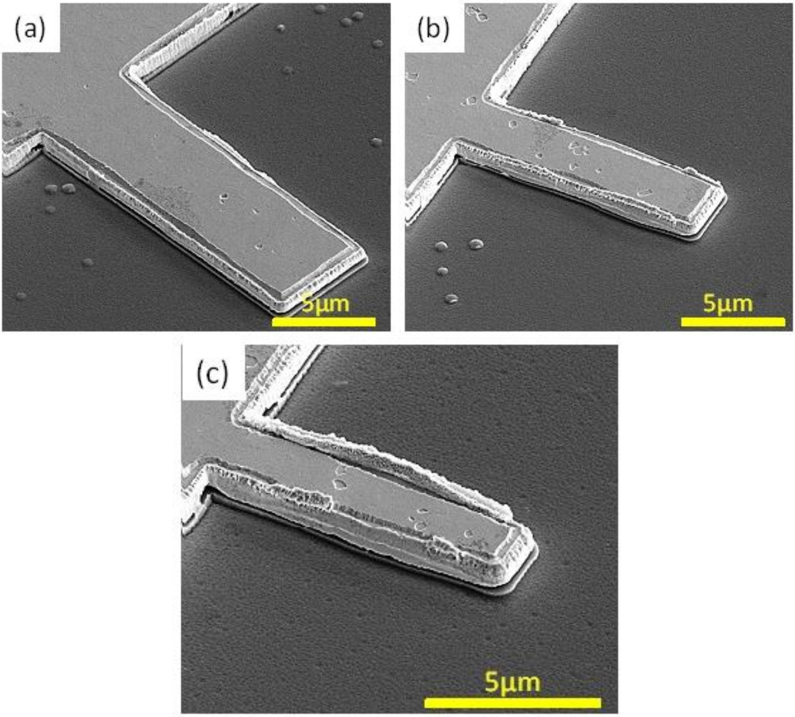

Figure 2.13: SEM images of cantilevers after IBE to display redeposition as a function of cantilever aspect ratio length over width. (a), $l_0/w = 3$, (b) 4, (c) 5.

An attempt to reduce the amount of redeposition while leaving the rest of the thin film unaffected is done by wet-etching. The sample is shortly dipped into a silver wet-etchant, while the remaining PMMA layer is still on top shielding the surface of the cantilevers. The etchant used consists of $NH_3:H_2O_2:H_2O$ in a concentration of 1:1:16 and the exposure lasts about 5 s. It can be observed that this helps removing the desired parts while leaving the cantilevers themselves mostly unchanged. This etch step needs to be short since PMMA (or the altered version after IBE) is also being attacked. Moreover, the crater-like surface of the PMMA after ion bombardment represents some weak spots through which the etchant can quickly attack the surface of the Ag film if the exposure lasts too long. Drastic alterations in the topology of the Ag film can only be observed for longer etching times. Afterwards, the remaining PMMA resist is stripped, as mentioned above.

2.7 Anisotropic Si etching

The final step in the fabrication route is the anisotropic etching of the Si substrate in order to make the cantilevers free-standing. In general, the most straightforward lithography-based strategy to fabricate free-standing cantilevers is to benefit from the anisotropic etching of Si by potassium hydroxide (KOH), tetra-methyl ammonium hydroxide (TMAH) or ethylene di-amine pyro-catechol (EDP). For these three particular etchants, it is known that their etch rate of Si is highly sensitive to the crystal orientation. In a KOH solution with a concentration of 44 % and temperature of 358 K for instance, the {111} crystal planes of Si are attacked about 300 times slower than the {100} planes. In other words, the {111} planes act as an etch stop. They do not terminate the attack entirely, but reduce the etch rate strongly enough to result in characteristic etch patterns. For example, as a result of such a chemical attack on the top surface of a {100} Si wafer, V-shaped pits with flanks corresponding to the {111} planes rather than randomly oriented holes. For an overview of possible etch patterns arising from this anisotropic etching, the reader is referred to Elwenspoek and Jansen (Elwenspoek & Jansen, 1998). Some models attempting to explain the reactions taking place during this anisotropic etching along with the kinetics and other influencing parameters such as dopants in the Si have been developed as well (Seidel et al., 1990). In order to fabricate cantilever structures, the wafer needs to be partially masked by a material resistant to the etchant. The mask's openings allow the etchant to remove material from beneath the mask. This "undercut" results in free-standing structures. In a {100} oriented wafer, the wafer flat conventionally marks the <110> direction and in turn the position of the

{111} planes which can stop the advance of material removal. The idea behind cantilever fabrication is to design etch pits with rectangular insets, whose borders are given by {111} planes (or the <110> directions in the plane of the wafer surface). In such an arrangement another phenomenon occurs, which is highlighted in Fig.2.14: Structures with concave corners ("inner" corners) are almost not attacked, as the {111} planes block the advance of etchant almost entirely, while for convex corners ("outer" corners), the etchant finds higher indexed planes which can be dissolved at normal rates. Fig.2.14 displays the results of this phenomenon on the example of a mask patterned into the form of the letter A. The middle part of the A consists of 4 convex corners and will thus dissolve entirely if the exposure to the etchant is long enough. The four external borders of the A are all concave and therefore are not being attacked. When looking at the lower part of the A in Fig.2.14a it can be seen how this phenomenon can be used in cantilever fabrication: The natural design of a rectangular cantilever having 2 convex and 2 concave corners assures that it will be under etched with a wedge- like progression of material removal and that the removal will almost stop, once it reaches the support of the desired bending structure. So to speak, if the etching is continued long enough the lower part of the A in the example would therefore become a large cantilever. This is the basic idea behind the fabrication procedure used in this project.

In this project KOH is used as an etchant with a concentration of 30 % at 343 K. It should be pointed out that this step also limits the possible cantilever orientations. More precisely, only {100} wafers can be used, which means that the surface normal of the growing film has to belong to the <100> family as well. Otherwise the under etching mechanism as explained would not work. In the lateral dimension, however, the cantilevers are still free to be rotated, but for example a single glide constellation is still impossible to realize with this given constraint. The two orientations chosen (HS, DG) therefore already represent the cases in which cantilever bending will have the smallest amount of activated glide systems possible.

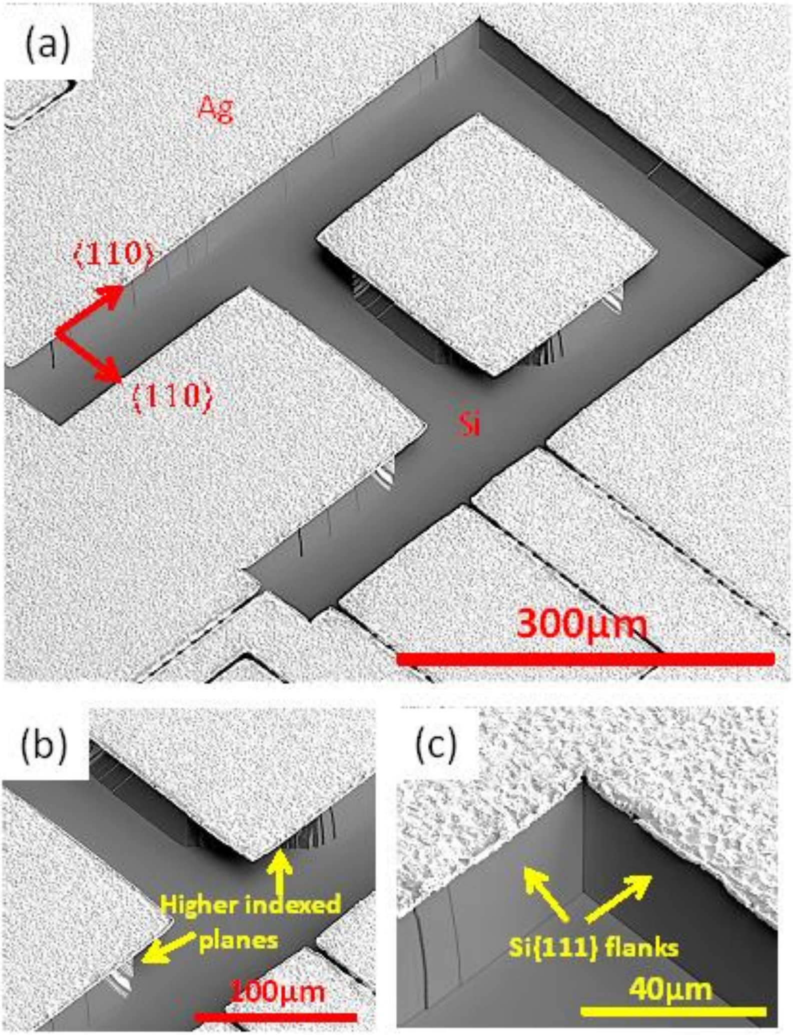
(a)
Ag
⟨110⟩
⟨110⟩
Si
300µm
(b)
Higher indexed planes
100µm
(c)
Si{111} flanks
40µm

Figure 2.14: SEM images of the undercut mechanism of Si by an anisotropic etchant. The pictures are taken under 40° tilt. (a) Overview of the structure, (b) zoom on convex corners where under-etching takes place, (c) zoom on concave corners where under-etching is mostly inhibited.

Ag does not react with KOH and is conventionally used as an etch mask against KOH, so no additional protection for the thin film is needed and the stripped wafer can be exposed to the etchant directly. Depending on beam thickness and feature sizes the time of exposure ranges from 10 min up to 45 min for the larger beams of the 3 µm thick films. Because of this rather short time no backside protection of the wafer is needed.

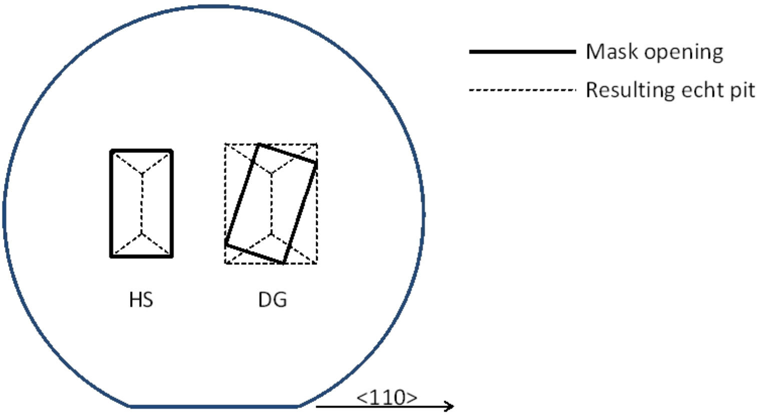

Figure 2.15: Schematic of resulting etch pits in HS and DG due to KOH etching in top view as a function of mask design.

The main issue with this last step in the process chain is an unwanted undercut, because the etching is only slowed down by Si {111} planes but does not entirely terminate at the designed support. For cantilevers in HS, the effect is reduced to its minimum and only a few 100 nm are expected for cantilevers of about 10 µm in length (based on theoretical calculations). However, in other orientations the effect becomes more critical the more the cantilever axis is tilted away from the flat. In theory, the size of the etch pit will correspond to the smallest rectangle that can be drawn containing all edges of the mask (Fig.2.15). This explains why the large overall etch pit used for HS is modified for DG. By splitting it into several smaller pits each containing only two cantilevers, the effect is reduced but still, for structures of size comparable to the ones just mentioned, an undercut of several µm is expected. In order to further minimize the undercut, the KOH etching is done in several time intervals with visual inspection via optical microscopy. An experimental determination of the undercut length is given in chapter 3.

3 Characterization of the as-fabricated cantilevers

3.1 Characterization of initial shape

For data evaluation of the mechanical tests, a precise determination of the geometrical parameters of the as-fabricated structures is necessary. The relevant ones are listed in Fig.3.1.

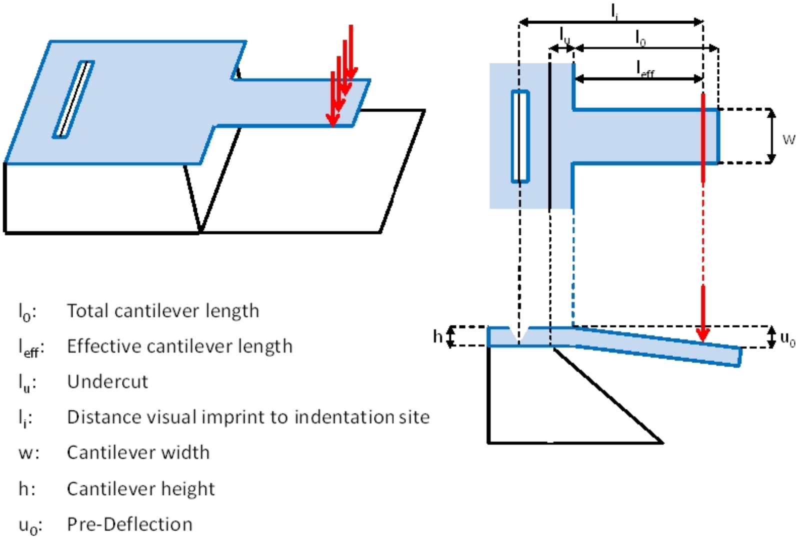

l_i
l_u
l_0
l_eff
w
h
u_0
l_0: Total cantilever length
l_eff: Effective cantilever length
l_u: Undercut
l_i: Distance visual imprint to indentation site
w: Cantilever width
h: Cantilever height
u_0: Pre-Deflection

Figure 3.1: Sketch of the bending setup with all relevant geometric parameters. The Ag layer is shown in blue while the Si substrate is grey and the external load is red. On the right hand side, a top view and cross section is shown. The visual imprint left to the testing structure serves for drift correction and plays an important role in determination of geometric parameters.

The main tool for measuring the geometrical parameters is a 3D laser scanning microscope. Additionally to its basic function as an optical microscope, it can be operated in a confocal mode. This mode represents a measurement technique where the focus point of the microscope is gradually changed with a predefined step size and the images recorded are stitched together to create a quasi 3D reconstruction of the cantilevers. Here the term quasi means that this kind of tomography does not capture all geometrical features. For example, no information is obtained from the bottom surface of the cantilevers. Moreover, a measurement of the cantilever thickness with this method is impossible. The only height that could be captured this way would be the distance between cantilever top surface and the ground of the etch pit. The lateral resolution is limited by the numerical aperture of the machine and does not differ significantly from conventional optical microscopes. However, the out-of-plane resolution can be increased down to 10 nm. In the following the different parameters shown in Fig.3.1 are explained in detail.

The effective length l_{eff} is the length at which the indenter tip strikes the cantilever with respect to the edge of the Ag film. During the mechanical loading of the cantilevers by the nanoindenter system, the tip does not precisely strike the very end of the structure, so the total length l_0 cannot be used for calculating the moment applied upon bending. Moreover, as will be shown in the following chapter, the tip does not penetrate the film's surface when deflecting the cantilevers, which means no visual imprint is seen, that could serve for a straightforward determination of l_{eff}. For an estimation of l_{eff} of the cantilever, the imprint used for drift adjustment can be taken. Here, the indenter tip is pushed into the thin film and held until the drift is reduced below a preset value. Afterwards the tip is lifted again and moved horizontally for a preset distance l_i and then the test is initiated. Since the horizontal displacement of the tip is known, this visible indent can be used to recalculate l_{eff}. Another aspect that needs to be mentioned is that l_{eff} is not necessarily constant during the test. In fact, as will be shown in chapter 4, the indenter tip slides over the cantilever surface especially during unloading. Therefore l_{eff} describes only the value at the initial stage of deformation and is less accurate for higher deflection angles.

The width *w* is not constant along the cantilever axis due to the aforementioned softening problem of the PMMA resist during IBE. Additionally, there is some randomness in this lateral spreading among the individual structures, so there is no easy way to find some kind of approximation to describe *w* as a function of coordinates along the cantilever axis $\boldsymbol{x_1}$. It is, however, not necessary to do this, due to the loading geometry. During cantilever bending, plastic deformation is strongly localized at the supported end and the zone of plastic deformation can be assumed to have a size close to the cantilever height (Motz et al., 2005). Therefore *w* is taken within the region closest to the support and is supposed to be constant. As will be shown in chapter 4, this assumption of localization of deformation is justified.

As mentioned, the cantilever height *h* cannot be determined using the 3D laser scanning microscope. However, the film thickness which corresponds to this value is supposed to be known to sufficient precision from the deposition rate during PVD. Two wafers ended up having slightly less than the desired thickness after PVD. The cantilevers from these particular sample sets where measured by SEM under a given sample tilt to verify the real value of *h* revealing a deviation of about 190 nm and *h* was corrected accordingly.

Because the progress of the anisotropic Si etching is observed manually from time to time as stated in chapter 2, there can be differences for the length of the undercut l_u for different wafers. In some extreme cases the undercut is even found to be shorter than required to make the entire cantilever freestanding. Likewise, the undercut may also end up several µm deeper than indented, in which case the cantilevers stiffness drops considerably. On the other hand, for some cantilevers oriented in DG the undercut could even be reduced below its expected value mentioned previously and be only a few 100 nm, if the precise point for stopping the etching is found. Some examples for good undercuts are displayed in Fig.3.2. Overall, in terms of the undercut there is a spread of some µm throughout the samples. The undercut l_u is determined by benefiting from the fact, that the flanks of the etch-pit are formed by {111} planes. As the surface normal of the sample is <100>, the flank angle α is necessarily 54.7°. Due to the extraordinarily high perfection of single crystalline wafers, this value can be assumed to be precise. In order to obtain l_u, the depth of the etch pit h_u, as well as the foot position of the flank needs to be found. The situation is displayed in Fig.3.3.

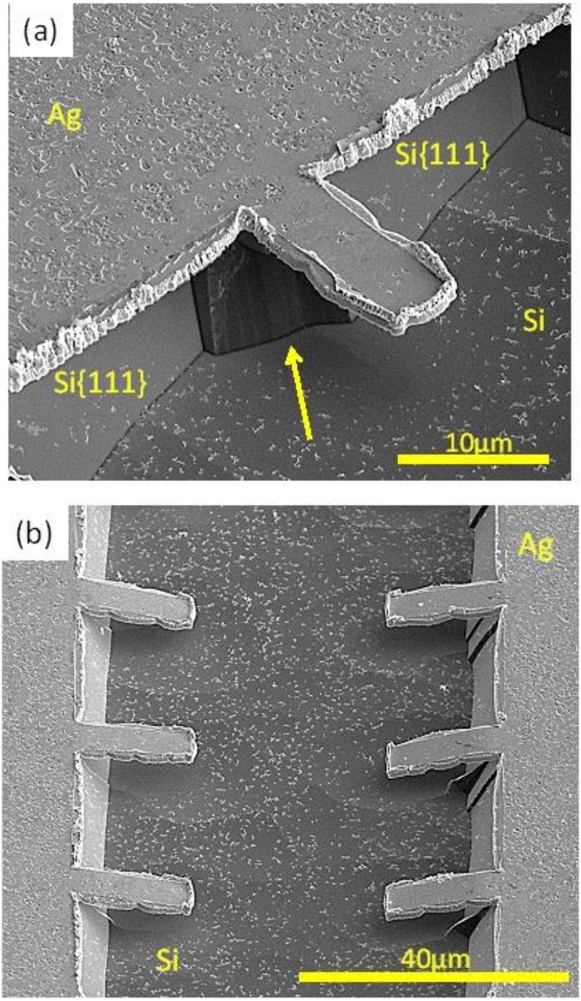

Figure 3.2: Some SEM images displaying the minimal undercut feasible for (a) DG and (b) HS. In (a), the arrow marks the edge where material removal advances.

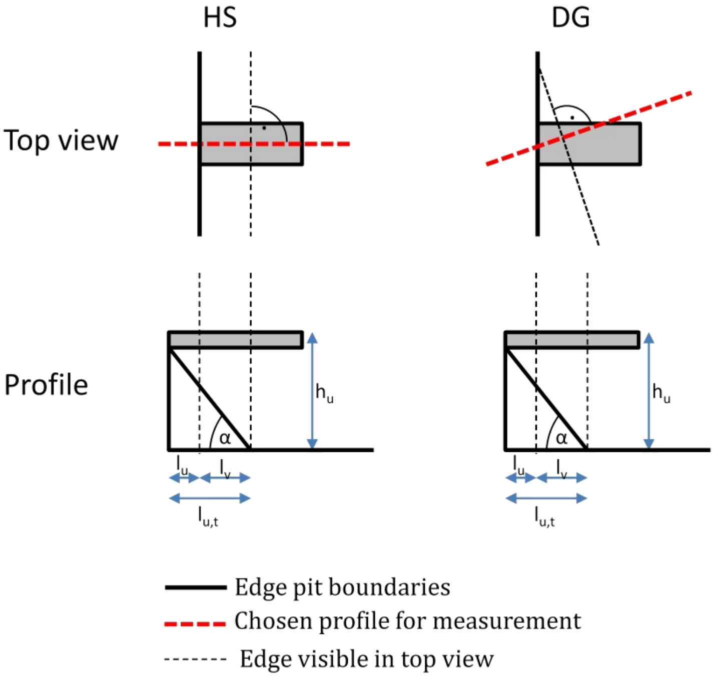
HS
DG
Top view
Profile
h_u
h_u
α
α
l_u
l_v
l_u,t
l_u
l_v
l_u,t
Edge pit boundaries
Chosen profile for measurement
Edge visible in top view

Figure 3.3: Sketch of the determination of l_u in HS and DG orientation. The upper figures show a top view onto the cantilever and the edge pit. The dotted black line represents the visible foot of the {111} flank. The lower parts shows a cross section for the HS case explaining the calculation of the undercut.

Since the foot of the flank is readily seen by microscopy the visual undercut l_v can be measured directly. Using basic trigonometry, the total length $l_{u,t}$ spanned by the flank can then be calculated from

$$\tan(\alpha) = \frac{h_u}{l_{u,t}} \tag{3.1}$$

and if the visible undercut l_v is subtracted from that value, l_u is found (Fig.3.2):

$$l_u = l_{u,t} - l_v \tag{3.2}$$

The profile measurement is done along a line which is chosen to be perpendicular to the flanks of the etch pit. In the case of the DG orientation, the undercut is not constant but slightly varies over the cantilever width. As an approximation, l_u is here calculated for the center position and assumed to be constant, as shown in Fig.3.3. Given the lateral inclination of the flank, this should also be equal to the mean value of the undercut.

Finally, the pre-deflection u_0 of the cantilever before testing needs to be taken into account when determining the remaining plastic strain after the experiment. The value is found as the absolute height difference between one measurement point at the support and the one at the very end of the cantilever. The absolute values of u_0 are generally only a few 100 nm and corresponding to deflection angles below 5°.

Because the smallest cantilevers have lateral sizes of a few µm, one might argue that optical microscopy is not the best choice and an SEM analysis would be better suited. However, the Keyence has several advantages compared to SEM. The first one is that due to the confocal mode, the Keyence allows an accurate depth measurement of the etch pit with high resolution which is needed for the determination of the undercut l_u. Another aspect is that in contrast to the cantilever sizes, the distance of the visual imprint l_i used for the measurement of l_{eff} to the supported end of the cantilever is fairly high (typically l_i = 40 µm). About 500 cantilevers have been tested, so a considerable amount of time can be saved, if only one single measurement is taken of each cantilever before and after the mechanical test. In order to determine l_{eff}, the picture taken afterwards needs to include the visual imprint done prior to indentation for drift correction, as mentioned above. For that reason the magnification of the picture is low enough so an SEM measurement has no significant advantages over optical microscopy in terms of resolution. Nevertheless, some structures have been measured with SEM to quantify the difference between the methods. Even if SEM measurements grant a higher accuracy in determining the dimensions needed, it was found that the values acquired with SEM do not differ significantly from the ones obtained by optical microscopy and the improved accuracy has no significant impact on determining the mechanical properties.

Now the variation of the geometrical parameters from cantilever to cantilever is addressed. The situation is illustrated in Fig.3.4 where cumulative distribution of the measured parameters is shown for the example of four different sample sets, namely the aspect ratios B and C for the Ag film thicknesses of 1 µm and 3 µm. First, the values for l_0 and w, i.e. the initial geometry of the as-fabricated structures, are considered. The standard deviation for these values is found to be of the order of 1-1.5 µm for length and even less than 1 µm for the width (Tab.3.1). This deviation relates to the resolution provided by the laser microscope. Therefore, it can be concluded that the fabrication process reliably produces cantilevers of comparable size. An important issue, however, is seen when the total cantilever length l_0 is compared to the effective cantilever length l_{eff}. l_{eff} does have a slightly higher spread and more importantly, the deviation from l_0 is on the order of 5 µm in total which becomes a significant issue for the smaller cantilevers. The problem arises as mentioned previously from the fact that the free end of the structures can hardly be pinpointed by the indenter tip. This becomes more impactful if the structure is smaller. As a result, the aspect ratios, which were designed based on the initial values of h, l_0 and w deviate from the desired values. In Tab.3.1 it is seen that the ratio l_{eff}/l_0 is strongly different for cantilevers of 1 µm and 3 µm in height. Due to these deviations, an interpretation of mechanical behavior (chapter 4) or microstructure (chapter 5) as a function of the designed aspect ratios is not possible. Instead, for the derivation of scaling laws etc. the real aspect ratios using l_{eff} have to be taken rather than l_0. The most striking feature seen in Fig.3.4, however, is the spread in the undercut l_u. The respective data points of l_u are divided in different colors depending whether they belong to cantilevers in HS or DG orientation. Overall, it can be seen that l_u is usually 1µm or less for HS samples while it reaches several µm for DG orientation. Additionally, the spread of l_u can vary considerably from sample to sample, which is due to the manual control of the relatively short KOH etching. From all geometric data, l_u can therefore be considered the be the most limiting factor for a direct comparison of the individual structures. An attempt for its correction will be discussed in chapter 4.

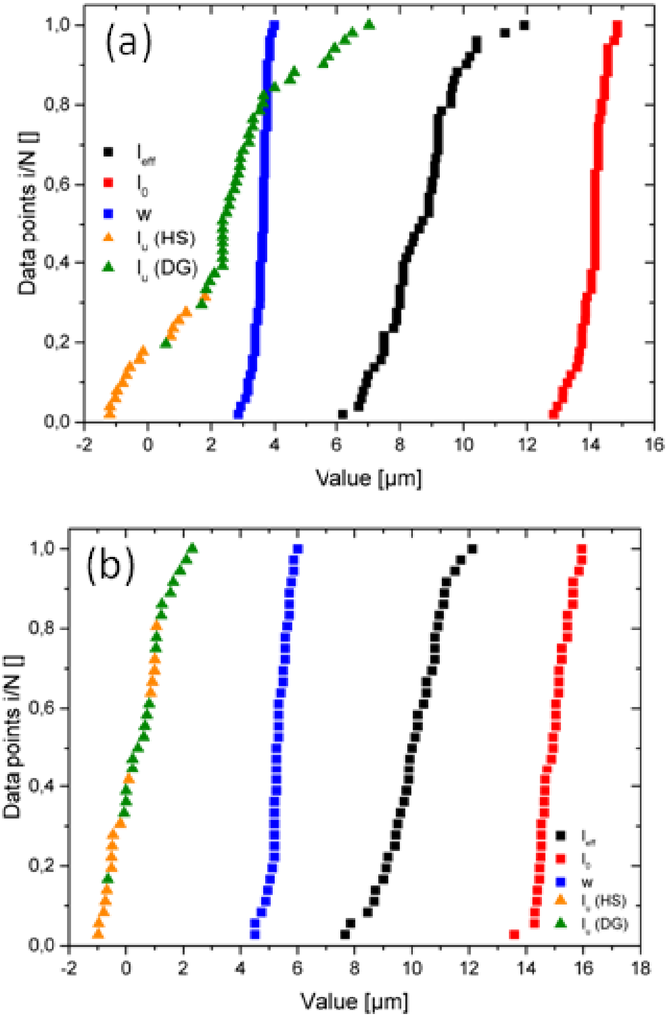

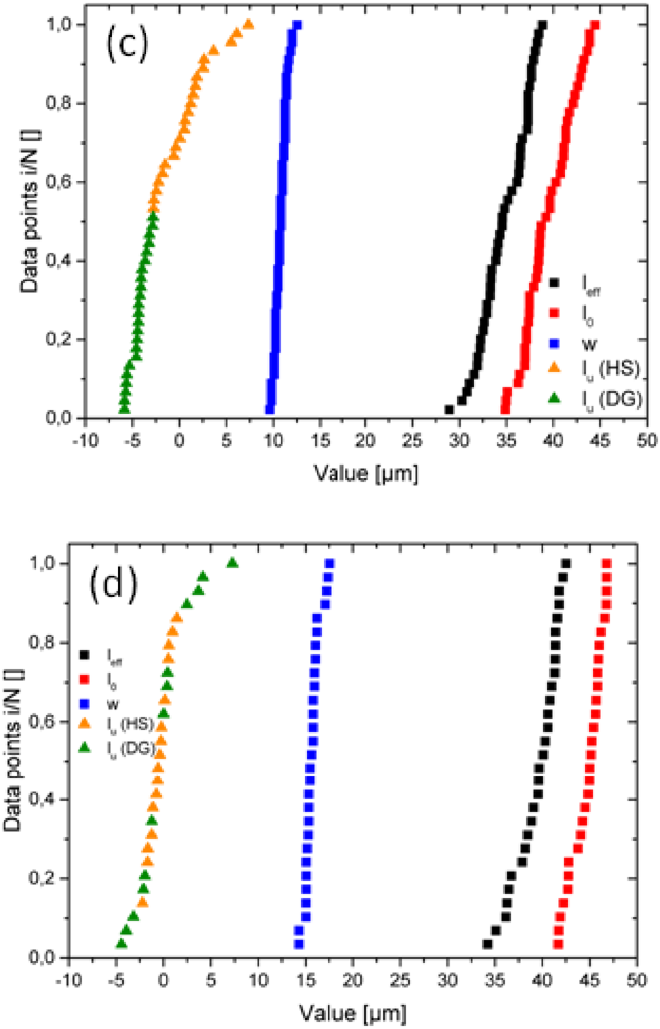

Figure 3.4: Cumulative distribution of the parameters l_{eff}, l_0, w and l_u the sample sets (a) B-1 µm, (b) C-1 µm, (c) B-3 µm, (d) D-3 µm. Each set both comprises HS and DG orientations and contains about 30 individual cantilevers. l_u is further distinguished by the respective orientations HS and DG.

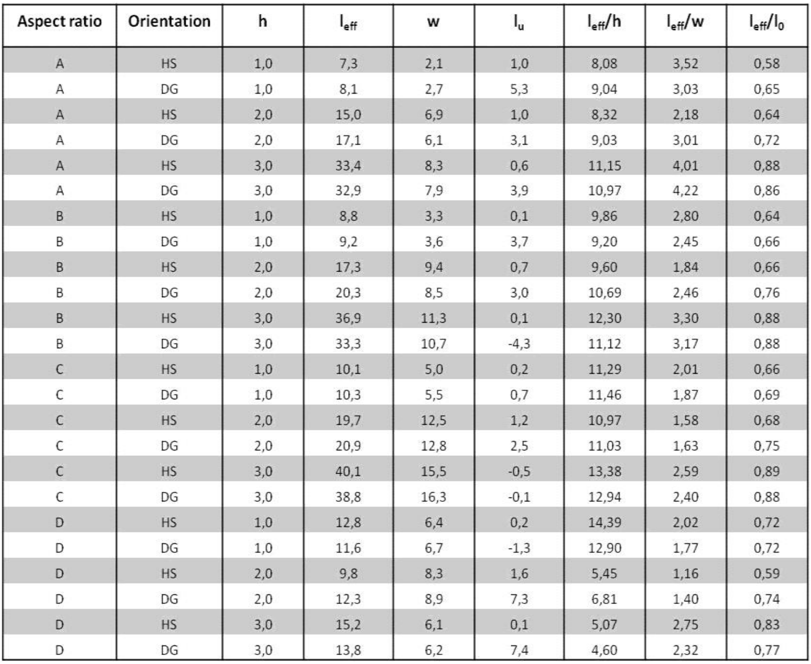

Aspect ratio	Orientation	h	l_{eff}	w	l_u	l_{eff}/h	l_{eff}/w	l_{eff}/l_0
A	HS	1,0	7,3	2,1	1,0	8,08	3,52	0,58
A	DG	1,0	8,1	2,7	5,3	9,04	3,03	0,65
A	HS	2,0	15,0	6,9	1,0	8,32	2,18	0,64
A	DG	2,0	17,1	6,1	3,1	9,03	3,01	0,72
A	HS	3,0	33,4	8,3	0,6	11,15	4,01	0,88
A	DG	3,0	32,9	7,9	3,9	10,97	4,22	0,86
B	HS	1,0	8,8	3,3	0,1	9,86	2,80	0,64
B	DG	1,0	9,2	3,6	3,7	9,20	2,45	0,66
B	HS	2,0	17,3	9,4	0,7	9,60	1,84	0,66
B	DG	2,0	20,3	8,5	3,0	10,69	2,46	0,76
B	HS	3,0	36,9	11,3	0,1	12,30	3,30	0,88
B	DG	3,0	33,3	10,7	-4,3	11,12	3,17	0,88
C	HS	1,0	10,1	5,0	0,2	11,29	2,01	0,66
C	DG	1,0	10,3	5,5	0,7	11,46	1,87	0,69
C	HS	2,0	19,7	12,5	1,2	10,97	1,58	0,68
C	DG	2,0	20,9	12,8	2,5	11,03	1,63	0,75
C	HS	3,0	40,1	15,5	-0,5	13,38	2,59	0,89
C	DG	3,0	38,8	16,3	-0,1	12,94	2,40	0,88
D	HS	1,0	12,8	6,4	0,2	14,39	2,02	0,72
D	DG	1,0	11,6	6,7	-1,3	12,90	1,77	0,72
D	HS	2,0	9,8	8,3	1,6	5,45	1,16	0,59
D	DG	2,0	12,3	8,9	7,3	6,81	1,40	0,74
D	HS	3,0	15,2	6,1	0,1	5,07	2,75	0,83
D	DG	3,0	13,8	6,2	7,4	4,60	2,32	0,77

Table 3.1: Mean values of the geometric parameters and aspect ratios for all 24 categories of cantilevers in the as-fabricated state. Dimensions in [µm].

3.2 FIB treatment of the as-fabricated cantilevers

Most research groups rely on FIB milling as fabrication route (Motz et al., 2005; Demir et al., 2010; Demir, Roters, et al., 2010; Armstrong et al., 2011; Kupka & Lilleodden, 2011; Kirchlechner et al., 2012) assuming its influence to be insignificant, if ion beam currents below 500 pA are used and/or that the penetration depth of the ions beam with respect to sample size makes the contamination negligible. However, both assumptions may be critical. Bei et al. (Bei et al., 2007) did show that the changes in mechanical response of FIB treated structures can be significant even if the final milling step is performed at only 300 pA. As for the penetration depth, an altered layer of a few ten nm beneath the top surface of the sample might have a tremendous influence for the case of bending geometries. Motz et al. (Motz et al., 2008) showed for example by simulations that in the case of bending, Frank-Read source activation is only possible within the most outer fibers. The outer fibers of the tensile half (i.e. the top surface of the cantilever) are inevitably irradiated during FIB milling, as soon as a snapshot with FIB is taken. This is necessary to position the milling pattern correctly. Consequently, FIB milling plays a decisive role on mechanical properties of cantilevers. The fabrication route presented in this project guarantees the total absence of such an influence. Therefore, it seems worthy to voluntarily contaminate some cantilevers with FIB in order to quantify the effect of ion implantation. The samples used for this study are of DG orientation, aspect ratio B, and from all three thicknesses. Four different ways of contamination have been tested and in each case the ion current was varied to be 50 pA, 100 pA, 300 pA, 500 pA and 1000 pA. The treatments are denoted as "flattening", "nose cutting", "blind cutting" and "snapshot only" and are detailed in the following section.

During the flattening procedure the contamination is introduced by cutting the rounded edges of the cantilevers (Fig.3.5b). In contrast, the nose cutting consist only of a short pattern to cut the free end of the cantilever (so to say the "nose") (Fig.3.5c). Only a single snap shot is taken by FIB in the snapshot only treatment without any patterning at all. The size of the scanned region is illustrated in Fig.3.5d. Finally, blind cutting describes a milling step in which the nose of the cantilever is cut, but without taking a snapshot of the cantilever before. To realize this, the cantilever is focused in SEM such that eucentric conditions are assured. Then the ion source beam shift is moved to the most extreme value possible, so the FIB alignment to the SEM beam is way off. From this position, the FIB image is gradually moved in live mode until the nose appears in the image. Then, the scan is stopped and everything within the picture belonging to the cantilever (i.e. the nose) is entirely cut by a basic rectangular pattern.

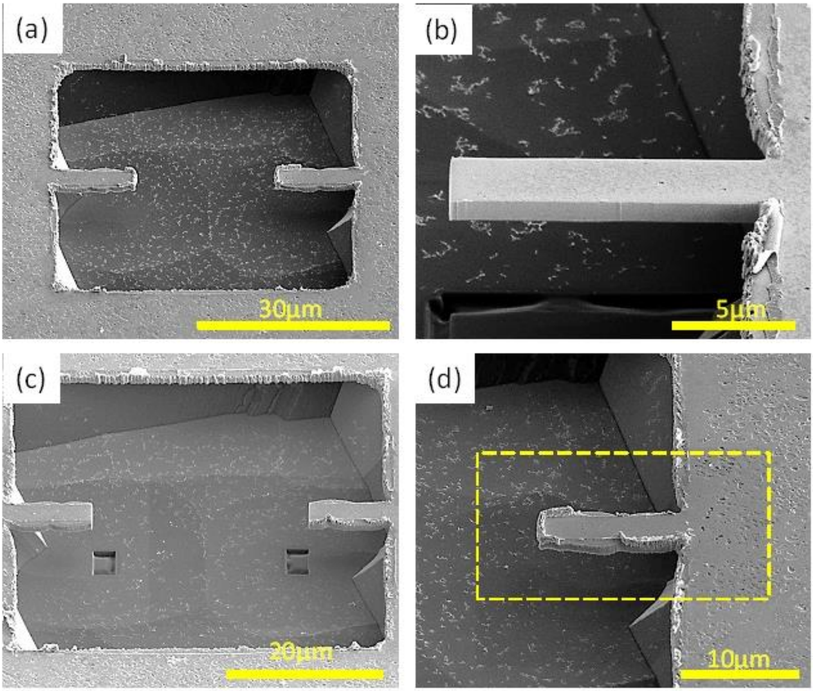

Figure 3.5: SEM images of FIB contamination experiments. (a) As-fabricated, non-irradiated state. (b) Flattening procedure. (c) Nose cutting procedure. The imprint of the pattern that is cut can be seen on the bottom of the etch pit. (d) Only snapshot procedure. The dashed line shows the size of the irradiated area.

The reasoning behind the choice of these methods for contamination is the following: Taking a snapshot during the equally named procedure is vital as it quantifies the minimum of contamination that occurs during any FIB fabrication route, since an entire cantilever cannot be cut blindly. Flattening the cantilever flanks is chosen, because to some extend it mimics the last milling step material removal done during conventional FIB micro machining. It should be mentioned that this (supposedly last milling) step is usually even followed by a final cleaning cross section step which is not performed in this project. Intuitively, the flattening procedure should give a good comparison of how standard FIB processing may affect mechanical properties and microstructure of the sample. However, the rounded shape of the as-fabricated samples might have an influence as well, since flattening results in sharp edges. If this flattened geometry has a notch-like effect then a new factor arises that might play a role in material response. To analyze this aspect, the nose cutting procedure is applied which leaves the zone of deformation with its rounded shape unaffected, so any notch-like effect – if existent – remains unchanged. Now that the geometry is dealt with, another uncertainty has to be tackled, which deals with the physical origin of the contamination. Both in flattening and in nose cutting a snapshot is taken before patterning. It cannot be stated for sure, whether the physical origin for the change in material properties is related to direct ion implantation during the snapshot or rather due to ion diffusion, or both. Therefore the blind cutting procedure is utilized where diffusion is the only possible process, since the zone of plastic deformation is not directly irradiated.

To quantify the amount of minimum contamination during the snapshot only treatment, the ion fluence φ is calculated. As the terms describing the number of ions impinging on the sample surface are used inconsistently in literature, some clarifications are needed. In this project, the term "fluence" is applied as introduced in Giannuzzi and Stevie (Giannuzzi & Stevie, 2005) which denotes the total number of ions striking the selected area during the scan and has therefore a unit of m^{-2}. In contrast to that the term ion "flux" refers to the flow of ions (in $m^{-2}s^{-1}$). In literature, the term ion "dose" is often being used, as well, which is also different from ion fluence as it stands for the total number of ions that are actually absorbed by the medium at the end of the scan, i.e. it requires an absorption coefficient for quantification. Since for this test, the medium is always a single crystalline Ag cantilever, ion fluence should be sufficient to evaluate the severity of the irradiation.

From the size of the image, the dwell time and the ion current, the ion fluence φ applied to the sample can be calculated for the snapshot only procedure. For the remaining three procedures, calculating φ has not been done as the calculation is more complex: The patterning time needs to be stopped accurately and the fluence during patterning has to be added. So φ is higher and not homogenously distributed over the entire cantilever. However, the calculation of φ for snapshot only is very straightforward: The horizontal field width (HFW) value of the scan (i.e. length of the square area scanned) is 25.6 µm, the image contains 1024x884 pixels and the dwell time describing how long the ion beam illuminates each pixel is 3 µs. The ion current is varied within the intervals already mentioned. The irradiated area A is easily found as the square of the HFW value to be 655 µm² and the total time of the scan t is 2.7 s. The electrical charge Q is calculated supposing a constant ion current I_{Ga+}

$$Q_{Ga^+} = \int I_{Ga^+} dt = I_{Ga^+} \cdot t \tag{3.3}$$

and in order to find the total amount of Ga$^+$ ions n_{Ga+} striking this area during this time, Q is divided by the elemental charge e

$$n_{Ga^+} = \frac{I_{Ga^+} \cdot t}{e} \tag{3.4}$$

Dividing n_{Ga+} by A then gives the fluence φ

$$\varphi = \frac{n_{Ga^+}}{A} \tag{3.5}$$

Again, the fluence values during the snapshot are only used to quantify the minimum contamination of the samples that occurs during the snapshot. It can be assumed that for the remaining three contamination procedures, φ will be significantly higher.

4 Mechanical Testing

This chapter deals with the setup for the bending experiments of the cantilevers, the data evaluation and the results obtained. The structures are tested for different conditions and geometries: cantilever height (1 µm, 2 µm or 3 µm), aspect ratio (A, B, C and D), orientation (HS or DG) and after FIB irradiation. The load is applied by a nanoindenter system. In the first section of this chapter, the testing setup for deflecting the cantilevers is described and the framework used to evaluate the mechanical response of the samples is explained. Possible error sources related to the setup and an estimation of their effect upon this behavior are given, as well. The main part of this chapter focuses on a detailed presentation of the observed behavior of the cantilevers upon plastic deformation with special emphasis being put on the quantification of the mechanical size effect as a function of the mentioned conditions.

4.1 Experimental setup

The bending experiments are carried out using an Agilent Technologies G200 nanoindenter system. Bending takes place as a result of the indenter tip pushing the free-standing end of the cantilevers downwards. The loading is stopped when a preset deflection is reached. This total deflection is the only parameter varied between the tests, so different remaining plastic strains can be studied.

For nanoindentation, a Berkovitch-type indenter tip (tetrahedron shape) is by far the most common tip geometry. In this work, however, a wedge-type tip is used because this particular geometry causes the load to be applied as a line parallel to the support (axis x_3). This is an essential advantage as it prevents inclined bending. As mentioned the tip is positioned using optical microscopy and it is hard to pinpoint exact coordinates, especially for the smaller cantilevers. While the length of the wedge (either 6 µm or 40 µm) is longer than the cantilever width (with the exception of some cantilevers with

3 µm in height), a uniform distribution of the load is assured. The supplier (Synton-MDP AG) quantifies the uncertainty in flatness of the wedge the be on the order of 1°. By means of optical profilometry it was confirmed that no form of inclined bending has taken place.

The test is load controlled with the indentation force being applied at a constant load rate of 20 $\mu N \cdot s^{-1}$. This loading segment needs to be initiated as soon as the tip contacts the cantilever. A stiffness criterion is used to pinpoint this event, i.e. the tip is continuously lowered and the test starts when the tip encounters a sufficiently high resistance to its vertical movement. In this project the chosen stiffness value is 25 $N \cdot m^{-1}$ which corresponds to the minimum value recommended for the machine. Depending on the sample size this value might even have to be adjusted for certain structures. This particularly refers to sample sets with an unusual undercut length l_u. In some extreme cases, when the cantilever is only 1 µm thick and the undercut is too deep, the stiffness threshold is lowered to about 17-20 $N \cdot m^{-1}$ while for some of the 3 µm thick cantilever it can be beneficial to raise it up to 30-40 $N \cdot m^{-1}$ to assure that the test and the data recording is only initiated by the testing structure itself.

The positioning of the indenter tip over the free end of the cantilever is also a crucial issue and is done by optical microscopy. The coordinates of a spot close to the free end are chosen by the user. This involves a certain scatter of l_{eff} and a deviation from l_0, which becomes more significant for smaller cantilevers (see chapter 3).

Before initiating the testing procedure as described above, the tip is moved horizontally about 40-80 µm away from the cantilever (distance l_i in Fig.3.1). Here the software executes an imprint into the sample surface for drift adjustment. That means that the tip is pushed into the surface and kept at this position while the drift rate is continuously measured until the amount of drift drops to a value of at least 0.5 $nm \cdot s^{-1}$.

The software captures the change in vertical position of the tip (by capacitors), i.e. the displacement u, the load F applied and the time t passed at any measurement point with respect to the start of the test. In order to use the data collected this way, some corrections have to be made.

First, possible errors which stem from machine compliance and from drift events need to be corrected. Fig.4.1a shows an exemplary curve of the raw load applied and the resulting raw displacement measured. The inset in Fig.4.1a highlights the effect of drift during indentation. One would expect the starting and end point of the mechanical tests to coincide in terms of force and displacement value. However, due to the unwanted but inevitable drift, the absolute value of displacement at the end of the test differs by a value of Δu from the one at which the test was initiated. Correcting this drift is the first modification that has to be made. As mentioned, the drift is assured to be less than 0.5 $\mathrm{nm \cdot s^{-1}}$ before the test is started and the entire test itself with loading and unloading usually last between 15 and 80 s. Given the fact that even the smallest cantilevers tested throughout the project are deflected for at least 2-3 µm (usually deeper), it can be seen that the absolute amount of drift caused during the test is very low compared to the total deflection imposed. Nevertheless, the drift needs to be corrected. However, at least fluctuations within the drift rate can be assumed to be of minor importance and in turn the assumption can be made of the drift being a constant value named within the drift rate can be assumed to be of minor importance and in turn the assumption can be made of the drift being of a constant value named $\dot{h}$. To approximate $\dot{h}$, the gap in displacement Δu between starting and end point is divided by the total testing time Δt:

$$\dot{h} = \frac{\Delta u}{\Delta t} \tag{4.1}$$

The corrected displacement $u_{i,corr}$ can then be easily found for each captured data point i by multiplying this constant drift value $\dot{h}$ with the time t_i passed. The amount of drift in nm obtained is then subtracted from the measured value.

$$u_{i,corr} = u_i - \dot{h}t_i \tag{4.2}$$

Fig.4.1b displays how the drift correction causes the starting and end point of the segment to coincide. What remains to be corrected, is the machine compliance, i.e. the resistance to the tip movement when there is no contact with the sample itself. As the compliance is a constant value, it causes a constant offset in the slope of the raw force-raw displacement curve. A linear fit is executed for the unloading part of the curve (Fig.4.1c) and the line obtained is subtracted from all measurement values (Fig.4.1d). One might argue that it should be sufficient to execute such compliance correction only one single time, as the machine compliance is supposed to be constant. Since the linear fitting and subtraction operation, however, imposes no significant effort, the correction was carried out for each single cantilever individually. Throughout the samples, the machine compliance is always of the order of 47-49 N·m^{-1}. The value does vary slightly depending on the exact vertical position of the indenter and, thus, from sample to sample but is found to be practically constant for structures on the same sample tested on the same day.

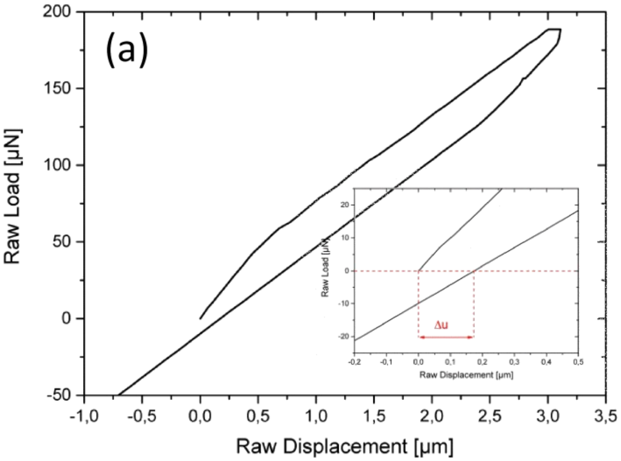

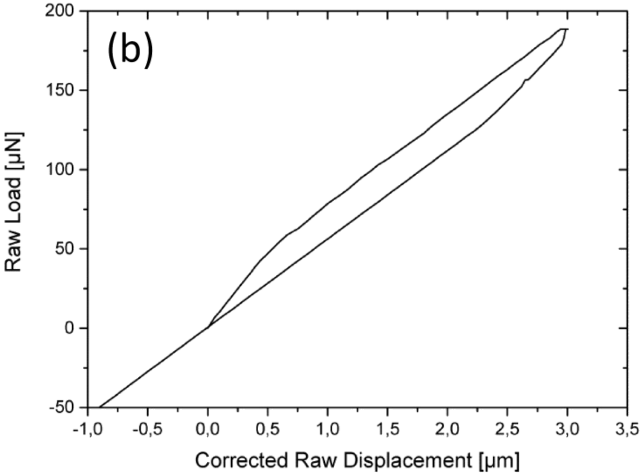
(b)
Raw Load [µN]
200
150
100
50
0
-50
-1,0
-0,5
0,0
0,5
1,0
1,5
2,0
2,5
3,0
3,5
Corrected Raw Displacement [µm]

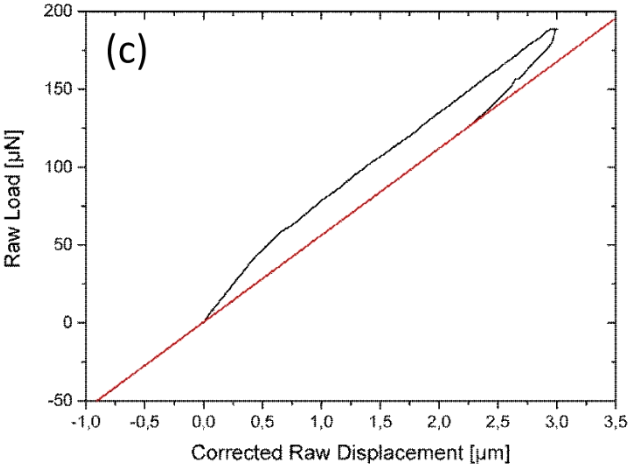
(c)
Raw Load [µN]
200
150
100
50
0
-50
-1,0
-0,5
0,0
0,5
1,0
1,5
2,0
2,5
3,0
3,5
Corrected Raw Displacement [µm]

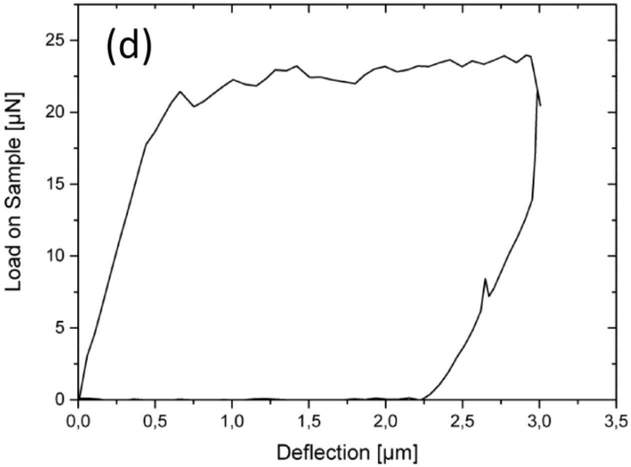

Figure 4.1: (a) Exemplary raw load vs. displacement curve without correction. The inset highlights drift effects. The same curve is shown after drift correction in (b). In (c) the machine compliance is fitted with the red line. After subtraction of this line, the final load versus deflection curve (d) is obtained.

After executing these corrections, viable force-displacement curves are obtained. They will be named force-deflection curves throughout the project. In the following, the assumption made to transform force and deflection into stress and strain values considering the given loading geometry are detailed. For bending the stress σ at a given height position $\boldsymbol{x_2}$ is calculated using the flexure formula

$$\sigma = \frac{M}{I} x_2 \tag{4.3}$$

Where M is the bending moment and I is the axial moment of inertia for a rectangular cross section. In this project, the outmost fiber, at which the stress is at maximum, is chosen as a reference. For the outermost fiber the formula can be written in terms of the geometric parameters introduced as

$$\sigma\left(x_2 = \frac{h}{2}\right) = 6\frac{Fl_{eff}}{wh^2} \tag{4.4}$$

The flexure formula assumes a linear gradient within the cross-section and is only valid within the elastic regime. The transformation according to (4.4) can therefore only be considered as an approximation which is valid for small deformations. Moreover, it is assumed that we are dealing with pure bending and shear forces are neglected, and the stress calculated by (4.4) is the only non-zero component σ_{11} of the stress tensor. Accordingly, only the strain along the $\boldsymbol{x_1}$ axis ε_{11} imposed by bending is calculated. For the plane bending of the single crystalline cantilevers that are submitted to small deformations only, it can be assumed that the curvature is localized within in a small region close to the support, while the remaining part of the cantilever remains flat. This can for example be seen on the set of deflection curves recorded with optical profilometry in Fig.4.2. Following this assumption, it appears valid to approximate the cantilever shape upon bending with a right angled triangle. The strain along $\boldsymbol{x_1}$ can therefore be approximated from the effective length l_{eff} and the deflection u of the cantilever to be

$$\varepsilon = \frac{\sqrt{u^2 + {l_{eff}}^2} - l_{eff}}{l_{eff}} \tag{4.5}$$

The value of the remaining plastic strain after bending is often used throughout this project. Besides transforming the force-deflection data points recorded during the bending experiment, the maximum remaining strain is also measured by optical profilometry by comparing the cantilevers before and after bending. The two remaining strain values obtained with the different methods are in good agreement. Only for larger deflections deviations are found.

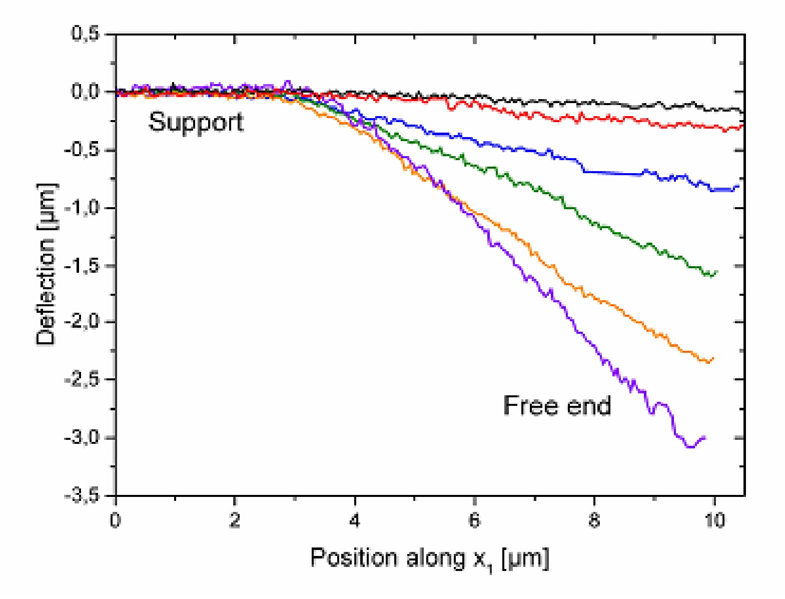

Figure 4.2: Deflection curves for some cantilevers that have been submitted to different amounts of strain recorded with laser profilometry.

The best way to compare the mechanical behavior of individual cantilevers is to transform the force-deflection curves into normalized bending moment curves. For the normalized bending moment $\bar{M}$, the forces are normalized to the product of cantilever width and the square of its height

$$\bar{M} = \frac{F l_{eff}}{w h^2} \tag{4.6}$$

while the normalized deflections $\bar{u}$ are obtained trough division by the height

$$\bar{u} = \frac{u}{h} \tag{4.7}$$

This kind of representation is also used in literature (Evans & Stölken, 1998; Motz et al., 2008) and has a considerable advantage over conventional stress-strain curves, since there are no further geometrical or other assumptions required for the transformation. Moreover, stress-strain curves tend to show a very strong scatter when large strain values on the order of 0.1 are reached. Plotting bending moment versus normalized displacement curve is thus more reliable (Fig.4.3).

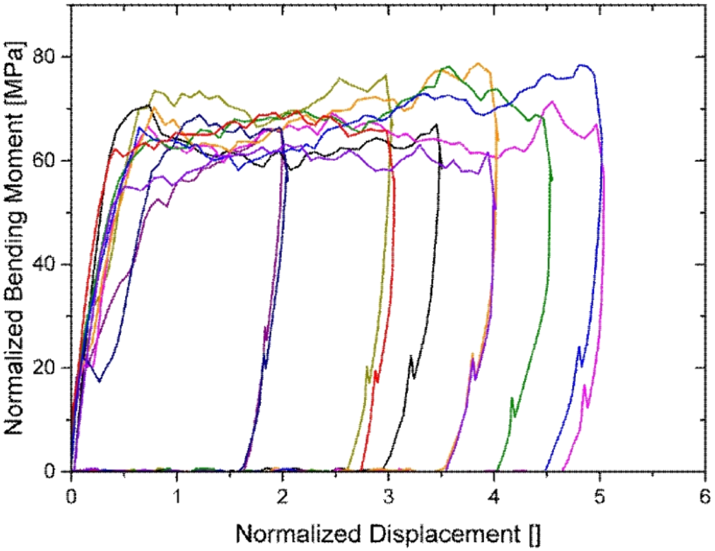

Figure 4.3: Some exemplary bending moment curves for cantilever structures comparable in size (HS orientation, 1 µm thickness, aspect ratio A.

Stress-strain curves are needed to describe the specimen's hardening behavior, as the latter requires the derivative of the stress-strain curve. In this project hardening is analyzed by fitting the elastic-plastic transition region toward the pronounced plateau within the stress-strain curves with two different hardening laws. The first one is a Voce-type model which suggests the stress to be exponentially decaying with increasing strain. This model goes back to Voce (Voce, 1948) and can mathematically expressed by

$$\sigma(\varepsilon) = y_0 + R_{Sat}(1 - e^{-\tau\varepsilon}) \tag{4.8}$$

where y_0 is the function's constant offset, R_{Sat} is the saturation stress that Voce postulated and the exponential decay is expressed by the parameter τ. It is obvious that this kind of function is able the describe a plateau stress very well. The second model used follows the suggestion of Ludwik, i.e. a power law with the exponent being one of the fitting parameters:

$$\sigma(\varepsilon) = y_0 + C\varepsilon^n \tag{4.9}$$

where C and y_0 are constants.

4.2 Calculation of flow stress

The most important parameter in terms of mechanical response to plastic deformation that has to be determined is the flow stress. Moreover, the flow stress is especially relevant when the size effect is to be quantified. An assumption is needed in what way plastification will occur: According to the flexure formula (4.3) the stress within the cantilever cross section is not distributed homogenously and in turn the flow stress will not be reached simultaneously for all fibers within a given cross section. Instead the outermost fibers will be deformed plastically first and then this zone of plastification will gradually expand towards the neutral fiber as the strain increases. One way to define flow stress could therefore be to select a certain strain value, like $\varepsilon = 0.2$ %, and define the onset of plastic flow as the point at which the corresponding stress value $R_{p0.2}$ - as it is conventionally used in mechanics - is reached within a particular fiber. For the bending geometry used in this project one criterion for the onset of plastic flow can therefore be expressed as the stress value at which the outermost fiber reaches a strain of 0.2 %. The procedure of finding this point starting from force-deflection curves is given in the following.

The basic idea is to find the force value $F_{p0.2}$ which corresponds to this particular strain and then to use the flexure formula (4.3) to transform it into a stress value. The first step is therefore to determine $F_{p0.2}$. Much like $R_{p0.2}$ it can be found from the intersection of a line parallel to the elastic slope with the measurement curve. The only difference is that the force-deflection curve is used and thus, the elastic slope corresponds to the sample stiffness S. The function $f(u)$ intersecting the force-deflection curve can be written as

$$f(u) = S \cdot u + F_0 \tag{4.10}$$

Finding the slope of this function is readily done by a linear fit of the elastic region. The fitting function's offset value F_0 for a deflection of $u = 0$ can be calculated from the corresponding stress value σ_0 using the definition of $R_{p0.2}$

$$\sigma_0(\varepsilon = 0.002) = 0 \Leftrightarrow \sigma_0 = E \cdot 0.002 \tag{4.11}$$

where E is the Young's modulus for HS or DG depending on the sample under consideration. The flexure formula (4.3) is used to transform this value σ_0 into the force value F_0 needed.

$$F_0 = 2\frac{\sigma_0 I}{l_{eff} h} \tag{4.12}$$

With these input values, (4.10) gives $F_{p0.2}$ as the intersection with of $f(u)$ the measurement points. After applying the flexure formula (4.3) again, the flow stress $R_{p0.2}$ is obtained as

$$R_{p0.2} = 6\frac{F_{p0.2}l_{eff}}{wh^2} \qquad (4.13)$$

An alternative way to find the flow stress, which is also applied in this project, goes back to Motz et al. (Motz et al., 2005): Because of the very pronounced elastic-plastic plateau, it might be justified to assume a constant stress distribution over the cantilever cross section (with exception of the neutral fiber) for any measurement point belonging to the plateau. If based on this approximation, the entire cross section is assumed to be plastic, then the absolute value of this stress can be obtained by integration. The bending moment M is correlated with the (constant) flow stress σ_f by

$$M = F_{max} \cdot l_{eff} = w \int_{-h/2}^{h/2} \sigma_f x_2 dx_2 \qquad (4.14)$$

Here the force value F_{max} is taken from the elastic-plastic plateau of the force-deflection curve. Since the plateau is not perfectly flat, the maximum value F_{max} has to be taken. The position of both $F_{p0.2}$ and F_{max} are illustrated in Fig.4.4. Integration over the cross section then leads to the flow stress value σ_f

$$\sigma_f = 4\frac{F_{max}l_{eff}}{wh^2} \qquad (4.15)$$

which may be defined as the stress needed to cause plastic flow within the entire cross section.

If equation (4.13) and (4.15) are compared, it is noticed that they only differ in a constant factor and their respective force value. Fig.4.4 also displays that the difference between F_{max} and $F_{p0.2}$ is small due to sharp transition into the pronounced plateau. From a mathematical point of view it can already be seen that the $R_{p.02}$ method will most likely result in higher flow stress values. This aspect will be discussed later in this chapter.

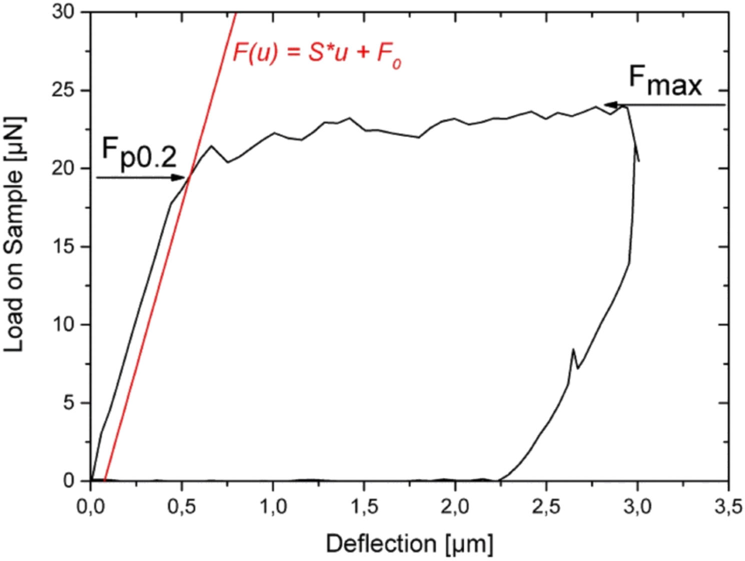

Figure 4.4: Force-deflection diagram showing force values $F_{p0.2}$ and F_{max} used for the determination of the flow stress.

4.3 Normalized bending moment curves

Fig.4.5 shows normalized bending moment curves for a sample set of cantilevers of comparable size and orientation. The most striking feature seen is the pronounced load plateau in the elastic-plastic region. The plateau is particularly flat with only a small slope close to zero. This behavior is consistent for all samples with only a few exceptions where a slightly stronger slope is found within the plateau. However, no clear trend can be seen for these exceptions. The abrupt transition along with the flatness of the plateau implies and that little to no hardening is taking place upon plastic deformation. This behavior may be expected because the sample is single crystalline. In the absence of grain boundaries, dislocation interaction and multiplication is the most likely hardening mechanism and is thus related to an increase in dislocation density as expressed in the Taylor relationship.

Another remarkable aspect in the measured mechanical response is the presence of two individual segments upon unloading, with two different slopes. This behavior results from the bending geometry of the cantilever itself and has already been reported by Weihs et al. (Weihs et al., 1988). Once the cantilever is unloaded, the indenter tip will inevitably slip over the cantilevers surface in the direction of the support until it reaches a stable position. The regular unloading segment, i.e. a strictly vertical lifting of the tip, is not taking place before this stabilization happened. As a consequence the bending moment caused by the load gradually changes upon unloading. This also explains why the elastic slope of the loading segment is again different from any of the slopes seen during unloading. Obviously, the difference in the slopes will be more pronounced the more the cantilever is deflected. This is also seen in Fig.4.5.

The fact that the indenter tip is sliding across the cantilever surface calls for further investigation. For example, the question should be answered, if it might also be possible that a similar movement towards the free end occurs during the loading segment. This would make the absolute force and in turn stress values less reliable, especially for higher deflections. Sliding might also explain some of the fluctuations in the load plateau seen in Fig,4.5. When looking at the top surface of the deflected structures in SEM, no visual imprint is found on the cantilevers, regardless of the total displacement or the sample size. Rather than penetrating the material the tip simply pushes the structures downwards. From a mechanical point of view this is beneficial as it favors the assumption of the load being applied as pure bending but it also makes the mentioned friction or sliding events more likely and impactful.

In order to verify if such sliding events really take place, the following experiment was conducted: Before bending, the FIB was used to sputter a thin layer of Pt with a thickness of a few 100 nm onto the top surface of some selected samples. This experiment is only meant to visualize sliding; retrieving mechanical parameters is considered to be irrelevant for the given task and would have been difficult to realize since the sample has now a bilayer system and the Ag layer is inevitably contaminated by Ga^+ ions during the process. After bending of these modified cantilevers, visible wear tracks appear that are directed towards the free end (Fig.4.6). It is also seen, that the wear tracks are more significant at the edges of the cantilever which can be explained by the cantilever shape: The redeposited Ag after IBE is not entirely removed by the wet-etching and some remnants may still be found at the edges of the structure. Besides the fact, that sliding events are therefore proven to take place, we can further state that the force is not applied in an entirely homogenous way but that the area of contact with the indenter tip is more concentrated at both edges of the cantilever. However, the assumption of non-inclined bending and an overall homogenous load distribution should still be justified.

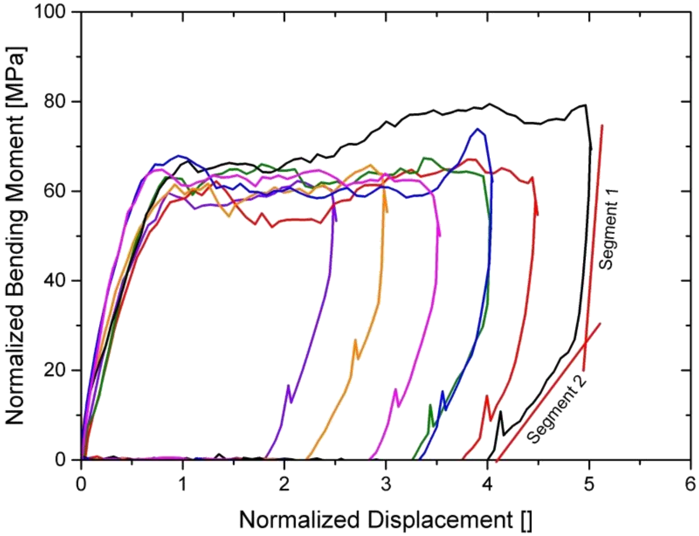

Figure 4.5: Bending moment curves for some cantilevers of 1µm thickness, DG orientation and aspect ratio A. The difference of the slope within the second unloading segment becomes more pronounced with increasing maximum strain imposed.

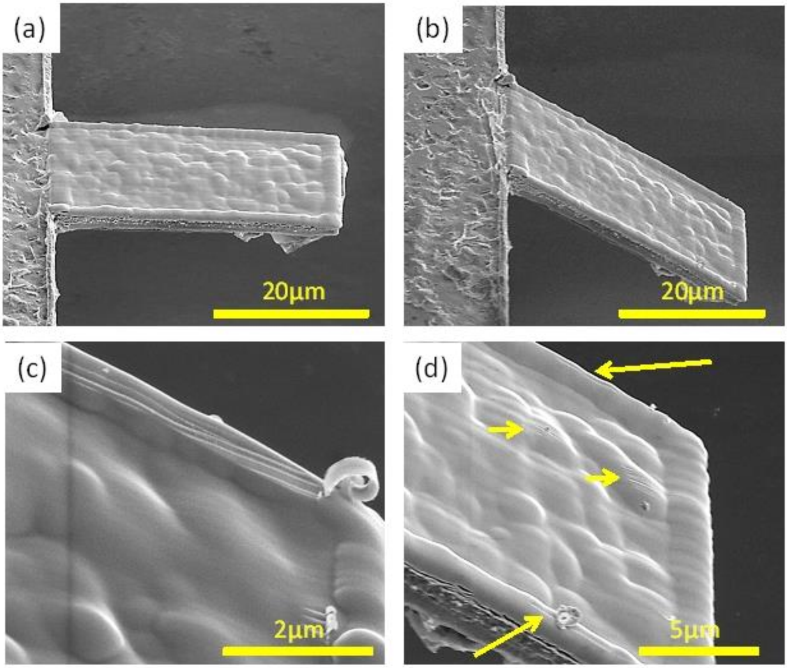

Figure 4.6: A cantilever with 100 nm of Pt deposited by FIB on the sample surface (a) before and (b), (c), (d) after deformation. (c) and (d) show a zoom onto the free end of the structure and highlight the wear tracks which can be visualized this way. They tend to be more significant at the edges of the cantilever.

The experiment proves that tip sliding does happen and consequently the effective cantilever length l_{eff} and in turn the bending moment M may increase during the test. However, a correction of the bending moment values cannot be done in this project, because such a correction still lacks further information: The amount of slipping would have to be expressed as a function of cantilever deflection. While an estimation of the total length of the wear track and thus a value for the maximum change in effective length l_{eff} could be obtained, no justified statement can be made about the interval within the force-deflection curve in which this event occurs. The tip might either slide abruptly towards the free end or instead move rather continuously downwards with increasing deflection. Furthermore, it was mentioned previously that the initial value for l_{eff} is not constant for all samples due to the problems with tip positioning. This initial positioning with respect to the free end will have a non-negligible effect on tip sliding as well, because the cantilever stiffness is affected by l_{eff}. Finally, it needs to be considered that the sample material plays a role as well: The sliding can only be proven for the tip sliding on Pt and the deposited amorphous Pt layer has different properties in terms of friction than the Ag layer beneath it. Therefore, the effect can hardly be quantified adequately from the data at hand. Upon loading, friction events are taking place and no correction is done, so there is an additional uncertainty concerning measurement values especially at large deflections.

Another significant characteristic that is observed in the normalized bending moment curves is a strong deviation of the measured cantilever stiffness based on the analytical solution according to equation (2.1), which is derived from simple beam theory, from the experimentally measured stiffness, which is identified as the elastic slope of the force-deflection curves. The case of cantilever bending with fixation at one end is one of the simplest loading geometries in applied mechanics and the underlying framework is sufficiently known. However, for a non-negligible amount of sample structures, the deviation between analytically calculated and experimentally determined stiffness can even lie between 100 % and 200 %. This phenomenon was already observed by various research groups (Baker & Nix, 1994; Armstrong et al., 2011). The main reason for this behavior is the fact, that some assumptions made for the analytical model are not met in reality. The main issue in this regard is the mathematical description of the supported region. In the analytical model, it is assumed that the cantilever is perfectly fixed at the supported end. The tested cantilevers, however, are not fixed in that sense. Instead, at the supported region the free-standing Ag thin film is reinforced by a Si substrate. There, the cantilever abruptly turns into a bilayer system with a base material that has a significantly higher Young's Modulus and is about 275 times thicker than the Ag layer. Moreover, the adhesion between the layers also plays an important role in this context and is not respected by the analytical model. Finally, the undercut has to be taken into account. With the undercut in mind, the cantilever would have to be described as an element consisting of two parts: The regular element which is actually bending and the undercut support region which is also free-standing but is of infinite width. In the case of the DG orientation, the problem would become even more complex due to the 18.4° inclination, because the amount of undercut is not a constant value but a function of the $\boldsymbol{x_3}$ coordinate (width). Cantilevers with a negative undercut (i.e. too short), would pose another problem as Si support beneath the layer would now be of triangular shape (wedge-like progression of the KOH etchant). With all these inevitable features in mind, it becomes obvious that the resistance of the cantilevers to deformation will be significantly lower than that provided by an analytical approach involving a fixation. The deflection curves recorded by profilometry and the images taken by SEM prove that neither the supported parts of the cantilevers nor the undercut parts which are of "infinite width" are significantly deformed during the tests as long as the undercut remains within reasonable values. However, non-zero stresses will always be imposed onto the region beyond the bending element which cannot be neglected. Describing this system with the framework from simple beam theory is therefore not valid and inevitably leads to an overestimation of the stiffness.

To deal with the stiffness problem Baker and Nix (Baker & Nix, 1994) suggested introducing a "compliance length" l_c in order to mathematically account for the loss in stiffness. By mathematically stretching the cantilever this way the stiffness will drop significantly and thus approach the measured value. In order to find l_c, they approximated the compliance by the following function:

$$S = \frac{3EI}{(1 - v^2)} \left(l_{eff} + l_c\right)^{-3} \tag{4.16}$$

If the stiffness is inverted, the compliance C of the cantilevers can be expressed as

$$C = \frac{(1 - v^2)}{3EI}\left(l_{eff} + l_c\right)^3 \tag{4.17}$$

If higher order terms are ignored, and l_c is assumed to be small against the effective length l_{eff} the compliance can be simplified by a function of the general form

$$C(l) = Al^3 + Bl^2 \tag{4.18}$$

where A and B are constants. If the compliance is mapped versus the cantilever length and such a function is used to fit the data, the mechanical data can be corrected. The same procedure is essentially applicable for the project at hand, when some slight modifications are made: While in Baker and Nix (Baker & Nix, 1994), equation (4.18) was derived based on a set of cantilevers of the same polycrystalline material (E constant) and varying only in the height dimension h (I constant), the situation looks different for the samples used in this project. Because of the different aspect ratios (A, B, C, D) used here, the moment of inertia I is not constant for all cantilevers and neither is the Young's Modulus E due to the two different orientations HS and DG of the single crystalline specimen. Therefore rather than plotting the compliance, the product of compliance and flexural modulus EI needs to be plotted versus the length (Fig.4.7). Moreover, since in the project at hand, l_u has been measured for each sample, it seems reasonable to add its value to the initial cantilever length, which essentially follows the compliance length idea. If l_u is negative, then strictly speaking the length would have to be accordingly reduced, but since the analytical stiffness values are always found to be overestimations even for the case where is undercut is shorter than in the design, it was decided not to modify the length value in this particular case. So if the undercut is positive (too deep) l_u is added to the cantilever length, if the undercut is negative (too short), no modifications are made. Moreover, as a result of the term CEI being plotted versus the length, the fitting parameter A in equation (4.18) consists entirely of constants (Poisson ratio), so its value was preset to be 0.2852 for Ag. Fig.4.7 shows this attempt based on the initial work of Baker and Nix (Baker & Nix, 1994) for the project at hand.

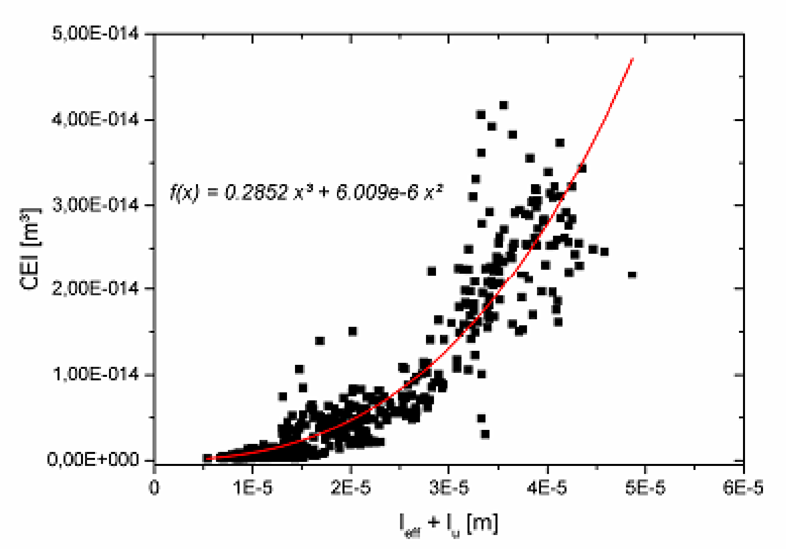

Figure 4.7: Correction of mechanical data by introducing a compliance length. The undercut length l_u is only added to the effective length l_{eff} if its value is positive.

From Fig.4.7 it can be seen that the data points recorded throughout this project can generally be described by the suggested function. However, it is also seen that the scatter is significant, so a stiffness correction based on a compliance length would only improve the situation for some data points while it would cause even stronger deviations for others. On the other hand, simply adding l_u to the initial length if $l_u > 0$ is already found to be a valuable universal correction which at least lowers the deviation from experimental and analytical values. Fig.4.8 displays the cumulative distribution of the experimentally measured stiffness and its deviation from the analytical results illustrating the severity of the error in stiffness. Fig.4.8a shows the absolute stiffness values found experimentally, calculated using the analytical approach and calculated from experimental data using the aforementioned correction. It should be pointed out, that in the analytical (non-corrected) model, if l_u is negative then l_{eff} is reduced accordingly. Fig.4.8b shows the relative error of the stiffness values. It can be seen that the correction at least guarantees that about 75 % of the data points have an error of less than 100 %. This is still significant but the only procedure that can consistently be applied to all data points alike.

Armstrong et al. (Armstrong et al., 2011) made observations concerning deviations of experimental data from simple beam theory as well. They fabricated cantilevers of triangular cross section with FIB, so there is no undercut. Nevertheless, it was stated that the support cannot be described as a fixation. They found that the difference between the experimental and analytical values becomes less significant, if the cantilever length is increased and conducted experiments on cantilevers of different length and consequently aspect ratios. They found the x^3 term in equation (4.18) to become dominant (and consequently simple beam theory to be a good fit) if the aspect ratio l_{eff}/w is at least 6. Such a ratio was not tested in the project at hand due to increased redeposition as mentioned in chapter 2.

4.4 Evaluation of the size effect

An interesting aspect to be studied is the material's response to plastic deformation as a function of sample size. It has been mentioned in chapter 1 that microplasticity is a wide and ongoing field of research, because there is still uncertainty about the exact scaling laws and the physical background of this size effect observed at the µm and sub-µm scale. The project at hand offers the possibility to investigate the size effect in a very fundamental way, since the samples can be considered to be idealized. The large amount of single crystalline cantilevers, which are free from any process-induced damage allow analyzing the size effect as a function of spatial confinement only and with reasonable statistics.

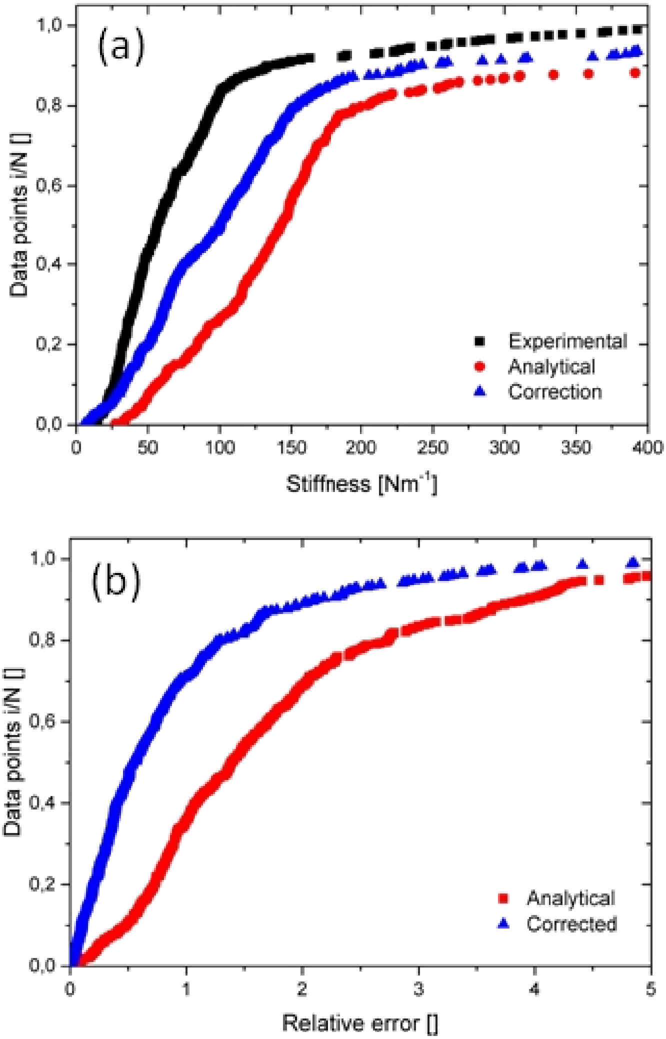

Figure 4.8: Cumulative distribution of the cantilever stiffness. (a) Shows the absolute values and (b) the relative difference with respect to the experimentally found values.

After mechanically testing all cantilevers and having processed the obtained data in the way described above, about 500 structures remain for evaluation. The first approach to interpret this large amount of data is by plotting the calculated flow stress versus sample size (Fig.4.9). Rather than expressing the spatial confinement by the entire effective cantilever volume V_{eff} itself, in literature the size effect is usually expressed by the reduction of the dimension that has the most limiting effect on deformation mechanisms. For thin film samples this limiting dimension is the film thickness i.e. in this project the cantilever height h. The fact, that the height has the most impact compared to the other dimensions can also directly be seen when looking at the mathematical calculations of the flow stress (4.13 and 4.15) where the height enters with the highest exponent. For the samples in this project, however, mapping flow stress versus height would be difficult to fit properly from a mathematical point of view, because there are only three different height values under consideration. To be exact there are also a few sample sets with thicknesses of 0.8 µm and 1.8 µm as mentioned previously. Nevertheless, representing the entire data set at hand in one single flow stress versus cantilever height plot would not produce the most reasonable fit. Instead, the data set should be categorized so at least several fits can be obtained and compared. In order to avoid having only three separate clusters of data points, Fig.4.9 shows the flow stress as a function of effective cantilever volume V_{eff} first. The effective volume is the product of height h, width w and effective length l_{eff} and is slightly different for each structure, as all three values are measured independently for each cantilever. As a criterion for the flow stress, here the $R_{p0.2}$ method is applied. It is seen, that the flow stress increases with decreasing sample volume. For the biggest structures the flow stress asymptotically approaches a threshold value of about 150 MPa. When decreasing V_{eff} below values of about 250 µm^3, the flow stress quickly rises up to 450 MPa.

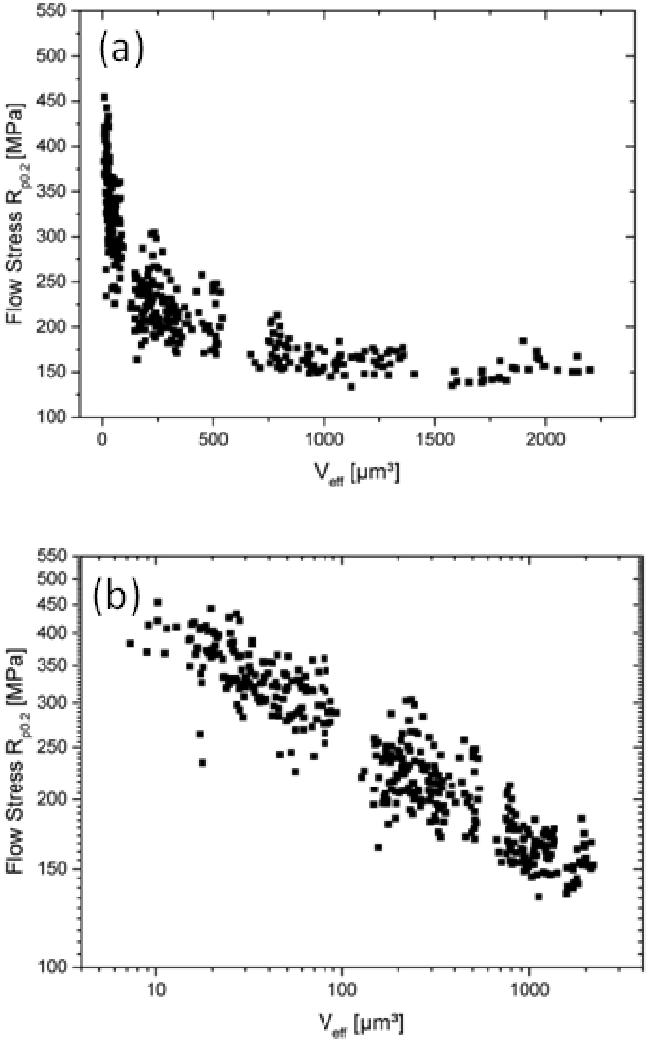

Figure 4.9: Flow Stress $R_{p0.2}$ versus effective cantilever volume V_{eff} in (a) linear and (b) double logarithmic representation.

To allow a comparison of the results to other research groups, the flow stress is fitted versus the cantilever height h as well. Because of the vast amount of data gathered, the fitting can be improved if the structures are categorized according to their aspect ratios and orientations. However, as shown in Tab.3.1, the effective aspect ratios somewhat differ from the 4 groups intended by the design (Tab.2.2), because of the scatter of l_{eff} with respect to l_0. A categorization based on the aspect ratios intended by design A, B, C and D is therefore not meaningful. Instead, the categorization needs to be done based on the effective aspect ratios. Some trial and error was necessary to find the best borders for a categorization of the entire set of cantilevers according to their true aspect ratio. The best fits were provided when all cantilevers are grouped into one of the two following classes: $l_{eff}/w > 2.8$ and $2 < l_{eff}/w < 2.8$ (Fig.4.10). The few cantilevers of $l_{eff}/w < 2$ are disregarded for the fit. Since the remaining aspect ratio l_{eff}/h is bigger than 10 for all samples, it is assumed to be of negligible influence for the categorization. Only the particular case of the sample sets of aspect ratio D at 3 µm is disregarded in the fit, because here l_{eff}/h is only about 5 and thus strongly deviated from the other sets. It can be seen that the scaling behavior for the two groups is practically the same. The constant offset can be explained by the total cantilever volume which is somewhat lower for the samples belonging to $l_{eff}/w > 2.8$. It can therefore be stated that the flow stress scales with an exponent of about $n = 0.69 \pm 0.03$ for the cantilevers in this project if an power law function of type

$$\sigma_f(h) = A \cdot h^{-n} \tag{4.19}$$

is chosen, where A and n are constants.

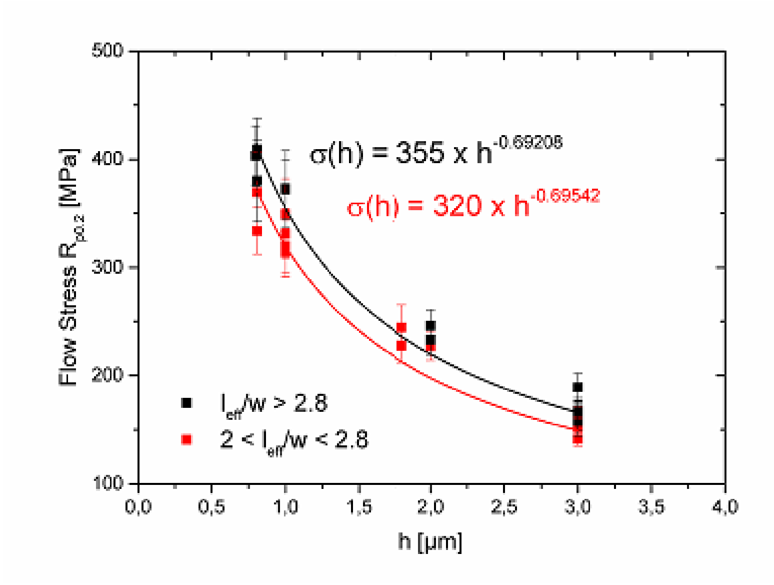

Figure 4.10: Flow Stress $R_{p0.2}$ versus cantilever height h.

4.5 Effect of the flow stress criterion used

The two criterions used for the calculation of the onset of plastic flow in this project - namely $R_{p0.2}$ being reached in the outermost fiber and an entirely plastic cantilever cross section - result in different absolute values of flow stress. However, if the methods are applied, the scaling law found through a power law fit according to (4.19) is essentially the same for both only with an different constant offset value. Fig.4.11 displays this very well: The data points seem to differ only in their absolute values, but not in their dependence on the effective volume V_{eff}, which means both approaches successfully display the size dependence.

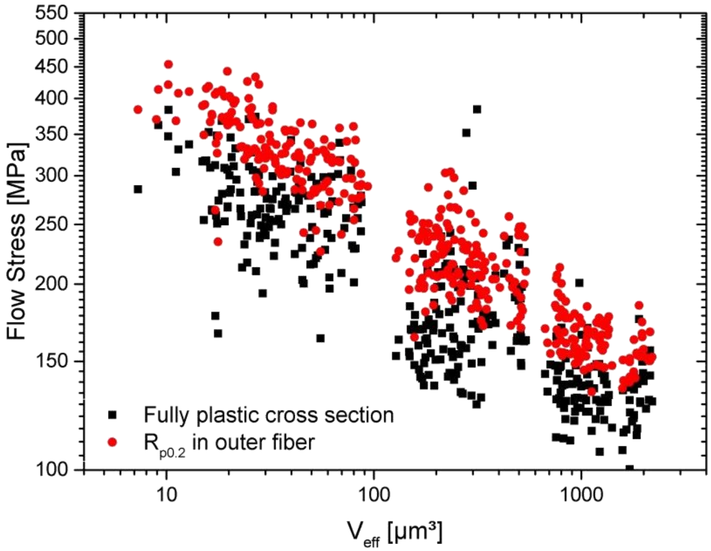

Figure 4.11: Flow stress versus V_{eff} as a function of the criteria used to define plastic flow.

From a mathematical point of view this offset is readily seen, because the final formulas (4.13 and 4.15) used to evaluate the flow stress look much alike; the difference is only a constant factor, which is 6 in the case of R_{p02} at the outermost fiber and 4 in the case of a fully plastic cross section. Besides this constant factor the formulas differ in the force input value $F_{p0.2}$ and F_{max}. F_{max} is in fact bigger but due to the very small slope of the plateau the force values are found to be very close to one another. The difference may therefore be explained because the flow stress calculated from the measurements is an integral value, which is related to either the outermost fiber only, or the entire cross section for $R_{p0.2}$ and σ_f, respectively.

The scatter of the data points in Fig.4.11 is about the same for both methods. It has to be mentioned, however, that for the calculation of the flow stress, using the criterion of a fully plastic cross section, a significant amount of data

- roughly about 50 cantilevers out of 500 - were excluded from the analysis as the plateau stress could not be estimated with satisfying precision, because the total strain imposed was either too low to reveal the plateau properly or the plateau itself not sufficiently flat. If these data points were included, a general advantage of the $R_{p0.2}$ criterion in terms of scatter would be evident.

4.6 Influence of cantilever orientation

The dependence of the crystal orientation on plastic flow is shown in Fig.4.12. Overall, the graph reveals that there is practically no difference between HS and DG in terms of absolute flow stress values or their evolution with sample size. Additionally, Fig.4.13 displays the flow stress of the cantilevers as a function of crystallographic orientation for the example of all cantilevers of aspect ratio B. As mentioned in chapter 2, the difference between the two orientations is a rotation around the cantilever's surface normal $\boldsymbol{x_2}$ by 18.4°. In DG, glide is carried by activation of two main slip systems, while the remaining ones are of minor importance. In HS only four systems should be activated and they can be reduced down to two effective slip systems due to their coplanar relationship. Therefore, in order to enable plastic flow, for both orientations, the activation of two systems is sufficient. This may explain why no significant difference in flow stress is seen between HS and DG.

4.7 Characterization of hardening behavior

Just like the flow stress, other mechanical properties of the cantilevers are found to be strongly dependent of the sample size as well. Especially the hardening behavior changes drastically when the sample size is reduced, as can be seen when examining the stress-strain curves shown in Fig.4.14. The transition region, which connects the elastic behavior with the load plateau reveals a significantly different shape when samples of different size are compared. The figure displays each of the four aspect ratios A, B, C and D. For each, one selected sample for each cantilever height is shown.

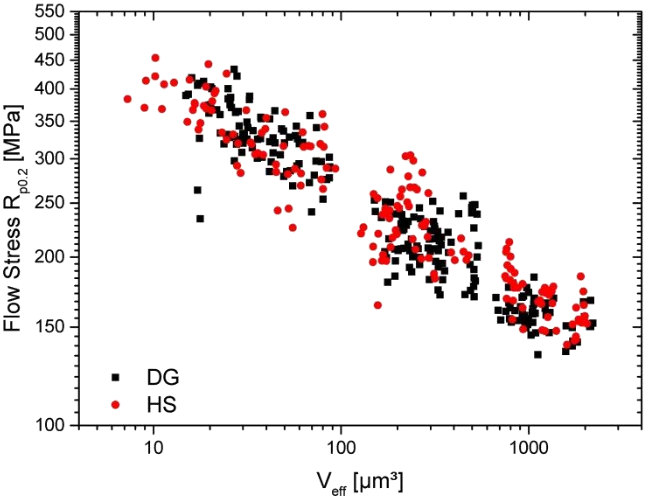

Figure 4.12: Flow stress versus V_{eff} as a function of cantilever orientation.

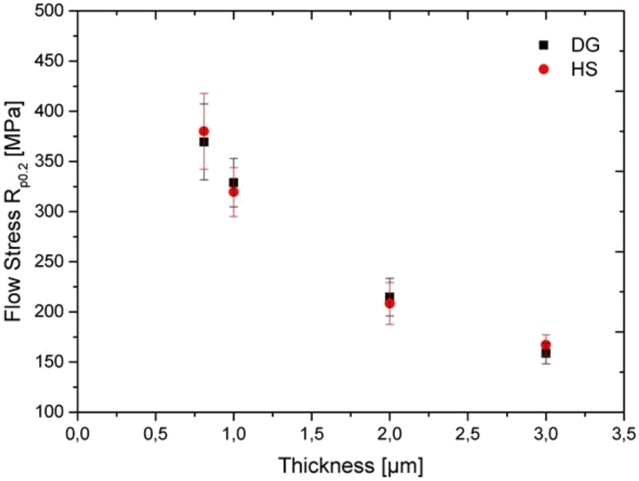

Figure 4.13: Flow stress versus cantilever height, for samples of aspect ratio B with DG and HS orientation

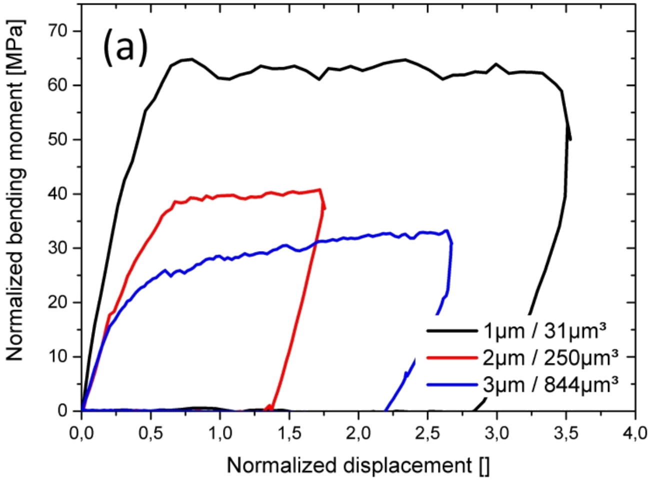
(a)
Normalized bending moment [MPa]
0
10
20
30
40
50
60
70
0,0
0,5
1,0
1,5
2,0
2,5
3,0
3,5
4,0
Normalized displacement []
1µm / 31µm³
2µm / 250µm³
3µm / 844µm³

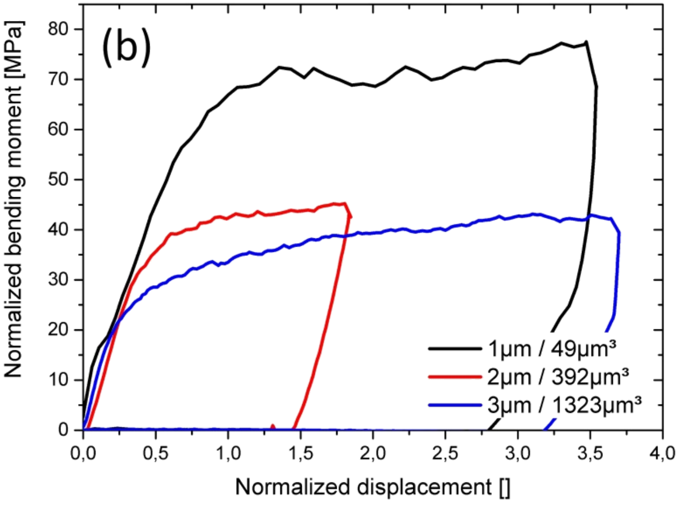
(b)
Normalized bending moment [MPa]
0
10
20
30
40
50
60
70
80
0,0
0,5
1,0
1,5
2,0
2,5
3,0
3,5
4,0
Normalized displacement []
1µm / 49µm³
2µm / 392µm³
3µm / 1323µm³

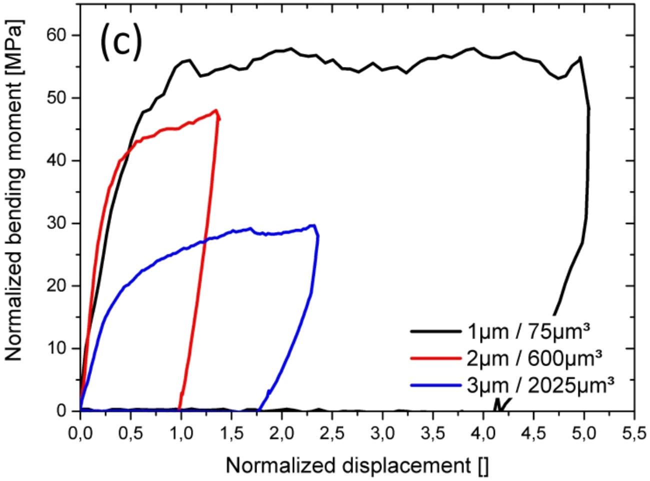

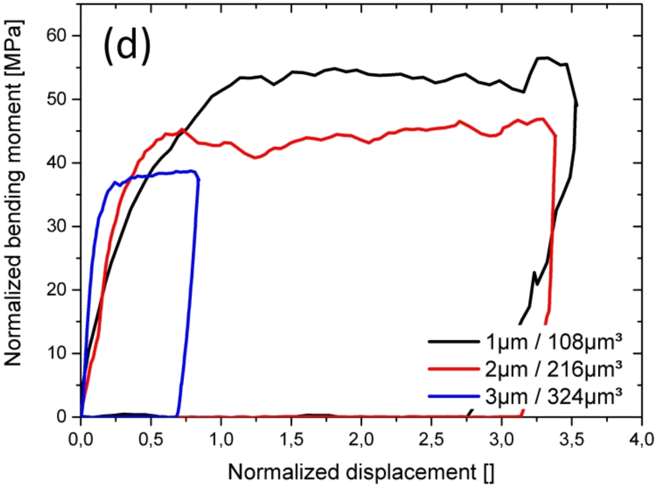

Figure 4.14: Normalized bending moment curves for all three cantilever heights. (a) Aspect ratio A, (b) B, (c) C and (D) D. The total volume (calculated from mask layout values) are indicated as well in the caption.

Upon downscaling from 3 µm to 1 µm in height, a clear transition in hardening is observed. Large samples show a rather smooth transition whereas for smaller samples less pronounced work hardening is detected. In Fig.4.15 an attempt to fit the elastic-plastic transition region for the two extremes is done revealing that the behavior of large cantilevers can be described using a Ludwik-type relationship, whereas small cantilevers are more adequately described by a Voce-type equation which accounts for a more pronounced elastic-plastic plateau.

This observation is found to be consistent for the majority of samples tested. In this regard, the 2 µm thick samples represent a transition region between the two extremes. If the entire set of data gathered throughout the project is considered, the 2 µm thick structures tend to be slightly better described by the Voce-type hardening. This transition in hardening behavior from Ludwik towards Voce type upon downscaling is observed for all samples belonging to the aspect ratios A, B and C (Fig.4.14). Moreover, it is found that the transition is best seen for the category C. Cantilevers from the category D, however, do not reveal this transition at all keeping a Voce type hardening behavior even for cantilever of 3 µm height. The change in the elastic slope, i.e. in cantilever stiffness, seen in Fig.4.14d stems from the fact that for aspect ratio D, only the height is modified upon downscaling while all other dimensions are kept constant. Apart from the aspect ratios, the four individual classes differ strongly in the total effective bending volume V_{eff}. This in indicated in the figure as well, which shows the theoretical values from the mask layout in the figure caption. This particularly highlights that with respect to all other aspect ratios, for D the volume of the cantilevers barely changes upon downscaling. The transition in hardening behavior therefore appears to be linked to a spatial confinement of the entire cantilever volume and not in height only.

This change can also be quantified by the difference between the plateau load F_{max} and $F_{p0.2}$ or consequently by calculating the difference between the two flow stress values σ_f and $R_{p0.2}$ that are based on them. Fig.4.16 displays this difference as a function of V_{eff} showing that the difference becomes smaller with increasing sample size. Keeping in mind that (4.13) and (4.15) differ by a constant factor of 1.5, the observed trend implies that the gap between F_{max} and $F_{p0.2}$ widens with increasing sample size and consequently, hardening becomes more pronounced.

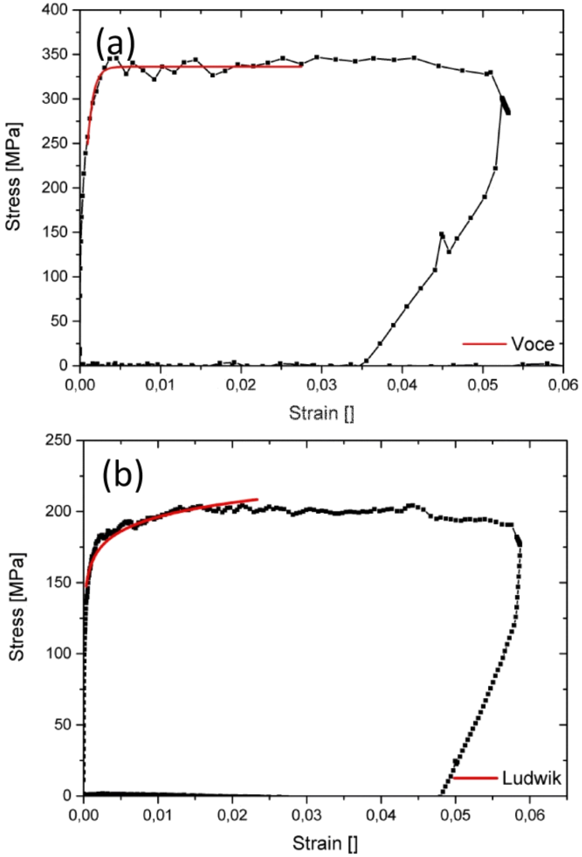

Figure 4.15: Stress-strain curves with an attempt to fit the transition toward the elastic-plastic plateau (i.e. the hardening). The cantilever differ in aspect ratio, thickness and orientation and are (a) B-1µm-HS, (b) B-3µm-HS. (a) is fitted using a Voce-type function and (b) with a Ludwik-type relationship.

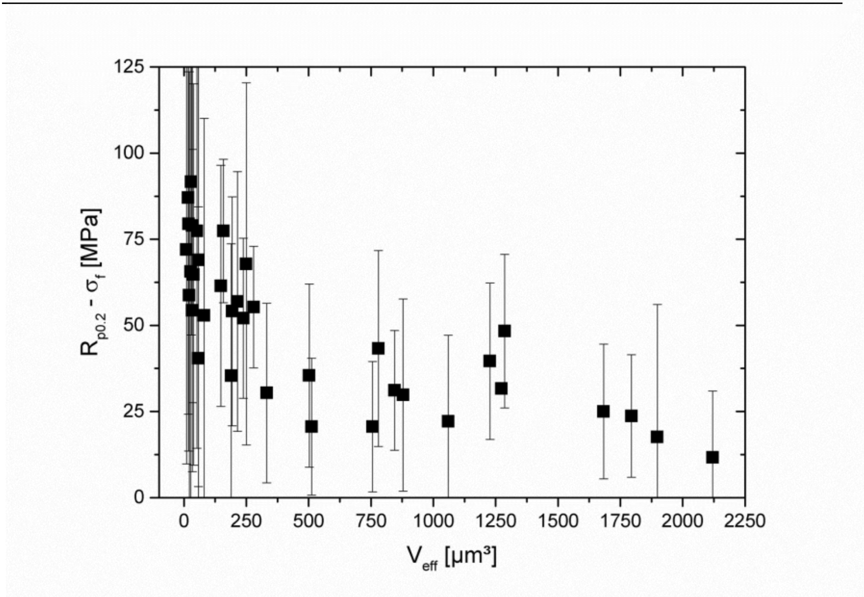

Figure 4.16: Difference in flow stress values $R_{p0.2}$ and σ_f versus V_{eff}.

4.8 Influence of FIB contamination

To study the influence of Ga^+ implantation, some cantilevers were purposely contaminated after fabrication according to the 4 contamination procedures introduced in chapter 3.2, namely flattening, nose cutting, blind cutting and snapshot only. The influence of these treatments is directly compared to the as-fabricated, non-contaminated structures and allows a precise evaluation of the mechanical changes caused. The sample set chosen for the analysis contains about 100 cantilevers in total which are all of DG orientation and aspect ratio B. Before contamination is introduced to a subset of this sample set, the thickness is the only parameter that is varied (from 1 to 3 µm).

The first kind of contamination that is addressed is the flattening procedure which to some extent mimics the last milling step of conventional FIB micromachining. Fig.4.17 shows the change in bending moment curves that the FIB treatment provokes. The curves in the figure are averaged curves of 4 individual tests. The 3 µm thick cantilevers lack a treatment at 50 pA, because the samples were too big to be cut at such a low current. The effect of the flattening treatment is best seen on Fig.4.17a which comprises the smallest cantilevers: The bending moments and in turn the flow stress and yield strength of the samples significantly increases and the hardening behavior changes as well.

The influence of ion current on the flow stress during flattening is displayed in Fig.4.18. The figure reveals that the treatment significantly raises the flow stress and that when increasing the ion current, an asymptotic behavior is found. The threshold value is reached at about 100-300 pA, which is a comparatively low current and is usually only used for the final cut of very small testing structures (Kiener et al., 2010; Iqbal et al., 2012). The absolute change in flow stress is smaller, if the size of the cantilever is larger. However, when plotting the relative change in flow stress (Fig.4.18b), it can be stated that the contamination affects small and large structures more or less alike.

Moreover, the flattening treatment also affects the scaling law describing the size effect. This is shown in Fig.4.19. It displays the scaling law found for the cantilevers of the respective sample sets in their as-fabricated state and after FIB treatment. The scaling exponent increases as a result of the flattening procedure from $n = 0.62 \pm 0.04$ to $n = 0.74 \pm 0.03$.It should be pointed out again, that for the scaling law of the as-fabricated structures only a subset from the data pool is used. The subset for as-fabricated cantilevers is therefore not necessarily statistically representative for the entire sample set used in the project and can only be considered as the reference structures for the contamination experiments. For the as-fabricated cantilevers, n has about the same deviation from the value found in Fig.4.10 as the contaminated ones. The flow stress values for the flattened samples are found to be higher which is in agreement with the aforementioned observations.

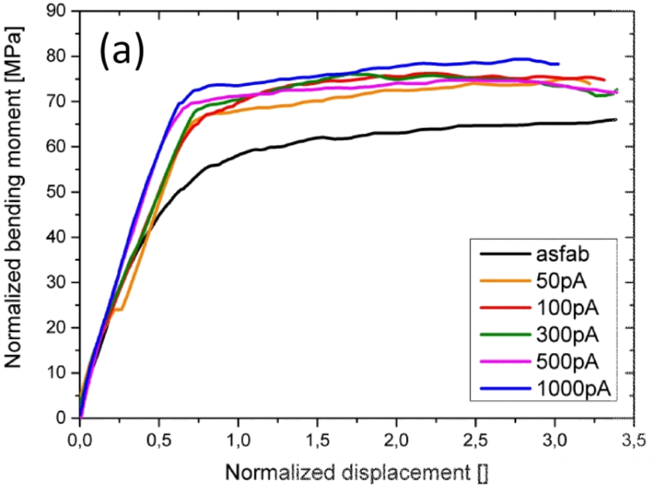
(a)
Normalized bending moment [MPa]
0
10
20
30
40
50
60
70
80
90
0,0
0,5
1,0
1,5
2,0
2,5
3,0
3,5
Normalized displacement []
asfab
50pA
100pA
300pA
500pA
1000pA

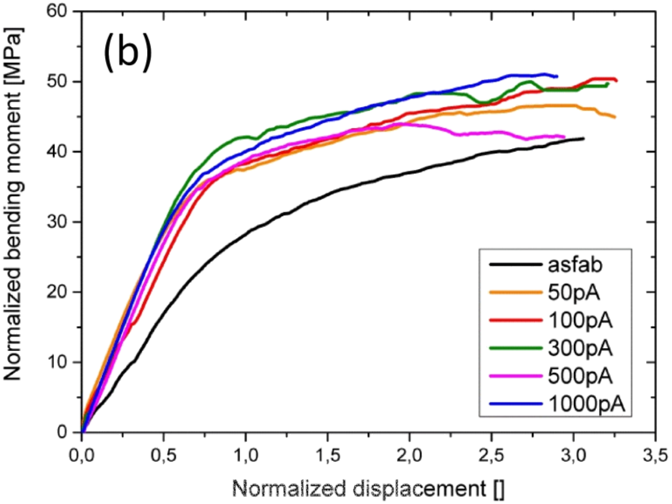
(b)
Normalized bending moment [MPa]
0
10
20
30
40
50
60
0,0
0,5
1,0
1,5
2,0
2,5
3,0
3,5
Normalized displacement []
asfab
50pA
100pA
300pA
500pA
1000pA

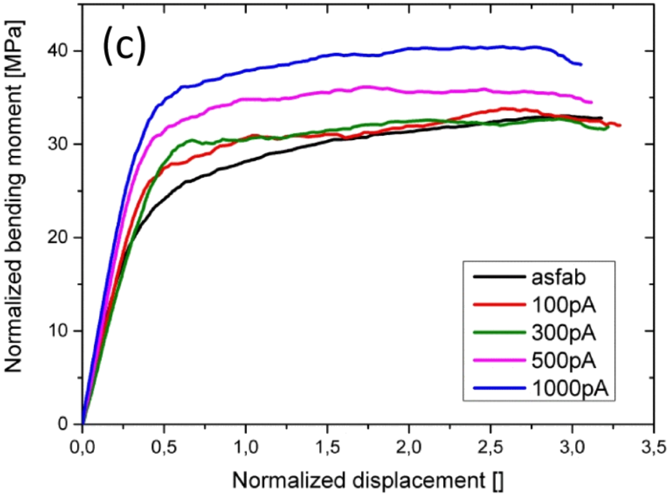

Figure 4.17: Bending moment curves showing the changes in mechanical behavior of the as-fabricated cantilevers by the flattening procedure under different ion currents. Samples taken are in DG orientation, aspect ratio B and (a) 1 µm, (b) 2 µm and (c) 3 µm in height.

It is also attempted to determine the scaling exponent *n* as a function of ion current used during the flattening procedure. However, it needs to be pointed out that the data set to conduct such a fitting is very limited as well, because all results obtained from the flattening procedure have to be categorized according to ion current used and each subset then comprises only about 4 individual cantilevers. The 50 pA category even has to be discarded entirely because there are no cantilever of 3 µm height that could be cut under these conditions. Nevertheless, all remaining currents give about the same scaling exponent, and is on the order of $n = 0.7 \pm 0.05$.

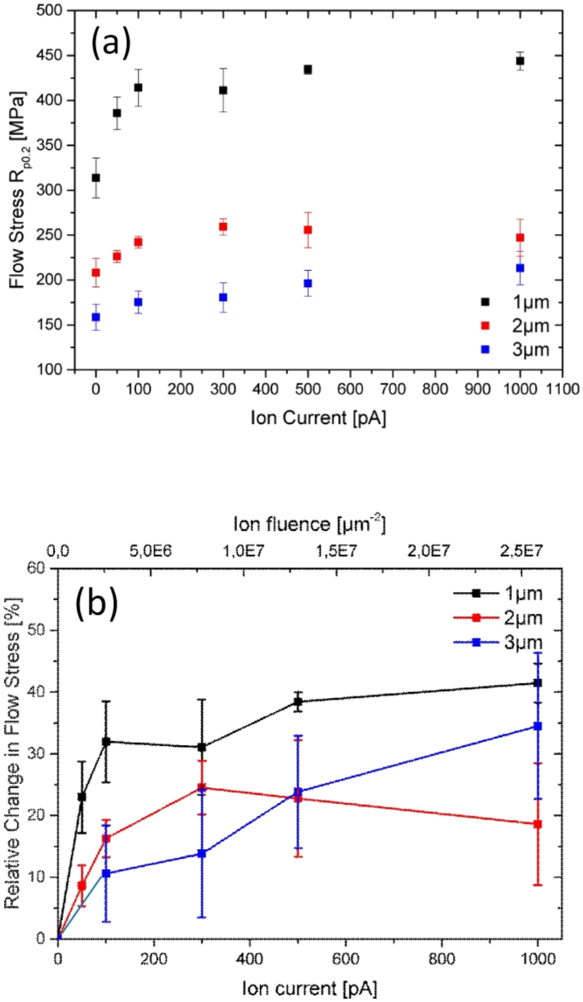

Figure 4.18: FIB damage by flattening the cantilever edges. (a) Absolute flow stress values and (b) relative change of flow stress with respect to the non-treated cantilever plotted as a function of the ion current applied.

Apart from the absolute value of the flow stress, the treatment is also found to change the shape of the bending moment curves. While the absolute values within the elastic-plastic plateau are raised, the hardening behavior is modified, as well. The transition interval from elastic to elastic-plastic shows less pronounced work hardening whereas for an as-fabricated (i.e. non-irradiated) cantilever the transition can be described as much smoother (Fig.4.17). The phenomenon is found to be consistent for all different initial sample sizes. An attempt to fit stress-strain curves showed that FIB treated samples tend to be described more accurately by the Voce-type fit. In analogy to Fig.4.16, the change in hardening behavior can also be expressed by plotting the difference $R_{p0.2}$ - σ_f (Fig.4.20). As the flattening procedure removes material from the edges, V_{eff} drops after patterning. However, it is seen that for cantilevers of about the same size, the difference between the two stress values is larger if the sample was treated by FIB. In analogy to the deductions made from Fig.4.16 this implies a stronger pronounced work hardening.

In the following, the results of the remaining three contamination procedures are presented. Nose cutting, blind cutting and snapshot only as described in chapter 3 were applied to the sample set with 1 μm in height (DG orientation, aspect ratio B). Fig.4.21 shows the result of the mechanical tests of the contaminated samples. The x-axis on top of Fig.4.21a displays the ion fluences φ for the case of the snapshot only procedure. They are not viable for the other treatments. Fig.4.21 demonstrates that with the exception of blind cutting, all FIB treatments have the same effect on the flow stress of the cantilevers. The similarity of the results from nose cutting and flattening proves that the samples are in fact comparable even if flattening produces structures with sharp edges, i.e. alters the overall geometry. Moreover, it implies that the shape, size and position of the milling pattern appears to be of minor influence. One might assume that the contamination and the changes in mechanical response involved are existent as soon as any kind of patterning is executed, regardless of its shape and position. The fact that the results from the snapshot only procedure again match with both nose cutting and flattening, leads to the conclusion that the reason behind this is, that the Ga^+ contamination is being introduced well before the patterning itself.

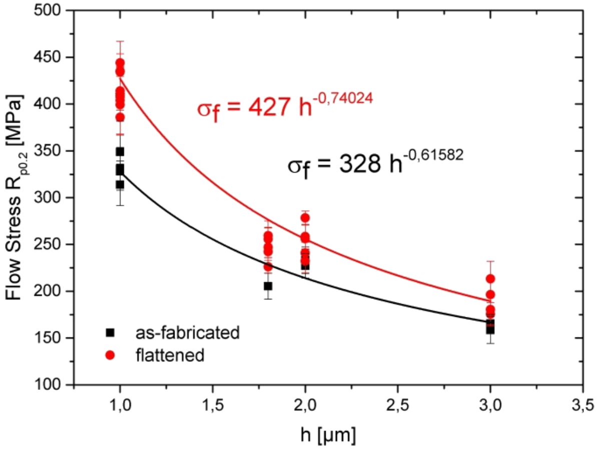

Figure 4.19: Flow Stress $R_{p0.2}$ versus cantilever height h for as-fabricated samples of identical aspect ratios and orientations after FIB contamination via the flattening procedure. The values of the allometric fitting function are given as an inset and the numbers are dyed in the color of the corresponding plot.

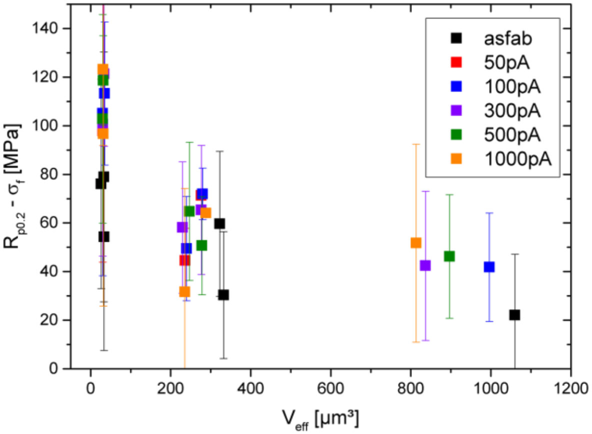

Figure 4.20: Difference in flow stress values $R_{p0.2}$ and σ_f versus V_{eff} for cantilevers milled by the flattening treatment.

Moreover, it should be pointed out that already a snapshot under the given fluences is sufficient to attain the threshold flow stress value found in Fig.4.21. The fluences used during the snapshot are comparably low corresponding to short standard scans with FIB. Kiener et al. (Kiener et al., 2007) stated that Ga^+ ions accelerated with 30 kV reach a depth of 50 nm within a polycrystalline Cu sample. Even if the ions implanted during the snapshot only reach a depth of about 50 nm they are still located within the outermost fiber, i.e. in the region where their presence will have the strongest influence on mechanical properties. Kiener et al. (Kiener et al., 2007) report the concentration of implanted Ga^+ under conditions mentioned above to be about 20 at% within the surface layer. Within that affected zone, various defects such as dislocations, point defects, etc. can be generated from Ga^+ implantation as pointed out in literature (Bei et al., 2007; Kiener et al., 2007). Motz et al. (Motz et al., 2008) mentioned that Frank-Read sources are only activated in the outermost regions of the cantilevers so contamination of them is likely to play an important role. Taking a snapshot can therefore be considered as the essential problem of fabricating cantilever structures with FIB.

The only treatment that significantly differs from the other ones is the blind cutting. While in the project at hand all other FIB treatments are found to rise the flow stress by about 25-30 % with respect to the non-treated samples, the blind cutting procedure produces changes in flow stress of only about 15 %. The observation, that changes in mechanical behavior are found even if the zone of plastic deformation is not directly irradiated by FIB implies that diffusion of Ga^+ ions from the cutting region towards that zone of interest must be taking place as well. The diffusion path for the given case is at least 10 µm in length (distance between the blind cutting pattern and the cantilever support). A diffusion about such a length through the volume of the cantilever appears unlikely, since the sample is single crystalline and does not provide any grain boundaries or comparable features which might serve as potential diffusion paths. Therefore, the diffusion of Ga^+ ions must take place along the sample surface which is also known to be the most efficient diffusion. From all of these observations, the following statements are justified: The Ga^+ ions causing changes in mechanical behavior mainly stem from direct implantation due to the snapshot taken before patterning which is inevitable in FIB micro machining. Additionally, a certain amount of Ga^+ ions diffuse, probably over the metal surface, and contaminate the entire sample leading to a change in mechanical properties.

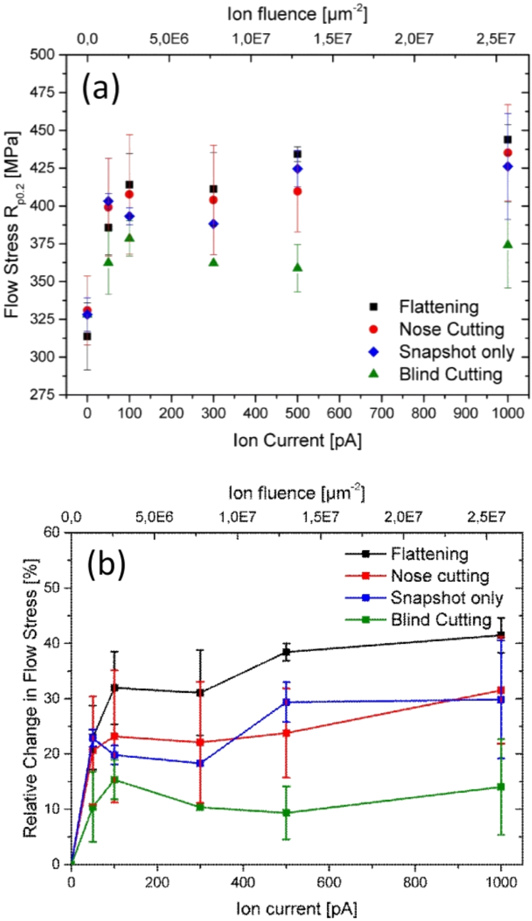

Figure 4.21: FIB damage by various contamination procedures. The sample set is 1µm in height, DG orientation and aspect ratio B. (a) Absolute flow stress values and (b) relative change of flow stress. Fluence values refer to blind cutting procedure only.

5 Microstructural analysis

Now that the mechanical properties of the single crystalline cantilevers have been measured and analyzed, the microstructural changes occurring during deformation are investigated. The aim of the analysis is to localize dislocation networks, to determine their Burgers and line vectors and as far as possible give quantitative values of the dislocation densities within the sample. Then, it is attempted to find out how all of these microstructural aspects change as a function of sample size, orientation and total strain imposed.

Capturing dislocations experimentally is a challenging task, because it requires methods with very high lateral resolution. As mentioned in chapter 1 these methods are usually based on diffraction, e.g. dark field images in TEM (diffraction contrast) or X-ray diffraction using synchrotron sources. Quantifying the amount of dislocations is even more difficult because the diffraction signal is always influenced by a variety of factors aside from the dislocation density and the absolute values found can usually only be considered as estimates. In this project, TKD is introduced for this kind of study. It will be shown that due to its about 5 times better lateral resolution, TKD allows studying far more details of the microstructure than EBSD. Like EBSD it allows indexing the activated slip systems, but provides much more detailed visualization of dislocation networks within a given cross section of the cantilevers. The latter becomes particularly interesting when a method introduced by Pantleon (Pantleon, 2008) is applied where it is possible to distinguish the dislocations by their respective Burgers and line vector. Moreover, due to the chosen orientation of the single crystals, the dislocation networks recorded by a single TKD scan can justifiably be considered to be representative for the entire cantilever volume.

5.1 Experimental Setup

Preparing the cantilevers for TKD and EBSD is essentially comparable to cutting a TEM lamella with FIB. Detailed descriptions of the procedure for TEM lamella fabrication using FIB can be found in literature (Giannuzzi & Stevie, 2005). In comparison to other materials, Ag is sputtered relatively fast with Ga^+ ions, so care has to be taken when the cantilevers are thinned. Preparing TEM lamellas out of Ag is known to be a rather difficult task. At first glance, the sole difference to the standard lamella cutting procedure is that the cantilevers are already free-standing so no crater has to be milled in front and behind the designated sample. However, the non-deformed region, i.e. the region that is still supported by Si is vital for the measurement as well because a reference pattern for the undisturbed lattice is needed in order to align the orientation data. Therefore the FIB procedure is designed so a sufficiently large region of the support is being extracted as well (Fig.5.1). This region should be chosen to be several µm in length because the sample will be attached to a TEM grid and: The grid is considerably thicker than the lamella itself, so once attached, it is likely to shadow the part of the sample which is closest to the attachment. If such a long region from the support is cut, then it is assured that the shadowed region is practically of no interest, and a diffraction signal from the non-deformed single crystal can still be obtained and used as a reference pattern.

Before any information can be retrieved from the orientation data obtained, an alignment step has to be executed. For this purpose, data points from the supported region are useful, since their orientation is known. The alignment is done using pole figures. When looking at the pole figures from an exemplary data set (Fig.5.3), it is readily seen, that all poles are streaking in a consistent way. One single pole, however, stands out showing no change at all. In other words, one crystallographic direction is fixed over the entire cross section and thus obviously corresponds to the overall rotation axis of the bending process $\boldsymbol{x_3}$. Upon closer inspection of the pole figure, it is noticed that all other poles are indeed rotating around that particular one. The alignment step now consists in finding the rotation axis and then centering its pole onto the origin of the stereographic projection. This is done by adjusting

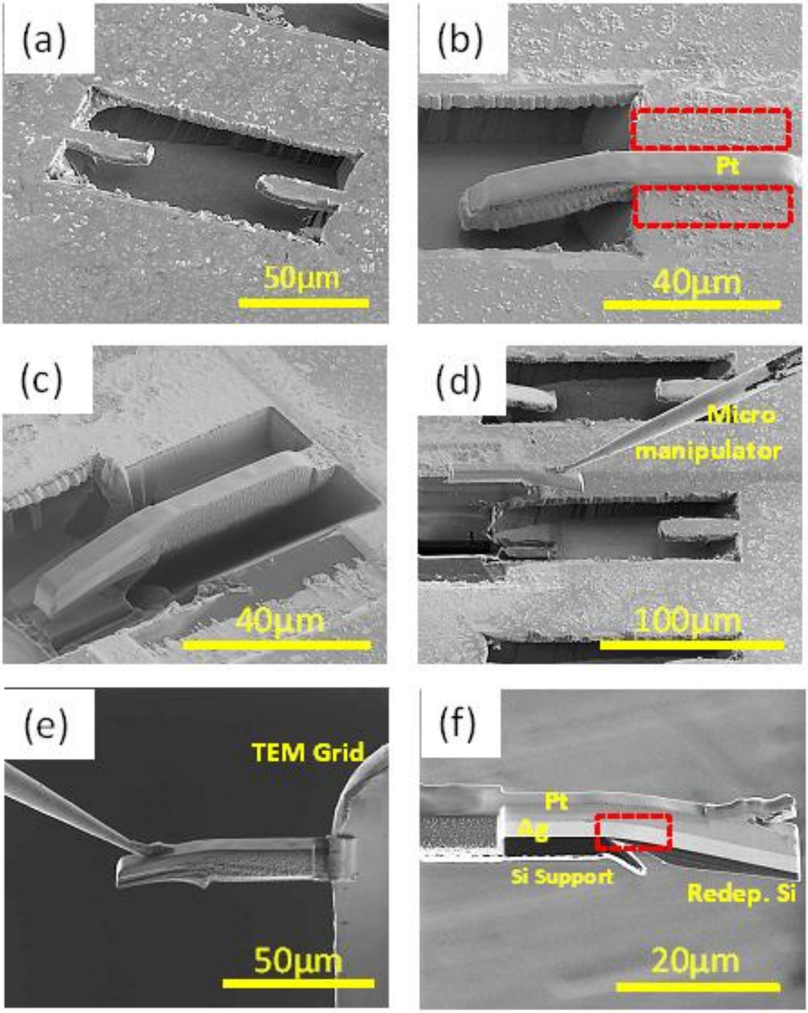
(a)
50µm
(b)
Pt
40µm
(c)
40µm
(d)
Micro manipulator
100µm
(e)
TEM Grid
50µm
(f)
Pt
Ag
Si Support
Redep. Si
20µm

Figure 5.1: Sample preparation for EBSD and TKD. Images are taken with SEM and (e) is taken with FIB. (a) Overview over one etch pit from which one cantilever is chosen. (b) After Pt deposition on top of the cantilever. Red area marks the cuts for lift-off. (c) shows result of this cut. (d) Lift-off with micro manipulator. (e) Attachment to TEM Grid. (f) Flattening/Cleaning for EBSD. For TKD further thinning would be needed. The red square marks the typical size and location of a region that can be scanned with TKD.

the Eulerian angles of the data set. These static poles are found to stem from the (101) plane for HS and (102) for DG orientation. From a mechanical point of view this is plausible as well, because of the sample orientation and the plane bending assumption. After centering the rotation axis at the origin of the pole figure, a rotation is executed around that centre until the {001} poles stemming from the supported region lie on the equatorial line or the 0° great circle of the pole figure.

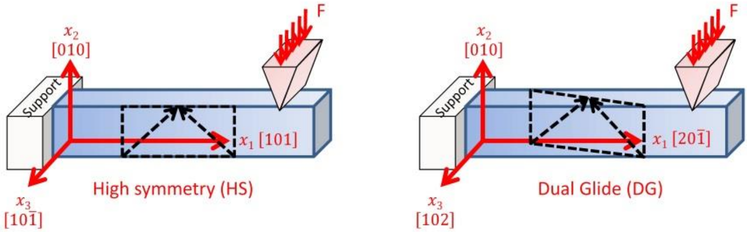

Figure 5.2: Schematic of the sample orientations HS and DG. The effective Burgers vectors are sketched in black.

As the analysis method that follows the approach of Pantleon (Pantleon, 2008) requires a precise indexing of crystallographic directions, it needs to be checked that the rotation axes x_3 are exactly $[10\bar{1}]$ for HS and [102] for DG. Therefore inverse pole figure maps are generated along different sample directions and in agreement with the previous statements there is only one single map where the entire cantilever shows no change in orientation across the entire scanned area: Fig.5.4c, which is the inverse pole figure map along the *sample* direction [001] (corresponding to axis x_3), displays this situation. The scans reveal that x_3 coincides with the *crystallographic* direction [101].

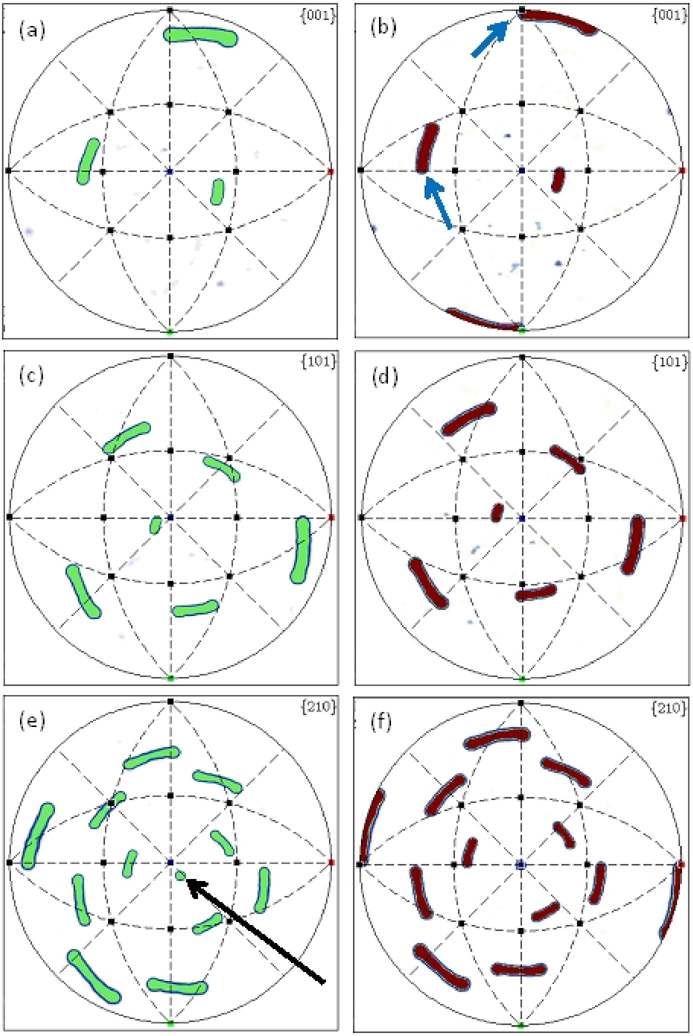

Figure 5.3: Pole figures from an EBSD scan of a non-aligned cantilever (green) in DG orientation and after alignment (red) for the planes (a, b) {001}, (c, d) {101}, (e, f) {210}. The black arrow in (e) marks the sole pole that shows no apparent streaking and is therefore centered. The blue arrows in (b) highlight how a rotation around this pole is then executed so {001} poles lie on the equatorial line and 0° great circle.

Note that indexing $\boldsymbol{x_3}$ with the crystallographic direction $[10\bar{1}]$ (to match the coordinate system introduced in chapter 2) is justified because of cubic symmetry. For DG, a similar analysis leads to the identification of $\boldsymbol{x_3}$ with the crystallographic direction [102]. Now that the indices of the rotation axis $\boldsymbol{x_3}$ upon bending are known, the crystallographic indices corresponding to the other two axes can be deducted. From the epitaxial growth, it is known that the axis along the cantilever height $\boldsymbol{x_2}$ belongs to the <100> family and since it must be perpendicular to $\boldsymbol{x_3}$, it can be indexed as [010] both for HS and DG. From the cross product of these two vectors the $\boldsymbol{x_1}$ axis is found to be $[101]$ for HS and $[20\bar{1}]$ for DG.

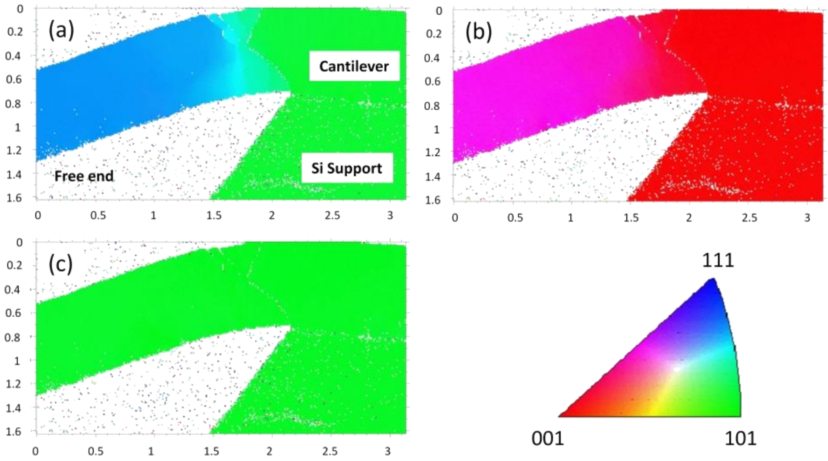

Figure 5.4: Inverse Pole figure maps of a cantilever in HS orientation scanned with TKD. The maps are calculated for (a) the sample direction x_1, (b) x_2 and (c) x_3.

5.2 Estimating GND densities from misorientation data

From EBSD and TKD it is possible to obtain information about the dislocation arrangement across the scanned area in a qualitative and with some assumptions in a quantitative way as well. This possibility arises from the fact that any dislocation will cause a localized rotation of the crystal lattice around its core. That means that once the orientation has been mapped, dislocations can be visualized if the misorientation of each data point with respect to its surroundings is calculated. Connected data points of high misorientation can then be interpreted as a dislocation network. The orientation matrix $\overline{\boldsymbol{g}}$ which links the coordinate system of the crystal structure $\boldsymbol{C_C}$ to the given specimen coordinate system $\boldsymbol{C_S}$ is defined as (Engler & Randle, 2010)

$$\boldsymbol{C_C} = \overline{\boldsymbol{g}} \cdot \boldsymbol{C_s} \tag{5.1}$$

where $\overline{\boldsymbol{g}}$ contains the nine angular relations (cosini) needed for this transformation. The exact angular relations can be expressed by these nine values or alternatively by the three Eulerian angles. In the approach presented in this section another way to express the transformation from one coordinate system into the other is chosen: It is known as the angle/axis of rotation representation (Engler & Randle, 2010). The basis of the description is that any Cartesian coordinate system can also be transformed into another by one single rotation operation about an angle θ that is executed around one single axis $\boldsymbol{r}$. This angle/axis pair for any data point can be calculated from the orientation matrix $\overline{\boldsymbol{g}}$ by

$$\cos(\theta) = \frac{(g_{11} + g_{22} + g_{33} - 1)}{2} \tag{5.2}$$

$$r_1 = \frac{(g_{23} - g_{32})}{2sin(\theta)} \quad (5.3a)$$

$$r_2 = \frac{(g_{31} - g_{13})}{2sin(\theta)} \quad (5.3b)$$

$$r_3 = \frac{(g_{12} - g_{21})}{2sin(\theta)} \quad (5.3c)$$

An access to dislocations can be obtained if instead of the angular relation between one measurement and the specimen coordinate system the differences in orientation between neighboring measurements points are considered. From the matrices of two neighboring points the misorientation matrix $\overline{\boldsymbol{M}}_{12}$ can be derived by (Engler & Randle, 2010):

$$\overline{\boldsymbol{M}_{12}} = (\overline{\boldsymbol{g}_1})^{-1}\,\overline{\boldsymbol{g}_2} \quad (5.4)$$

The angle θ that can be calculated from this misorientation matrix is called the misorientation angle throughout this project. It expresses the difference in orientation between a scanned data point and its surroundings ($\overline{\boldsymbol{g}}_1$ and $\overline{\boldsymbol{g}}_2$) in a very straightforward way. Now, it needs to be clarified, how many data points contribute to the coordinate system of the data points' surroundings, i.e. are to be considered as its neighbors. For EBSD scans executed on the given samples, the amount of measure a data is very limited, because of the small cantilever height compared to the step size (50 nm) and the 70° tilt angle of the sample. In fact, for 1 µm thick cantilevers usually less than 10 data points are recorded in the $\boldsymbol{x_2}$ direction. Therefore, a Kernel average misorientation (KAM) is found to produce at best blurry results. So instead of using a KAM, the misorientation angle is calculated along the $\boldsymbol{x_1}$ direction and the $\boldsymbol{x_2}$ direction, individually and only directly adjacent data points are considered neighbors, diagonally adjacent points are disregarded and the misorientation along $\boldsymbol{x_1}$ and $\boldsymbol{x_2}$ are treated as two independent quantities. In TKD scans, much more data points are obtained from a single scan (due to 10 nm step size and only 20° sample tilt in opposite direction) so KAM over all direct neighbors is possible and applied in addition to the latter method.

As mentioned, mapping the misorientation gives a fingerprint of the dislocation arrangement within the cross section. It is also worth pointing out the nature of the dislocations that can be accessed with this approach: The method is only sensitive to sets of dislocations which cause the lattice to rotate within the respective volume element. Following this statement, only GND can be detected because a set of SSD have a net Burgers vector that equals zero which means that all individual rotations cancel out within the respective volume. All quantitative results and methods shown throughout this chapter are therefore limited to GND only. There are some approaches to gain information about SSD as well, which rely on image quality. The idea is that any kind of dislocation – GND as well as SSD – will blur the diffraction signal and thus should locally influence the image quality of the scan. However, such approaches are qualitative and hard to apply because the band contrast is affected by a large variety of parameters (some can even vary during the scan itself), such as beam voltage and current, cleanliness and smoothness of the scanned area, the quality of the vacuum, sample material and orientation, etc. On the other hand, for GND it is possible to obtain an estimation of the actual dislocation density if the magnitude of misorientation for each data point is calculated. If it is assumed that all dislocations are GND and thus contribute to the overall curvature the relation between their density ρ and the misorientation angle θ writes

$$\rho = \frac{\theta}{ub} \tag{5.5}$$

where b is the absolute value of the Burgers vector and u is the unit length (step size of the scan). The relationship has already been formulated for example in the work of Nye and various other groups (Nye, 1953; Kubin &

Mortensen, 2003; Taylor & Ashby, 2006; Calcagnotto et al., 2010) and is used to quantify the dislocation density in this work. The procedure explained above is applied to find two independent GND densities for each measurement point, one from the misorientation along $\boldsymbol{x_1}$ and one along the $\boldsymbol{x_2}$ direction. The two density values are added to give the total dislocation density ρ. Treating dislocation densities along $\boldsymbol{x_1}$ and $\boldsymbol{x_2}$ as independent values this way is possible because only the misorientation angle θ is used in (5.5) while the direction of the misorientation axis is disregarded.

This approach to calculate GND densities cannot be applied for any kind of sample, because any lattice rotation is considered to be caused by a set of dislocations. At the edges of the samples, the diffraction patterns tend to be unreliable and, therefore, the dislocation densities at these extremities are most likely evaluated incorrectly, usually too high. Furthermore the method assumes that all dislocations detected are alike, in the sense that they all cause the same kind of lattice rotation. This is evident because from the angle/axis notation where only the absolute value of the misorientation angle is used for the calculation, but the orientation of the axis, which determines the direction around which the rotation is executed, is neglected. Instead, dislocations are assumed to be of the same Burgers vector. Considering the sample orientations used in this project - HS and DG - the assumption is not met since plastic deformation is at least carried by two effective Burgers vectors. From these assumptions the GND densities found with equation (5.5) can only be regarded as approximations.

A more detailed approach based on Nye's tensor was suggested by Pantleon (Pantleon, 2008). Here, the misorientation is expressed as a misorientation vector $\boldsymbol{\Delta\theta}$ which, in contrast to the angle/axis pair notation, takes the components of the rotation axis $\boldsymbol{r}$ into account for the calculation of the dislocation density. In this approach, the orientation of the dislocations is no longer neglected. The three components of $\boldsymbol{\Delta\theta}$ can be obtained by multiplying the misorientation angle with the respective components of $\boldsymbol{r}$ by

$$\Delta\theta_i = r_i\theta \tag{5.6}$$

$\boldsymbol{\Delta\theta}$ is then used to approximate the tensor of curvature $\overline{\boldsymbol{\kappa}}$

$$\kappa_{kl} \approx \frac{\Delta\theta_k}{\Delta x_l} \tag{5.7}$$

where Δx_i is the unit length or step size of the scan along one of the sample directions. Since both EBSD and TKD are only executed within the $\boldsymbol{x_1}$-$\boldsymbol{x_2}$-plane, there is no Δx_3 and only six components of $\overline{\boldsymbol{\kappa}}$ can be determined. Nevertheless, the information that can be retrieved from these six components is relevant because $\overline{\boldsymbol{\kappa}}$ is related to Nye's tensor $\overline{\boldsymbol{\alpha}}$ (Nye, 1953). The components building Nye's tensor can be imagined as a description of the net closure failure of a 3D Burgers circuit along a specific volume element. That means, if within this circuit the amount of any kind of dislocations n as well as their orientations (Burgers vector $\boldsymbol{b}$ and line vector $\boldsymbol{t}$) are known, then Nye's tensor produces the closure failure and is in turn able to derive the resulting lattice curvature, caused by that arrangement. This is mathematically expressed as

$$\alpha_{ij} = \sum_m n b_i^m t_j^m \tag{5.8}$$

The way in which Nye's tensor and curvature tensor are related is

$$\alpha_{ik} = \kappa_{ki} - \delta_{ki}\kappa_{mm} \tag{5.9}$$

where δ_{ki} is the Kronecker symbol. Because only six components of $\overline{\boldsymbol{\kappa}}$ are known, the method only grants access to five components of Nye's tensor directly and to one term which is the difference of two individual components. The 6th component describing a difference may not be identified with a quantitative value but it can still be used for mathematical minimization algorithms.

The idea behind the approach is now to predefine a set of possible dislocation types of different ***b*** and ***t*** values and to use them to reconstruct the distorted crystal whose curvature has been measured. For an fcc crystal, there are 36 possible dislocation types, if only pure edge and pure screw dislocations are considered and if sign convention is respected. Tab.5.1 shows their respective vectors and their notation which is used throughout this work. The notation is chosen in analogy to the Schmid-Boas notation for slip systems introduced in chapter 2. The sign convention is respected by the addition of the + or - symbol and screw dislocations are denoted with the letter E, since they cannot be attributed to one single crystal plane. Fig.5.5 also gives an illustration of the positions of the individual planes and vectors in Schmid-Boas notation.

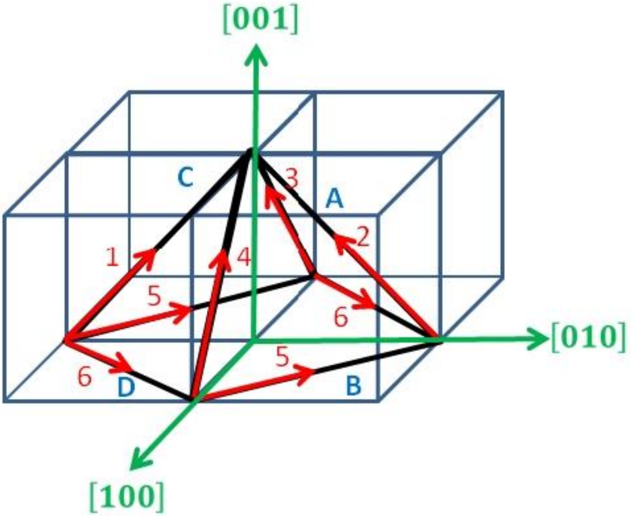

Figure 5.5: Illustration of the slip systems and their notation (Schmid-Boas notation). The individual slip planes are marked with letters while the directions are indicated by numbers.

Notation	Burgers vector	Slip plane	Line Vector
A2+	$[0\bar{1}1]$	$(\bar{1}11)$	$[\bar{2}\bar{1}\bar{1}]$
A2-	$[0\bar{1}1]$	$(\bar{1}11)$	$[211]$
A3+	$[101]$	$(\bar{1}11)$	$[\bar{1}\bar{2}1]$
A3-	$[101]$	$(\bar{1}11)$	$[12\bar{1}]$
A6+	$[110]$	$(\bar{1}11)$	$[1\bar{1}2]$
A6-	$[110]$	$(\bar{1}11)$	$[\bar{1}1\bar{2}]$
B2+	$[0\bar{1}1]$	(111)	$[\bar{2}11]$
B2-	$[0\bar{1}1]$	(111)	$[2\bar{1}\bar{1}]$
B4+	$[\bar{1}01]$	(111)	$[\bar{1}2\bar{1}]$
B4-	$[\bar{1}01]$	(111)	$[1\bar{2}1]$
B5+	$[\bar{1}10]$	(111)	$[11\bar{2}]$
B5-	$[\bar{1}10]$	(111)	$[\bar{1}\bar{1}2]$
C1+	$[011]$	$(\bar{1}\bar{1}1)$	$[2\bar{1}1]$
C1-	$[011]$	$(\bar{1}\bar{1}1)$	$[\bar{2}1\bar{1}]$
C3+	$[101]$	$(\bar{1}\bar{1}1)$	$[1\bar{2}\bar{1}]$
C3-	$[101]$	$(\bar{1}\bar{1}1)$	$[\bar{1}21]$
C5+	$[\bar{1}10]$	$(\bar{1}\bar{1}1)$	$[112]$
C5-	$[\bar{1}10]$	$(\bar{1}\bar{1}1)$	$[\bar{1}\bar{1}\bar{2}]$
D1+	$[011]$	$(1\bar{1}1)$	$[21\bar{1}]$
D1-	$[011]$	$(1\bar{1}1)$	$[\bar{2}\bar{1}1]$
D4+	$[\bar{1}01]$	$(1\bar{1}1)$	$[121]$
D4-	$[\bar{1}01]$	$(1\bar{1}1)$	$[\bar{1}\bar{2}\bar{1}]$
D6+	$[110]$	$(1\bar{1}1)$	$[1\bar{1}\bar{2}]$
D6-	$[110]$	$(1\bar{1}1)$	$[\bar{1}12]$
E1+	$[011]$	-	$[011]$
E1-	$[011]$	-	$[0\bar{1}\bar{1}]$
E2+	$[0\bar{1}1]$	-	$[0\bar{1}1]$
E2-	$[0\bar{1}1]$	-	$[01\bar{1}]$
E3+	$[101]$	-	$[101]$
E3-	$[101]$	-	$[\bar{1}0\bar{1}]$
E4+	$[\bar{1}01]$	-	$[\bar{1}01]$
E4-	$[\bar{1}01]$	-	$[10\bar{1}]$
E5+	$[\bar{1}10]$	-	$[\bar{1}10]$
E5-	$[\bar{1}10]$	-	$[1\bar{1}0]$
E6+	$[110]$	-	$[110]$
E6-	$[110]$	-	$[\bar{1}\bar{1}0]$

Table 5.1: Dislocation types and their notation used in this project.

For the calculation of $\overline{\boldsymbol{\alpha}}$ for each data point of the scanned area, an important aspect that needs to be discussed once more is the decision which data points from its neighborhood are taken for the calculation of each individual component α_{ij}. In this case the problem consists in the mathematical connection between the components of $\overline{\boldsymbol{\kappa}}$ and $\overline{\boldsymbol{\alpha}}$ with the misorientation data. For the method that follows equation (5.5) it was argued that misorientation is calculated independently along $\boldsymbol{x_1}$ and $\boldsymbol{x_2}$, so two independent dislocation densities are obtained and the total dislocation density is found as their sum. Likewise, in the approach based on Nye's tensor, after determining $\boldsymbol{\Delta\theta}$ for each measurement point, the components κ_{i1} are calculated from the misorientation obtained from neighboring points in $\boldsymbol{x_1}$ direction only and likewise for the components κ_{i2} the misorientation matrix is obtained from neighboring points in $\boldsymbol{x_2}$ direction only (equation 5.7). Consequently, once the six components of $\overline{\boldsymbol{\kappa}}$ are found for each data point, the corresponding components of $\overline{\boldsymbol{\alpha}}$, which can be calculated following equation (5.8) should be obtained in a similar way. However, it is not meaningful to apply a Kernel average misorientation (KAM) approach for the calculation of $\overline{\boldsymbol{\alpha}}$ in this case. Instead, if for example for the determination of α_{1i} only κ_{i1} is used, this selection assures that when calculating dislocation densities from $\overline{\boldsymbol{\alpha}}$, averaging is only performed over data points whose orientations actually contribute to the curvature of the component under consideration. For the remaining term of $\alpha_{33,}$ the curvatures and misorientations of neighboring points in both $\boldsymbol{x_1}$ and $\boldsymbol{x_2}$ are equally taken into account and the total curvature is obtained by their sum.

Because only 5 components of the curvature tensor $\boldsymbol{\kappa}$ are known, while there are 36 variable dislocation densities, the problem will result in an infinity of possible solutions. Therefore a minimization step is needed to specify the desired solution. Several suggestions are made by Pantleon (Pantleon, 2008) and also summarized in the work of Kysar et al. (Kysar et al., 2010). The only minimization approach that yields a physical meaning is the so called L^1 norm (Kysar et al., 2010). In this norm the term designated to be minimized L^1 and has the general form of

$$L^1 = \sum_{\alpha=1}^{36} |\rho^\alpha w^\alpha| \tag{5.10}$$

Where ρ is the GND density of dislocation type α and w is a weighting factor. The minimization criterion used in this project follows this approach using a weighting factor that is 1 for all types. Then the L^1 norm results in the minimum amount of total dislocations needed. Assuming that the line energy and core energy of the dislocations is isotropic and constant for all dislocation types using the weighting factor $w = 1$, this approach can also be interpreted as the minimization of the total dislocation line energy (Pantleon, 2008). This approach is also widely used in literature (Kysar et al., 2010; Littlewood et al., 2011). As various dislocation reactions show – such as the possibility of dislocations to decompose into partials – the minimum amount of dislocations is not always the situation met in reality, since there are cases where such a decomposition of a full dislocation into several partials reduces the strain energy of the dislocation arrangement. So instead, one might consider using the criterion of minimizing the strain energy created by the dislocations, which would correspond to a weighting factor of $w = b^2$, where b is the absolute value of the Burgers vector. Interestingly, as pointed out by Kysar et al. (Kysar et al., 2010), the results of the GND densities would still be the same. The densities calculated by this minimization approach can be considered as a lower bound of the actual situation. Besides the L^1 norm there is also the L^2 norm (Kysar et al., 2010) which can be defined as

$$L^2 = \sqrt{\sum_{\alpha=1}^{36} (\rho^\alpha w^\alpha)^2} \tag{5.11}$$

This approach has mathematical benefits as it attempts to minimize square values but is not applied in this project as it yields no physical meaning. The minimization is executed using a Simplex algorithm, so the absolute minimum is found unambiguously. As a result, Pantleon's approach gives 36 individual dislocation densities for each data points, i.e. 36 individual GND density maps for each cross section.

5.3 Results

5.3.1 Slip systems

From the orientation data gathered, it is possible to index the slip systems activated during plastic deformation. This can be done by following the lattice rotation that results from the glide process. If several slip systems are activated at once, then the overall lattice rotation can be expressed as the sum of all individual rotations involved. If the orientation data obtained from the entire cantilever (from support until free end) is mapped in the form of a pole figure or inverse pole figure, then the slip systems activated can be indexed by analyzing the movement direction of the poles: The poles will gradually shift from their initial position towards a new pole whose crystallographic indices are consequently the sum of all Burgers vectors that contribute to the deformation process.

This pole shift can be seen in Fig.5.6. which displays the inverse pole figures for both HS and DG orientation inside the stereographic projection. After adjusting the Wulff net appropriately, it is readily seen that for HS, the plane whose normal vector is initially pointing towards [101] gradually rotates towards [010]. The same behavior is found for the normal vector [102] in DG geometry. For HS, the rotation is easily understood since [101] equals the sample direction $\boldsymbol{x_1}$ and the shift direction of the poles [010] is obtained by the sum of the four expected slip systems B2, B5, D1 and D6 (strictly speaking B2 needs to be reversed in its line sense with respect to Schmid-Boas notation introduced in Tab.2.1 before applying Schmid's law). A similar glide behavior, in agreement with analytical expectations was reported by Motz et al. (Motz et al., 2005) who performed EBSD on the cross section of Cu cantilevers in HS orientation fabricated by FIB. For DG on the other hand, the pole seen in Fig.5.6b generated from the normal vector of the (102) plane is not expected to change its position upon deformation, since it coincides with x_3 sample direction. Note that the borders of the stereographic triangle used by the analysis software are fixed to be [001], [101] and [111], so the sample direction x_1 $[\bar{2}01]$ which will rotate upon deformation is not included in it. Consequently, the interpretation of the shift towards [010] being caused by B2 and D1 are responsible for glide in DG needs to be transformed into its crystallographic equivalent for the axis convention used in this project, which can easily be done due to cubic symmetry. The activation of B2 and D1 in a [102] oriented sample is equivalent to the activation of A6 and C5 in a $[\bar{2}01]$ orientation, which matches expectation from the analytical approach (Tab.2.1).

For the given resolution, no statement can be made concerning secondary glide systems. In DG, Schmid's law predicts six secondary glide systems of equal Schmid factor of 0.24, namely A2, A3, C1, C3, B4 and D4. However, the overall streaking is clearly oriented towards [010], and no remarkable activation of these systems is detected. Even for large deflections, it is clearly seen that plastic deformation is still carried by the principal systems. In Fig.5.6, the poles for both HS and DG even reach the opposing borders of the stereographic triangle, [111] for HS and [112] for DG orientation, respectively. The bending angle needed to enable this is about 35° for HS and 25° for DG which corresponds to fairly large strains. In this work, no tests were executed beyond these limits. For completeness, if a cantilever in [111] orientation would be deflected further, a six-fold glide process would occur leading to an overall pole shifting towards [001] in the stereographic triangle. For DG, once the cantilever reaches [112] orientation, 8 glide systems would be possible, of which the two dominant ones would cause no further rotation away from the [112] pole. Therefore, no significant pole shifting would be expected.

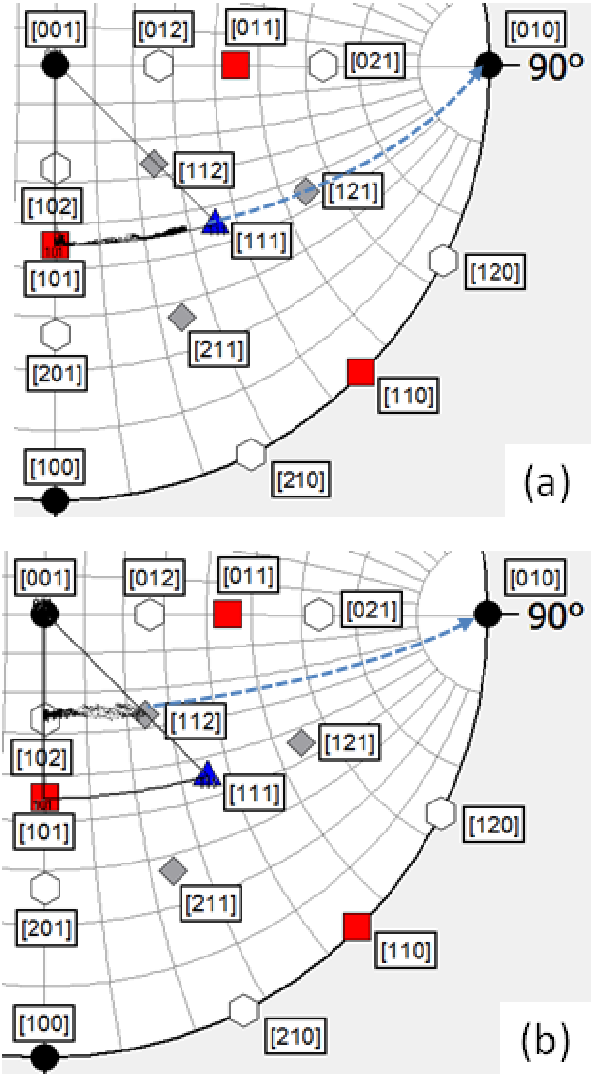
[001]
[012]
[011]
[021]
[010]
90°
[112]
[121]
[102]
[111]
[101]
[120]
[211]
[201]
[110]
[100]
[210]
(a)
[001]
[012]
[011]
[021]
[010]
90°
[112]
[121]
[102]
[111]
[101]
[120]
[211]
[201]
[110]
[100]
[210]
(b)

Figure 5.6: Inverse pole figures withtin stereographic projection (equal angle, upper hemisphere) for HS (a) and DG (b) for the traingle with borders [001], [101] , [111].

5.3.2 Glide steps

Due to the single crystalline nature of the specimen and the loading geometry, the deformation is highly localized within a small region close to the support. If the top surface of the specimen is sufficiently flat, which is usually the case for the cantilevers in this study, glide steps are found by standard SEM analysis (Fig.5.7). These glide steps mark the locations were dislocations left the crystal. For both given geometries, a set of strictly parallel glide steps are found. These lines run parallel to the support for HS and with a slight inclination of about 18° for DG.

The glide step analysis also allows to estimate the size of the zone of plastic deformation. It can be seen that the glide steps and in turn dislocation activity are indeed clustered within a very small region at the support. The cantilevers in the figure are 1 µm in height which is about the same order of magnitude as the lateral spread of the visible lines along the beam length axis $\boldsymbol{x_1}$. Over all sample sets, it is found that the lateral size of this zone is usually on the same order as the cantilever height. The cantilevers in the figure both have an undercut of $l_u > 0$. It was argued in chapter 3 that due to the undercut stresses will be mitigated beyond the assumed location of the support. However, Fig.5.7 demonstrates that plastic deformation is confined within the free standing part of the structures for HS and for DG only a negligible small portion of glide steps are found in the supported region.

5.3.3 Dislocation arrangement and densities

As sketched in Fig.5.2, both in HS and DG geometry, the dislocations activated for plastic deformation move on their respective glide planes diagonally through the volume until they leave the crystal. It was just shown that when looking at the $\boldsymbol{x_1}$-$\boldsymbol{x_3}$-plane, a set of parallel lines (glide steps) becomes visible at the sample surface. A more interesting aspect is the arrangement of the dislocations within the cantilever volume, which is done by analyzing cross sections of the $\boldsymbol{x_1}$-$\boldsymbol{x_2}$-plane.

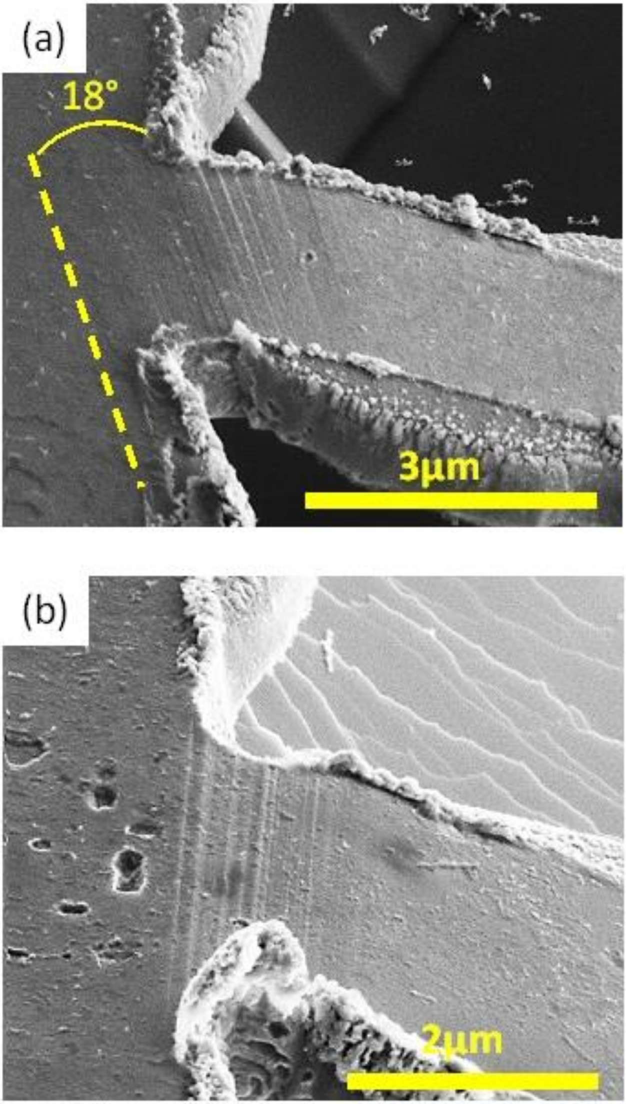

Figure 5.7: SEM images showing glide steps on the cantilever surface (a) in DG and (b) in HS geometry.

A straightforward way to qualitatively visualize dislocation networks from an EBSD or TKD scan is by mapping band contrast. As a simplification, the band contrast describes the quality of the Kikuchi pattern for the given data sample. If the electron diffraction at the data points is sharp then a good band contrast is seen while crystallographic defects, impurities on the sample surface etc., which tend to blur the Kikuchi pattern, cause a poor band contrast. For more precise information on the subject, the reader is referred to Schwartz et al. (Schwartz et al., 2009). In band contrast images shown throughout the project, poor contrast is represented by darker regions in the grayscale images. Due to the single crystalline nature of the specimen used, usually the darker zones can directly be interpreted as zones of high dislocation density. It should be pointed out, however, that all crystal defects which cause disturbances in the diffraction pattern - i.e. particularly both GND and SSD - contribute to the band contrast. Along with the GND maps calculated from equation (5.5), these maps will be used throughout the project to visualize segments of high dislocation density.

The information that can be gathered by the two methods TKD and EBSD is strongly different. Fig.5.8 displays a GND density map captured with an EBSD scan of a 3 µm thick cantilever, while Fig.5.9 displays several maps created from a TKD scan for a 1 µm thick one. An important aspect that distinguishes TKD and EBSD is the amount of data gathered both in total and with respect to the sample size. Because of the 70° sample tilt in EBSD with respect for the electron beam and the bigger step size of 50 nm the amount of data points captured per unit area of the sample is very limited considering the given cantilever thickness. This can be seen in Fig.5.8 since the cantilever is 3 µm in height but in the projection shown the data points recorded at a step size of 50 nm built only a total height of 1-1.5 µm. In TKD geometry the sample tilt with respect to the scanning electron beam is only 20° and along with the superior lateral resolution of 10 nm, not only is the entire cantilever thickness displayed in the projection (Fig.5.9), but it reveals much more details on dislocation structures while EBSD only allows suggestions and estimations of the dislocation networks. Another striking difference is the big discrepancy in terms of the total size of the scanned area: While EBSD can map orientation data from the entire cantilever, i.e. from support up to the free end, TKD is only able to capture the zone of plastic deformation (only a few µm^2 in area), which conveniently is the region of primary interest in this project. Because the entire cantilever and the corresponding total rotation are mapped, EBSD is better suited for the glide system analysis mentioned earlier than TKD which lacks data points from the free end. However, due to the better lateral resolution combined with the lower sample tilt granting a larger data set, for microstructural analysis TKD scans are used almost exclusively.

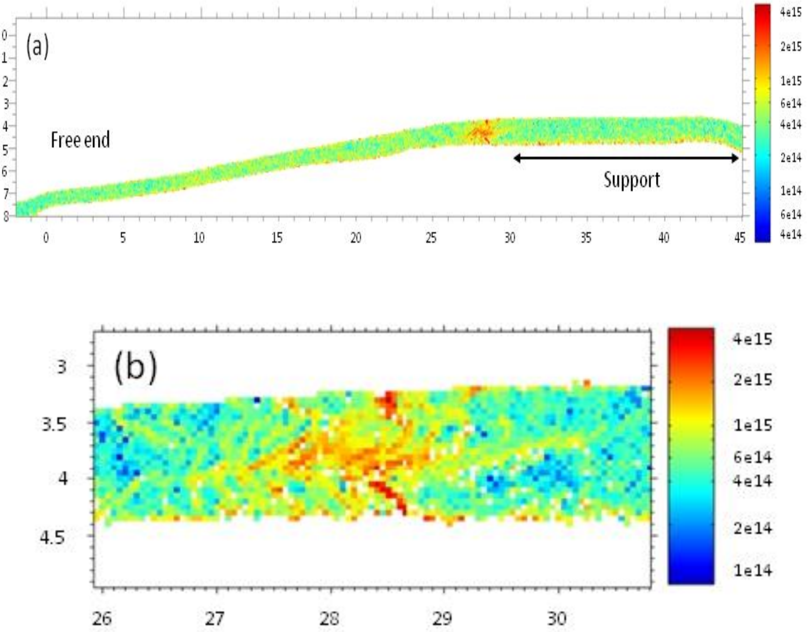

Figure 5.8: GND density [m^{-2}] calculated from an EBSD scan of a 3 µm HS cantilever of aspect ratio C with a remaining strain 0.041. Lateral dimensions in [µm]. (b) shows a zoom onto the zone of plastic deformation.

Fig.5.9 shows a variety of plots that can be generated from a TKD scan: The band contrast map displays dislocation networks, the inverse pole figure map shows the locus of crystal rotation and in turn plastic deformation while the remaining figures are GND density maps. Fig.5.9c shows a GND density map calculated using the approach expressed by equation (5.5) while the remaining ones are maps of some particular dislocation types using the minimization approach based on Nye's tensor. The dislocation types displayed here chosen to visualize all the extreme cases of the possible outcomes of the minimization procedure: Dislocations of type A3- or C3+ clearly play an dominant role in the plastic deformation and are localized primary within the zone of plastic deformation. Other dislocations, such as of type D6+ show strong concentrations only for selected spots within the zone of plastic deformation. The screw type dislocation E3+ is mainly found outside the region of interest, i.e. appears to be needed for the "background" dislocation density only. More results like these will be detailed in this section.

From Fig.5.9 it can be seen that the GND density distribution mimics the shape of the band contrast map as expected. Segments of data points which have a blurred Kikuchi pattern stand out by darker lines and also reveal higher misorientation angles and in turn higher GND densities. The absolute values for the dislocation densities in Fig.5.9 range from 10^{15} m^{-2} within the supported part of the cantilever up to 10^{16} m^{-2} within the visible dislocation bands. These values quantify the length of a dislocation line within a given volume element. To get an idea of the order of magnitude, these values are compared to the GND densities calculated by strain gradient plasticity using equation (1.3): The cantilever shown in Fig.5.9 has a deflection angle of 27.3° after deformation and the curvature is concentrated within a segment of about 1 μm in length. For Ag, which has a Burgers vector of 0.289 nm (lattice parameter introduced in chapter 3), this would result in a GND density of about $1.4 \cdot 10^{15}$ m^{-2} to accommodate the strain. The dislocation spacing would then be 26.4 nm. The average dislocation density found in the zone of plastic deformation of Fig.5.9 is on the order of $7 \cdot 10^{15}$ m^{-2} leading to a dislocation spacing of about 12 nm.

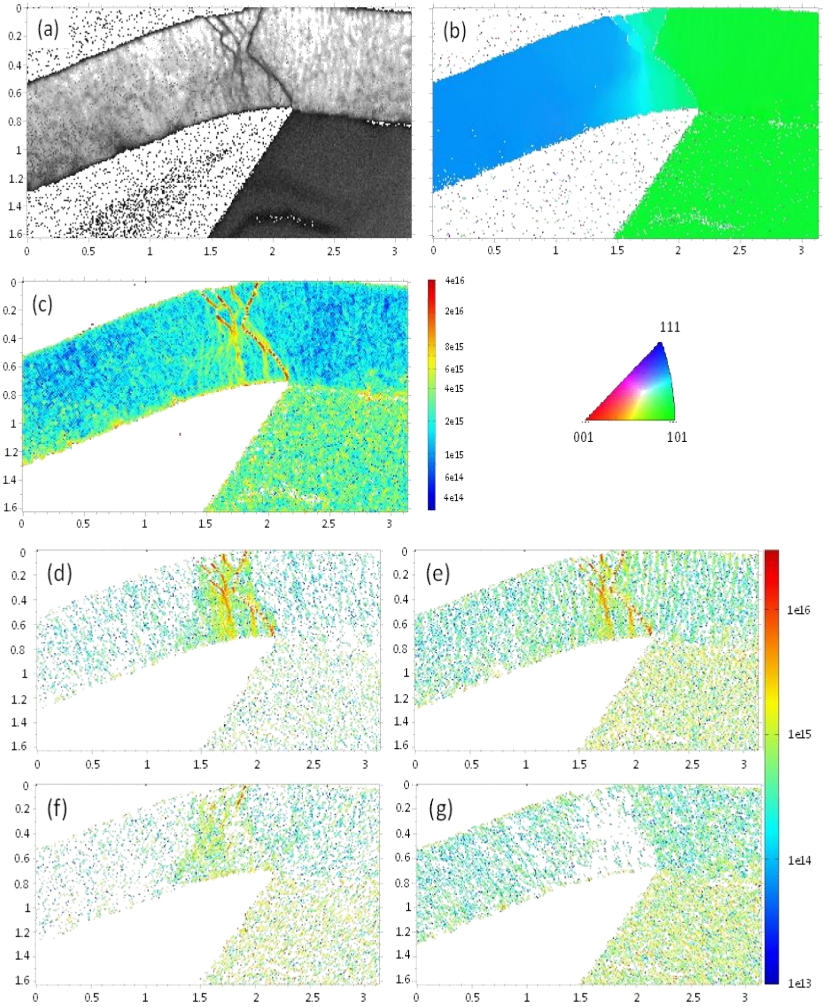

Figure 5.9: TKD scan results for a 1µm thick HS cantilever of aspect ratio B with plastic strain of 0.086. (a) Band contrast, (b) inverse pole figure along x_1, (c) GND density map [m^{-2}] according to equation (5.5), dislocation type maps for (d) A3-, (e) C3+, (f) D6+ and (g) E3+. Lateral dimensions in [µm].

At this point, the question arises how reliable the experimental values are based on the resolution of the scanning method. The limiting factor is the combination of the precision in angular resolution and the step size which determines the lateral resolution. The angular resolution for EBSD as well as TKD is usually on the order of 0.5°-1° (Zaefferer, 2011). In conjunction with the low step size chosen this poses a problem: In order to execute a lattice rotation of 0.5° within a distance of 10 nm (TKD) or 50 nm (EBSD), according to (5.5) a GND density of about $3{\cdot}10^{15}$ m^{-2} and $6{\cdot}10^{14}$ m^{-2} would be required for TKD and EBSD, respectively. Fig.5.8 shows that the non-deformed region scanned with EBSD indeed has GND densities on the order of about $6{\cdot}10^{14}$ m^{-2} while the values for the non-deformed regions in TKD also match the aforementioned expectations for the background having densities of a few 10^{15} m^{-2} due to the poor angular resolution of the method. One might argue that with a higher step size, the background noise could therefore significantly be reduced. However, the focus of this project is not to give the most accurate values for GND densities but rather to display as many microstructural features as possible, so the low step size is vital. For more information about adequate choices of step size in EBSD the reader is referred to Zaefferer (Zaefferer, 2011).

To sum up, the background noise poses a considerable problem for GND densities below the above mentioned values. Throughout the project, it will be shown that within the region of interest the pronounced dislocation networks usually have GND density values that exceed this background noise considerably. That means that the absolute values are most reliable for strong deformations and GND densities of spots outside the region of interest should be handled with care. At this point, it should be mentioned as well that high dislocation densities are accompanied with poor band contrast and typically, data points whose calculated density would exceed 10^{16} m^{-2} could not be indexed at all. Finally, for a few structures, data points from the Si support itself are recorded as well. Fig.5.9a reveals, however, that their Kikuchi pattern, has a very poor band contrast. It is precise enough the determine the crystal orientation and e.g. suffices to verify the cube-on-cube growth of the thin film, but fails to produce reliable GND values.

In the following, the results from all successful TKD scans of the project are presented (Fig.5.10-5.14). Each of these figures, which sometimes even occupy more than one page, is built up the same way: First the band contrast map and/or the GND density map calculated by equation (5.5) is shown to give an idea of the dislocation structure. Next, the evolution of GND density along a striking feature is displayed in a profile measurement. The line of the profile itself is sketched within the respective plot as well. In order to select such a line for profile measurement, some of the coordinates of the data points belonging to it (start and end points) are read and a line is traced between them. As this line should connect as many data points as possible, the slope is approximated as an integer of the step size value. To account for the possible error in slope that might be induced this way, several lines next to each other (still part of the feature) are generated and the dislocation density is averaged over all lines (typically 5 lines in total). For the same feature, the same profile measurement is executed for some dislocation types found with the approach based on Nye's tensor.

From the 5 scans presented in the following, 2 cantilevers are in DG orientation and are analyzed first. The cantilever shown in Fig.5.10 is in DG orientation, has 1 μm height, its aspect ratio is of type B and the plastic strain is 0.053. The supported region is on the right hand side of Fig.5.10a. The sample shows very few significant dislocation bands. The most striking one is a line within the upper half of the cross section with a diagonal inclination that does not travel through the entire cross-section but stops near the neutral fiber. This is also the feature chosen for the profile plots. When looking at the GND density profile it is seen that the values rapidly drop at the neutral fiber. The dislocation type that is found to have the strongest contribution is indexed as A6-, followed by a variety of systems like C1-, D4+ and E4+. The mean value of the GND density of the non-zero dislocation types are presented in Tab.5.2. The data points used for the generation of this table stem only from visible dislocation bands within the zone of plastic deformation. These are the dislocations which mainly carry plastic deformation and it was already argued that due to angular resolution, dislocations from the non-deformed region are rather classified as background noise and should be excluded from the analysis. From slip system analysis, the expected glide systems are A6 and C5 which are both seen to be represented within the data displayed in the table. As can be seen on the profile plot in Fig.5.10, the dominance of the dislocation type such as A6- becomes more significant if the overall density is higher. As the line profile enters the lower half of the cross section, were the overall dislocation density is close to the background ($3\cdot10^{15}$ m^{-2}) little to no preferred types can be detected. This cantilever most likely displays the early stage of deformation, where dislocations are generated and start traveling in the direction of the two Burgers vectors on diagonal traces. However, some of the diagonals still have not bridged the entire cross-section, yet. A feature of this scan that is common to all following scans is the dependence of band contrast from the scanning direction. Data points that are scanned earlier by the progressing electron beam are less affected by C contamination and consequently show better band contrast. The scan starts at the coordinates $x = 0, y = 0$ in Fig.5.10 and advances in vertical segments. So when comparing the band contrast and the GND density of data points on the left and right hand side, the discrepancy is strongly seen.

Fig.5.11 shows the scan of a cantilever of comparable size and orientation (DG, 1µm thickness, aspect ratio B). However, it has been strained further and the plastic strain is about 0.071. Again the supported region is on the right hand side of the map. It reveals some striking line patterns, whose orientation is strictly parallel to one of two different diagonal directions. In contrast to Fig.5.10, the lines travel through the entire cross section and diagonal lines of the opposite orientation are even intersecting each other. The points of intersection are particularly interesting, which is why one such structure is chosen for a line profile measurement. The GND density measures at least $3\cdot10^{15}$ m^{-2} for all points but one strong peak is found at a position marked as point "1". Here the overall GND density rises up to 10^{16} m^{-2} and the dislocation types A6- and D4+ become dominant. All non-zero dislocation types are again displayed in Table.5.2. When comparing both DG cantilevers, the same dislocation types are identified and even their ranking with descending absolute value matches almost perfectly. In the case of the cantilever that is strained further, the selection of dominant types becomes even more pronounced, especially in the case of A6-. Overall,

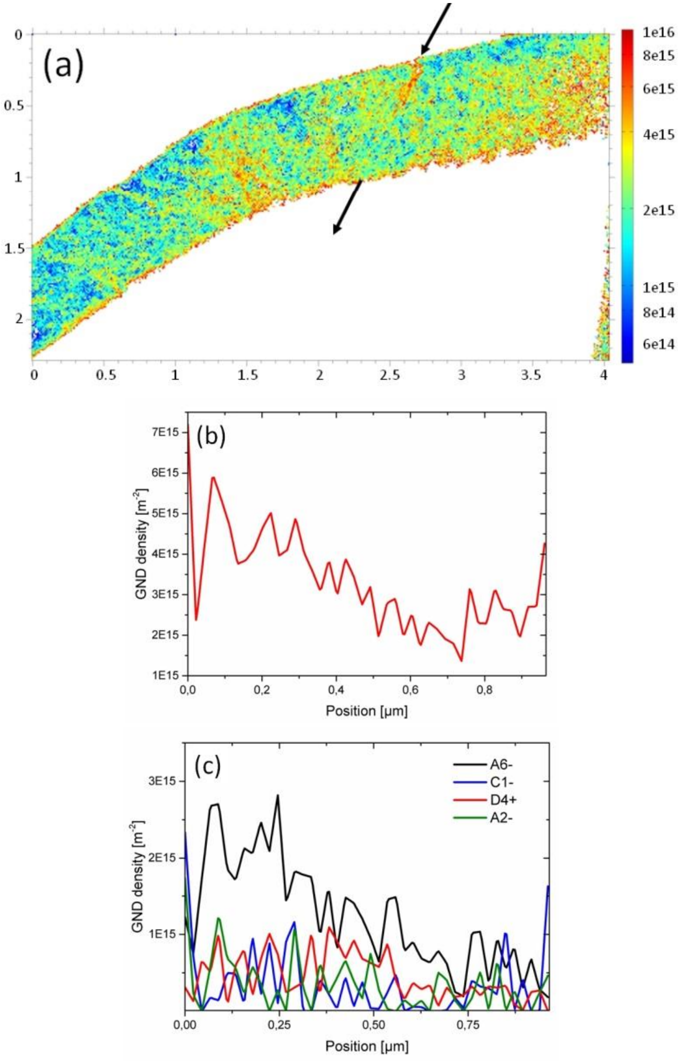

Figure 5.10: Cantilever of 1µm thickness, DG orientation, aspect ratio B, plastic strain of 0.053. (a) GND density map. Line profiles along the black arrow for (b) total GND density and (c) some dislocation types. Densities in [m^{-2}] and lateral dimensions in [µm].

amongst the possible dislocation types, all planes and directions are found, with the exception of direction type 3. The Schmid factor for such systems is also among the lowest possible with $m = 0.08$ (see chapter 2). The cantilever in Fig.5.11 reveals that with increasing strain, more diagonal dislocation bands seem to emerge, traveling through the entire cross section and interactions between them (intersections) becoming more frequent. And again the poor band contrast on the right hand side of the pictures can be explained by carbon contamination and is therefore a function of the TKD scan direction.

The following three TKD scans all show cantilevers in HS orientation. The first one shown in Fig.5.12 is probably the best scan in terms of achievable pattern quality of the entire project. In this particular case the FIB thinning procedure was very successful and the dislocation networks are very pronounced and can easily be distinguished from the non-deformed region. The cantilever in the figure has a height of 1 µm, aspect ratio B and a plastic strain of 0.086. It is seen that at these high strains, the diagonal bands do not simply cross each other but form a complex network within a small volume element were plastic deformation is localized. The network displays several interesting features. One example is that the scan gives insights into the dislocation arrangement that leads to the observed glide steps on the sample surface. When looking at the band contrast, on the upper part of the cantilever it can easily be seen that some lines are leaving the crystal and leave behind a visible step in the surface. Considering the GND arrangement, some difference is seen with respect to Fig.5.11. Here, there are no diagonals that pass through the entire cross section unimpaired. Instead, the lines seem to split into several smaller bands that are still parallel to the two diagonal directions. In some cases these smaller bands even seem to form isolated segments of very high dislocation density within the volume that reach neither the top or the bottom surface of the cantilever. An example for such a segment is the band between the points "4" and "5" in the figure. Within the visible bands the GND density is found to be particularly high with values that even exceed at some points 10^{16} m^{-2}. The two line profiles chosen show how much dislocations are concentrated within these band structures. As long as the profile follows visible dislocation bands the density is very high but drops rapidly by almost one order of magnitude in between band structures.

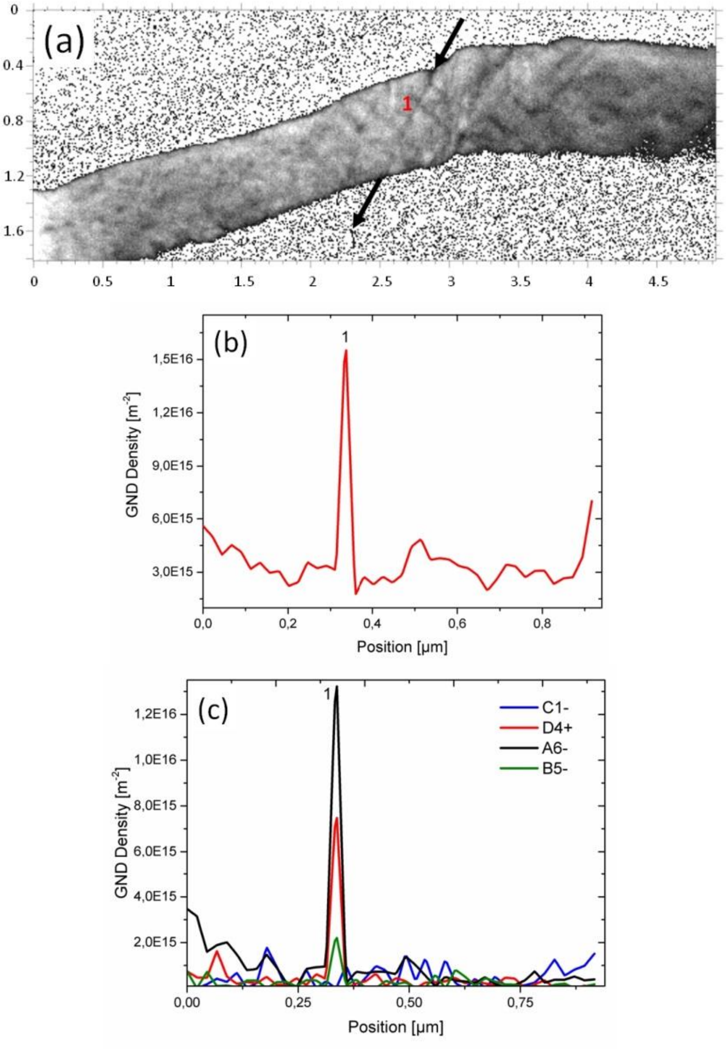

Figure 5.11: Cantilever of 1µm thickness, DG orientation and aspect ratio B, total plastic strain 0.071. (a) Band contrast map. Line profiles along the black arrows, which are sketched in (a), are shown for (b) the total GND density and (c) some selected dislocation types. The black arrows mark the line along which the profile plot is taken. Point *1* marks an intersection of bands. Densities in [m^{-2}] and lateral dimensions in [µm].

Figure	5.11	5.10
Plastic Strain	0.071	0.053
Dislocation Type	Mean GND Density [$10^{14}m^{-2}$]	
A6-	8.0	6.5
C1-	3.8	4.6
D4+	3.7	3.5
E4+	3.6	3.4
D6+	2.3	1.9
A2-	2.1	2.8
B5-	1.6	2.3
E5+	1.6	2.0
C5-	1.0	1.1
D1-	0.7	0.6
B4+	0.4	0.2
E6-	0.3	0.3
C5+	0.0	0.1

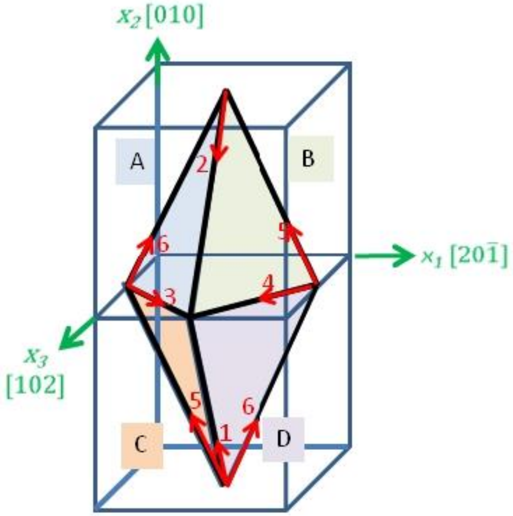

Table 5.2: Mean GND density for all dislocation types with non-zero GND density found in the visible dislocation bands belonging to the DG cantilevers displayed in Fig.5.10 and Fig5.11. The schematic below illustrates the planes and directions for DG geometry in the given coordinate system.

Moreover, there is a very clear dominance of the dislocation types A3- and C3+. This dominance is seen in the line profiles and even better displayed in Tab.5.3. The table highlights that for HS orientation these two dislocation types have the highest densities and for the particular example of the 1 μm thick cantilever strained to a value of 0.086 the GND density even exceeds 10^{15} m^{-2} within all visible bands. For HS, crystallographic direction 3 coincides with the sample direction $\boldsymbol{x_1}$. The glide systems needed for plastic deformation according to Schmid's law are B2, B5, D1 and D6. It should be pointed out, that the TKD pattern of the aforementioned cantilever (also displayed in Fig.5.12) have the highest pattern quality of the entire project. This implies that the preference of certain dislocation types might be also be a function of pattern quality and in turn sample preparation. It appears that the minimization approach tends to narrow down the selection of certain dislocation types increasing their respective GND densities, if either the accuracy of the orientation measurement is higher, and/or if the imposed strain increases. which is in agreement with the previous statements on DG cantilevers.

Another remarkable observation concerns the dislocation density in between the pronounced band structures (Fig.5.12c). While these regions are overall dyed in blue corresponding in the GND density maps, i.e. correspond to density values of about $3 \cdot 10^{15}$ m^{-2}, the core region of the cross section (where the strongly visible lines meet) has a much higher dislocation population of about $6 \cdot 10^{15}$ $m^{-2}$and is consequently displayed in green. Finally, another interesting feature that can be seen in this figure is the location of the supported region. As mentioned the TKD scan was very successful and even diffraction patterns from the Si support could be obtained, even if their band contrast is very poor (Fig.5.12a). In this example, the location of the support coincides very well with the zone of plastic deformation, i.e. with the locus of dislocation activity.

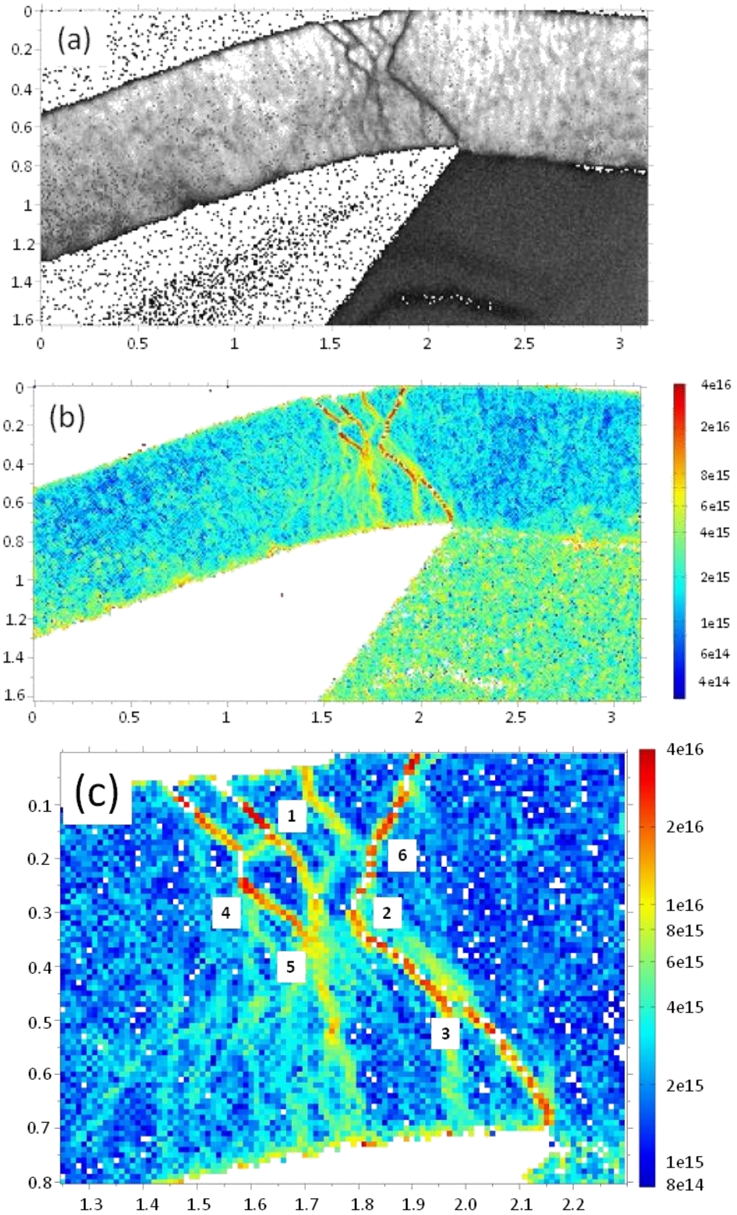
(a)
0
0.2
0.4
0.6
0.8
1
1.2
1.4
1.6
0
0.5
1
1.5
2
2.5
3
(b)
0
0.2
0.4
0.6
0.8
1
1.2
1.4
1.6
0
0.5
1
1.5
2
2.5
3
4e16
2e16
8e15
6e15
4e15
2e15
1e15
6e14
4e14
(c)
0.1
0.2
0.3
0.4
0.5
0.6
0.7
0.8
1.3
1.4
1.5
1.6
1.7
1.8
1.9
2.0
2.1
2.2
1
2
3
4
5
6
4e16
2e16
1e16
8e15
6e15
4e15
2e15
1e15
8e14

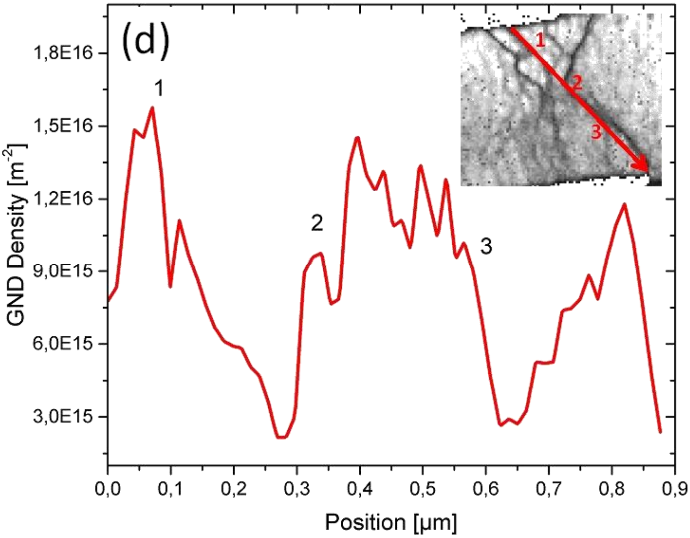
(d)
1
2
3
GND Density [m^{-2}]
1,8E16
1,5E16
1,2E16
9,0E15
6,0E15
3,0E15
0,0
0,1
0,2
0,3
0,4
0,5
0,6
0,7
0,8
0,9
Position [µm]

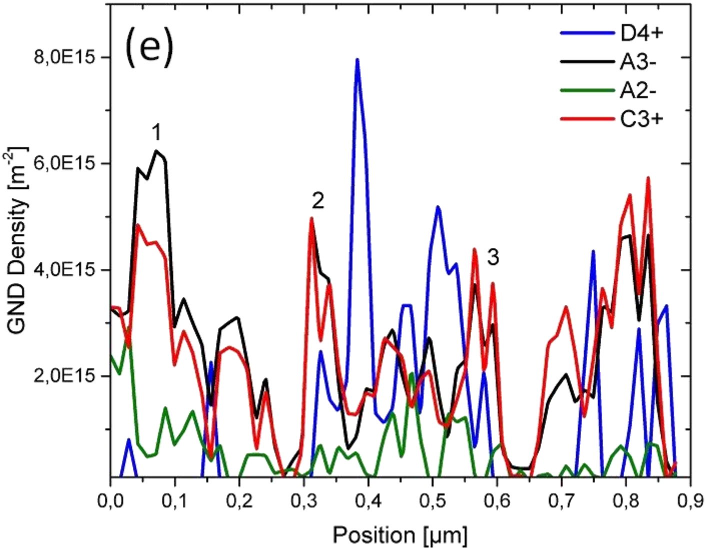
(e)
D4+
A3-
A2-
C3+
1
2
3
GND Density [m^{-2}]
8,0E15
6,0E15
4,0E15
2,0E15
0,0
0,1
0,2
0,3
0,4
0,5
0,6
0,7
0,8
0,9
Position [µm]

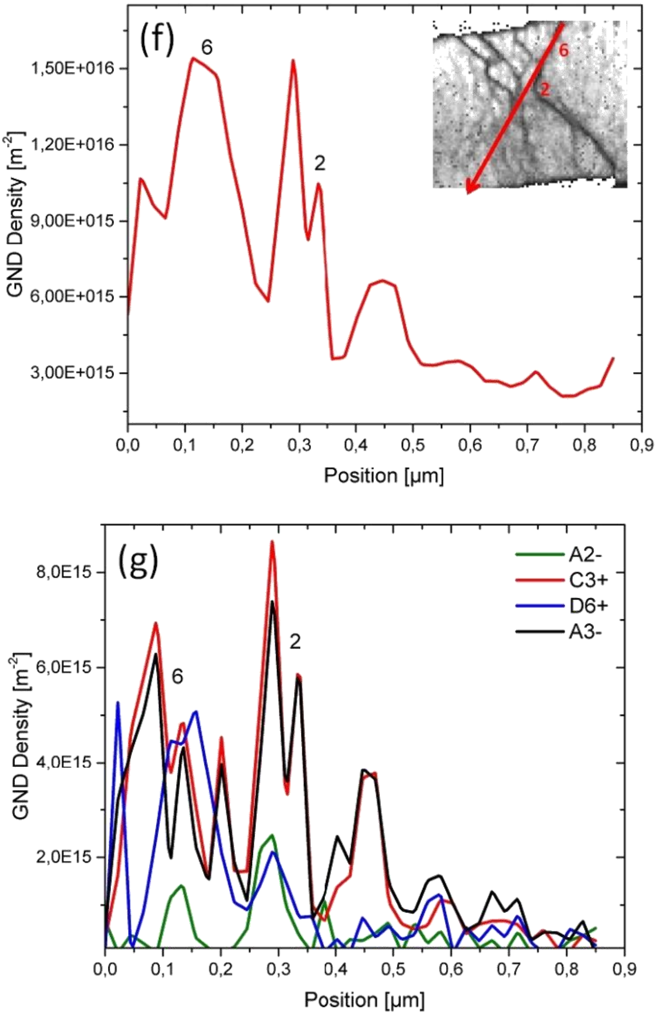

Figure 5.12: Cantilever of 1µm thickness, HS orientation and aspect ratio B, total plastic strain 0.086 (a) Band contrast, (b) GND density map with (c) zoom on the zone of plastic deformation with markings of relevant points in the profile plots. Two line profiles are taken: (d-e) and (f-g). (d) and (f) are overall GND densities while (e) and (g) show some prominent dislocation types. GND densities in [m^{-2}] and lateral dimensions in [µm].

Figure	5.12	5.14	5.13
Thickness	1μm	3μm	3μm
Plastic Strain	0.086	0.05	0.043
Dislocation types	Mean GND density [10^{14}m^{-2}]		
A3-	22.0	0.8	1.8
C3+	19.4	5.0	2.6
D1+	9.6	2.1	2.1
D6+	6.0	3.5	2.2
B2-	3.6	3.7	1.5
A2-	2.5	1.5	0.0
E3+	0.9	3.0	3.3
B5+	0.3	3.0	1.8
C5-	0.3	0.3	1.2
A2+	0.0	0.0	1.2
A3+	0.0	0.4	0.0
A6-	0.0	3.1	0.0
C1-	0.0	0.6	0.0
E1-	0.0	0.0	0.6
E2+	0.0	0.5	0.0
E5+	0.0	0.5	0.1
E4-	0.0	0.0	0.4
E1+	0.0	1.1	0.0
D4+	0.0	0.7	0.0

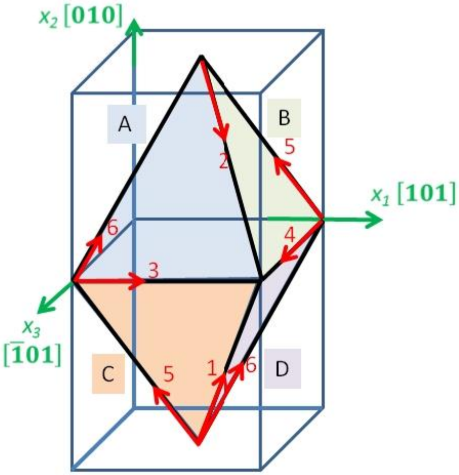

Table 5.3: Mean GND density for all dislocation types with non-zero GND density found in the visible dislocation bands belonging to the HS cantilevers displayed in Fig.5.12, Fig.5.13 and Fig5.14. The schematic below illustrates the planes and directions for HS geometry in the given coordinate system.

The remaining TKD scans show cantilevers of 3 µm thickness and in HS orientation. The first one, displayed in Fig.5.13 has been strained to 0.043 and has aspect ratio B. In contrast to the scans executed on the 1 µm thick samples, no sharp dislocation bands are seen at all. For this cantilever, GND appear to be more homogeneously distributed over a large area. The profile scan is taken along one of the few band structures that can be found after adjusting band contrast (Fig.5.13b). The dislocation density shows no significant peaks or drops and along the entire profile and equals about $3 \cdot 10^{15}$ m^{-2} which has previously been identified as the background noise of the method. On this scan again, the dependence of scanning direction - or time passed during the scan - is found to affect the pattern quality. The data points at the right hand side were scanned last and show a poorer contrast and are attributed higher dislocation densities. When examining the dislocation types found for this cantilever in Tab.5.3, they are generally the same ones as in the other HS orientated cantilevers. However, no clear dominance of a certain type is seen and the absolute density values are lower.

Finally, the cantilever shown in Fig.5.14 reveals another remarkable feature. This one is in HS orientation too, with 3 µm height, aspect ratio C and plastic strain of 0.057. The supported region is on the left hand side. Not only, does this cantilever reveal at least a few striking diagonal dislocation bands, especially within its upper half, giving rise to glide steps, it also reveals a new characteristic with has been identified as a deformation twin. The reason for this interpretation is that the feature has a particularly high GND density of over 10^{17} m^{-2} but still the Kikuchi pattern is sharp enough to be indexed accurately. The fact that its dislocation density is that high contradicts the aforementioned finding that the patterns which cause dislocation densities well above 10^{16} m^{-2} tend to be too blurry to be indexed. The conclusion from that is that the lattice rotation observed within these features is not caused by defects that affect the quality of the diffraction such as dislocations. The rotation of the lines with respect to the surrounding lattice is about 60° which is in agreement with a twin in an fcc crystal. Unambiguous verification of this interpretation is obtained when looking at the inverse pole figure maps (Fig.5.15). The twin shows a strong deviation in orientation from the surrounding lattice but no difference at all if the orientation map is calculated along x_3. As this clearly is the most prominent feature of the sample. the line profile has been drawn to include the twin. GND densities are particularly high in the region as mentioned but following the line profile further, the dislocation densities become more homogenously distributed with almost no preferred dislocation type. The dislocation types chosen by the software to realize the twin's curvature is mainly C3+. For the rest of the cantilever, dislocation types found are in agreement with the results for the other HS samples (Tab.5.3). The dislocation densities found in the twin region, are not taken into account within the table.

Concerning the selection of dislocation types from among the 36 possibilities, some interesting trends are found and discussed in this section (Tab.5.2 and Tab.5.3). First, some general observations can be made: One is that the GND density of the majority of the 36 dislocation types is set to 0 within the entire region of interest (zone of plastic deformation). Overall, only about 10 different types are found within this region. It is remarkable that for both orientations and for all thicknesses, the majority of the 36 systems are not populated at all within the region of interest. Moreover, it is found that from a pair of dislocation types that differ just in the sign of their Burgers vector, the minimization approach only chooses one of the two types for a given data point and sets the other density to zero. For example, A6- is the strongest type in DG orientations but A6+ is not being used at all. This again accounts for the consistency of the method itself, because otherwise it would lead to a circular logic: If two such types were present within the same volume element, they would cancel out and consequently the lattice would not be distorted. Another remarkable feature is the nature of dislocations chosen for the reconstruction of lattice curvature: The 36 possible dislocation types comprise 24 edge dislocations and 12 screw dislocations. Both in HS and in DG there is a variety of edge dislocations which have noticeable GND densities while there is only one screw type for each that significantly contributes to the crystal rotation. The fact that screw dislocations tend to be less used for the given bending geometry appears plausible as the crystal lattice needs to be continuously tilted and not twisted.

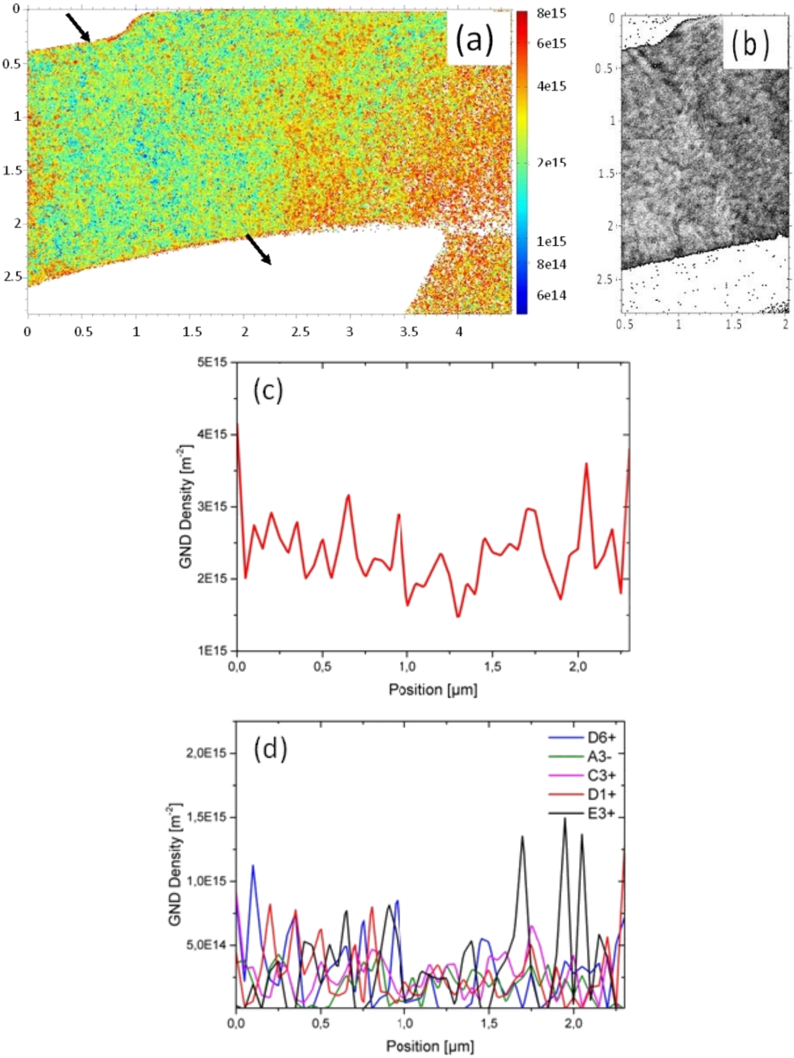

Figure 5.13: Cantilever of 3µm thickness, HS orientation and aspect ratio B, total plastic strain 0.043. (a) GND density map (b) Band contrast showing a zoom onto the only prominent band structure. (c) line profile for overall GND density and (d) for some selected dislocation types taken along the black arrows in (a). Density values in [m^{-2}] and lateral dimensions in [µm].

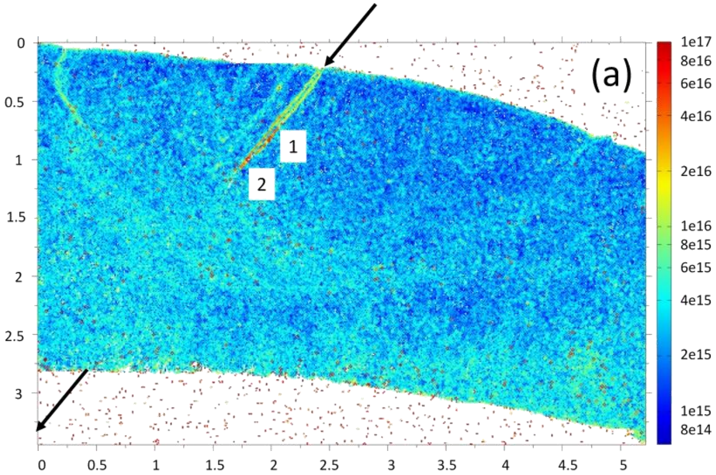
(a)
1
2
0
0.5
1
1.5
2
2.5
3
0
0.5
1
1.5
2
2.5
3
3.5
4
4.5
5
1e17
8e16
6e16
4e16
2e16
1e16
8e15
6e15
4e15
2e15
1e15
8e14

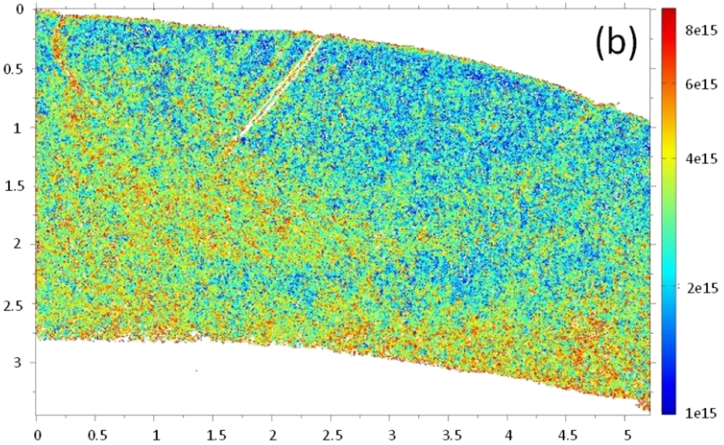
(b)
0
0.5
1
1.5
2
2.5
3
0
0.5
1
1.5
2
2.5
3
3.5
4
4.5
5
8e15
6e15
4e15
2e15
1e15

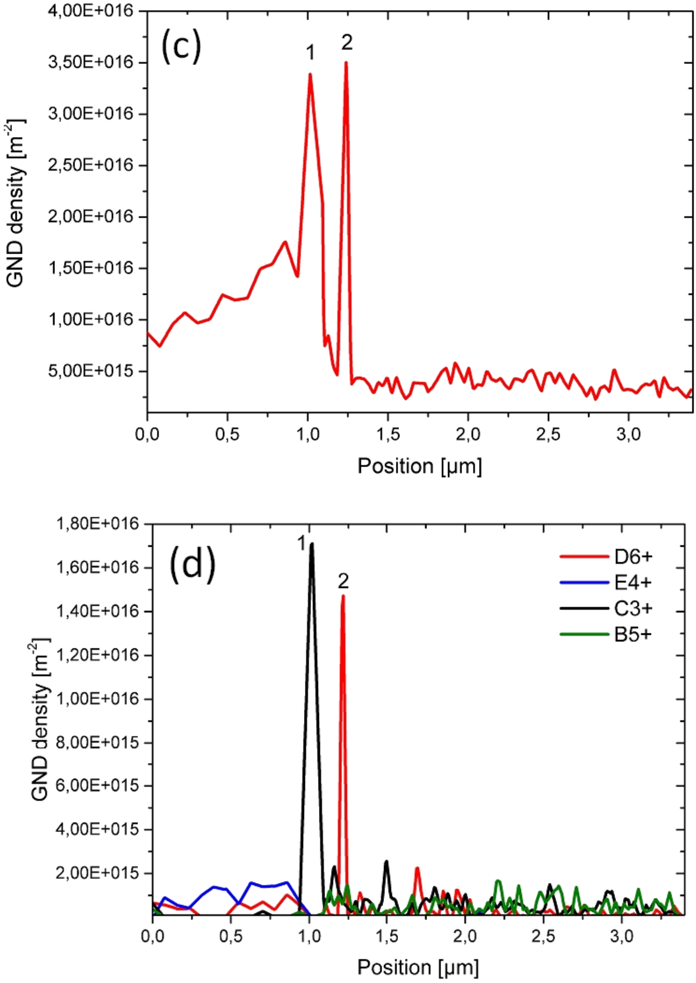

Figure 5.14: Cantilever of 3µm thickness, HS orientation and aspect ratio C, total remaining strain 0.05. (a, b) GND density maps with markings of relevant points in the profile plots. The GND density scale if different for (a) and (b). Profile plots for (c) overall GND density and (d) some selected dislocation types taken along the line marked by the black arrows in (a). Densities in [m^{-2}] and lateral dimensions in [µm].

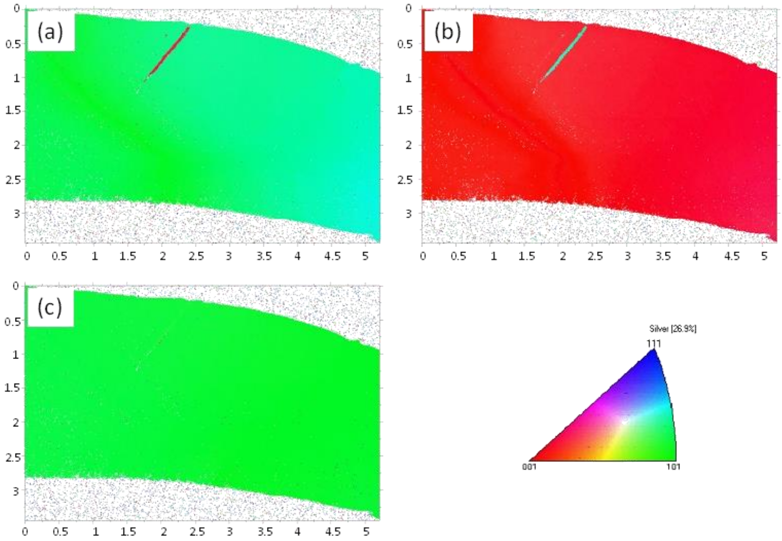

Figure 5.15: Inverse pole figure maps for the cantilever displayed in Fig.5.14 along (a) x_1, (b) x_2 and (c) x_3, respectively. Lateral dimensions in [µm].

Finally, the GND densities found are connected to the plastic strain within the sample. Again, only data points belonging to visible dislocation bands are taken for the analysis. Fig.5.16 displays the median density calculated according to (5.5) ("overall density") averaged over all bands under consideration and the sum of the GND densities of all 36 dislocation types for the same data points. The square symbols represent 1 µm thick samples while the triangles stand for the two 3 µm thick cantilevers. From Fig.5.16 it is seen that the total GND density calculated following both approaches usually does not differ very much and that the sum of all 36 dislocation types is always the smaller absolute value. More importantly, the GND density increases with increasing strain as expected.

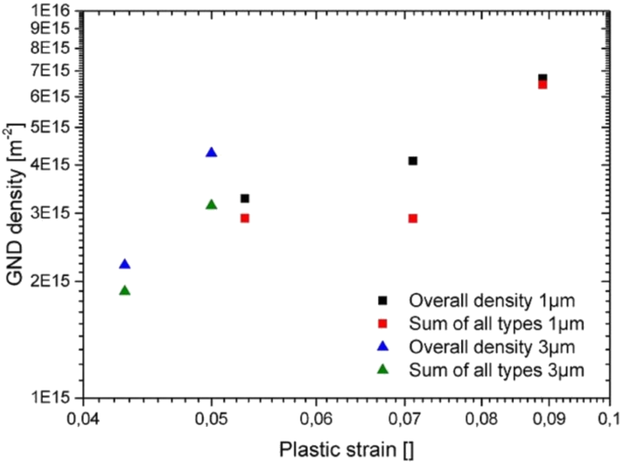

Figure 5.16: GND Densities obtained from TKD scans versus remaining plastic strain determined by optical profilometry. The density values are calculated as the medians of the averages of each visible dislocation band. Overall density refers to GND densities calculated via equation (5.5). The TKD scans of the cantilevers for each data point displayed in the figure is also shown in this chapter (Fig5.10-.514).

The generation of deformation twins is a common deformation mechanism in fcc samples of sufficiently low stacking fault energy, which is also the case for Ag. Forming a twin can be achieved when instead of full dislocations only partial dislocations on parallel glide planes are activated causing a stable stacking fault within the crystal lattice. If Schmid's law is used on partial dislocations instead of full dislocations (Tab.5.4) it is seen that for HS orientation two partials, namely $(111)[\bar{1}2\bar{1}]$ and $(\bar{1}1\bar{1})[121]$ (Hirth-Lothe notation) have a very high Schmid factor of -0.47 and are thus likely to be activated. Using Thompson's tetrahedron (Fig.5.17), the relation of these partials to potential full dislocations can be seen. The 4 full dislocation on which glide takes place in HS can be formed by recombination of the following partials:

$$C\delta + \delta A \ \rightarrow (111)[0\bar{1}1] \tag{5.12a}$$

$$A\delta + \delta B \ \rightarrow (111)[\bar{1}10] \tag{5.12b}$$

$$D\alpha + \alpha C \ \rightarrow (\bar{1}1\bar{1})[110] \tag{5.12c}$$

$$D\alpha + \alpha B \ \rightarrow (\bar{1}1\bar{1})[011] \tag{5.12d}$$

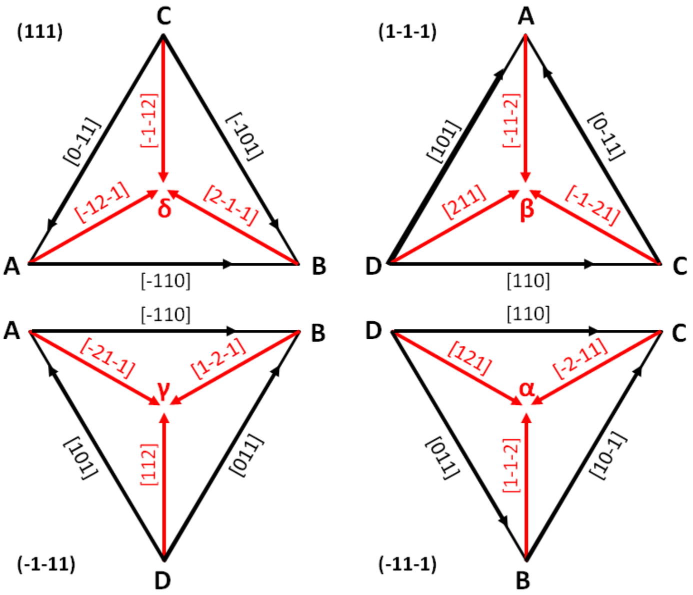
(111)
C
[0-11]
[-1-12]
[-101]
[-12-1]
δ
[2-1-1]
A
B
[-110]
(1-1-1)
A
[101]
[-11-2]
[0-11]
[211]
β
[-1-21]
D
C
[110]
[-110]
A
B
[-21-1]
[1-2-1]
γ
[101]
[112]
[011]
(-1-11)
D
[110]
D
C
[121]
[-2-11]
α
[011]
[1-1-2]
[10-1]
(-11-1)
B

Figure 5.17: Inverse pole figure map of a cantilever of 3µm height, in HS orientation, aspect ratio B and a remaining strain of 0.05. Twin structures are marked by red arrows.

Tab5.4 shows that for the individual partials, the Schmid factor *m* differs significantly for the leading and the trailing partial. In the cases where a twin is formed by a leading partial over either δA or αD, then the trailing partial might not be activated at all, causing twinning. In this calculation, the sign convention is relevant and in the given case, the sign of their Schmid factors implies that the two respective twins can only be formed if the sample is submitted to tension which limits the twin's existence to the upper half of the cross section. This perfectly matches the experimental observations.

HS	Slip plane	Slip direction	Schmid factor m	Notation
Full dislo-cations	(111)	$[\bar{1}10]$	0.41	B5
	(111)	$[0\bar{1}1]$	0.41	B2
	$(\bar{1}1\bar{1})$	$[110]$	0.41	D6
	$(\bar{1}1\bar{1})$	$[011]$	0.41	D1
Partial dislocations	(111)	$[\bar{1}2\bar{1}]$	-0.47	Aδ
	(111)	$[2\bar{1}\bar{1}]$	0.24	Bδ
	(111)	$[\bar{1}\bar{1}2]$	0.24	Cδ
	$(\bar{1}1\bar{1})$	$[121]$	-0.47	Dα
	$(\bar{1}1\bar{1})$	$[\bar{2}\bar{1}1]$	0.24	Cα
	$(\bar{1}1\bar{1})$	$[1\bar{1}\bar{2}]$	0.24	Bα

DG	Slip plane	Slip direction	Schmid factor m	Notation
Full dislo-cations	$(1\bar{1}\bar{1})$	$[110]$	0.49	A6
	$(\bar{1}\bar{1}1)$	$[\bar{1}10]$	0.49	C5
Partial dislocations	$(1\bar{1}\bar{1})$	$[211]$	0.42	Dβ
	$(1\bar{1}\bar{1})$	$[\bar{1}\bar{2}1]$	-0.42	Cβ
	$(\bar{1}\bar{1}1)$	$[1\bar{2}\bar{1}]$	-0.42	Bγ
	$(\bar{1}\bar{1}1)$	$[\bar{2}1\bar{1}]$	0.42	Aγ

Table 5.4: Schmid law applied to partials for HS and DG orientation. Schmid-Boas notation is used for full dislocations while for partials Thompson's tetrahedron serves as a reference.

Fig.5.18 shows another TKD shows another TKD scan executed on a 3 µm thick HS cantilever with a plastic strain of 0.05. The scan was not mentioned previously as C contamination prevented a significant part of the structure from being evaluated. Nevertheless, within the upper half of the sample, several twins are detected with the same orientation as the one in Fig.5.14 that appear to be stopping before reaching the neutral fiber. Therefore, it can be said that twinning is a possible deformation mechanism for HS orientation but is only observed in the 3 µm thick samples. Tab.5.4 also shows the analogous calculation for the partials in DG orientation. Unfortunately, there no scans for DG samples of 3 µm thickness have been executed. Nevertheless, it can be seen that in this orientations, twinning should not be taking place, as leading and trailing partial have the same probability of being activated.

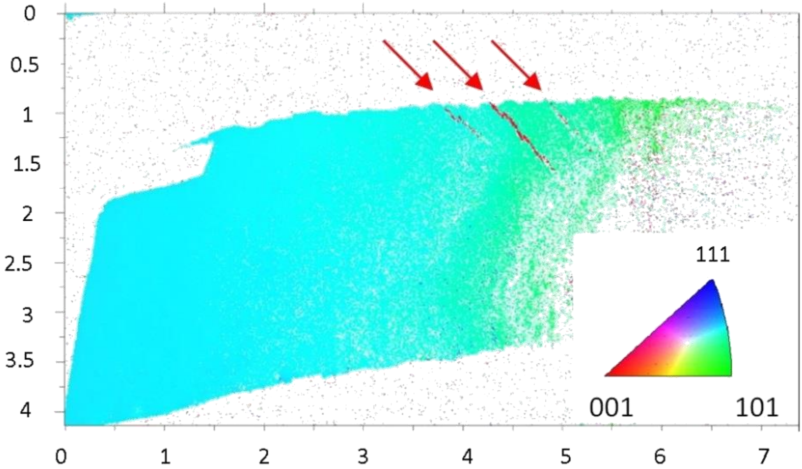

Figure 5.18: Inverse pole figure map of a cantilever of 3µm height, in HS orientation, aspect ratio B and a remaining strain of 0.05. Twin structures are marked by red arrows.

5.3.4 Cross court

The results from the previous section yield some interesting information which will be further discussed in chapter 6. However, as mentioned the poor angular resolution of the measurement techniques TKD and EBSD is a critical factor which considerably limits the possibility of interpreting the results correctly. Due to this resolution limit, retrieving information from any kind of dislocation structure which causes a local lattice rotation of less than 0.5° is unreliable. Therefore it would be highly beneficial to improve the angular resolution. This may be done using the Cross Court software developed by Wilkinson (Wilkinson, 2001). It was shown that with Cross Court, angular resolutions down to 0.003° are feasible which enables detecting GND densities in the range of 10^{13} - 10^{14} m^{-2} with conventional EBSD (Wilkinson et al., 2010). For example, in Littlewood et al. (Littlewood et al., 2011) Cross Court is used for EBSD scans and coupled with the minimization procedure based on Nye's tensor as described in this chapter. In contrast to the methods used in this project, Cross Court does not index the pattern after a Hough transformation but instead quantifies the pattern shift via digital image correlation. Therefore, it requires the pattern recorded to be of very high quality. Littlewood et al. (Littlewood et al., 2011) report that the best results are obtained when no binning is applied and the exposure time per pixel is as long as possible.

However, as mentioned before, TKDs scans in this project are performed rather quickly and the images are binned to improve the scan speed even further. Especially the latter has a strongly negative influence for digital image correlation because the amount of pixels available is reduced. Therefore, digital image correlation is not likely to have a great success in this project. Nevertheless, the method was applied and the results are shown in Fig.5.19. The cantilever displayed is the same as in Fig.5.11. The GND density maps generated using Cross Court look entirely different than the ones based on the conventional method. Instead of dislocation bands, the Cross Court method only reveals a zone of high dislocation density with no apparent pattern. The non-deformed regions, for example at the left hand side also differ strongly in GND density. To explain these phenomena, the error made by digital image correlation is plotted in the figure as well revealing a strong error (bright color) in dislocation rich regions and a very low error at the left hand side of the figure. The scan direction was along $\boldsymbol{x_1}$ in vertical lines from the upper left to the lower right, so the pattern quality degrades towards the right which can be explained by C contamination.

When looking only at the pattern on the left hand side, Cross Court appears to work better than the conventional method. In agreement with the angular resolution limits, the digital image correlation gives access to densities even below 10^{14} m^{-2} which would be plausible in this part of the sample. It can be seen that a pattern of high quality being recorded with this method of superior angular resolution then is attributed a dislocation density down to $6 \cdot 10^{13}$ m^{-2} which is considerably smaller than the GND densities found with conventional analysis. However in middle of the scan, which is the zone of plastic deformation and the region of highest interest, the error in orientation determination using Cross Court becomes significant. In fact while the conventional method becomes unreliable outside of this region, Cross Courts does so within and no dislocation networks can be visualized. Cross Court is therefore not useful for the project presented here. To make it work, the patterns would have to be of significantly better image quality. The sample is already single crystalline and therefore has ideal diffraction conditions. It may be possible to improve the quality slightly by finding better scanning parameters but it can be argued that this would not be enough to obtain patterns of high enough quality for the method to be applicable.

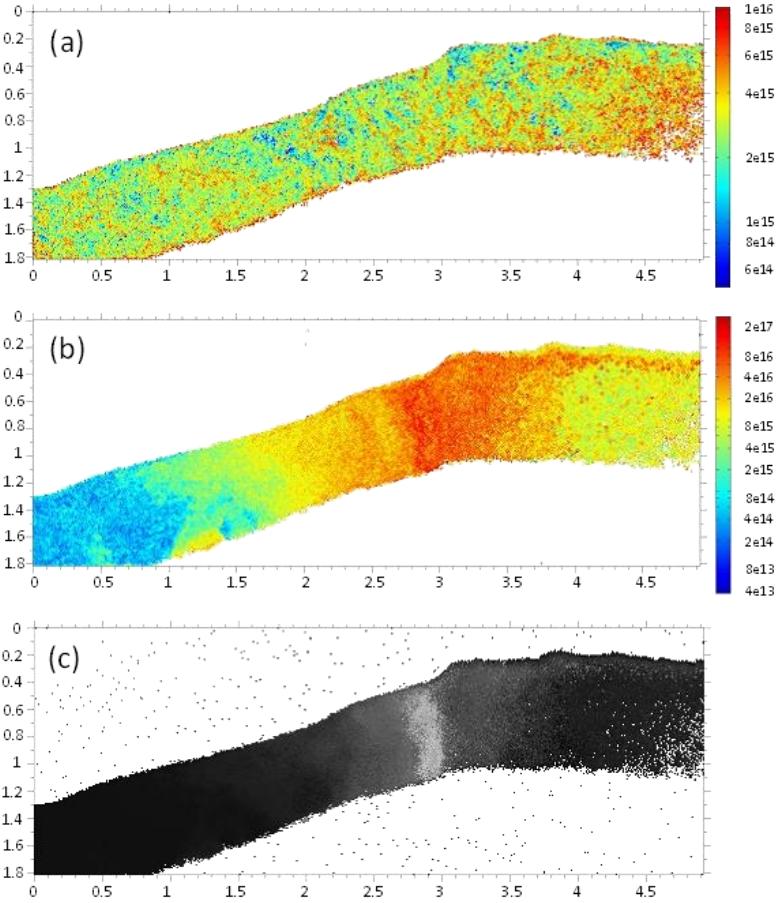

Figure 5.19: GND density maps calculated using equation (5.5) following (a) the conventional data evaluation and (b)using cross-court. (c) displays the error in digital image correlation showing that the values of (b) are most critical when the dislocation density is high. Dislocation density in [m^{-2}] and lateral dimensions.

6 Summary and Discussion

The main goal of the project is to gain deeper insights into the deformation behavior and dislocation structures at the micron scale. Both the results from the mechanical tests (chapter 4), the observed microstructural changes after plastic deformation (chapter 5) are discussed in this chapter. Moreover, 3D discrete dislocation dynamics simulations have been executed by Stricker and Weygand as a cooperative project within the DFG research group FOR1650, whose results will be presented in this section as well. For details on the framework used for the simulations, the reader is referred to the appendix. In contrast to TKD, which displays the relaxed state of the samples, DDD provides information about the dislocation interaction during loading, thus delivering essential information for a concise interpretation of the deformation mechanism. It should be pointed out, that the notation of glide systems used in DDD differs from the one introduced for the cantilevers experiments and moreover the simulated structures are smaller and have different aspect ratios, in order to save computation time. While the thickness is the same as in experiments, lateral dimension are about 10 times smaller. Therefore, linking the results from simulations to experimental findings is only possible on a qualitative scale and a comparison of mechanical properties in terms of absolute values is not meaningful. This chapter focuses on summarizing all results and on explaining the deductions that can be made from the combination of these methods about the deformation behavior.

6.1 Evaluation of specific dislocation types

The first statement that can be made is that the general deformation behavior of the single crystalline cantilevers is in agreement with predictions made by Schmid’s law. Pole figure analysis revealed that the dominant deformation mechanism is glide along the principal slip systems. Using the Schmid-Boas notation introduced in chapter 2, the principal systems are B2, B5, D1 and D6 for HS and A6 and C5 for DG. A schematic of the corresponding planes and directions is given in Fig.6.1. Experimental pole figure analysis fails to provide detailed information on secondary glide systems as their contribution to the overall deformation process is too weak with respect to the resolution of the scanning method, even for strong deformations. The agreement with Schmid's law is further supported by the spatial dislocation arrangement within the cross sections: TKD scans reveal dislocation networks within the cross section (x_1-x_2-plane), which have the form of diagonal bands while on the top surface (x_1-x_3-plane) the glide steps detected run strictly parallel to the x_2 axis for HS and with an inclination of about 18.4° for DG. Both observations are in agreement with the position of the glide plane and the direction of their Burgers vectors expected from analytical calculations. The described glide mechanism along two effective Burgers vectors are found to hold true even for very large deflections (deflection angle of 25° for DG and 35° for HS). In turn the plane bending assumption as well as the plane strain approximation can be considered to be justified.

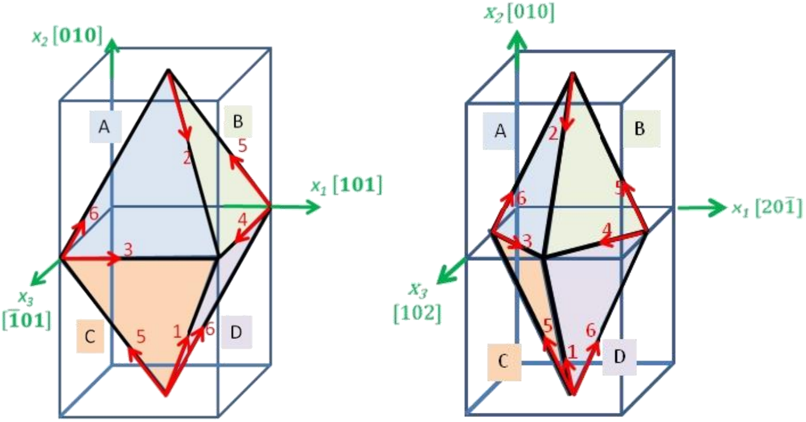

Figure 6.1: Schematic of the location of the dislocation types in HS and DG. During bending the rotation axis is around x_1.

DDD simulations support this finding for the early stages of deformation. This is shown in Fig.6.2, which displays the evolution of the dislocation densities for all 12 slip systems. Note that the indexing of the respective slip systems is different (see also appendix), but the conclusions that can be made from DDD simulations are crystallorgaphically equivalent. It is seen that for HS orientation (Fig.6.2a) the initial dislocation density of most of the systems barely changes with increasing strain. However, four systems, namely A2, A3, D1 and D4 become higher populated and after a normalized displacement of about 0.02 can be clearly distinguished from the remaining systems. Obviously, these four activated slip systems carry plastic deformation. Moreover, it is clearly seen that the systems are activated to equal amounts. Likewise for DG orientation, two principal glide systems, namely A2 and D1 are enabling plastic deformation (Fig.6.2b). In the particular case of DG orientation, DDD simulations show that glide on secondary slip systems is taking place as well. At a normalized strain of about 0.08 the figure shows that some secondary glide systems are being activated as well and their dislocation density is slightly increasing. The most striking ones are A3, D4, C5 and B5, which are among the six expected secondary glide systems predicted by Schmid's law. The remaining two, A6 and D6, can barely be distinguished from the background density.

In both orientations only a small amount of dislocation sources is activated during loading. The initial Frank-Read sources are distributed equally over all slip plane normals and only the sources belonging to this limited set of slip systems are being activated. This is in agreement with the increase in dislocation density displayed in Fig.6.2 which is comparatively small. Therefore, it is justified to assume that the individual sources do not impair each other.

The dominance of these principal slip systems is also recognized by the minimization approach based on Nye’s tensor. When looking at the 36 individual dislocation types, the minimization selects about 10 different ones and attributes them a non-zero dislocation density (Tab.5.2 and Tab.5.3). This choice is consistent for all cantilevers of one particular orientation.

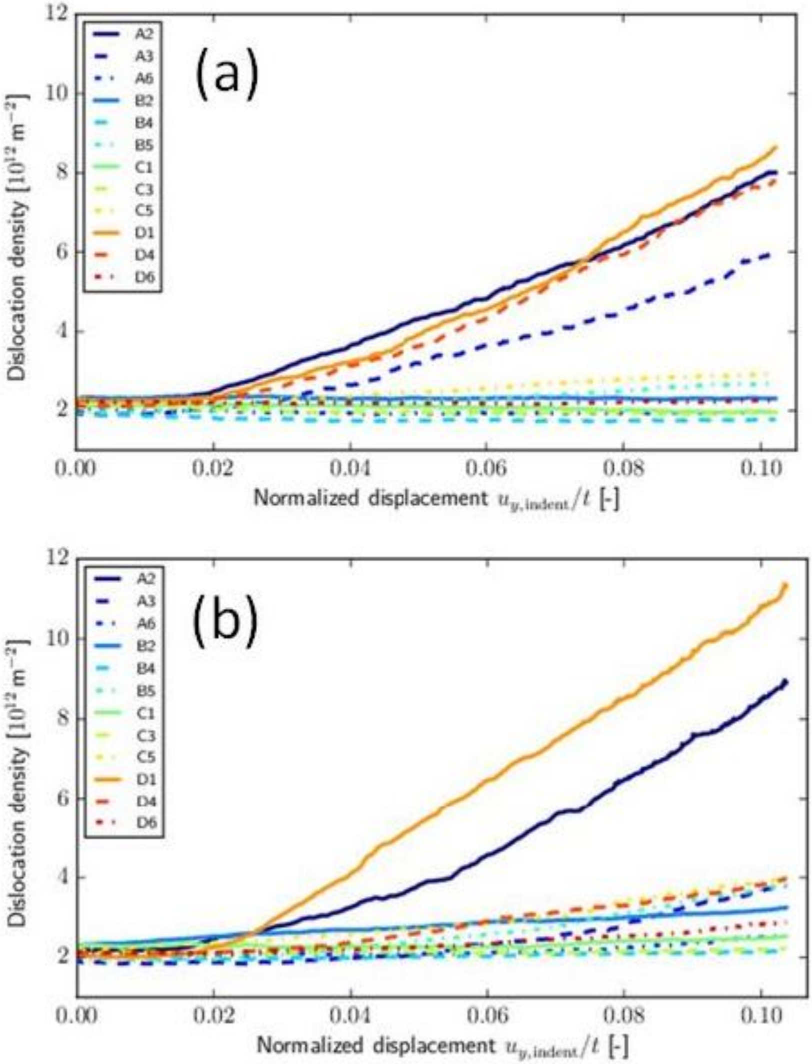

Figure 6.2: Dislocation density evolution with increasing strain found with DDD for the individual glide systems. The curves are averaged over the results from 10 realizations. Note that their indices differ from experiments due to different axis convention.

Among the chosen dislocation types, some belong to the aforementioned glide systems and are among the most strongly populated ones. These are B2, B5+, D1+ and D6+ for HS and A6- and C5- for DG, respectively. Apart from these systems which are needed to sustain the glide process mentioned above, some additional tendencies are found in the choice of dislocation types: (i) The minimization procedure utilizes each possible crystallographic direction (1, 2, 3, 4, 5, 6) and plane (A, B, C, D) at least once with exception of one particular direction for HS and DG, (ii) does not chose two dislocation types that only differ in their sign for the same data point and (iii) tends to favor edge dislocations significantly over screw dislocations. The fact that practically each crystallographic plane and (almost) each direction are always found to be represented by at least one dislocation type may account for a more or less random initial dislocation distribution in the non-deformed state that is preserved to some extent even after deformation. The lack of dislocation types along Burgers vector 4 in HS and 3 in DG can be understood from the arrangement shown in Fig.6.1. These two directions are not needed to accommodate the bending around the rotation axis $\boldsymbol{x_3}$ and their respective Schmid factors are 0 or close to 0, as well. The unambiguous sign convention mentioned earlier accounts for the consistency of the method, while the preference of edge dislocations over screw dislocations is in agreement with the overall bending geometry.

The further the strain is increased, the more the amount of different dislocation types chosen by the minimization approach narrows down. The reaming ones stand out with particularly high GND densities. However, not all dislocation types of this selection are needed to sustain the glide process, or could be explained solely as a remnant of the initial density before deformation. This is best seen on the example in Fig.5.12, which shows a cantilever in HS orientation: Here the systems A3- and C3+ reach values even beyond 10^{15}m^{-2} (Tab.5.3). However, following the argumentation from the glide system analysis, for HS, neither the planes A or C, nor the direction 3 are needed for the deformation process. Likewise, the fact that in DG dislocations of the type A6- have significantly higher densities than C5+ is an issue as well, since the glide system analysis revealed that both systems should be activated to equal amounts. The choice of these dislocation types may be understood considering that TKD captures the cantilever in its relaxed state under a remnant plastic strain. GND are not mobile by definition, so the activation of a certain glide system implies the generation of more dislocations of the respective type, and once the load is released most of these dislocations may leave the crystal again. Nevertheless, detecting some dislocations belonging to these principal glide systems in the relaxed state is in agreement with this statement. However, an aspect that cannot be explained this way is how the overall remnant sample curvature can be sustained. Looking at the general bending geometry (Fig.6.1), it becomes evident that upholding the curvature after bending is best achieved by dislocations whose Burgers circuit leads to a closure failure along the $\boldsymbol{x_1}$ direction (i.e. Burgers vector along $\boldsymbol{x_1}$). In HS, $\boldsymbol{x_1}$ equals the 3 direction, which makes the strong representation of A3- and C3+ reasonable, especially for larger deflections. The same reasoning can also be used for the observation in the DG case: In this geometry, $\boldsymbol{x_1}$ does not coincide with one single Burgers vector but has to be expressed as a linear combination of several vectors. For example, the resulting Burgers vector along $\boldsymbol{x_1}$, i.e. $[20\bar{1}]$ might be explained by a combination of the three linearly independent Burgers vectors $[110]$, $[011]$ and $[0\bar{1}1]$. These Burgers vectors correspond to the dislocation types A6-, C1- and A2-, respectively, which are all found to be strongly represented in experiments. The decomposition of the vector along $\boldsymbol{x_1}$ would then be of the form

$$\begin{pmatrix} 2 \\ 0 \\ -1 \end{pmatrix} \rightarrow 4\begin{pmatrix} 1 \\ 1 \\ 0 \end{pmatrix} - 3\begin{pmatrix} 0 \\ 1 \\ 1 \end{pmatrix} + 1\begin{pmatrix} 0 \\ -1 \\ 1 \end{pmatrix} \tag{6.1}$$

This example illustrates that dislocation types such as A6-, C1- and A2- could combine to uphold the sample curvature. In the described scenario, type A6- would have to be present more often than the other two and C1- should have higher densities as A2-. Both statements quantitatively match experimental results (Tab.5.3). Therefore, the density of the dislocation type A6- might be that high because it can fulfill two roles at once, which are carrying glide during deformation and contributing to uphold the sample curvature after deformation.

6.2 Evolution of dislocation networks

All TKD scans shown throughout this project reveal a similar arrangement of dislocations which has the form of parallel bands that move on diagonal traces through the cross section. Within the cross section only two possible orientations for these diagonals are found. If several dislocation band structures are detected they are always found to run parallel to one of these two directions.

This kind of spatial dislocation constellation is also seen in DDD simulations. 3D DDD offers the possibility of obtaining a clear view of the structures developing upon plastic deformation. Fig.6.3 shows some 3D images of the dislocation networks. What can be seen from the figure is that dislocations are strongly concentrated within a small volume at the left hand side of the cantilever corresponding to the support. To illustrate this arrangement even more detailed, Fig.6.4 displays lattice rotations within a cross section taken along the $\boldsymbol{x_1}$-$\boldsymbol{x_2}$-plane and $\boldsymbol{x_1}$-$\boldsymbol{x_3}$-plane of the cantilevers for both orientations. The cross section along $\boldsymbol{x_1}$-$\boldsymbol{x_3}$ may be compared to the glide steps seen experimentally by SEM. If the crystal rotations are followed it is also seen that an arrangement strictly parallel to the support is seen for HS while line structures with a tilt of about 20° form in DG. The cross sections along $\boldsymbol{x_1}$-$\boldsymbol{x_2}$ on the lower side of the figures may be compared to the TKD scans shown in chapter 5. Even if the strain imposed is very small in comparison to the experiments, in the region close to the support, clearly some diagonal bands of dislocations are seen. For both HS and DG, there are only two possible orientations found for the diagonals. In Fig.6.4b the bands do not cross the entire cross section. Rather, for the most striking ones, it is observed that they are terminating in the region close to the neutral fiber of the cantilever.

In contrast, Fig.6.4a which shows the simulation for the DG orientation, one single band structure can be seen on the bottom surface of the $\boldsymbol{x_1}$-$\boldsymbol{x_2}$ cross section that passes the neutral fiber. It still causes lattice rotations of about ω_{12} = 0.01 rad at a position $x_2 \approx 0.55$ µm, i.e. slightly beyond the neutral fiber. In additional experiments which are not published, yet, this behavior is found to be consistent for the given set of parameters. Observing the behavior of dislocations during loading, Stricker et al. (Stricker et al., 2017) detected that dislocations emerge from sources within the outermost fiber and travel towards the neutral fiber where they are found to pile-up. As the Frank-Read sources keep producing dislocations pushing them towards the neutral fiber, some dislocations from the pile-up are found to pass it. However, their motion stops entirely before reaching the surface of the cantilever. Once the load is released, these dislocations exit the volume over the nearest surface (i.e. over the opposite surface from where they were generated). In contrast to e.g. grain boundaries the dislocation spacing within the pile-up is found to be constant. If the loading is simulated again starting from the relaxed structure, the process is found to perfectly reproduce itself.

Due to the chosen crystallographic orientation of the cantilevers, a plane strain approximation can be made for the bending process and it can be concluded that the diagonal pattern detected in the cross sections during experiments and simulations is representative for the entire cantilever volume. In HS, the entire volume can be assumed to consist of a set of parallel slices in the $\boldsymbol{x_1}$-$\boldsymbol{x_2}$-plane which all show the same dislocation arrangement as in the TKD scan. For DG, the overall arrangement within each $\boldsymbol{x_1}$-$\boldsymbol{x_2}$ slice should be comparable but does not perfectly coincide with the other ones. Instead, due to the 18.4° tilt angle between HS and DG, the entire pattern should match in appearance but will be slightly displaced in lateral direction when the cross section was to be taken at another position.

To illustrate the conclusions made about the formation of dislocation networks, Fig.6.5 shows a schematic of the assumed mechanism. First, dislocations of the types required to allow plastic flow on the principal glide systems start to nucleate close to the top and bottom surface of the cantilever. One of these sources is sketched in Fig.6.5a. At these regions the shear stresses are maximum according to the flexure formula. The Burgers vectors $\boldsymbol{b_1}$ and $\boldsymbol{b_2}$ are oriented along the diagonal traces. The generated dislocations then move towards the surface and the neutral fiber of the cantilever. In the early stage of deformation, these dislocation bands have not traveled through the entire cross section, yet, but terminate in proximity of the neutral fiber. Once the load is released, these dislocations may leave the volume again, while a set of

GND with Burgers vector ***b*** oriented along the direction of the normal stress caused by bending remains to sustain the plastic curvature. This particular situation is seen in both the TKD scan of the 1 µm thick DG cantilever with a plastic strain of 0.053 (Fig.5.10) and in DDD simulations (Fig.6.4). As a simple recombination of all dislocations involved in the glide process described in section 6.1 would only result in a net Burgers vector along $\boldsymbol{x_2}$, it appears more likely that the aforementioned GND upholding the curvature in the relaxed state, are created via a rotation process.

If the imposed strain is pushed further, experiments show that dislocation structures are found to evolve, so in the relaxed state fully developed bands are seen connecting both top and bottom surface (Fig.6.5d). The mechanisms involved can be explained following the argumentation of Motz et al. (Motz et al., 2005). They stated that the more dislocations approach the neutral fiber, the more the resolved shear stress decreases, slowing the dislocations down. Consequently, dislocations will form a soft pile-up as the strain increases. The fact that no GND pile-ups are seen in the line profiles shown in chapter 5 may also be understood because TKD was performed on the unloaded state. Once the loading is terminated, there is no external force to counter the backstress of the soft pile-up, so dislocations will spread over the diagonal bands attempting to leave the crystal. This reasoning was already made by Demir et al. (Demir & Raabe, 2010) in order to explain a strong Bauschinger effect in their bending experiments. Since in the project at hand, the microstructural analysis was not carried out in-situ, it cannot be said whether such a soft pile-up effectively formed. The TKD scans only reveal the diagonal traces with Burgers vectors along $\boldsymbol{x_1}$ and no significant peaks or drops of dislocation density within. Therefore, it might be just as plausible to assume that the GND population within the bands developed in a more homogenous way until the density becomes too high for further source activation, i.e. a soft pile-up of dislocations did not necessarily establish. As long as the microstructure is analyzed ex-situ, this homogeneous model would result in an identical dislocation network compared to the one deducted from pile-up theory.

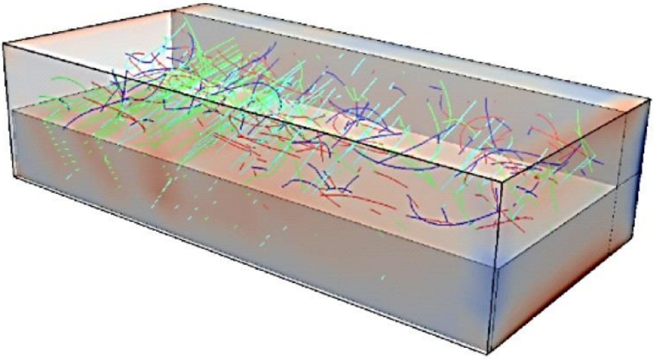

a) Dual glide

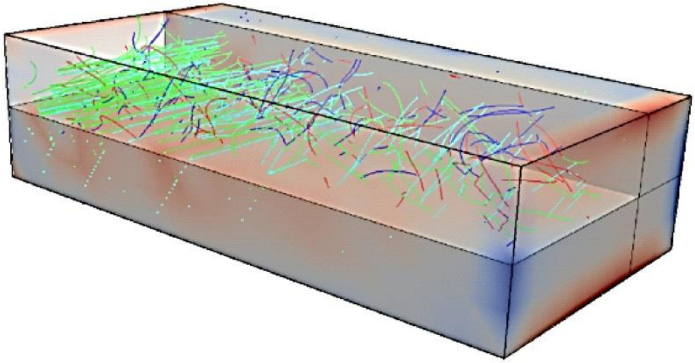

b) High symmetry

Figure 6.3: A cut through one (a) DG and (b) one HS orientation simulation. Dislocations are colored according to their glide plane normal. The sample volume is colored according to the shear stress in bending direction.

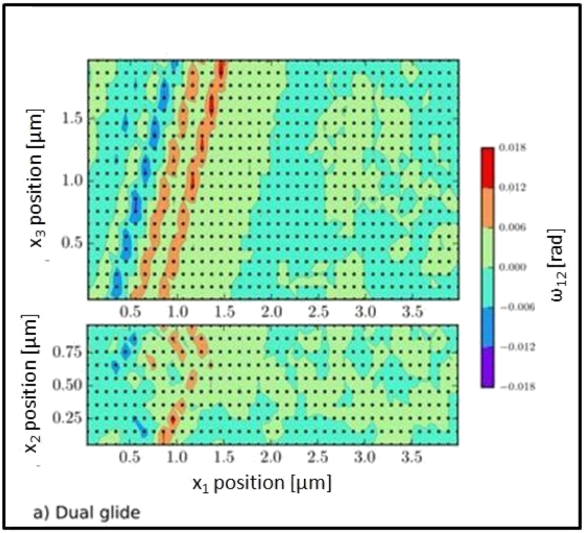

a) Dual glide

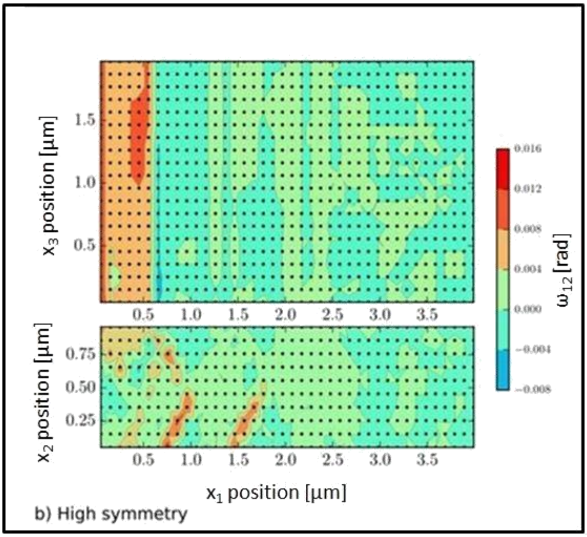

b) High symmetry

Figure 6.4: Lattice rotation angle around the bending axis for (a) DG and (b) HS orientation within slices of the x_1-x_3 plane (top) and x_1-x_2 plane (bottom). To the left of both plots is the fixed boundary condition and to the right, the wedge indent displacement is applied. The colors indicate the rotation angle, dots show the center of the corresponding voxels.

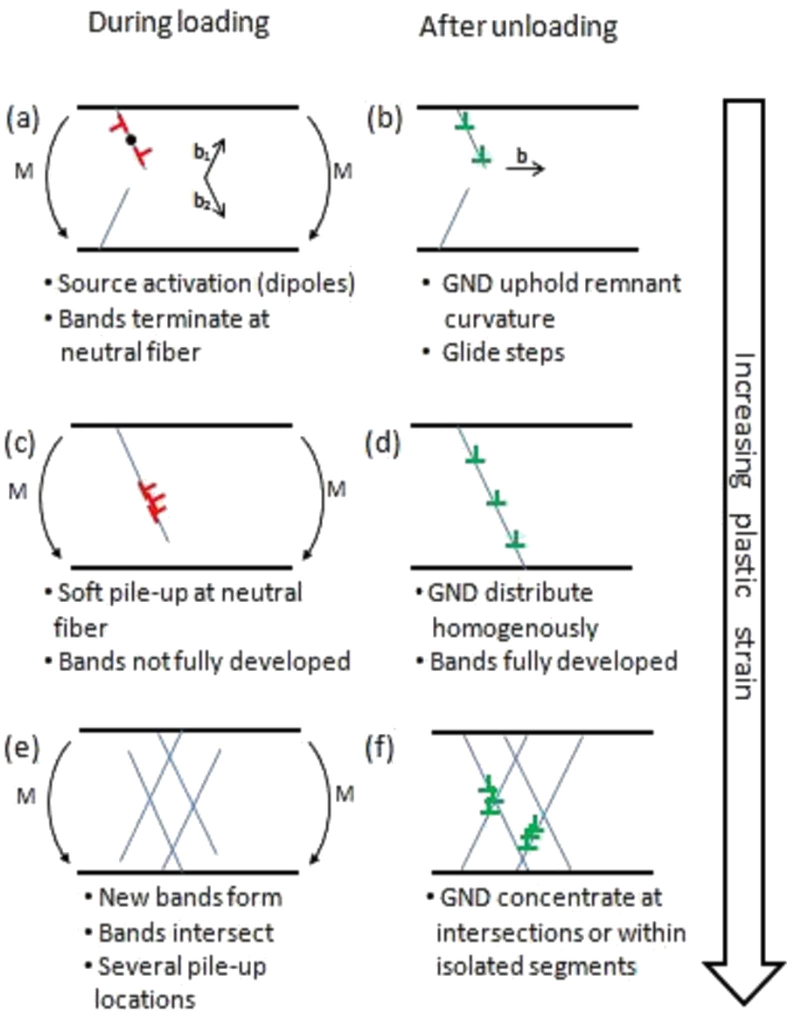
During loading
After unloading
(a)
M
b1
b2
M
• Source activation (dipoles)
• Bands terminate at neutral fiber
(b)
b
• GND uphold remnant curvature
• Glide steps
(c)
M
M
• Soft pile-up at neutral fiber
• Bands not fully developed
(d)
• GND distribute homogenously
• Bands fully developed
(e)
M
M
• New bands form
• Bands intersect
• Several pile-up locations
(f)
• GND concentrate at intersections or within isolated segments
Increasing plastic strain

Figure 6.5: Schematic of the dislocation network formation. The lines correspond to the traces of high dislocation densities observed in experiments and simulations. (a), (c) and (e) show the situation during loading with increasing strain. (b), (d) and (f) display the situation for the arrangement shown on the left hand side after unloading.

An important aspect in this theory to be discussed is why experiments reveal fully developed band structures in the relaxed state, if there is a soft pile-up preventing dislocations from moving across the neutral fiber. This question may be answered from the observations from DDD simulations. As mentioned previously, Stricker et. al (Stricker et. al, 2017) found that if a dislocation source keeps generating dislocations pushing them towards the neutral fiber, then some may even pass this region. That means that the stress caused by the successive generation of dislocations will surpass the backstress of the pile-up. When entering the opposite half of the cross sections, dislocation motion towards the free surface stops as the resolved stress acting on it reverses its sign. The band structure created this way does not bridge the entire cross section of the cantilever. This is displayed schematically in Fig.6.5c and principally seen in DDD simulations (Fig.6.4a). The simulations revealed that once the load is released, dislocations needed for the glide process leave the volume by the nearest surface. That means a few dislocations did travel through the entire cross section, which ultimately explains the observation of fully developed bands in experiments.

Another important aspect to the pile-up theory is its relation to a dislocation source limitation mechanism: The soft pile-up causes a backstress which may block the activation of dislocation sources within the same band. Once the dislocation density within the existing bands grows too high, dislocation sources may shut down and additional bands have to be formed. As the region of plastic deformation is spatially confined, the newly generated bands will form intersections which the remaining ones. Fig.6.5e displays the situation during loading as it is suggested to proceed. In experiments these points of intersection between bands are found to be locations of potentially high dislocation densities that may even persist after the stress is released. Therefore, it is even possible that upon deformation several soft pile-ups formed apart from the one at the neutral fiber due to interactions of the different dislocation bands. The situation is shown experimentally for example in Fig.5.11 and Fig.5.12 for cantilever of remaining strain of 0.071 and 0.086, respectively.

Fig.5.12 depicts best the situation that arises if numerous band structures are generated and intersect. Due to the high number of bands and their concentration within a very confined region (within 1 µm from the support), the networks generated from intersections may become very complex. Rather than forming only one or two intersections with other bands (e.g. Fig.5.11) the individual bands can be crossed multiple times, splitting into several smaller segments. Following the argumentation of the intersections as potential pinning points for dislocations once the load is released, it may be possible that in between them, isolated segments of high dislocation density remain in the relaxed state. The dislocations here appear trapped within the sample with possibly no connection to either top or bottom surface. The strong concentration of dislocations at intersections and within isolated segments after unloading is sketched in Fig.6.5f. It matches the experimental results shown in Fig.5.12. Moreover, in this particular experiment, at least some hint for a pile-up at the neutral fiber according to the aforementioned theory of the cantilever may be seen as well: The core region of the cross section in Fig.5.12 in between the visible dislocation bands has a higher GND density than at the extremities of the cantilever. This may be interpreted as a possible effect from a soft pile-up that formed at the neutral fiber but could not dissolve entirely after deformation.

All of the aforementioned findings about dislocation structures are only confirmed for small samples of 1 µm thickness. Large cantilevers of 3 µm thickness subjected to the same amount of plastic strain reveal a different behavior: (i) Instead of a cross-shaped network, only a few individual dislocation bands can be seen, (ii) the dominance of certain dislocation types within the bands is less pronounced compared to their 1 µm counterparts and (iii) deformation by twinning is taking place in addition to glide. The dislocation density within a visible band is distributed homogenously, just as for the 1 µm counterparts, but in terms of absolute values the densities barely exceed the background noise. Deformation by twinning is displayed in Fig.5.14, Fig.5.15 and Fig.5.18. These particular samples in HS orientation show that twins are only found within the tensile half of the cross section. If Schmid's law is applied to partial dislocations for this loading geometry (Tab.5.4), it matches the observation as partial dislocations are likely to form under tension but are less favorable than full dislocations under compression. In contrast to the interaction of full dislocations with one another, partial dislocations will gradually cause stable stacking faults on parallel planes and in turn a deformation twin. The twin initiates most likely at the outermost fiber and then gradually expands towards the center until it reaches the neutral fiber. If the external strain imposed on the sample is further increased, additional parallel twins are formed. Such a situation is displayed in Fig.5.18.

The main question is why twinning is only observed for large cantilevers. There are several differences between the two size extremes, which play a role in the argumentation: The most striking one is that, if the same amount of strain is applied, the strain gradient will be smaller for large samples. The next crucial aspect is the initial dislocation density: In chapter 3, the XRD experiments revealed that in 3 µm thick thin Ag films, the initial dislocation density is lower than in 1 µm thick ones, which reduces the amount of potential dislocation sources. Both aspects combined increase the distance a dislocation can travel within the volume unimpaired by other dislocations. If Schmid's law is applied to partial dislocations, it is seen that there is large difference in Schmid factor *m* between the leading and trailing partial. If a twin is formed via δA and αD, then a recombination with the respective trailing partial is thus unlikely. Along with the argumentation of reduced dislocation interaction this allows the stacking faults to stabilize. The twin then expands even up to the neutral fiber where the dislocation movement stops.

6.3 Interpretation of the size effect

In literature, the size effect upon cantilever bending is usually explained by a combination of strain gradient plasticity and dislocation source limitation. The latter is assumed to be caused by a the backstress of a soft pile-up of dislocations in the proximity of the neutral fiber (Motz et al., 2005; Demir et al., 2010; Kirchlechner et al., 2012; Tarleton et al., 2015). If the size effect is explained by an increase in dislocation density due to a strain gradient, then the exponent *n* of the scaling law should be equal to 0.5 as was pointed out in chapter 1. Apart from the strain gradient, Motz et al. (Motz et al., 2005) derived the scaling exponent for a source limitation mechanism caused by a dislocation soft pile-up to be $n = 1$. The scaling exponent for flow stress found in the project at hand is $n = 0.69$ i.e. in between the two limits, which is partly in agreement with the findings of other research groups: For example Motz et al. (Motz et al., 2008) found for their FIB fabricated Cu cantilevers an exponent of $n = 0.75$ while Demir et al. (Demir et al., 2010) report values closer to $n = 0.5$. Overall, it can be stated that there is an uncertainty about the exact scaling law.

An important aspect detected in the project at hand is the observation of crossing dislocation bands if the strain is sufficiently high. As a consequence, it was stated in section 6.2 that during loading dislocations may not necessarily pile-up exclusively around the neutral fiber. Instead, the crossings form additional potential pinning points for dislocations. Moreover, one isolated dislocation band contains about 10 different dislocation types according to the minimization procedure which means dislocation interaction within the band itself may be even more complex. To derive a scaling law based on pile-up backstress, Motz et al. (Motz et al., 2005) assumed only the pile-up within one single band structure populated with one particular dislocation type. From the findings in this project, it might therefore be necessary to include more than one pile-up location in the analytical model and furthermore the existence of more than one dislocation type within a band structure. But this would make analytical calculations probably too complex to be solved.

Experimental evidence for the two mechanisms driving the size effect - strain gradient and source limitation - is given to some extent: From the TKD scans, the increase in GND density with imposed strain was quantified (Fig.5.16). This relationship is in agreement with strain gradient plasticity. The existence of a source limitation mechanism, however, is harder to deduct from the experiments. A hint might be the number of visible dislocation bands, which is found to increase with increasing strain: If due to a source limitation effect, dislocation sources within the observed band structures can no longer be activated, then additional bands will necessarily have to be formed and their total number gradually increases. Dislocation band structures which cannot produce any more dislocations due to source limitation have very high GND densities and will most likely still have elevated densities after deformation which also matches experimental observations. The physical reasons for source limitation, however, i.e. whether the source limitation arises from a dislocation soft pile-up or from a more homogeneous hardening cannot be decided from the scans at hand.

Another aspect to be discussed is the different hardening behavior of 1 µm and 3 µm thick cantilevers. When looking at the stress-strain curves presented in chapter 4, it is seen that large samples tend to show a pronounced work-hardening that can be described by a Ludwik-type relation whereas small samples show no apparent hardening and are more accurately described by a Voce-type fit. The XRD scans shown in chapter 3 reveal a higher initial dislocation density for small samples which means the stress needed to activate dislocation sources and thus enable plastic flow increases. Due to the large strain gradient, dislocations quickly move along their respective glide plane and the fact that no significant hardening is observed for these cantilevers might be related to a lack of dislocation multiplication during the deformation process. In contrast, the more pronounced work-hardening in large samples favors the assumption that dislocation sources are easier to be activated than for their 1 µm thick counterparts and that interactions become more dominant. To some extent, the Voce-type hardening model might therefore also be interpreted as an indicator for source limitation becoming a more dominant mechanism than dislocation multiplication.

The hardening behavior is found to be independent of the sample orientation as no difference is seen, when comparing HS to DG cantilevers. This may be understood because the activation of two independent glide systems (two effective Burgers vectors) is sufficient to enable plastic flow for both geometries.

6.4 FIB contamination

In practically all of the studies dealing with size effect on cantilevers cited throughout this project, an aspect that could not be quantified but may have a significant influence on the scaling law is the FIB fabrication method. The authors confirm Ga^+ ions being introduced into the matrix but its effect on the scaling law could not be measured. In chapter 4 it was shown that Ga^+ contamination has a strong influence on the mechanical response of the cantilevers. Three observations are made: (i) The contaminated cantilevers are found to have a 20-30 % higher flow stress, (ii) the hardening behavior tends to change showing less pronounced work hardening and (iii) the value of the exponent of the scaling law describing the size effect increases by about $\Delta n = 0.12$. The effects (i) and (ii) are found to be more pronounced for high ion fluences but reach a saturation behavior at ion currents between 100-300 pA. In contrast, for the scaling law exponent n no dependence with respect to the ion current was be found.

A very important issue found during this project is that the contamination is not only introduced by the patterning, but that a single FIB snapshot of the cantilever is sufficient to cause the above mentioned changes in mechanical behavior. This phenomenon arises because of the bending geometry: The top surface, which is directly exposed to the ion beam, is also submitted to the highest stresses, i.e. the activation of dislocation sources will start within the irradiated zone. Even if the Ga^+ ions only reach depth of a few ten nm beneath the sample surface, the effect can therefore not be assumed to be negligible. Bei et al. (Bei et al., 2007) for example used SRIM (stopping and range of ions in matter) calculations and found the penetration depth to be 20-30 nm under normal incidence for their samples. In the project at hand, the only FIB procedure which left the structures mostly unaffected was the blind cutting where no snapshot of the cantilever was taken at all. Here the region that is effectively deformed was not irradiated with FIB but still an increase in flow stress of about 10-15 % is found. The latter observation implies that besides the direct implantation of Ga^+ beneath the surface, a surface diffusion mechanism is taking place that allows the Ga^+ ions to move towards the region where plastic deformation is localized. This diffusion path is at least

10 µm long which is the distance between the location of the blind cut and the bending zone.

The reason for the mechanical changes can be explained in different ways. The most likely one is that dislocations are pinned by Ga^+ ions being introduced into the matrix. Then some additional stress would be required before dislocation movement can take place. This would explain the higher flow stress and the less pronounced hardening observed in experiments. On the other hand, this assumption of Ga^+ ions blocking dislocation sources and/or pinning existing dislocations is not entirely in agreement with literature. In their work, Bei et al. (Bei et al., 2007) found the flow stress to decrease due to FIB radiation and suggested that the treatment may either introduce dislocations or ease the accessibility of sources. FIB treatment introducing various kinds of crystal defects into the crystal matrix is also reported in Kiener et al. (Kiener et al., 2007). A high dislocation density concentrated at the outermost fiber of the cantilever, caused by FIB irradiation, might explain the observed mechanical behavior but does not seem to be the dominant mechanism in the given experiment. The introduction of dislocations would not explain the changes caused by the blind cutting procedure: As mentioned above, in this case the changes in mechanical response are related to Ga^+ ions diffusing from the position of the FIB cut toward the zone where plastic deformation is concentrated. Through diffusion, no significant defects can be introduced, except for point defects such as Ga^+ interstitials and substitutional atoms. This reasoning does not exclude the introduction of e.g. line defects by FIB affecting mechanical properties. However, it favors the idea that Ga^+ ions are pinning existing dislocations and thus blocking their activation, whether they are implanted directly or move to the region of interest through diffusion.

The extent of the changes in mechanical response becomes already measureable at very low ion currents (100-300 pA) for small and large samples alike. Larger currents modify the microstructure as well but the changes in mechanical response find a saturation behavior. This saturation may be explained by the small size of the penetration depth of the ions and the fact that altering the microstructure of the outermost fiber is enough to impair the activation of dislocations and thus the onset of plastic flow. It appears that a state of "full contamination" is reached rather quickly and ultimately further increase of the ion current beyond this point will only lead to sputtering, i.e. destruction of the sample material. It was stated before that Ga^+ ions diffuse over the sample surface and that surface diffusion is more likely than a diffusion into the volume given the single crystalline nature of the samples. However, even if diffusion is taken into account, an increase in ion fluence does not significantly change the size (especially not the depth) of the interaction volume for the given case and might therefore play a role in the explanation the saturation behavior.

The observations made contradict several sources in literature where Ga^+ contamination is assumed to be of negligible influence. The common arguments presented for this assumption are (i) the low penetration depth of the ions (Motz et al., 2005) compared to the overall sample size and (ii) the sufficient reduction of harmful effects down to a point at which they can be considered negligible which can be realized by minimizing the ion current (Motz et al., 2005; Motz et al., 2008; Demir et al., 2010; Demir, Roters, et al., 2010; Kiener et al., 2010; Iqbal et al., 2012; Kirchlechner et al., 2012; Tarleton et al., 2015). In this project, argumentation (i) is proven to be invalid as long the designated sample structures are cantilevers submitted to bending and the irradiated surface coincides with the surface of maximum stress. The snapshot only experiment shows that if the FIB is used as a tool for cantilever fabrication, the contamination will reveal its full extent practically regardless what kind of pattern is cut or even regardless whether any pattern is cut at all. This finding only applies to bending geometries where the region of maximum strain is inevitably exposed to the ion beam and loses its validity for example in the case of pillar fabrication. For geometries such as pillars, where the applied stress is distributed more homogenously over the entire sample, the situation will be less severe. Nevertheless, the FIB milling procedure can cause microstructural changes within such samples as well, as reported by Kheradmand (Kheradmand, 2012) who observed local lattice rotations at the flanks of micropillars after cutting them with FIB.

It has to be mentioned that for the cantilevers fabricated using the lithography-based method, process-induced damage can at least not entirely be excluded and implantation of Ar^+ during IBE is known to be possible. However, the only possible way for Ar^+ implantation during IBE would be by penetrating the PMMA resist or through the exposed flanks of the structures which both seem unlikely. This is readily seen, because the PMMA resist shields the top surface during the entire process. Even if its chemical structure has changed after IBE, a small layer of resist with a crater-like surface (Fig.2.11) still remains on the sample surface until it is stripped. The microstructural changes due to IBE and due to FIB should therefore be far from being of comparable degree.

Argumentation (ii) – the reduction of operating ion current – is the next aspect that should be discussed. From a technical point of view, in most applications the ion current cannot be reduced to 100 pA and below unless the structures are considerably small. The usual choice for the finishing step of the patterning is between 100-200 pA (Iqbal et al., 2012; Kiener et al., 2010), but sometimes even higher values are used such as 200 pA-1 nA (Motz et al., 2005) or 500 pA (Demir, Raabe, et al., 2010). Based on the observation of the saturation behavior in this project being reached for very low fluences already, the argumentation of negligible influence due to a low ion current might be questioned as well. An important point in this regard is, that all the milling steps executed before the final cut will have an impact as well. As mentioned in this project (blind cutting experiment) a surface diffusion of Ga^+ ions of at least 10 μm appears to be always taking place. Regardless of the way how the Ga^+ ions are introduced into the matrix (direct implantation or diffusion), the extent of changes in mechanical properties varies with the ion current applied and is found to reach a saturation behavior between 100-300 pA. Therefore the change in operating parameters even down to 100 pA might not noticeably reduce the amount of changes caused. Here it has to be discussed whether the observations made in this project can justifiably be retraced to other work on single crystalline cantilevers of different materials. The most common choice in literature for sample material is Cu (Demir & Raabe, 2010; Demir, Raabe, et al., 2010; Kiener et al., 2010; Kirchlechner et al., 2012; Motz et al., 2005, 2008) which forms a similar phase diagram with Ga as Ag. But even if there is comparability in terms of solubility of Ga in the respective matrix, the observation that the ions are already introduced during the snapshot essentially implies that cantilevers in any work published might likewise be affected. In the project at hand, only one snapshot is taken and the saturation behavior is rapidly reached. The same is found for the flattening procedure which mimics the last milling step of the conventional cutting procedure. In the works cited above, the entire cantilever structure is cut by FIB which implies that several snapshots are most likely taken, to counter sample drift etc. Therefore the total fluence is probably even higher. Consequently, it is possible that the contamination resembles the saturation state presented in this project. Based on the observation that the size effect exponent increases as a result of FIB treatment by $\Delta n = 0.12$ a comparable or even larger effect might be expected for any cantilever FIB cutting procedure.

In the following, the strengthening effect of Ga^+ into an Ag matrix is compared to theoretical predictions from solid solution strengthening models. The formula developed by Fleischer (Fleischer, 1963) describes the increase in flow stress $\Delta\tau$ due to the introduction of a foreign species of concentration c and shear modulus G by

$$\Delta\tau = \frac{G}{700}|\eta - 3\delta|^{\frac{3}{2}}\sqrt{c} \tag{6.2}$$

where δ and η represent the parelastic and dielastic interaction of the two different materials. δ can be approximated by

$$\delta = \frac{\Delta r}{r} \tag{6.3}$$

where r is the atomic radius of the matrix atoms and Δr is its difference from the foreign species. The dielastic interaction η may be approximated from the difference in shear moduli ΔG of the two materials and the shear modulus of the matrix G:

$$\eta = \frac{\frac{\Delta G}{G}}{1 + 0.5\left|\frac{\Delta G}{G}\right|} \tag{6.4}$$

For FIB contamination, only DG oriented cantilevers are used, so *G(Ag)* = 23 GPa, while *G(Ga) = 6 GPa* (Baskes et al., 2002) and the atomic radii of Ag and Ga are *r(Ag) = 0.165nm* and *r(Ga) = 0.136nm* (webelements.com). From Ag-Ga phase diagram (Okamoto, 1991; Gunnaes et al., 2000) , no information about the solubility of Ga in Ag at room temperature is given (no stable phase). Thus we use the value for maximum solubility which is *c* = 18 at% at 885 K as a worst case scenario.

With this data, equation (6.2) predicts an increase in flow stress of *Δτ = 15 MPa*. This value has to be compared to the results from blind cutting experiments, where Ga^+ diffuses to the region of plastic deformation and no direct ion implantation is taking place. The absolute change in flow stress observed in these experiments is about 50 MPa (Fig.4.21). It can be stated that models for solid solution strengthening give the right order of magnitude but tend to slightly underestimate the effect.

If in addition to the diffusion of Ga^+ ions, direct implantation is taking place, as during the flattening procedure, the increase in flow stress reaches up to 150 MPa for 1 µm thick cantilevers (Fig.4.18), implying that the change in mechanical properties cannot be explained solely by solid solution hardening. Instead, the increase in flow stress may be explained by Ga^+ ions raising the defect density within the sample (vacancies, dislocations, dislocation loops etc.) which matches reports of other research groups (Bei et al., 2007; Kiener et al., 2007).

6.5 Concluding remarks

After all the results and interpretations that this project was capable to provide, there are still some further aspects to be discussed that go beyond the scope of this work. There are at least two aspects worth mentioning, which are (i) the ability to further improve the accuracy of the GND analysis and (ii) the fabrication procedure itself.

TKD has been proven to be a powerful tool for microstructural analysis when combined with methods such as the Pantleon approach. With respect to EBSD the lateral resolution can be reduced from 50 nm down to about 10 nm. However, the angular resolution is still only about 0.5° which was discussed as a critical aspect limiting the precision of the information that the minimization approach can provide. In chapter 3 it was discussed that the Cross Court software developed by Wilkinson (Wilkinson, 2001) might address this problem providing higher angular resolution. It did for example show a smaller background dislocation density. However, for the given samples, the application of this pattern shift based method produced large errors in regions of higher dislocation content. The question might now be asked whether an improvement in scanning parameters and/or the data acquisition/storage rate or a variation of sample material, might improve pattern quality even at the highly deformed zones and thus tackle the problem. Especially the binning of the images is a considerable hindrance for any digital image correlation-based method, but was found to be vital in order to minimize the amount of C contamination of the sample surface during the scan. From visual inspection of the Kikuchi patterns recorded from the zones of high defect density, Cross Court seems unlikely to succeed even under optimized scanning/recording conditions. The patterns seen on the thin lamellas are of inferior quality than regular EBSD on the surface of a bulk material and once the defect density rises the pattern blurs even stronger.

So far the fabrication route works only for Ag as a sample material and still has some critical aspects. The main one is the fact that the patterning step is purely physical and causes redeposition which can only partly be handled by the following wet-etch step. In theory, when adjusting the etchants etc. the process should be transferable to other metallic thin films that can be deposited epitaxially onto a Si{100} wafer substrate. Besides the choice of thin film material an interesting aspect is the choice of substrate as well, or more precisely of substrate orientation. In this project, since KOH is used for under etching of the cantilevers, Si{100} is the only option available. In turn, the fabrication of fcc cantilevers in orientations such as single glide is strictly impossible from a crystallographic point of view. The under-etching might, however, also be feasible by dry-etching using for example sulfur hexafluoride (SF_6). However, the depth that can be realized with this method is most likely too low (a few µm) for the cantilevers within this project which are at least about 10 µm in length. However the fact that a variety of orientations is generally possible might offer new and interesting options for further study.

Finally, the most interesting aspect that may be studied in even further detail is the size effect. The deflection of cantilevers within the sub-µm regime was not touched in this project. This aspect is mentioned here, because theoretically, the developed fabrication route is able to adapt to that size: Depositing thin films of thickness lower than 1 µm by PVD is not an issue. For lithography (EBL), reducing the lateral cantilever dimensions EBL below 1 µm is not a problem either. The parameters would have to be re-adjusted but so far no essential problem in fabrication route is seen. This would then allow studying the behavior of sub-µm sized single crystalline, FIB-free cantilevers in terms of microplasticity. The reason why such structures were not analyzed in the project is that the G200 nanoindenter system used here cannot detect and deform such small samples: If the aspect ratios of the cantilevers are designed so the machines stiffness resolution is met, then they will be too small to be seen within the optical microscope. In fact, the system was already being pushed close to its limits in this project (in some cases even slightly beyond it recommended stiffness resolution). However, with a bending setup of superior lateral and force resolution were available (in-situ SEM device), such sub-µm sized cantilevers might be investigated as well.

Appendix

Framework for DDD simulations

3D discrete dislocation dynamics simulations have been executed by Stricker and Weygand as a cooperative project within the DFG research group FOR1650. The results are not published, yet. 3D DDD simulations have been carried out with a framework described in (Weygand et al., 2002; Motz et al., 2008; Senger et al., 2011). In this framework, plasticity is the direct result of the motion of individual dislocations. Dislocations are discredited using piecewise straight segments and their motion is governed by the Peach-Koehler force acting along the segments. The code is based on the superposition principle valid for linear elasticity and two problems are solved: an infinite homogeneous solid treating the plastic behavior by the glide of discrete dislocations and an inhomogeneous body with correction fields for taking both the boundary conditions and image forces into account (Giessen & Needleman, 1999). Junction formation, annihilation and cross-slip are implemented as constitutive rules (Weygand & Gumbsch, 2005).

The dimensions of the DDD samples are $1 \cdot 2 \cdot 4$ µm^3 in height h, width w and length l and both crystallographic orientations (DG, HS) are tested. The coordinate system convention used for simulations also slightly differs from the one chosen for the experiments. As illustrated in Fig.A.1 for DDD simulations, $\boldsymbol{x_1}$ corresponds to $[\bar{1}10]$, $[\bar{1}20]$ $\boldsymbol{x_2}$ to $[001]$, and $\boldsymbol{x_3}$ to $[110]$, $[210]$, for HS and DG, respectively. Material parameters for a fcc crystal mimicking those of isotropic Aluminum are used (shear modulus $G = 27\ GPa$, Poisson's ratio $\upsilon = 0.347$, lattice constant $a = 0.404\ nm$, drag coefficient $\eta = 1 \cdot 10^{-4}\ Pa{\cdot}s$). As an initial dislocation microstructure, Frank-Read sources with length of approximately 0.5 µm are distributed randomly in the sample, where an equal number of sources per glide plane normal ($n = 100$) is chosen. This results in an initial dislocation density of $\rho_0 = 2.5\ x\ 10^{13}\ m^{-2}$. For each orientation the results for ten realizations are compared.

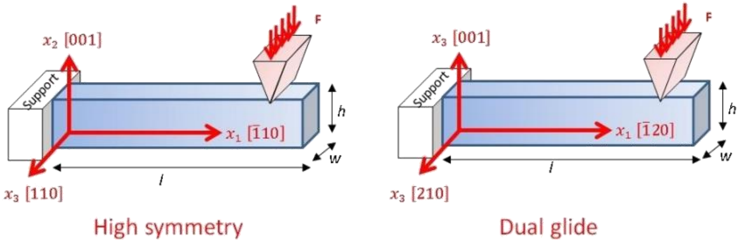
F
x_2 [001]
Support
x_1 [$\bar{1}$10]
h
w
l
x_3 [110]
High symmetry
F
x_3 [001]
Support
x_1 [$\bar{1}$20]
h
w
l
x_3 [210]
Dual glide

Figure A.1: Setup and coordinate system chosen for DDD.

A wedge indent bending boundary condition is imposed to mimic the experimental conditions. On one end, the displacement of the whole surface is set to zero and close to the other end a displacement is prescribed along a line of nodes on top surface of the sample with a strain rate of 15000 s^{-1} in relation to the beam length l_0 at the second last finite element row, as it would be on a perfectly sharp wedge indenter. All other boundaries are traction free and dislocations are allowed to leave the volume.

List of figures

Figure 1.1: Some exemplary values of the measured material strength for a variety of small Cu samples tested by different research groups as a function of characteristic length *d.* The plot is based on Kraft et al. (Kraft et al., 2010). The theoretical shear strength for Cu is calculated along <110>. 7

Figure 1.2: Schematic illustration how geometrically necessary edge dislocations accumulate within a sample to cause bending. 8

Figure 1.3: Schematic of the dislocation pile up near the neutral fiber upon bending as suggested by Motz et al. (Motz et al., 2005). Dislocation dipoles are emitted from the source at the outer fibers of the tensile (+τ) and compressive (-τ) half of the bending structure. 12

Figure 1.4: Illustration of the setups used for (a) EBSD and (b) TKD. (c) Cantilever transferred to a TEM grid (before thinning) as an example of a potential TKD sample. 25

Figure 1.5: Illustration of the interaction volume of electrons in SEM with a conductive sample to illustrate lateral resolution. (a) General shape and some exemplary values, (b) situation for EBSD with increase of useable backscattered electron by 70° sample tilt and (c) situation for TKD with lamella of about 100 nm thickness. 26

Figure 2.1: Schematic of the sample orientations HS and DG. The effective Burgers vectors are sketched in black. 32

Figure 2.2: Cantilever fabrication procedure in five consecutive steps. (a) epitaxial thin film deposition, (b) lithography, (c) pattering by dry-etching, (d) redeposition removal by wet-etching and stripping of the resist, (e) under-etching of the structures using KOH. 38

Figure 2.3: Illustration of a misfit dislocation arising from cube-on-cube growth of a 4x4 unit cell mesh (Ag) onto a 3x3 unit cell mesh (Si) (view in cross section). The stacking of unit cells (a) without and (b) with misfit dislocation is displayed. 40

Figure 2.4: (a) Bragg-Brentano Scan of a 1 µm thick Ag thin film. (a) The entire phase diagram, (b) Zoom onto the Ag{200} peak............................. 43

Figure 2.5: (a) Rocking Curves for 100 nm thick Ag films deposited at different temperatures. The intensity and the peak centers have been normalized for comparison. (b) FWHM for the rocking curves as a function of substrate temperature. 44

Figure 2.6: Change in rocking curve FWHM of the Lorentzian fit versus the Ag layer thickness. The peak used is Ag{200}. 47

Figure 2.7: TEM bright field image of a cross section of an as-deposited Ag thin revealing misfit dislocations located at the film-substrate interface. 48

Figure 2.8: EBL mask design. (a) Shows the entire 2” wafer after fabrication with 4 HS arrays on the upper and 4 DG arrays on the lower half. (b) highlights the design for HS and (c) for DG. In (b) and (c) the black layer corresponds to the cantilevers, while the red one represents the etch pits. The logical subtraction operation of these both layers gives the area that is exposed to the electron beam in EBL. 50

Figure 2.9: SEM images of single crystalline cantilevers. The patterning has been done by wet-etching (a) and dry-etching (b), respectively.................. 51

Figure 2.10: Wafers after IBE displaying the color change of the resist. Initial PMMA thickness: (a) 3.2µm, (b) 1.5µm. The remaining PMMA on (b) is supposed to be very thin which explains the high reflectivity of the wafer.. 53

Figure 2.11: SEM images to visualize change in electrical conductivity of PMMA resist after IBE. (a) Sample after EBL, i.e. before dry-etching. Here the PMMA resist is insulating and the resist charges strongly causing bad image quality. (b) and (c) show the sample after IBE. The Si on the bottom of the etch pit appears to be unaffected. 54

Figure 2.12: SEM images of cantilever structures after IBE (a, b) before and (c, d) after stripping. The process conditions as they are supposed to be result in sharp edges (a, c), while the images (b) and (d) display the state encountered in this work due to insufficient cooling during IBE................ 55

Figure 2.13: SEM images of cantilevers after IBE to display redeposition as a function of cantilever aspect ratio length over width. (a), $l_0/w = 3$, (b) 4, (c) 5. 56

Figure 2.14: SEM images of the undercut mechanism of Si by an anisotropic etchant. The pictures are taken under 40° tilt. (a) Overview of the structure, (b) zoom on convex corners where under-etching takes place, (c) zoom on concave corners where under-etching is mostly inhibited. 59

Figure 2.15: Schematic of resulting etch pits in HS and DG due to KOH etching in top view as a function of mask design. 60

Figure 3.1: Sketch of the bending setup with all relevant geometric parameters. The Ag layer is shown in blue while the Si substrate is grey and the external load is red. On the right hand side, a top view and cross section is shown. The visual imprint left to the testing structure serves for drift correction and plays an important role in determination of geometric parameters. 63

Figure 3.2: Some SEM images displaying the minimal undercut feasible for (a) DG and (b) HS. In (a), the arrow marks the edge where material removal advances. 66

Figure 3.3: Sketch of the determination of l_u in HS and DG orientation. The upper figures show a top view onto the cantilever and the edge pit. The dotted black line represents the visible foot of the {111} flank. The lower parts shows a cross section for the HS case explaining the calculation of the undercut. 67

Figure 3.4: Cumulative distribution of the parameters l_{eff}, l_0, w and l_u the sample sets (a) B-1 µm, (b) C-1 µm, (c) B-3 µm, (d) D-3 µm. Each set both comprises HS and DG orientations and contains about 30 individual cantilevers. l_u is further distinguished by the respective orientations HS and DG. 71

Figure 3.5: SEM images of FIB contamination experiments. (a) As-fabricated, non-irradiated state. (b) Flattening procedure. (c) Nose cutting procedure. The imprint of the pattern that is cut can be seen on the bottom of the etch pit. (d) Only snapshot procedure. The dashed line shows the size of the irradiated area. 74

Figure 4.1: (a) Exemplary raw load vs. displacement curve without correction. The inset highlights drift effects. The same curve is shown after drift correction in (b). In (c) the machine compliance is fitted with the red line. After subtraction of this line, the final load versus deflection curve (d) is obtained. 82

Figure 4.2: Deflection curves for some cantilevers that have been submitted to different amounts of strain recorded with laser profilometry. 84
Figure 4.3: Some exemplary bending moment curves for cantilever structures comparable in size (HS orientation, 1 µm thickness, aspect ratio A. 85
Figure 4.4: Force-deflection diagram showing force values $F_{p0.2}$ and F_{max} used for the determination of the flow stress. 89
Figure 4.5: Bending moment curves for some cantilevers of 1µm thickness, DG orientation and aspect ratio A. The difference of the slope within the second unloading segment becomes more pronounced with increasing maximum strain imposed. 91
Figure 4.6: A cantilever with 100 nm of Pt deposited by FIB on the sample surface (a) before and (b), (c), (d) after deformation. (c) and (d) show a zoom onto the free end of the structure and highlight the wear tracks which can be visualized this way. They tend to be more significant at the edges of the cantilever. 92
Figure 4.7: Correction of mechanical data by introducing a compliance length. The undercut length l_u is only added to the effective length l_{eff} if its value is positive. 96
Figure 4.8: Cumulative distribution of the cantilever stiffness. (a) Shows the absolute values and (b) the relative difference with respect to the experimentally found values. 98
Figure 4.9: Flow Stress $R_{p0.2}$ versus effective cantilever volume V_{eff} in (a) linear and (b) double logarithmic representation. 100
Figure 4.10: Flow Stress $R_{p0.2}$ versus cantilever height h. 102
Figure 4.11: Flow stress versus V_{eff} as a function of the criteria used to define plastic flow. 103
Figure 4.12: Flow stress versus V_{eff} as a function of cantilever orientation. 105
Figure 4.13: Flow stress versus cantilever height, for samples of aspect ratio B with DG and HS orientation 105
Figure 4.14: Normalized bending moment curves for all three cantilever heights. (a) Aspect ratio A, (b) B, (c) C and (D) D. The total volume (calculated from mask layout values) are indicated as well in the caption. 107

Figure 4.15: Stress-strain curves with an attempt to fit the transition toward the elastic-plastic plateau (i.e. the hardening). The cantilever differ in aspect ratio, thickness and orientation and are (a) B-1µm-HS, (b) B-3µm-HS. (a) is fitted using a Voce-type function and (b) with a Ludwik-type relationship. 109

Figure 4.16: Difference in flow stress values $R_{p0.2}$ and σ_f versus V_{eff}. 110

Figure 4.17: Bending moment curves showing the changes in mechanical behavior of the as-fabricated cantilevers by the flattening procedure under different ion currents. Samples taken are in DG orientation, aspect ratio B and (a) 1 µm, (b) 2 µm and (c) 3 µm in height. 113

Figure 4.18: FIB damage by flattening the cantilever edges. (a) Absolute flow stress values and (b) relative change of flow stress with respect to the non-treated cantilever plotted as a function of the ion current applied....... 114

Figure 4.19: Flow Stress $R_{p0.2}$ versus cantilever height h for as-fabricated samples of identical aspect ratios and orientations after FIB contamination via the flattening procedure. The values of the allometric fitting function are given as an inset and the numbers are dyed in the color of the corresponding plot.. 116

Figure 4.20: Difference in flow stress values $R_{p0.2}$ and σ_f versus V_{eff} for cantilevers milled by the flattening treatment. 116

Figure 5.1: Sample preparation for EBSD and TKD. Images are taken with SEM and (e) is taken with FIB. (a) Overview over one etch pit from which one cantilever is chosen. (b) After Pt deposition on top of the cantilever. Red area marks the cuts for lift-off. (c) shows result of this cut. (d) Lift-off with micro manipulator. (e) Attachment to TEM Grid. (f) Flattening/Cleaning for EBSD. For TKD further thinning would be needed. The red square marks the typical size and location of a region that can be scanned with TKD. 121

Figure 5.2: Schematic of the sample orientations HS and DG. The effective Burgers vectors are sketched in black. 122

Figure 5.3: Pole figures from an EBSD scan of a non-aligned cantilever (green) in DG orientation and after alignment (red) for the planes (a, b) {001}, (c, d) {101}, (e, f) {210}. The black arrow in (e) marks the sole pole that shows no apparent streaking and is therefore centered. The blue arrows in (b) highlight how a rotation around this pole is then executed so {001} poles lie on the equatorial line and 0° great circle.................................... 123

Figure 5.4: Inverse Pole figure maps of a cantilever in HS orientation scanned with TKD. The maps are calculated for (a) the sample direction x_1, (b) x_2 and (c) x_3.......... 124

Figure 5.5: Illustration of the slip systems and their notation (Schmid-Boas notation). The individual slip planes are marked with letters while the directions are indicated by numbers.......... 130

Figure 5.6: Inverse pole figures withtin stereographic projection (equal angle, upper hemisphere) for HS (a) and DG (b) for the traingle with borders [001], [101] , [111].......... 136

Figure 5.7: SEM images showing glide steps on the cantilever surface (a) in DG and (b) in HS geometry. 138

Figure 5.8: GND density [m^{-2}] calculated from an EBSD scan of a 3 µm HS cantilever of aspect ratio C with a remaining strain 0.041. Lateral dimensions in [µm]. (b) shows a zoom onto the zone of plastic deformation. 140

Figure 5.9: TKD scan results for a 1µm thick HS cantilever of aspect ratio B with plastic strain of 0.086. (a) Band contrast, (b) inverse pole figure along x_1, (c) GND density map [m^{-2}] according to equation (5.5), dislocation type maps for (d) A3-, (e) C3+, (f) D6+ and (g) E3+. Lateral dimensions in [µm].......... 142

Figure 5.10: Cantilever of 1µm thickness, DG orientation, aspect ratio B, plastic strain of 0.053. (a) GND density map. Line profiles along the black arrow for (b) total GND density and (c) some dislocation types. Densities in [m^{-2}] and lateral dimensions in [µm].......... 146

Figure 5.11: Cantilever of 1µm thickness, DG orientation and aspect ratio B, total plastic strain 0.071. (a) Band contrast map. Line profiles along the black arrows, which are sketched in (a), are shown for (b) the total GND density and (c) some selected dislocation types. The black arrows mark the line along which the profile plot is taken. Point *1* marks an intersection of bands. Densities in [m^{-2}] and lateral dimensions in [µm].......... 148

Figure 5.12: Cantilever of 1µm thickness, HS orientation and aspect ratio B, total plastic strain 0.086 (a) Band contrast, (b) GND density map with (c) zoom on the zone of plastic deformation with markings of relevant points in the profile plots. Two line profiles are taken: (d-e) and (f-g). (d) and (f) are overall GND densities while (e) and (g) show some prominent dislocation types. GND densities in [m^{-2}] and lateral dimensions in [µm].......... 153

Figure 5.13: Cantilever of 3µm thickness, HS orientation and aspect ratio B, total plastic strain 0.043. (a) GND density map (b) Band contrast showing a zoom onto the only prominent band structure. (c) line profile for overall GND density and (d) for some selected dislocation types taken along the black arrows in (a). Density values in [m^{-2}] and lateral dimensions in [µm]. 157

Figure 5.14: Cantilever of 3µm thickness, HS orientation and aspect ratio C, total remaining strain 0.05. (a, b) GND density maps with markings of relevant points in the profile plots. The GND density scale if different for (a) and (b). Profile plots for (c) overall GND density and (d) some selected dislocation types taken along the line marked by the black arrows in (a). Densities in [m^{-2}] and lateral dimensions in [µm]. 159

Figure 5.15: Inverse pole figure maps for the cantilever displayed in Fig.5.14 along (a) x_1, (b) x_2 and (c) x_3, respectively. Lateral dimensions in [µm]. ... 160

Figure 5.16: GND Densities obtained from TKD scans versus remaining plastic strain determined by optical profilometry. The density values are calculated as the medians of the averages of each visible dislocation band. Overall density refers to GND densities calculated via equation (5.5). The TKD scans of the cantilevers for each data point displayed in the figure is also shown in this chapter (Fig5.10-.514). 161

Figure 5.17: Inverse pole figure map of a cantilever of 3µm height, in HS orientation, aspect ratio B and a remaining strain of 0.05. Twin structures are marked by red arrows. 162

Figure 5.18: Inverse pole figure map of a cantilever of 3µm height, in HS orientation, aspect ratio B and a remaining strain of 0.05. Twin structures are marked by red arrows. 164

Figure 6.1: Schematic of the location of the dislocation types in HS and DG. During bending the rotation axis is around x_1. 170

Figure 6.2: Dislocation density evolution with increasing strain found with DDD for the individual glide systems. The curves are averaged over the results from 10 realizations. Note that their indices differ from experiments due to different axis convention. 172

Figure 6.3: A cut through one (a) DG and (b) one HS orientation simulation. Dislocations are colored according to their glide plane normal. The sample volume is colored according to the shear stress in bending direction......... 178

Figure 6.4: Lattice rotation angle around the bending axis for (a) DG and (b) HS orientation within slices of the x_1-x_3 plane (top) and x_1-x_2 plane (bottom). To the left of both plots is the fixed boundary condition and to the right, the wedge indent displacement is applied. The colors indicate the rotation angle, dots show the center of the corresponding voxels. 179
Figure 6.5: Schematic of the dislocation network formation. The lines correspond to the traces of high dislocation densities observed in experiments and simulations. (a), (c) and (e) show the situation during loading with increasing strain. (b), (d) and (f) display the situation for the arrangement shown on the left hand side after unloading. 180
Figure A.1: Setup and coordinate system chosen for DDD. 196

List of tables

Table 2.1: Schmid's factors *m* for the given orientations HS and DG following the Schmid-Boas notation. 34
Table 2.2: Cantilever dimensions in [µm] of the structures effectively used in this project. Note that these values are the ones used during lithography (i.e. from the layout), and not perfectly equal to the dimensions of the as-fabricated testing structures. 37
Table 3.1: Mean values of the geometric parameters and aspect ratios for all 24 categories of cantilevers in the as-fabricated state. Dimensions in [µm]. 72
Table 5.1: Dislocation types and their notation used in this project. 131
Table 5.2: Mean GND density for all dislocation types with non-zero GND density found in the visible dislocation bands belonging to the DG cantilevers displayed in Fig.5.10 and Fig5.11. The schematic below illustrates the planes and directions for DG geometry in the given coordinate system. 149
Table 5.3: Mean GND density for all dislocation types with non-zero GND density found in the visible dislocation bands belonging to the HS cantilevers displayed in Fig.5.12, Fig.5.13 and Fig5.14. The schematic below illustrates the planes and directions for HS geometry in the given coordinate system. 154
Table 5.4: Schmid law applied to partials for HS and DG orientation. Schmid-Boas notation is used for full dislocations while for partials Thompson's tetrahedron serves as a reference. 163

References

Armstrong, D. E. J., Wilkinson, A. J., & Roberts, S. G. (2011). Measuring anisotropy in Young's modulus of copper using microcantilever testing. *Journal of Materials Research*, *24*(11), 3268–3276.

Arzt, E. (1998). Size effects in materials due to microstructural and dimensional constraints: a comparative review. *Acta Materialia*, *46*(16), 5611–5626.

Dehm, G., Balk, T. J., Edongue, H. & Arzt, E. (2003). Small-scale plasticity in thin Cu and Al films, *70*, 412–424.

Ashby, M. F. (1970). The deformation of plastically non-homogeneous materials. *Philosophical Magazine*, *21*(January 2015), 399–424.

Baker, S. P., & Nix, W. D. (1994). Mechanical properties of compositionally modulated Au-Ni thin films: Nanoindentation and microcantilever deflection experiments. *Journal of Materials Research*, *9*(12), 3131–3144.

Baskes, M., Chen, S., & Cherne, F. (2002). Atomistic model of gallium. *Physical Review B*, *66*(10), 104107.

Bate, P. S., Knutsen, R. D., Brough, I., & Humphreys, F. J. (2005). The characterization of low-angle boundaries by EBSD. *Journal of Microscopy*, *220*(1), 36–46.

Bayerschen, E., Prahs, A., Wulfinghoff, S., Ziemann, M., Gruber, P. A., Walter, M., & Böhlke, T. (2016). Modeling contrary size effects of tensile- and torsion-loaded oligocrystalline gold microwires. *Journal of Materials Science*, *51*(16), 7451–7470.

Bei, H., Shim, S., George, E., Miller, M., Herbert, E., & Pharr, G. (2007). Compressive strengths of molybdenum alloy micro-pillars prepared using a new technique. *Scripta Materialia*, *57*(5), 397–400.

Borzenko, T. B., Koval, Y. I., & Kudryashov, V. A. (1994). Ion beam etching mechanism of PMMA based resists by noble gas ions. *Microelectronic Engineering*, *23*(1–4), 337–340.

Brenner, S. S. (1956). Tensile strength of whiskers. *Journal of Applied Physics*, *27*(12), 1484–1491.

Brodusch, N., Demers, H., & Gauvin, R. (2013). Nanometres-resolution Kikuchi patterns from materials science specimens with transmission electron forward scatter diffraction in the scanning electron microscope. *Journal of Microscopy*, *250*(1), 1–14.

Calcagnotto, M., Ponge, D., Demir, E., & Raabe, D. (2010). Orientation gradients and geometrically necessary dislocations in ultrafine grained dual-phase steels studied by 2D and 3D EBSD. *Materials Science and Engineering: A*, *527*(10–11), 2738–2746.

Carlton, C. E., & Ferreira, P. J. (2007). What is behind the inverse Hall-Petch effect in nanocrystalline materials? *Acta Materialia*, *55*(11), 3749–3756.

Chen, Y., Kraft, O., & Walter, M. (2015). Size effects in thin coarse-grained gold microwires under tensile and torsional loading. *Acta Materialia*, *87*, 78–85.

Demir, E., & Raabe, D. (2010). Mechanical and microstructural single-crystal Bauschinger effects: Observation of reversible plasticity in copper during bending. *Acta Materialia*, *58*(18), 6055–6063.

Demir, E., Raabe, D., & Roters, F. (2010). The mechanical size effect as a mean-field breakdown phenomenon: Example of microscale single crystal beam bending. *Acta Materialia*, *58*(5), 1876–1886.

Demir, E., Roters, F., & Raabe, D. (2010). Bending of single crystal microcantilever beams of cube orientation: Finite element model and experiments. *Journal of the Mechanics and Physics of Solids*, *58*(10), 1599–1612.

Diebels, S. (2005). *Vorlesungsmanuskript zur Technische Mechanik II Elastostatik*. Universität des Saarlandes.

Dimiduk, D. M., Uchic, M. D., & Parthasarathy, T. A. (2005). Size-affected single-slip behavior of pure nickel microcrystals. *Acta Materialia*, *53*(15), 4065–4077.

Dunstan, D. J. (2012). Critical thickness theory applied to micromechanical testing. *Advanced Engineering Materials*, *14*(11), 942–947.

Elwenspoek, M., & Jansen, H. V. (1998). *Silicon micromachining*. *Cambridge studies in semiconductor physics and microelectronic engineering*. Cambridge University Press.

Engler, O., & Randle, V. (2010). *Introduction to Texture Analysis*. *Handbook Of Texture Analysis*. CRC Press, Taylor & Francis Group. S. 41

Evans, A. G., & Stölken, J. S. (1998). A microbend test method for measuring the plasticity length scale. *Acta Materialia*, *46*(14), 5109–5115.

Fleck, N. A., & Hutchinson, J. W. (1997). Strain gradient plasticity. *Advances in Applied Mechanics*, *33*(C), 295–361.

Fleck, N. A., Muller, G. M., Ashby, M. F., & Hutchinson, J. W. (1994). Strain gradient plasticity: Theory and experiment. *Acta Metallurgica et Materialia*.

Fleischer, R. L. (1963). Substitutional solution hardening. *Acta Metallurgica*, *11*, 203--209.

Frank, F. C., & van der Merwe, J. H. (1949). One-Dimensional Dislocations. II. Misfitting Monolayers and Oriented Overgrowth. *Proceedings of the Royal Society of London A: Mathematical, Physical and Engineering Sciences*, *198*(1053), 216–225.

Gao, H., Huang, Y., & Nix, W. D. (1999). Modeling Plasticity at the Micrometer Scale. *Naturwissenschaften*, *86*(11), 507–515.

Giannuzzi, L. A., & Stevie, F. A. (2005). *Introduction to focused ion beams: Instrumentation, theory, techniques and practice*. *Introduction to Focused Ion Beams: Instrumentation, Theory, Techniques and Practice*. Springer US. S.25

Giessen, E. Van Der, & Needleman, a. (1999). Discrete dislocation plasticity: a simple planar model. *Modelling and Simulation in Materials Science and Engineering*, *3*, 689–735.

Gong, J., & Wilkinson, A. J. (2009). Anisotropy in the plastic flow properties of single-crystal alpha titanium determined from micro-cantilever beams. *Acta Materialia*, *57*(19), 5693–5705.

Greer, J., & Nix, W. (2006). Nanoscale gold pillars strengthened through dislocation starvation. *Physical Review B*, *73*(24), 245410.

Gross, D., Hauger, W., Schröder, J., & Wall, W. A. (2009). *Technische Mechanik 2. Elastostatik*. Springer. S. 155

Gunnaes, A. E., Karlsen, O. B., Olsen, A., & Zagierski, P. T. (2000). Phase relations and crystal structures in the Ag-Ga system. *Journal of Alloys and Compounds*, *297*(1–2), 144–155.

Hall, E. O. (1951). The Deformation and Ageing of Mild Steel: III Discussion of Results. *Proceedings of the Physical Society. Section B*, *64*(9), 747.

Huang, Y., Gao, H., Nix, W. D., & Hutchinson, J. W. (2000). Mechanism-based strain gradient plasticityÐII . Analysis. *Journal of the Mechanics and Physics of Solids*, *48*(1), 99–128.

Hur, T.-B., Kim, H., & Blachere, J. (2007). Epitaxial growth of Ag films on native-oxide-covered Si substrates. *Physical Review B*, *75*(20), 205306.

Hutchinson, J. W. (2000). Plasticity at the micron scale. *International Journal of Solids and Structures*, *37*(1–2), 225–238.

Iqbal, F., Ast, J., G??ken, M., & Durst, K. (2012). In situ micro-cantilever tests to study fracture properties of NiAl single crystals. *Acta Materialia*, *60*(3), 1193–1200.

Jahan, M. P., Rahman, M., & Wong, Y. S. (2011). A review on the conventional and micro-electrodischarge machining of tungsten carbide. *International Journal of Machine Tools and Manufacture*, *51*(12), 837–858.

Keller, R.-M., Baker, S. P., & Arzt, E. (1998). Quantitative analysis of strengthening mechanisms in thin Cu films: Effects of film thickness, grain size, and passivation. *Journal of Materials Research*, *13*(5), 1307–1317.

Keller, R. R., & Geiss, R. H. (2012). Transmission EBSD from 10 nm domains in a scanning electron microscope. *Journal of Microscopy*, *245*(3), 245–251

Kheradmand, N. (2012). *Grain boundary-dislocation interaction : A local investigation via micron-sized bicrystals*. Universität des Saarlandes. S. 60

Kiener, D., & Minor, A. M. (2011). Source truncation and exhaustion: Insights from quantitative in situ TEM tensile testing. *Nano Letters*, *11*(9), 3816–3820.

Kiener, D., Motz, C., Grosinger, W., Weygand, D., & Pippan, R. (2010). Cyclic response of copper single crystal micro-beams. *Scripta Materialia*, *63*(5), 500–503.

Kiener, D., Motz, C., Rester, M., Jenko, M., & Dehm, G. (2007). FIB damage of Cu and possible consequences for miniaturized mechanical tests. *Materials Science and Engineering A*, *459*, 262–272.

Kirchlechner, C., Grosinger, W., Kapp, M. W., Imrich, P. J., Micha, J.-S., Ulrich, O., … Motz, C. (2012). Investigation of reversible plasticity in a micron-sized, single crystalline copper bending beam by X-ray µ Laue diffraction. *Philosophical Magazine*, *92*(25–27), 3231–3242.

Kirchlechner, C., Keckes, J., Micha, J.-S., & Dehm, G. (2011). In Situ µLaue: Instrumental Setup for the Deformation of Micron Sized Samples. *Advanced Engineering Materials*, *13*(8), 837–844.

Kisielowski, C. (2015). Observing Atoms at Work by Controlling Beam-Sample Interactions. *Advanced Materials*, *27*(38), 5838–5844.

Kittel. (2010). *Introduction to Solid State Physics*. *Solid-State Physics (Fourth Extensively Updated and Enlarged Edition): An Introduction to Principles of Materials Science*. S. 96

Koval, Y. (2004). Mechanism of etching and surface relief development of PMMA under low-energy ion bombardment. *Journal of Vacuum Science & Technology B: Microelectronics and Nanometer Structures*, *22*(2), 843.

Koval, Y., Borzenko, T., & Dubonos, S. (2003). Use of polymethylmethacrylate for pattern transfer by ion beam etching: Improvement of etching homogeneity and patterning quality. *Journal of Vacuum Science & Technology B: Microelectronics and Nanometer Structures*, *21*(5), 2217.

Kraft, O., Gruber, P. A., Mönig, R., & Weygand, D. (2010). Plasticity in Confined Dimensions. *Annual Review of Materials Research*, *40*(1), 293–317.

Kraft, O., & Volkert, C. A. (2001). Mechanical Testing of Thin Films and Small Structures. *Advanced Engineering Materials*, *3*(3), 99–110.

Kröner, E. (1958). *Allgemeine Kontinuumstheorie der Versetzungen und Eigenspannungen*. Springer Berlin.

Kubin, L. ., & Mortensen, a. (2003). Geometrically necessary dislocations and strain-gradient plasticity: a few critical issues. *Scripta Materialia*, *48*(2), 119–125.

Kupka, D., Huber, N., & Lilleodden, E. T. (2014). A combined experimental-numerical approach for elasto-plastic fracture of individual grain boundaries. *Journal of the Mechanics and Physics of Solids*, *64*, 455–467.

Kupka, D., & Lilleodden, E. T. (2011). Mechanical Testing of Solid–Solid Interfaces at the Microscale. *Experimental Mechanics*, *52*(6), 649–658.

Kysar, J. W., Saito, Y., Oztop, M. S., Lee, D., & Huh, W. T. (2010). Experimental lower bounds on geometrically necessary dislocation density. *International Journal of Plasticity*, *26*(8), 1097–1123.

Littlewood, P. D., Britton, T. B., & Wilkinson, a. J. (2011). Geometrically necessary dislocation density distributions in Ti–6Al–4V deformed in tension. *Acta Materialia*, *59*(16), 6489–6500.

Lohmiller, J., Baumbusch, R., Kerber, M. B., Castrup, A., Hahn, H., Schafler, E., … Gruber, P. A. (2013). Following the deformation behavior of nanocrystalline Pd films on polyimide substrates using in situ synchrotron XRD. *Mechanics of Materials*, *67*, 65–73.

Maaß, R., Van Petegem, S., Borca, C. N., & Van Swygenhoven, H. (2009). In situ Laue diffraction of metallic micropillars. *Materials Science and Engineering: A*, *524*(1–2), 40–45.

Matoy, K., Schönherr, H., Detzel, T., Schöberl, T., Pippan, R., Motz, C., & Dehm, G. (2009). A comparative micro-cantilever study of the mechanical behavior of silicon based passivation films. *Thin Solid Films*, *518*(1), 247–256.

Matthews, J. W., & Crawford, J. L. (1970). Accomodation of misfit between single-crystal films of nickel and copper. *Thin Solid Films*, *5*(3), 187–198.

Meyers, M. a., Mishra, a., & Benson, D. J. (2006). Mechanical properties of nanocrystalline materials. *Progress in Materials Science*, *51*, 427–556.

Motz, C., & Dunstan, D. J. (2012). Observation of the critical thickness phenomenon in dislocation dynamics simulation of microbeam bending. *Acta Materialia*, *60*(4), 1603–1609.

Motz, C., Schöberl, T., & Pippan, R. (2005). Mechanical properties of micro-sized copper bending beams machined by the focused ion beam technique. *Acta Materialia*, *53*(15), 4269–4279.

Motz, C., Weygand, D., Senger, J., & Gumbsch, P. (2008). Micro-bending tests: A comparison between three-dimensional discrete dislocation dynamics simulations and experiments. *Acta Materialia*, *56*(9), 1942–1955.

Nayak, M., Lodha, G. S., Sinha, A. K., Nandedkar, R. V., & Shivashankar, S. A. (2006). Determination of interlayer composition at buried interfaces using soft x-ray resonant reflectivity. *Applied Physics Letters*, *89*(18), 12–15.

Ng, K. S., & Ngan, A. H. W. (2008). Stochastic nature of plasticity of aluminum micro-pillars. *Acta Materialia*, *56*(8), 1712–1720.

Nye, J. F. (1953). Some geometrical relations in dislocated crystals. *Acta Metallurgica*.

Oh, S. R., Yao, K., & Tay, F. E. H. (2013). Fabrication of piezoelectric P(VDF-TrFE) microcantilevers by wafer-level surface micromachining. *Journal of Micromechanics and Microengineering*, *23*(9), 95023.

Okamoto, H. (1991). Phase Diagram Updates. *Journal of Phase Equilibria*, *12*(3), 390.

Orowan, E. (1934). Zur Kristallplastizität. III. Über den Mechanismus des Gleitvorganges. *Zeitschrift Für Physik*, *89*(9–10), 634–659.

Pande, C. S., & Cooper, K. P. (2009). Nanomechanics of Hall-Petch relationship in nanocrystalline materials. *Progress in Materials Science*, *54*(6), 689–706.

Pantleon, W. (2008). Resolving the geometrically necessary dislocation content by conventional electron backscattering diffraction. *Scripta Materialia*, *58*(11), 994–997.

Pecholt, B., & Molian, P. (2011). Nanoindentation of laser micromachined 3C-SiC thin film micro-cantilevers. *Materials and Design*, *32*(6), 3414–3420.

Petch, N. J. (1953). The Cleavage Strength of Polycrystals. *J. Iron Steel Inst*, *174*, 25–28.

Phillips, V. A., & Dash, W. C. (1962). Electron Microscopy of Prismatic Dislocations in Silicon. *Journal of Applied Physics*, *33*(2), 568.

Polanyi, M. (1934). ??ber eine Art Gitterst??rung, die einen Kristall plastisch machen k??nnte. *Zeitschrift F??r Physik*, *89*(9–10), 660–664.

Rao, S. I., Dimiduk, D. M., Parthasarathy, T. A., Uchic, M. D., Tang, M., & Woodward, C. (2008). Athermal mechanisms of size-dependent crystal flow gleaned from three-dimensional discrete dislocation simulations. *Acta Materialia*, *56*(13), 3245–3259.

Schmid, E., & Boas, W. (1935). *Kristallplastizität mit besonderer Berücksichtigung der Metalle*. (F. Hund & W. Mark, Eds.)*Springer-Verlag Berlin Heidelberg GmbH*. Springer-Verlag Berlin Heidelberg GmbH.

Schwartz, A. J., Kumar, M., Adams, B. L., & Field, D. P. (2009). *Electron Backscatter Diffraction in Materials Science*. Springer.

Seidel, H., Csepregi, L., & Heuberge, A. (1990). Anisotropic Etching of Crystalline Silicon in Alkaline Solutions. *J. Electrochem. Soc*, *137*(11), 249–260.

Senger, J., Weygand, D., Motz, C., Gumbsch, P., & Kraft, O. (2011). Aspect ratio and stochastic effects in the plasticity of uniformly loaded micrometer-sized specimens. *Acta Materialia*, *59*(8), 2937–2947.

Shimizu, R., & Ze-Jun, D. (1999). Monte Carlo modelling of electron-solid interactions. *Reports on Progress in Physics*, *55*(4), 487–531.

Sökmen, Ü., Stranz, a, Waag, a, Ababneh, a, Seidel, H., Schmid, U., & Peiner, E. (2010). Evaluation of resonating Si cantilevers sputter-deposited with AlN piezoelectric thin films for mass sensing applications. *Journal of Micromechanics and Microengineering*, *20*(6), 64007.

Stricker, M., Weygand, D., & Gumbsch, P. (2017). Irreversibility of dislocation motion under cyclic loading due to strain gradients. *Scripta Materialia*, *129*, 69–73.

Subramanian, P. R., Massalski, T. B., & Laughlin, D. E. (1988). Thermodynamic aspects of massive transformations in the CuGa and CuZn systems. *Acta Metallurgica*, *36*(4), 937–943.

Sun, J. L., Trimby, P. W., Si, X., Liao, X. Z., Tao, N. R., & Wang, J. T. (2013). Nano twins in ultrafine-grained Ti processed by dynamic plastic deformation. *Scripta Materialia*, *68*(7), 475–478.

Suzuki, S. (2013). Features of Transmission EBSD and its Application. *Jom*, *65*(9), 1254–1263.

Tarleton, E., Balint, D. S., Gong, J., & Wilkinson, a. J. (2015). A discrete dislocation plasticity study of the micro-cantilever size effect. *Acta Materialia*, *88*, 271–282.

Taylor, G. I. (1934). The Mechanism of Plastic Deformation of Crystals. Part I. Theoretical. *Proceedings of the Royal Society A: Mathematical, Physical and Engineering Sciences*, *145*(855), 362–387.

Taylor, P., & Ashby, M. F. (2006). The deformation of plastically non-homogeneous materials, (March 2012), 37–41.

Thompson, C. V. (1993). The yield stress of polycrystalline thin films. *Journal of Materials Research*.

Trimby, P. W. (2012). Orientation mapping of nanostructured materials using transmission Kikuchi diffraction in the scanning electron microscope. *Ultramicroscopy*, *120*, 16–24.

Uchic, M. D., Dimiduk, D. M., Florando, J. N., & Nix, W. D. (2004). Sample dimensions influence strength and crystal plasticity. *Science (New York, N.Y.)*, *305*(5686), 986–9.

Uchic, M. D., Dimiduk, D. M., Florando, J. N., & Nix, W. D. (2012). Sample Dimensions Influence Strength and Crystal Plasticity, *305*(5686), 986–989.

Uchic, M. D., Shade, P. a., & Dimiduk, D. M. (2009). Plasticity of Micrometer-Scale Single Crystals in Compression. *Annual Review of Materials Research*, *39*(1), 361–386.

Voce, E. (1948). The relationship between stress and strain for homogeneous deformation. *J Inst Met*, *74*, 537–562.

Weihs, T. P., Hong, S., Bravman, J. C., & Nix, W. D. (1988). Mechanical deflection of cantilever microbeams: A new technique for testing the mechanical properties of thin films. *Journal of Materials Research*.

Weygand, D., Friedman, L. H., Giessen, E. Van Der, & Needleman, a. (2002). Aspects of boundary-value problem solutions with three-dimensional dislocation dynamics. *Modelling and Simulation in Materials Science and Engineering*, *10*, 437–468.

Weygand, D., & Gumbsch, P. (2005). Study of dislocation reactions and rearrangements under different loading conditions. *Materials Science and Engineering A*, *400–401*, 158–161.

Wilkinson, A. J. (2001). A new method for determining small misorientations from electron back scatter diffraction patterns. *Scripta Materialia*, *44*(10), 2379–2385.

Wilkinson, A. J., Clarke, E. E., Britton, T. B., Littlewood, P., & Karamched, P. S. (2010). High-resolution electron backscatter diffraction: an emerging tool for studying local deformation. *The Journal of Strain Analysis for Engineering Design*, *45*(5), 365–376.

Williams, D. B., & Carter, C. B. (1996). *Transmission Electron Microscopy*. *International ophthalmology clinics* (Vol. 13). Springer US.

Wolff, S., Lägel, B., & Trellenkamp, S. (2010). Incident angle dependent damage of PMMA during Ar+-ion beam etching. *Microelectronic Engineering*, *87*(5–8), 1444–1446.

Yang, W., Lambeth, D. N., Tang, L., & Laughlin, D. E. (1997). Epitaxial Ag templates on Si(001) for bicrystal CoCrTa media. *Journal of Applied Physics*, *81*(1), 4370.

Yu, Q., Legros, M., & Minor, a. M. (2015). In situ TEM nanomechanics. *MRS Bulletin*, *40*(1), 62–70.

Zaefferer, S. (2011). A critical review of orientation microscopy in SEM and TEM. *Crystal Research and Technology*, *46*(6), 607–628.

Zhu, T. T., Bushby, A. J., & Dunstan, D. J. (2008). Materials mechanical size effects: a review. *Materials Technology: Advanced Performance Materials*, *23*(4), 193–209.

Ziemann, M., Chen, Y., Kraft, O., Bayerschen, E., Wulfinghoff, S., Kirchlechner, C., Gruber, P. A. (2015). Deformation patterns in cross-sections of twisted bamboo-structured Au microwires. *Acta Materialia*, *97*, 216–222.

Schriftenreihe des Instituts für Angewandte Materialien

ISSN 2192-9963

Band 1 Prachai Norajitra
Divertor Development for a Future Fusion Power Plant. 2011
ISBN 978-3-86644-738-7

Band 2 Jürgen Prokop
Entwicklung von Spritzgießsonderverfahren zur Herstellung von Mikrobauteilen durch galvanische Replikation. 2011
ISBN 978-3-86644-755-4

Band 3 Theo Fett
New contributions to R-curves and bridging stresses – Applications of weight functions. 2012
ISBN 978-3-86644-836-0

Band 4 Jérôme Acker
Einfluss des Alkali/Niob-Verhältnisses und der Kupferdotierung auf das Sinterverhalten, die Strukturbildung und die Mikrostruktur von bleifreier Piezokeramik $(K_{0,5}Na_{0,5})NbO_3$. 2012
ISBN 978-3-86644-867-4

Band 5 Holger Schwaab
Nichtlineare Modellierung von Ferroelektrika unter Berücksichtigung der elektrischen Leitfähigkeit. 2012
ISBN 978-3-86644-869-8

Band 6 Christian Dethloff
Modeling of Helium Bubble Nucleation and Growth in Neutron Irradiated RAFM Steels. 2012
ISBN 978-3-86644-901-5

Band 7 Jens Reiser
Duktilisierung von Wolfram. Synthese, Analyse und Charakterisierung von Wolframlaminaten aus Wolframfolie. 2012
ISBN 978-3-86644-902-2

Band 8 Andreas Sedlmayr
Experimental Investigations of Deformation Pathways in Nanowires. 2012
ISBN 978-3-86644-905-3

Die Bände sind unter www.ksp.kit.edu als PDF frei verfügbar oder als Druckausgabe bestellbar.

Band 9 Matthias Friedrich Funk
Microstructural stability of nanostructured fcc metals during cyclic deformation and fatigue. 2012
ISBN 978-3-86644-918-3

Band 10 Maximilian Schwenk
Entwicklung und Validierung eines numerischen Simulationsmodells zur Beschreibung der induktiven Ein- und Zweifrequenzrandschichthärtung am Beispiel von vergütetem 42CrMo4. 2012
ISBN 978-3-86644-929-9

Band 11 Matthias Merzkirch
Verformungs- und Schädigungsverhalten der verbundstranggepressten, federstahldrahtverstärkten Aluminiumlegierung EN AW-6082. 2012
ISBN 978-3-86644-933-6

Band 12 Thilo Hammers
Wärmebehandlung und Recken von verbundstranggepressten Luftfahrtprofilen. 2013
ISBN 978-3-86644-947-3

Band 13 Jochen Lohmiller
Investigation of deformation mechanisms in nanocrystalline metals and alloys by in situ synchrotron X-ray diffraction. 2013
ISBN 978-3-86644-962-6

Band 14 Simone Schreijäg
Microstructure and Mechanical Behavior of Deep Drawing DC04 Steel at Different Length Scales. 2013
ISBN 978-3-86644-967-1

Band 15 Zhiming Chen
Modelling the plastic deformation of iron. 2013
ISBN 978-3-86644-968-8

Band 16 Abdullah Fatih Çetinel
Oberflächendefektausheilung und Festigkeitssteigerung von niederdruckspritzgegossenen Mikrobiegebalken aus Zirkoniumdioxid. 2013
ISBN 978-3-86644-976-3

Band 17 Thomas Weber
Entwicklung und Optimierung von gradierten Wolfram/EUROFER97-Verbindungen für Divertorkomponenten. 2013
ISBN 978-3-86644-993-0

Die Bände sind unter www.ksp.kit.edu als PDF frei verfügbar oder als Druckausgabe bestellbar.

Band 18 Melanie Senn
Optimale Prozessführung mit merkmalsbasierter Zustandsverfolgung. 2013
ISBN 978-3-7315-0004-9

Band 19 Christian Mennerich
Phase-field modeling of multi-domain evolution in ferromagnetic shape memory alloys and of polycrystalline thin film growth. 2013
ISBN 978-3-7315-0009-4

Band 20 Spyridon Korres
On-Line Topographic Measurements of Lubricated Metallic Sliding Surfaces. 2013
ISBN 978-3-7315-0017-9

Band 21 Abhik Narayan Choudhury
Quantitative phase-field model for phase transformations in multi-component alloys. 2013
ISBN 978-3-7315-0020-9

Band 22 Oliver Ulrich
Isothermes und thermisch-mechanisches Ermüdungsverhalten von Verbundwerkstoffen mit Durchdringungsgefüge (Preform-MMCs). 2013
ISBN 978-3-7315-0024-7

Band 23 Sofie Burger
High Cycle Fatigue of Al and Cu Thin Films by a Novel High-Throughput Method. 2013
ISBN 978-3-7315-0025-4

Band 24 Michael Teutsch
Entwicklung von elektrochemisch abgeschiedenem LIGA-Ni-Al für Hochtemperatur-MEMS-Anwendungen. 2013
ISBN 978-3-7315-0026-1

Band 25 Wolfgang Rheinheimer
Zur Grenzflächenanisotropie von $SrTiO_3$. 2013
ISBN 978-3-7315-0027-8

Band 26 Ying Chen
Deformation Behavior of Thin Metallic Wires under Tensile and Torsional Loadings. 2013
ISBN 978-3-7315-0049-0

Band 27 Sascha Haller
Gestaltfindung: Untersuchungen zur Kraftkegelmethode. 2013
ISBN 978-3-7315-0050-6

Band 28 Nicht erschienen

Band 29 Gunnar Picht
Einfluss der Korngröße auf ferroelektrische Eigenschaften dotierter $Pb(Zr_{1-x}Ti_x)O_3$ Materialien. 2013
ISBN 978-3-7315-0106-0

Band 30 Esther Held
Eigenspannungsanalyse an Schichtverbunden mittels inkrementeller Bohrlochmethode. 2013
ISBN 978-3-7315-0127-5

Band 31 Pei He
On the structure-property correlation and the evolution of Nanofeatures in 12-13.5% Cr oxide dispersion strengthened ferritic steels. 2014
ISBN 978-3-7315-0141-1

Band 32 Jan Hoffmann
Ferritische ODS-Stähle – Herstellung, Umformung und Strukturanalyse. 2014
ISBN 978-3-7315-0157-2

Band 33 Wiebke Sittel
Entwicklung und Optimierung des Diffusionsschweißens von ODS Legierungen. 2014
ISBN 978-3-7315-0182-4

Band 34 Osama Khalil
Isothermes Kurzzeitermüdungsverhalten der hoch-warmfesten Aluminium-Knetlegierung 2618A (AlCu2Mg1,5Ni). 2014
ISBN 978-3-7315-0208-1

Band 35 Magalie Huttin
Phase-field modeling of the influence of mechanical stresses on charging and discharging processes in lithium ion batteries. 2014
ISBN 978-3-7315-0213-5

Band 36 Christoph Hage
Grundlegende Aspekte des 2K-Metallpulverspritzgießens. 2014
ISBN 978-3-7315-0217-3

Band 37 Bartłomiej Albiński
Instrumentierte Eindringprüfung bei Hochtemperatur für die Charakterisierung bestrahlter Materialien. 2014
ISBN 978-3-7315-0221-0

Band 38 Tim Feser
Untersuchungen zum Einlaufverhalten binärer alpha-Messinglegierungen unter Ölschmierung in Abhängigkeit des Zinkgehaltes. 2014
ISBN 978-3-7315-0224-1

Band 39 Jörg Ettrich
Fluid Flow and Heat Transfer in Cellular Solids. 2014
ISBN 978-3-7315-0241-8

Band 40 Melanie Syha
Microstructure evolution in strontium titanate Investigated by means of grain growth simulations and x-ray diffraction contrast tomography experiments. 2014
ISBN 978-3-7315-0242-5

Band 41 Thomas Haas
Mechanische Zuverlässigkeit von gedruckten und gasförmig abgeschiedenen Schichten auf flexiblem Substrat. 2014
ISBN 978-3-7315-0250-0

Band 42 Aron Kneer
Numerische Untersuchung des Wärmeübertragungsverhaltens in unterschiedlichen porösen Medien. 2014
ISBN 978-3-7315-0252-4

Band 43 Manuel Feuchter
Investigations on Joule heating applications by multiphysical continuum simulations in nanoscale systems. 2014
ISBN 978-3-7315-0261-6

Band 44 Alexander Vondrous
Grain growth behavior and efficient large scale simulations of recrystallization with the phase-field method. 2014
ISBN 978-3-7315-0280-7

Band 45 Tobias Kennerknecht
Fatigue of Micro Molded Materials – Aluminum Bronze and Yttria Stabilized Zirconia. 2014
ISBN 978-3-7315-0293-7

Die Bände sind unter www.ksp.kit.edu als PDF frei verfügbar oder als Druckausgabe bestellbar.

Band 46 Christopher Scherr
Elektrochemisches Verhalten von Lithium-Schwefel-Zellen mit unterschiedlicher Kathodenstruktur. 2015
ISBN 978-3-7315-0296-8

Band 47 Konstantin Frölich
Der Decal-Prozess zur Herstellung katalysatorbeschichteter Membranen für PEM-Brennstoffzellen. 2015
ISBN 978-3-7315-0334-7

Band 48 Benedikt Haspel
Werkstoffanalytische Betrachtung der Eigenschaften von mittels neuartiger RTM-Fertigungsprozesse hergestellten glasfaserverstärkten Polymerverbunden. 2015
ISBN 978-3-7315-0337-8

Band 49 Marco Berghoff
Skalenübergreifende Modellierung und Optimierung vom atomistischen kristallinen Phasenfeldmodell bis zur mesoskopischen Phasenfeldmethode. 2015
ISBN 978-3-7315-0416-0

Band 50 Michael Selzer
Mechanische und Strömungsmechanische Topologieoptimierung mit der Phasenfeldmethode. 2016
ISBN 978-3-7315-0431-3

Band 51 Michael Mahler
Entwicklung einer Auswertemethode für bruchmechanische Versuche an kleinen Proben auf der Basis eines Kohäsivzonenmodells. 2016
ISBN 978-3-7315-0441-2

Band 52 Christoph Bohnert
Numerische Untersuchung des Verformungs- und Bruchverhaltens von einkristallinem Wolfram auf mikroskopischer Ebene. 2016
ISBN 978-3-7315-0444-3

Band 53 Stefan Guth
Schädigung und Lebensdauer von Nickelbasislegierungen unter thermisch-mechanischer Ermüdungsbeanspruchung bei verschiedenen Phasenlagen. 2016
ISBN 978-3-7315-0445-0

Die Bände sind unter www.ksp.kit.edu als PDF frei verfügbar oder als Druckausgabe bestellbar.

Band 54 Markus Klinsmann
The Effects of Internal Stress and Lithium Transport on Fracture in Storage Materials in Lithium-Ion Batteries. 2016
ISBN 978-3-7315-0455-9

Band 55 Thomas Straub
Experimental Investigation of Crack Initiation in Face-Centered Cubic Materials in the High and Very High Cycle Fatigue Regime. 2016
ISBN 978-3-7315-0471-9

Band 56 Maren Lepple
Kupfer- und Eisenoxide als Konversions-Elektrodenmaterialien für Lithium-Ionen-Batterien: Thermodynamische und Elektrochemische Untersuchungen. 2016
ISBN 978-3-7315-0482-5

Band 57 Stefan Andreas Slaby
Charakterisierung und Bewertung der Zug- und Ermüdungseigenschaften von Mikrobauteilen aus 17-4PH Edelstahl. Ein Vergleich von mikropulverspritzgegossenem und konventionell hergestelltem Material. 2017
ISBN 978-3-7315-0484-9

Band 58 Kumar Ankit
Phase-field modeling of microstructural pattern formation in alloys and geological veins. 2016
ISBN 978-3-7315-0491-7

Band 59 Kuo Zhang
Characterization and Modeling of the Ratcheting Behavior of the Ferritic-Martensitic Steel P91. 2017
ISBN 978-3-7315-0503-7

Band 60 Jens Bauer
Mechanische Metamaterialien – Hohe Festigkeit und niedrige Dichte durch Mikroarchitektur und Materialdesign. 2017
ISBN 978-3-7315-0506-8

Band 61 Fabian Lemke
Untersuchung des Sinterverhaltens von $SrTiO_3$ unter Berücksichtigung der Defektchemie. 2016
ISBN 978-3-7315-0510-5

Band 62 Johannes Kümmel
Detaillierte Analyse der Aufbauschneidenbildung bei der Trockenzerspanung von Stahl C45E mit Berücksichtigung des Werkzeugverschleißes. 2016
ISBN 978-3-7315-0518-1

Band 63 László Hagymási
Modellierung der Stoffübertragung beim Niederdruckcarbonitrieren mit Ammoniak und Acetylen. 2016
ISBN 978-3-7315-0568-6

Band 64 Reza Eslami
A novel micro-mechanical model for prediction of multiaxial high cycle fatigue at small scales. 2017
ISBN 978-3-7315-0583-9

Band 65 Sebastian Schulz
Phase-field simulations of multi-component solidification and coarsening based on thermodynamic datasets. 2017
ISBN 978-3-7315-0618-8

Band 66 Markus Stricker
Die Übertragung von mikrostrukturellen Eigenschaften aus der diskreten Versetzungsdynamik in Kontinuumsbeschreibungen. 2017
ISBN 978-3-7315-0658-4

Band 67 Luis Straßberger
Untersuchung und Modellierung des viskoplastischen Verformungsverhaltens oxidpartikelverstärkter Stähle. 2017
ISBN 978-3-7315-0674-4

Band 68 Mark Wobrock
Microplasticity of idealized single crystalline Ag cantilevers characterized with methods of high resolution. 2017
ISBN 978-3-7315-0682-9

Die Bände sind unter www.ksp.kit.edu als PDF frei verfügbar oder als Druckausgabe bestellbar.

KARLSRUHER INSTITUT FÜR TECHNOLOGIE (KIT)
SCHRIFTENREIHE DES INSTITUTS FÜR ANGEWANDTE MATERIALIEN

Single crystalline, µm-sized cantilevers are fabricated out of epitaxially grown Ag thin films by a lithography-based procedure. The cantilevers have two different crystallographic orientations and are deflected by a nanoindenter system. The mechanical properties are determined and prior to deformation, some samples are contaminated with Ga+ ions which allows quantifying the changes induced during conventional Focused Ion Beam (FIB) fabrication. The microstructure of the plastically deformed cantilevers is investigated using transmission Kikuchi diffraction (TKD), which is performed on the cantilever cross section. Using a minimization approach based on Nye's tensor, dislocation structures can be distinguished by their respective Burgers and line vector and an estimation of their individual dislocation density is given. In addition to this experimental investigation, 3D discrete dislocation dynamics simulations (DDD) are performed to analyze the evolution of dislocation structures in even more detail. A mechanism to explain the formation of dislocation networks upon loading is suggested based on the results from experiments and simulations.

ISBN 978-3-7315-0682-9
9 783731 506829 >

Gedruckt auf FSC-zertifiziertem Papier

ISSN 2192-9963
ISBN 978-3-7315-0682-9